Integral bridges

A fundamental approach to the time-temperature loading problem

George L. England, Neil C. M. Tsang and David I. Bush

Imperial College
OF SCIENCE, TECHNOLOGY AND MEDICINE

HIGHWAYS
AGENCY

Contents

Part 1
The integral bridge

1 Introduction

An integral bridge is constructed without movement joints at the junction of the deck with the abutments, i.e. the construction is continuous. In its simplest form, therefore, an integral bridge may be viewed as a portal frame structure. In detail, several distinct forms can be identified by the height and stiffness of the abutments and whether or not a spread footing forms part of the construction.

The lateral loading on the abutments from the backfill soil is important but cannot be determined simply from statical calculations. The stresses at the soil–abutment interface are governed by a complex soil–structure interaction defined in terms of cyclic thermal movements (expansion and contraction) of the bridge deck, which result from solar heating. Knowledge of bridge temperatures and the manner in which they change on a daily and seasonal basis, together with an understanding of soil behaviour under cyclically imposed displacements at the soil–abutment boundary is therefore necessary when conducting design calculations.

It is known from the observed behaviour of circular biological filter bed retaining walls (CIRIA, 1976; England, 1994) and from site data from bridge abutments (Broms and Ingleson, 1972) that an escalation in the compressive soil–wall stresses occurs during successive temperature cycles, while the soil undergoes extensional straining. Card and Carder (1993) have also reported cases for related subjects with a detailed review of the problems associated with integral bridge abutment walls. Springman *et al.* (1996) confirmed the existence of stress escalation on retaining wall abutments in model centrifuge tests. The paradoxical feature of increasing compressive stresses during extensional straining results from the frictional flow and incremental ratcheting strain properties of the granular backfill material (England *et al.*, 1995). It is this special behaviour which precludes the ability to make sensible stress predictions from monotonic stress–strain data for the soil.

1.1 Objectives

The overall aim of the project was to produce guidance for bridge designers, by addressing the thermally induced soil–structure interaction problem created by environmental changes of temperature and the associated cyclic displacements imposed on the granular backfill to integral bridge abutments. The specific objectives of the research project were to:

(*a*) identify the governing soil parameters and their inter-relationships;
(*b*) develop a better theoretical understanding of the cyclic performance of the backfill soil, when in contact with a 'stiff' structure;
(*c*) develop numerical modelling procedures to predict the interactive soil–structure behaviour; and
(*d*) identify and quantify the controlling features of bridge structures relevant to the interaction problem.

1.2 Scope of the investigation

- The investigation comprised three parts:
  - theoretical analyses;
  - experimental results from soil and model retaining wall tests (done at University College London); and
  - numerical studies.
- Primary investigations were made of the escalation in lateral earth pressure behind the abutments to integral bridges. In addition, studies to determine the character of the deformations in the backfill were also done. Finally, an assessment was made of the foundation stresses and settlement of integral bridge abutments with strip footings. Some additional comments relate to the behaviour of a sheet pile abutment retaining wall. In all cases the approach embankment was assumed to be a drained granular material with a uniformly level top pavement.
- A stiff concrete abutment wall with a pinned base was considered in detail. Some comparisons of behaviour with the softer steel sheet pile cantilever wall were made and are commented on here, but no detailed studies are reported for the latter type of structure.
- Temperature data for UK conditions, as reviewed by Emerson (1976), form the basis of the input data for the determination of thermally induced cyclic strains. The combined influences of seasonal and daily temperature changes were considered theoretically.
- A retaining wall apparatus (designed for single-cycle operation) was used to perform one carefully chosen double-cycle test in order to indicate the nature of the interaction between daily and seasonal temperature cycles, and to compare the results with those obtained in single cycle tests of various amplitude fluctuating wall displacements.

1.3 The soil–structure interaction problem

- The integral bridge abutment considered was of the stiff type, constructed as a concrete wall and pinned to a strip footing (Figure 1.1).
- The longitudinal thermal movement of the bridge deck was assumed to be symmetrically shared by the two abutment walls, which were perpendicular to the longitudinal direction of the bridge deck (i.e. there was no skew). No horizontal movement of the pad footing was considered.
- The major investigation was focused on 40 and 60 m span bridges, which are currently identified in BA 42 as the limit for integral bridge design. Some longer bridges (100 and 160 m) are also considered here in order to investigate behavioural trends and to make sensible comparisons, including the possible uneven sharing of bridge movements between abutments.
- The soil–abutment interface was assumed to be smooth and to develop no friction. The soil behind and close to the wall was then idealized as being subjected to 90° jump changes in the principal stress directions during wall rotations. A detailed description of soil behaviour under this type of cyclic stressing is given in Part 2 of this book. Figure 1.2 shows the cyclic stress path of the backfill soil, for a soil element close to the wall.

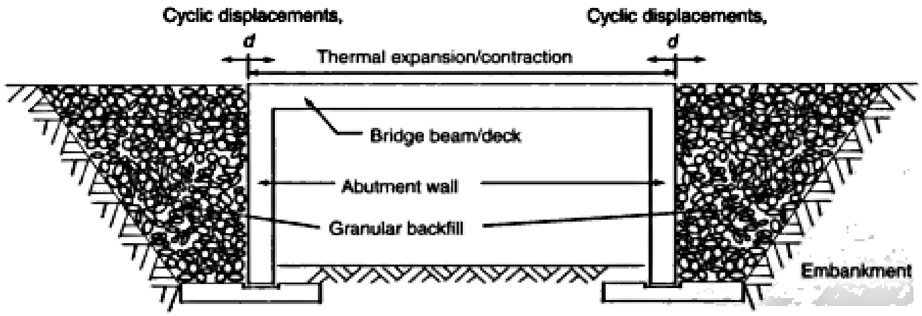

Figure 1.1 Typical frame-type integral bridge

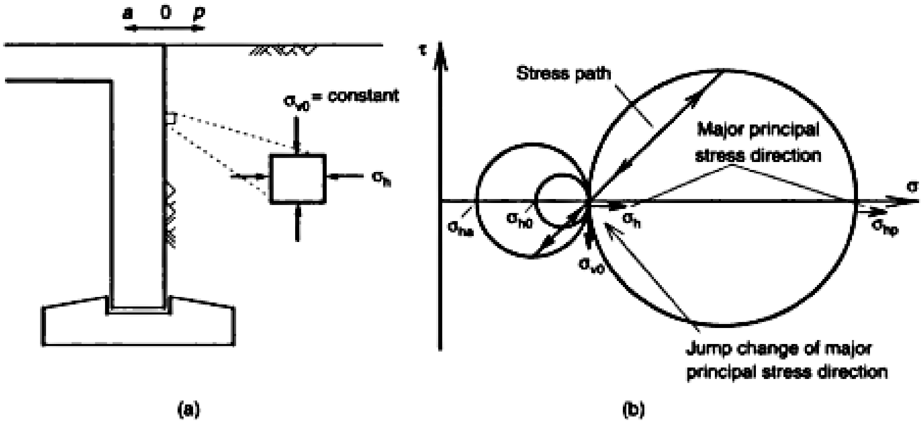

Figure 1.2 (a) A stiff abutment wall with a pinned base, showing the nature of wall rotations. (b) The associated cyclic stress path for a soil element close to the abutment face

2 Bridge form and temperature

2.1 Background

Bridge deck movements are caused primarily by changes in the environmental temperature and solar radiation. They change continuously. Due to variations in the thermal properties of the bridge materials, and the different thermal inertias of concrete and steel, bridges of different types respond in different ways to changes in environment. In addition, the temperature is not generally uniform throughout a structure. For these reasons longitudinal deck movements are difficult to predict from surrounding shade temperatures.

Much theoretical and practical research has been conducted (Emerson, 1973, 1976, 1977) to identify a representative bridge temperature from which design calculations can be made. A suitable parameter has been defined, the *effective bridge temperature* (EBT), and this has been correlated to extreme values of shade temperature as reported by the Meteorological Office. The data are applicable only to locations in the UK.

2.2 Daily and seasonal changes in bridge temperature

EBTs vary throughout the year. Maximum and minimum daily, and seasonal, changes have been identified. Figure 2.1 shows these variations. In general, the daily variation in the EBT in winter is about one-third to one-fifth of that in summer. However, as shown in Figure 1.2, the soil stress ratio in winter is likely to be close to the *active* stress state, and hence even small wall movements could induce significant ratcheting strain in the soil.

2.3 Type of bridge deck construction

The EBTs for three types of bridge deck at four different geographical locations are listed in Table 2.1. From the list of EBT values and their daily and seasonal changes, bridge deck movements can be calculated whenever the deck length and its thermal expansion properties are known. It is then possible to determine the magnitude of the cyclic displacements imposed on the granular backfill soil by the abutments throughout the year.

For a given bridge and geographical location the EBT always lies within the shaded area in Figure 2.1; daily variations are thus bounded by the two curves, max. EBT profile and min. EBT profile. Table 2.1 shows that for a given geographical location not all bridges have the same EBT profiles. This is because of the different thermal properties of the bridge materials (e.g. concrete, concrete–steel composite or steel) which produce different response times and characteristics for given shade temperatures and their variations. According to research from the Transport and Road Research Laboratory (Emerson, 1973, 1977) the EBT of a concrete bridge deck correlates strongly with the average environmental temperature over the previous 2 days, while the EBT of a composite deck (steel beams with concrete slab) is related to the average environmental temperature over the previous 8 hours only. Therefore, the nature and magnitude of the cyclic displacements imposed on the abutments and backfill soil are dependent not only on the environmental temperature but also on the type of construction of the bridge deck.

Table 2.1 Yearly variations in the EBT (°C) for three types of bridge deck at four locations in the UK[a]

		Geographical location			
Deck type	EBT[b]: °C	London	Birmingham	Newcastle	Scottish Highlands
Concrete	Max. EBT	34	32	29	29
	Max. summer daily EBT variation	6	6	6	6
	Peak of min. EBT in summer	28	26	23	23
	Annual EBT variation	38	42	35	42
	Max. winter daily EBT variation	1	1	1	1
	Min. EBT	–4	–10	–6	–13
Composite (steel–concrete)	Max. EBT	39	36	34	34
	Max. summer daily EBT variation	12	12	12	12
	Peak of min. EBT in summer	27	24	22	22
	Annual EBT variation	46	51	44	52
	Max. winter daily EBT variation	3	3	3	3
	Min. EBT	–7	–15	–10	–18
Steel box	Max. EBT	45	44	42	42
	Max. summer daily EBT variation	26	26	26	26
	Peak of min. EBT in summer	19	18	16	16
	Annual EBT variation	55	64	56	68
	Max. winter daily EBT variation	10	10	10	10
	Min. EBT	–10	–20	–14	–26

[a] The return period is 1 in 20 years

[b] For the definition of the terms see Figure 2.1

Different types of bridge deck will thus produce different patterns of cyclic wall rotations and cyclic soil displacements at the abutments, from a mixture of daily and seasonal temperature fluctuations. The comparisons given in Table 2.2 highlight these differences. Firstly, for the same location and the same deck lengths, the seasonal movement of a composite deck is about 121% of that of a concrete deck. An alternative interpretation is that the seasonal movement of a 42 m long steel deck is comparable to that of a 60 m long concrete deck in the same environment. Secondly, the maximum daily deck movement of a steel bridge is about three times that for a concrete bridge with the same seasonal deck movement as the steel deck. These examples indicate that the load-path histories for the backfill soil are complex and unique to each bridge type.

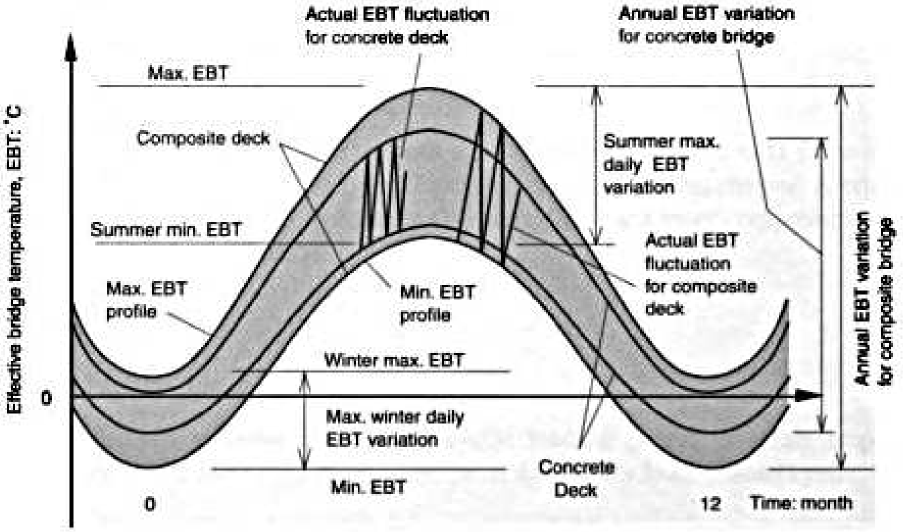

Figure 2.1 Effective bridge temperatures (EBTs) showing seasonal and daily variations for a composite deck and values for a concrete deck for comparison

Table 2.2 Comparisons of seasonal and daily deck movements for three types of deck construction*

			Deck movement (one end)			
	Length		Seasonal		Max. summer daily	
Deck type	m	%	mm	%	mm	%
Concrete	60		13.7	100	2.2	100
Composite	60		16.6	121	4.3	195
Steel	60		19.8	145	9.4	427
Concrete	60	100	13.7		2.2	100
Composite	50	83	13.7		3.6	164
Steel	42	70	13.7		6.5	295

*EBT data are for London; a 60 m long bridge was taken as reference for the comparisons shown

3 Granular flow behind abutment

To assist in the interpretation of the observations and comparisons of the next three chapters some general behaviour of granular soils during cyclic loading is described in this chapter. A brief explanation of the cyclic soil–structure interaction problem is also provided. For a more comprehensive description of soil behaviour, see Part 2 of this book.

3.1 Soil element behaviour

The behaviour of drained granular soils under cyclic loading (stress or strain imposed) can be characterized in terms of the following three phenomena during any load–unload cycle:

- densification or dilation (i.e. volume change);
- the development and collapse of interparticle load-carrying structures, referred to as soil fabric; and
- a change in shape resulting from ratcheting shear strains and a flow of particles.

The interplay between and possible dominance of any one of the above phenomena depends on the specific form of the loading in a given situation. It is important, therefore, to differentiate between stress cycling with and without a change in the principal stress directions, and between imposed stress fluctuations and imposed strain fluctuations. For the integral bridge described here the problem is one of displacement imposition at the soil–abutment interface, and this leads to two important descriptions of the fluctuating stresses:

- with 90° jump changes in the principal stress direction during a cycle; and
- without a change in the principal stress direction (known as *stress increment reversal loading*).

The temperature variations described in Chapter 2 coupled with the different types of integral bridges described in Section 2.3 lead to a wide range of cyclic stress paths for which the principal stress directions do and do not change direction during the loading cycles.

Examples to illustrate the various soil responses that can be expected are presented below. However, as an aid to understanding these the three characteristic phenomena mentioned above are firstly described in more detail. All relate here to plane strain situations, $\varepsilon_z = 0$.

Volume change. Generally, densification occurs during an increase in the stress ratio, $R = \sigma_y/\sigma_x$, when $R < 3$ and dilation results when $R > 3$. Imposed fluctuating stresses cause a rapid build-up of fabric and restrict the rate at which volume change can occur, whereas imposed fluctuating strains encourage volume change by restricting the build-up of excessive amounts of fabric.

Fabric. A rapid build-up of fabric occurs during stress increment reversal loading, coupled with the occurrence of ratcheting flow strains which reduce in magnitude cycle by cycle, except at high values of R. For imposed fluctuating strains the build-up of fabric is hindered; the soil thus remains more plastic and its flow properties persist.

Ratcheting strains leading to flow. Generally, cyclic shear stressing will lead to residual shear strains which accumulate cycle by cycle. These cause a unidirectional flow of particles to develop.

Example 1: stress increment reversal loading

Imposed fluctuating stresses. At peak stress ratios below about $R = 4$ (depending on the amplitude of the fluctuating stress) unidirectional ratcheting strains occur, coupled with an increase in density and an increase of soil fabric. The soil fabric inhibits the plastic response of the soil and, in turn, restricts the rate of densification. After many cycles a resilient elastic state can be identified, for which the soil response is much stiffer than that at virgin loading.

At high peak stress ratios dilation will occur. This will increase the magnitude of the incremental ratcheting strains and offset the stiffening caused by the repeated build-up of fabric. Eventually, if the cyclic stress fluctuations continue, a runaway ratcheting strain situation can develop.

Imposed fluctuating strains. Stress increment reversal loading can result from fluctuating strains which are imposed from an offset strain datum. During successive cycles the stress loop moves to span the isotropic stress state, and eventually the incremental stress reversals change to become 90° changes in the principal stress directions.

Example 2: 90° jump changes in the principal stress directions

When constant amplitude fluctuating strains are responsible for creating 90° jump changes in the principal stress directions, the stress fluctuations adjust themselves to centre closely with the hydrostatic stress state. The imposed strains inhibit the rate of build-up of fabric and thus maintain a soft soil response, which may be softer than that at virgin loading. Although plastic response is preserved this does not imply a large volume change. The net volume change during a complete stress–strain loop depends on the peak stress ratios and the direction of the ratcheting strains during the cycle. A limiting, or shakedown, state is reached when the dilation and densification that occur continuously throughout the stress–strain cycle, result in neither a net volume change nor any ratcheting strain over the whole cycle. In this condition the peak stress ratio R can be expected to be about 4–6. The two-element model described in Chapter 8 describes the interaction of an elastic structure and a granular soil leading to a shakedown state under imposed strain cycling.

3.2 Three-element model: creation of granular flow

The 90° jump changes in the principal stress direction can be visualized for a soil element adjacent to a stiff, smooth vertical retaining wall as shown in Figure 3.1, when the cyclic rotations of the wall are of sufficient magnitude to cause σ_h to be successively greater and then less than σ_{v0}. Stress increment reversals (for *passive* or *active* mode loading) can occur for σ_h during small-amplitude wall displacements (e.g. daily wall movements).

Normally it is not possible to represent the whole soil mass behind the bridge abutment by a single type of behaviour. Initially, small repeating wall displacements will cause soil stress increment reversals close to the wall, while the major principal stress remains vertical. Stress changes here move slowly, cycle by cycle, towards an isotropic ($R = 1$), or shakedown, state which is governed by the constant vertical stress (stress changes thus vary in depth). Eventually the soil behaviour changes to include 90° jump changes in the principal stress directions.

Further from the wall face similar changes take place but at a slower pace. However, soil more distant from the wall, is initially subjected to a monotonic loading, with increase in horizontal stress to a stress ratio of $R > 1$. Then, during unloading (i.e. *active* movement of the wall), the locked-in friction of the soil maintains the local stress ratio (σ_h/σ_{v0}) higher than those of soil elements adjacent to the wall. The soil stress fluctuations thus become limited to stress increment reversals only.

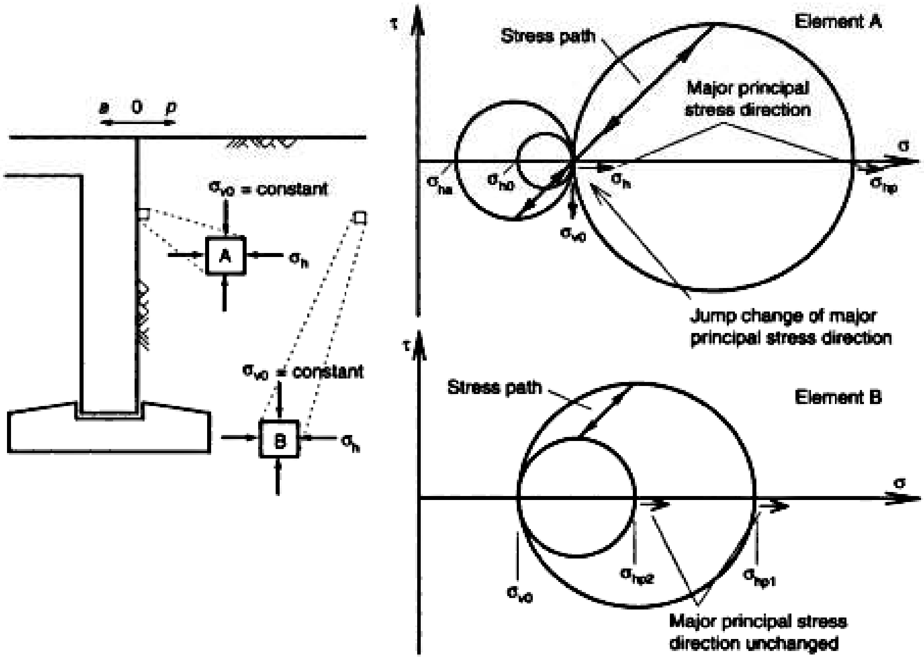

Figure 3.1 Cyclic stress variations in soil elements. Element A is close to the stiff abutment wall, while element B is at some distance from the wall

As the stress paths for soil elements at different depths and at different distances from the wall are quite different from each other, the overall soil behaviour is complex. To visualize the mechanics of the combined effects just described, a three-element model is developed here. Figure 3.2 shows two elements, namely A (adjacent to the abutment) and B (distant from the abutment), joined by a third element, C. The cyclic behaviour of element A results in negative ratcheting shear strains which relate to compressive vertical strains and extensional horizontal strains. In addition to densification, element A causes a substantial settlement to the soil surface near the abutment. Element B exhibits positive ratcheting shear strains which relate to extensional vertical strains and compressive horizontal strains. This feature is shown in Figure 3.3. For initially dense material, densification of element B due to cyclic stressing may be minimal. The positive ratcheting shear strains, however, cause overall heaving of the soil, which is at a horizontal distance from the abutment equal to about the height of the abutment. For soil element C, at a moderate distance from the wall, some densification occurs but without any ratcheting shear strain. Figure 3.2 illustrates the combined flow effect caused by these three elements, which form a connected flow path at depth for particles between the zones of settlement and heave. Ultimately a reverse flow path develops along the free surface from the zone of heave to the face of the wall. Although the initiation of this flow path has been observed in experiments, it is unlikely that any similar behaviour would develop within the service lifespan of an integral bridge.

3.3 Influence of the 'active' shear band

The granular backfill experiences *active* failure for a much smaller wall rotation than that for *passive* failure. It has been reported (Hambly and Burland, 1979) that *active* failure occurs at a wall rotation angle of 0.3–0.5%. This difference is due mainly to the difference in confining pressure between the two failure states. When failure occurs, a shear band of thickness approximately five to ten times the d_{50} particle size will form. The size of the shear band is also dependent on the confining pressure and void ratio.

At higher confining pressures and lower void ratio (lower part of the backfill) the material tends to form a thicker shear band. When a shear band is formed the soil elements in the band experience strain softening while others outside simply experience unloading (Figure 3.4). This causes a significant disparity of void ratio. The shear band with 'looser' material will dictate the soil response during the following *passive* wall rotation.

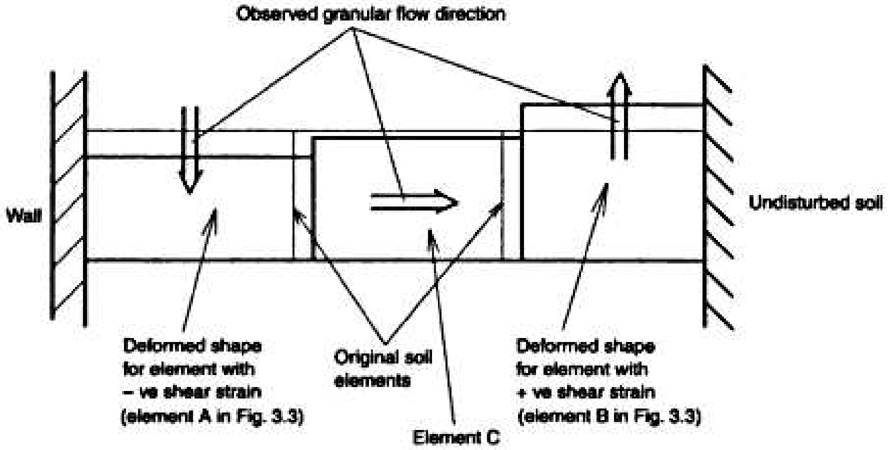

Figure 3.2 The three-element model illustrates the concept of granular flow (see Figure 3.3)

At lower confining pressures and higher void ratio (upper part of the backfill), the material is more brittle and tends to form a slip plane. Dilation occurs within a very thin layer of the failure zone. This can be seen as a fracture-type failure. Continued rotation of the wall may cause the soil wedge between the wall and the failure plane to slip bodily. Then, when the following *passive* wall rotation occurs, this thin fracture zone simply closes up. The loose zone, described above for thicker shear bands, does not exist in this case. Therefore, the existence of the thin shear band (slip plane) yields a higher soil stress than would be anticipated for the previous case.

In addition, during cyclic wall rotations, the soil properties (fabric and void ratio) of each element change at different rates depending on their relative locations, as described in Section 3.2. This will affect the location of the shear band which forms, and complicates the problem further.

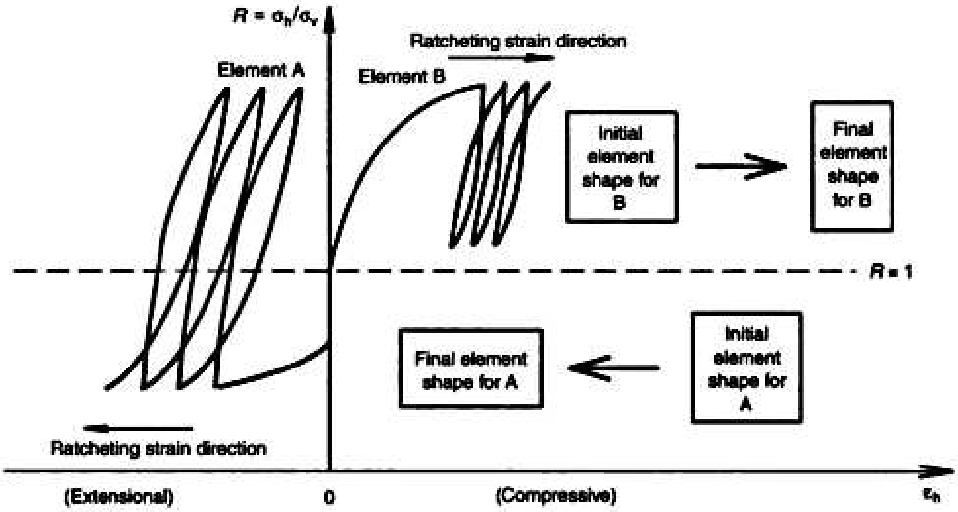

Figure 3.3 Directions of ratcheting strain and the deformed shapes of two soil elements. Element A is close to the wall face and suffers 90° jump changes in the principal stress directions. Element B is distant from the wall and undergoes stress increment reversals only. The connecting element C (shown in Figure 3.2) permits the horizontal flow of material between elements A and B without shear distortion. All elements undergo densification

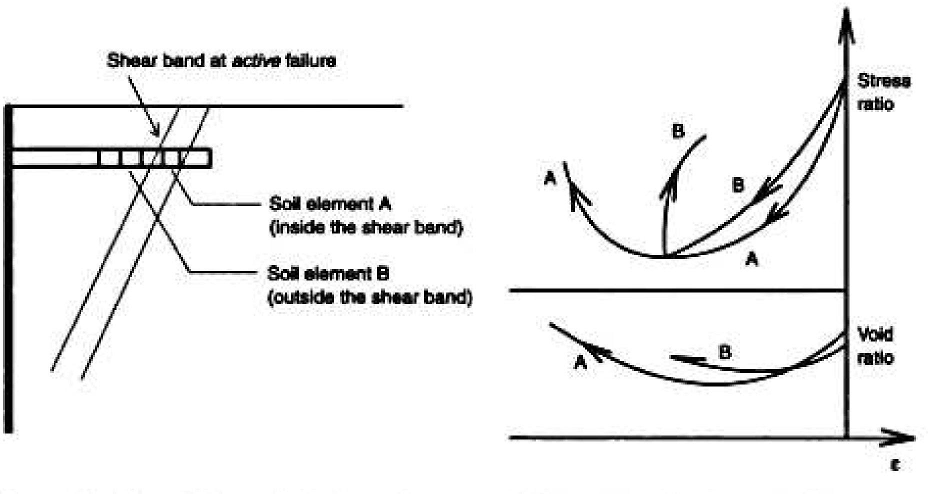

Figure 3.4 The variation in soil element behaviour close to and within a shear band at *active* failure

4 Model retaining wall test results

Details relating to the model retaining wall test apparatus are given in Part 2 of this book. In this chapter the results of seven individual tests are presented:

- Three preliminary single-cycle tests to:
  - verify the suitability of the test apparatus and
  - identify the importance of shakedown behaviour for controlling the escalation in lateral earth pressure during small rotational displacements of the wall.
- Three single-cycle tests of different amplitudes of wall rotation to simulate bridges of different lengths. Stress escalation and soil settlements are compared.
- One double-cycle test to investigate the combined influence of daily and seasonal temperature cycles on soil behaviour, stress escalation and settlement.

A complete set of results is presented for the equivalent 60 m bridge. Additional results from model tests simulating longer span bridges, not included in this chapter, are given in Appendix 1.2.

4.1 Cases studied

Three types of cyclic test are reported:

(*a*) Cyclic rotational displacements of the wall at four different amplitudes. These tests are defined as single-cycle tests and were done to investigate the influence of seasonal temperature changes.

(*b*) Cyclic rotational displacements of mixed amplitudes to investigate the combined influence of daily temperature changes and seasonal temperature changes. This test is defined as a double-cycle test.

(*c*) Single-cycle tests of small rotational amplitude commencing from large offset wall displacements, to demonstrate the importance of shakedown behaviour.

Details of the preliminary tests are presented in Table 4.1.

Table 4.1 Description of preliminary retaining wall tests

Test No.	d/H[a]: %	Initial wall reaction ratio[b] K
P1	±0.9[c]	0.40
P2	0.90 to 0.81	6.20
P3	−0.90 to −0.81	0.20

[a] The total angular rotation of the abutment, where $d/2$ is the amplitude of abutment displacement at bridge deck level and H is the abutment height

[b] The ratio of total lateral soil force acting on the wall to the total lateral force of a triangular hydrostatic stress distribution acting over the height of the wall, i.e. $R = 1$ over the whole wall

[c] This excessively large wall rotation equates to a bridge of 400 m long and was investigated only for the purposes described in Section 4.1, point (c)

The details of the four main tests carried out to simulate 60, 120 and 160 m long bridges are given in Table 4.2. The initial conditions for all tests were:

- a vertical wall,
- an *active* rotation (i.e. away from the sand) for the first loading cycle,
- an initial void ratio of the sand backfill $e_0 = 0.583 \pm 0.003$, i.e. a relative density of 94.1 ± 0.2%, and
- a height of the free sand surface above the toe of the wall $H = 520$ mm.

4.1.1 Stress changes resulting from cyclic wall displacements

The information in Table 4.1 and Figure 4.1 is included here to illustrate some important fundamental features of soil behaviour which result from repeated cyclic straining. The small displacement amplitude test P2 was conducted immediately after the large amplitude test P1 had been completed. The reasons for this were two-fold:

Table 4.2 Details of the four model retaining wall tests carried out to simulate 60, 120 and 160 m long bridges

Test No.	Seasonal rotation amplitude[a]: %	Equivalent deck length[b]: m	Daily wall rotation magnitude[c]: %	No. of daily wall movements per Seasonal cycle	No. of seasonal rotations completed
SW13	±0.13	60	NA	NA	300
SW25	±0.25	120	NA	NA	180
SW35	±0.35	160	NA	NA	160
DW25	±0.25	160	0.042[d]	60	65

[a] Amplitude = half maximum wall rotation $d/2H$ during a half cycle of movement

[b] Symmetrical deck movement assumed; concrete bridge

[c] Magnitude = total wall rotation d/H during a half cycle of movement

[d] For a daily temperature variation of approximately 3°C

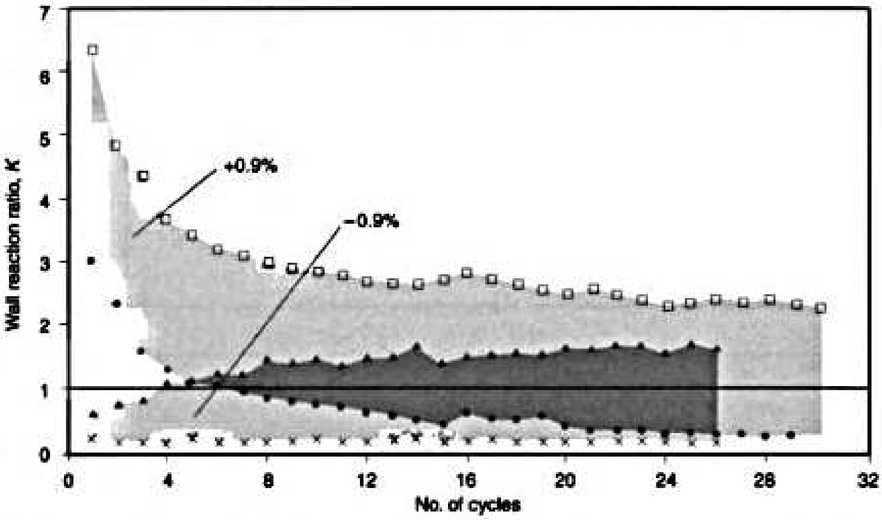

Figure 4.1 Influence of shakedown behaviour on the wall reaction ratio *K* for small-magnitude wall rotations (0.09%) from: a maximum *passive* wall rotation of 0.9%; and a maximum *active* wall rotation of −0.9%, following 40 cycles of amplitude ±0.9% from an initial vertical datum wall position

- To demonstrate that a significant escalation in lateral earth pressure occurs cycle by cycle at the soil–wall interface.
- To demonstrate that the high stress ratios created by the large-amplitude cyclic displacements in test P1 are mitigated rapidly by the subsequent small-amplitude cyclic displacements of tests P2 and P3. This is true for either the elevated interface stresses at the end of *passive* wall movements or the depressed interface stresses at the completion of *active* wall movements, at the end of test P1. Figure 4.1 illustrates the rapidity with which the stresses change from those achieved in Test P1 after reducing the overall cyclic displacements from 1.8% (i.e. –0.9% to +0.9%) to 0.09% (i.e. 0.9% to 0.81%). The wall reaction ratios in both cases quickly change to span the isotropic stress state (line $K = 1$ in Figure 4.1). At this stage the soil shows behaviour similar to that seen when approaching a shakedown state. In this example the stress fluctuations after 30 cycles were approaching similar values irrespective of whether the initial condition was $K = 6.2$ (highest *passive* value), $K = 0.2$ (lowest *active* value) or even $K = K_0 = 0.4$ (inferred from the lowest curve in Figure 4.8(a) for the larger strain amplitude of 0.125%). It can thus be concluded that the amplitude of the cyclic displacements determines the behaviour after many cycles, and that the stress and strain histories are of less importance.

The small-amplitude cyclic displacements just described have important implications for the behaviour of integral bridges when subjected to the combined influence of seasonal temperature changes (large cyclic displacements) and daily temperature changes (small cyclic displacements). The daily cycles create enhanced flow strains and restrict the wall stress ratios to remain closer to $K = 1$ values than would otherwise be observed for seasonal cycles alone.

In addition to the shakedown behaviour just described it will be necessary to develop a better understanding of the behaviour of the backfill soil in the presence of shear failure planes. Such slip planes can form during *active* rotation of the wall, for the larger values of d/H and after soil densification has occurred from earlier wall movements. The existence of such slip planes and the associated downward movement of the soil mass between the slip plane and retaining wall introduces an additional unidirectional feature to the overall performance of the retained soil and inhibits further reductions in lateral earth pressures. This response can be identified in the comparative results shown in Figure 4.8. Such behaviour was not observed for the smallest value of $d/2H$ (±0.125%, for a 60 m bridge) investigated.

4.2 Results for a 60 m bridge, $d/2H = \pm 0.125\%$

4.2.1 Wall stresses

The recorded *passive* wall stresses show a rapid escalation from the initial K_0 values during the first ten cycles (Figure 4.2(b)); thereafter changes were considerably slower, until at 300 cycles the increase was only 30% more. The maximum wall pressures occurred at a depth of approximately 0.5–0.6 of the wall height. Above this level stresses varied approximately linearly with depth, i.e. the stress ratios approximate to uniform values in this zone. This feature is shown in Figure 4.2(a).

The information in Figure 4.2 has been used to derive an equivalent wall reaction ratio K based on an assumed equivalent triangular stress distribution with depth (see footnote b to Table 4.1). Figures 4.3 and 4.4 show the variation in K during the cycling process for variations within selected *active–passive* rotation cycles (Figure 4.3) and an increasing number of cycles (Figure 4.4). It is clear from Figures 4.4(a) (linear plot) and 4.4(b) (logarithmic plot) that the maximum value of K (at maximum *passive* wall rotations) approached a nearly stable value at $K_{max} \approx 2.6$.

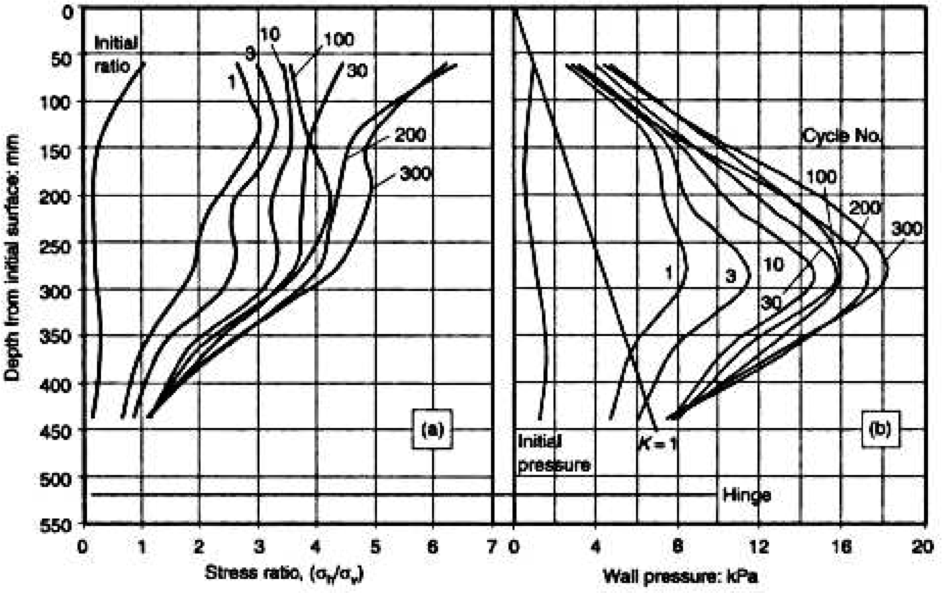

Figure 4.2 (a) Variation in the soil stress ratio $R = \sigma_h/\sigma_v$ and (b) recorded values of lateral wall pressure during 300 single (seasonal) cycles for an equivalent 60 m bridge. Values refer to the maximum *passive* wall rotation

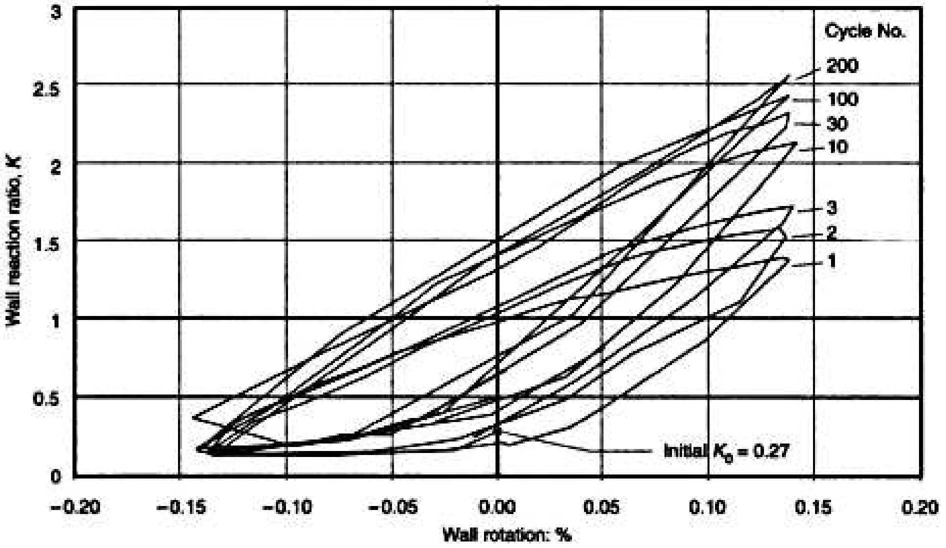

Figure 4.3 Variation in the wall reaction ratio *K* during cyclic wall rotations of amplitude 0.125% (60 m bridge) for 200 cycles

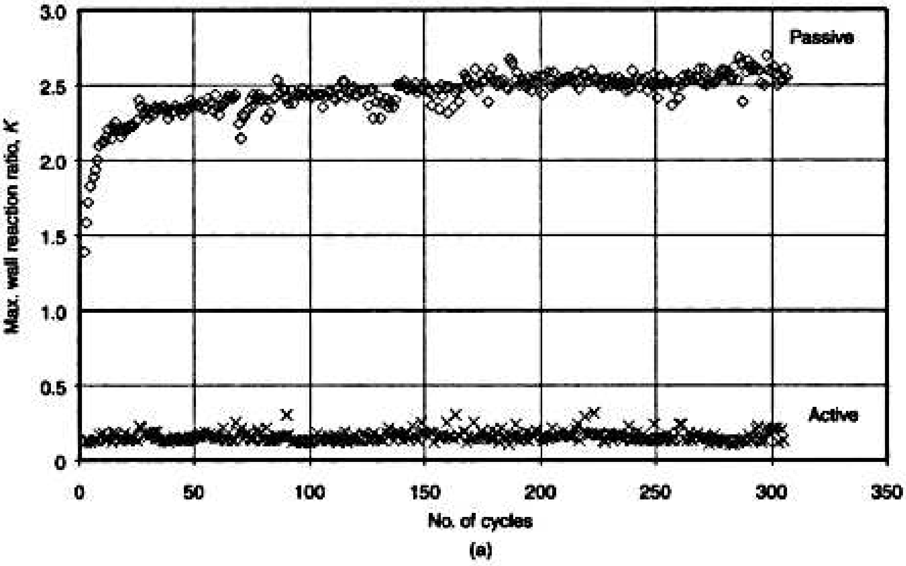

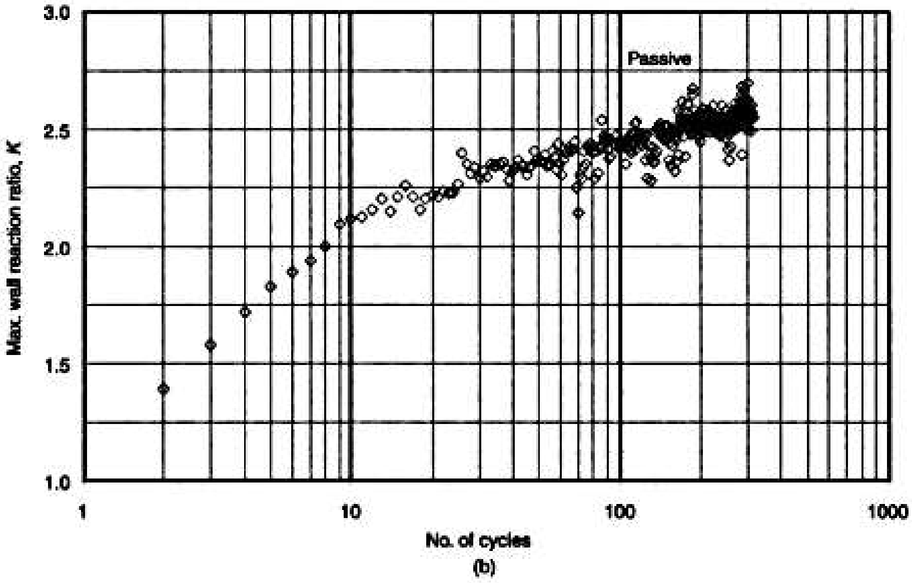

Figure 4.4 Variation in the wall reaction ratio *K* with the number of wall rotation cycles: (a) maximum *active* and *passive* values (linear plot); (b) maximum *passive* values (logarithmic plot)

4.2.2 Settlement of soil surface

Settlements of the soil surface did not show similar characteristics to the changes in lateral earth pressure. Settlement was progressive over an increasing number of cycles and, although a reduction in the settlement per cycle relationship was observed, there was no indication that a limiting settlement was being approached (Figure 4.5(b)). In fact, observations (Figure 4.5(a)) confirmed the existence of a flow mechanism, in addition to soil densification. This was identified by the heave of the free soil surface at a distance of approximately 350 mm from the wall. Further evidence of unidirectional flow is illustrated in Figure 4.6, which shows comparisons between the locations of the embedded soil markers after different numbers of cycles. The marker lines in the soil reveal the distribution of vertical settlement that occurred.

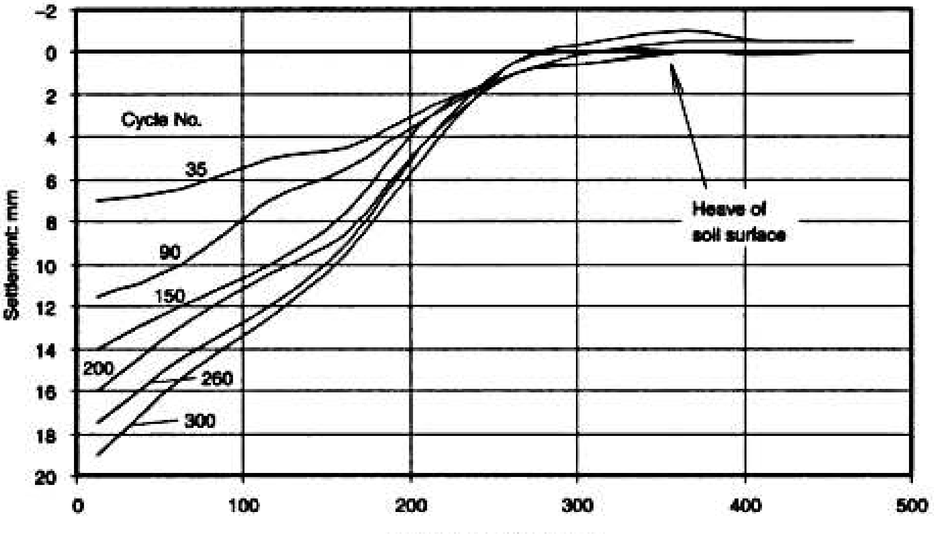

(a)

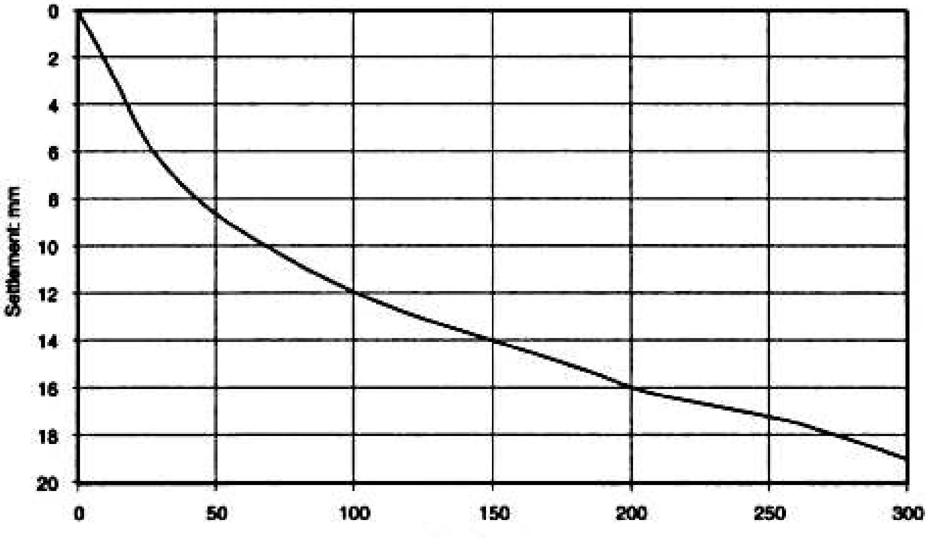

(b)

Figure 4.5 Soil settlement for an equivalent 60 m bridge: (a) variation in the surface profile for 300 cycles; (b) settlement close to the wall over 300 cycles

4.3 Influence of bridge length

4.3.1 Soil stress escalation

Generally the escalation of lateral earth pressure is higher for larger cyclic wall displacements and longer bridges. However, the relationship is complicated by the different mechanisms that contribute to the changing stress behaviour. The general behaviour for all single-cycle tests is shown in Figure 4.7.

For small wall rotations ($d/2H \leq \pm 0.125\%$) the shakedown stress behaviour dominates. At larger wall rotations ($d/2H \geq \pm 0.25\%$) the eventual occurrence of shear slip bands changes the behaviour by allowing rapid downward movements to occur for the soil located between the slip band and wall, during each *active* wall movement. The subsequent *passive* wall movements then produced an enhanced granular flow and increased surface heave. This new mechanism generated a more rapid soil flow than before the slip band was created and was responsible for sustaining higher wall stresses. The influence of wall rotation amplitudes on the wall reaction ratio K during cyclic wall movements is shown in Figure 4.8.

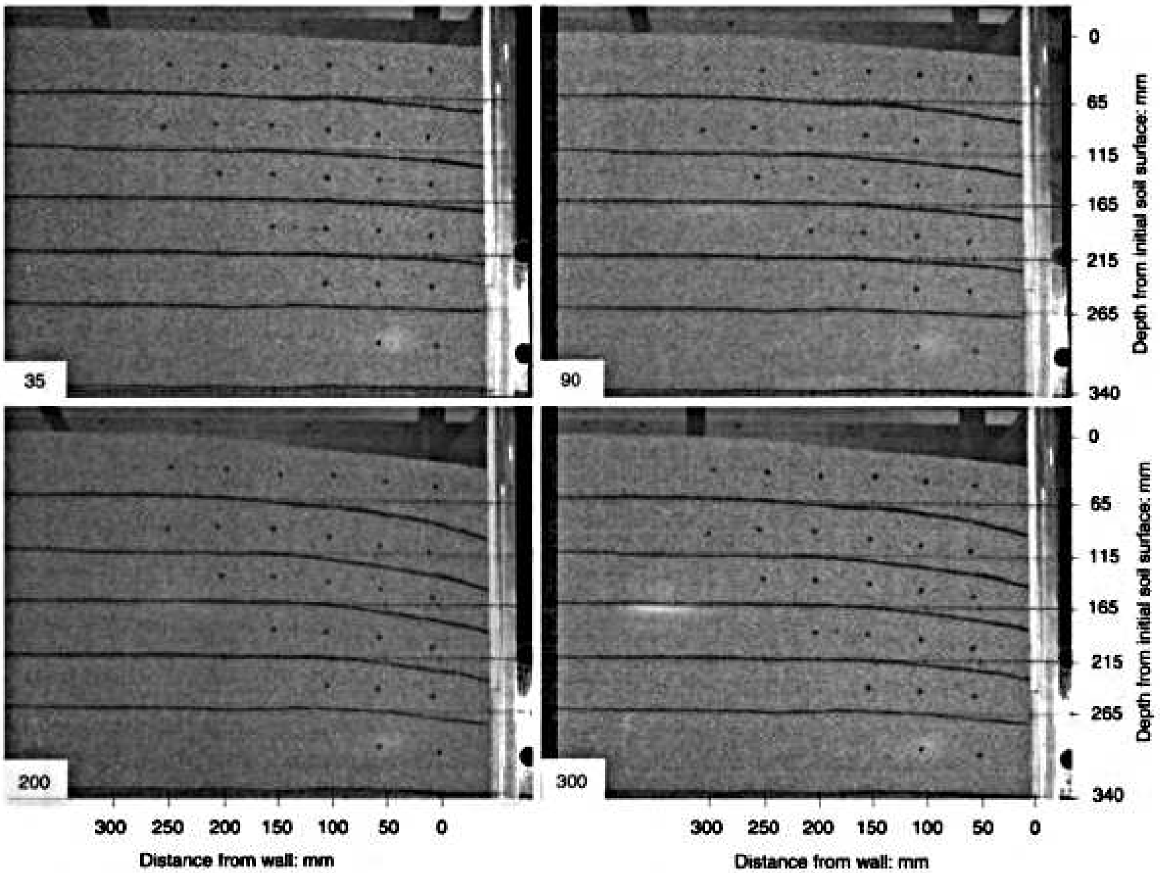

Figure 4.6 Deformation of Leighton Buzzard backfill material after 35, 90, 200 and 300 cycles of wall rotation for an equivalent 60 m bridge in test SW13 (see Table 4.2). The wall is in the datum vertical position

Also shown in Figure 4.8(a) are the results obtained from the small-displacement test P2, superimposed on the large-displacement results from test P1, after 40 cycles of wall rotation, $d/2H = \pm 0.9\%$. The offset wall displacement (maximum *passive* rotation) and associated high value of $K = 6.2$ from which the small cyclic wall displacements (0.9–0.81%, amplitude ±0.045%) of test P1 commenced, are seen to have little effect on the limiting value of K after more cycles. This result demonstrates that the shakedown behaviour dominates for small wall displacements, irrespective of the previous stress and strain history, even when previously created slip bands are present.

4.3.2 Soil settlement

Figures 4.9 and 4.10 illustrate clearly that greater soil settlement occurs for larger cyclic wall rotations (or longer bridges), for all the single-cycle tests. Comparative settlements after 30 cycles of wall rotation are shown in Figure 4.11.

4.4 Influence of daily temperature changes

The addition of daily temperature changes was investigated in test DW25. For this double-cycle test, single cycles of amplitude $d/2H = \pm 0.125\%$ were interspersed with 60 cycles of magnitude 0.042%, as illustrated in Figure 4.12. The initial effect of the smaller cycles (first 20–25 cycles) was to restrict the stress escalation to lie below the values for the corresponding single-cycle test (test SW25), as expected. After 25 cycles the soil behaviour changed when a shear band formed. This shear band developed, cycle by cycle, during each subsequent *active* rotation of the wall, as shown in Figure 4.13. The changed behaviour which followed was characterized by:

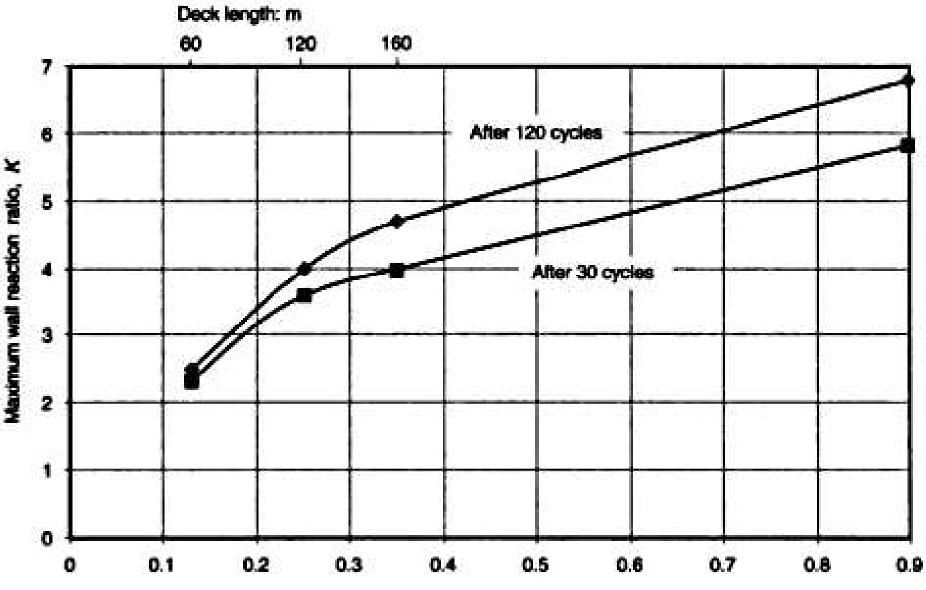

Figure 4.7 Variation in the maximum wall reaction ratio K (*passive* wall position) with wall rotation amplitude $d/2H$ after 30 and 120 cycles

- a cyclic downward movement of the soil contained in the wedge between the slip band and wall, during each *active* wall movement;
- similar (or slightly higher) soil–wall stresses than for the corresponding single-cycle case;
- greater densification of the soil close to the wall; and
- greater soil settlements close to the wall and greater heave away from the wall.

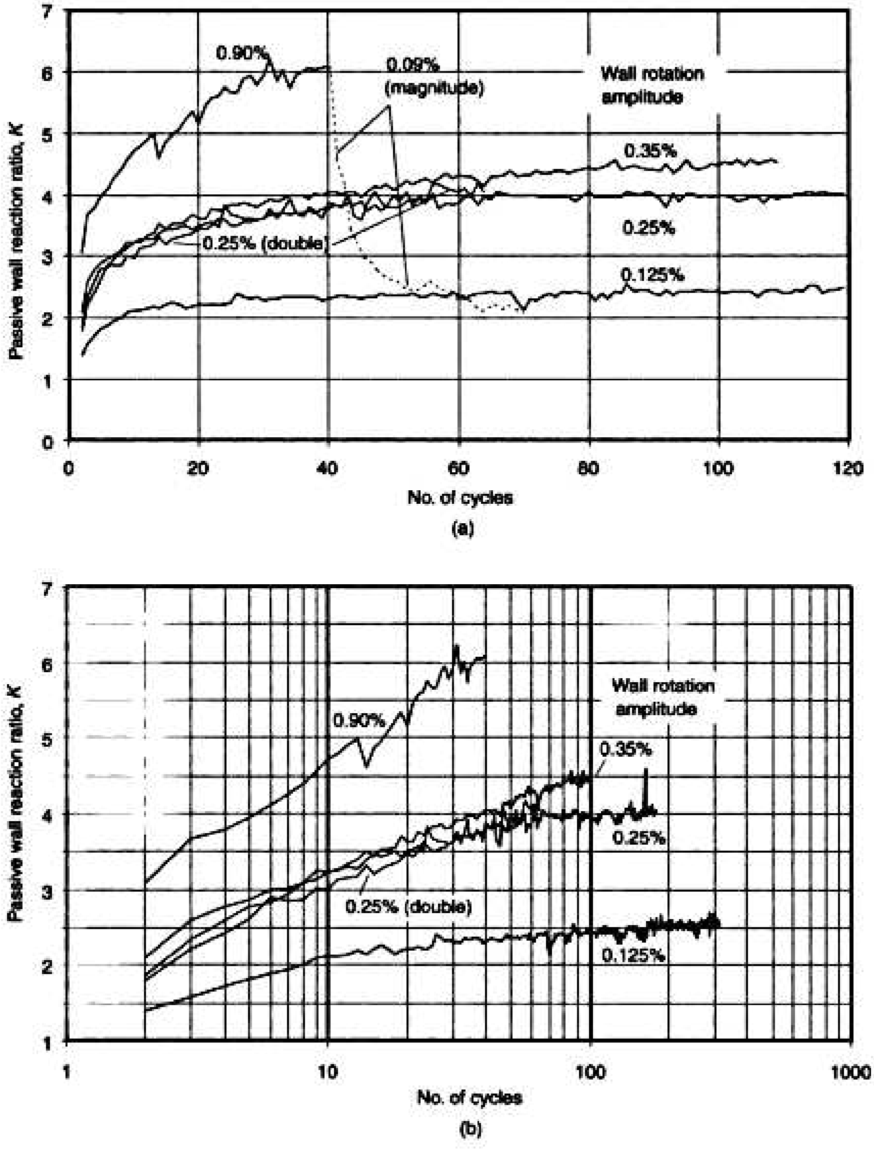

Figure 4.8 Influence of the wall rotation amplitude $d/2H$ on the wall reaction ratio K for various numbers of cycles of wall displacement: (a) linear plot; (b) logarithmic plot. The double-cycle result relates to 64 'seasonal' cycles and 3840 'daily' cycles. The 0.09% magnitude cycles in (a) refer to the small displacement cycles in test P2 from an offset origin defined by the test P1

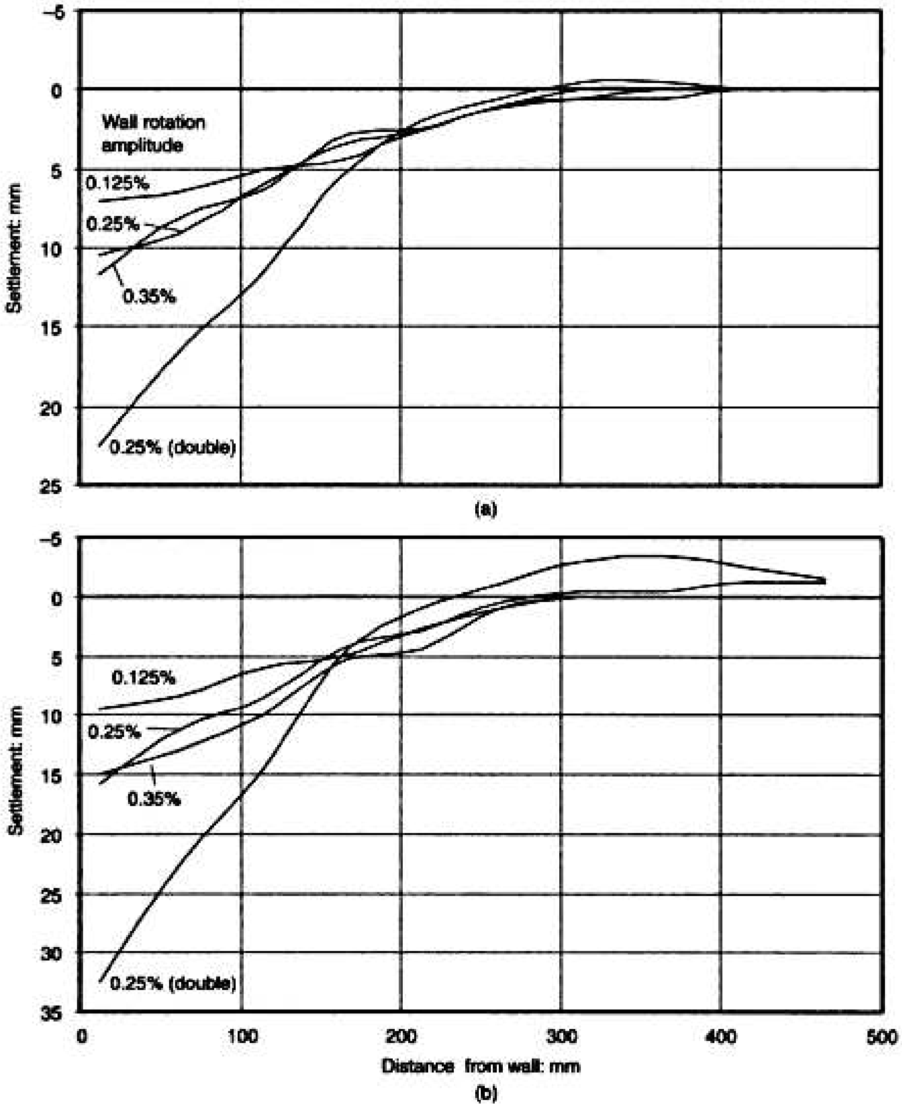

Figure 4.9 Influence of the wall rotation amplitude *d/2H* and double-cycle behaviour on surface settlements after (a) 35 and (b) 65 cycles

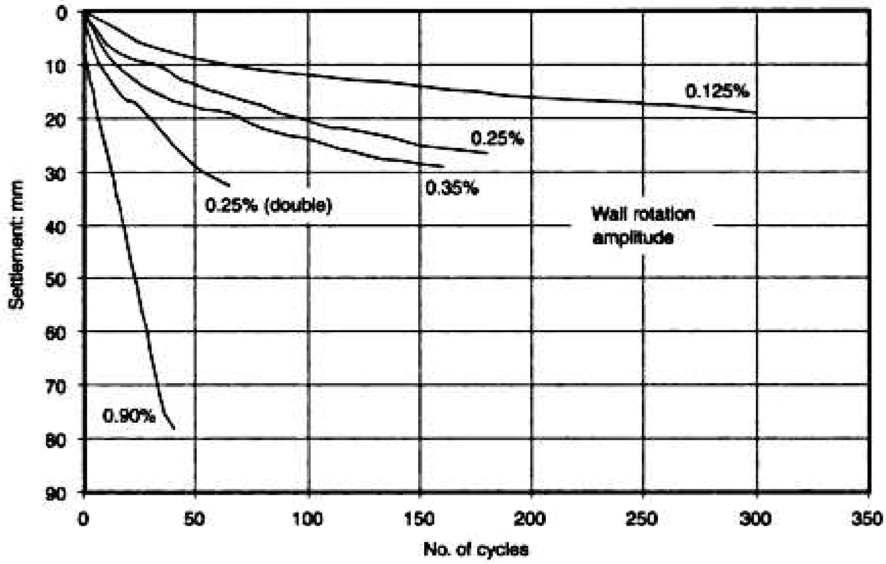

Figure 4.10 Influence of the wall rotation amplitude *d/2H* and double-cycle behaviour on the soil settlement close (10 mm) to the wall

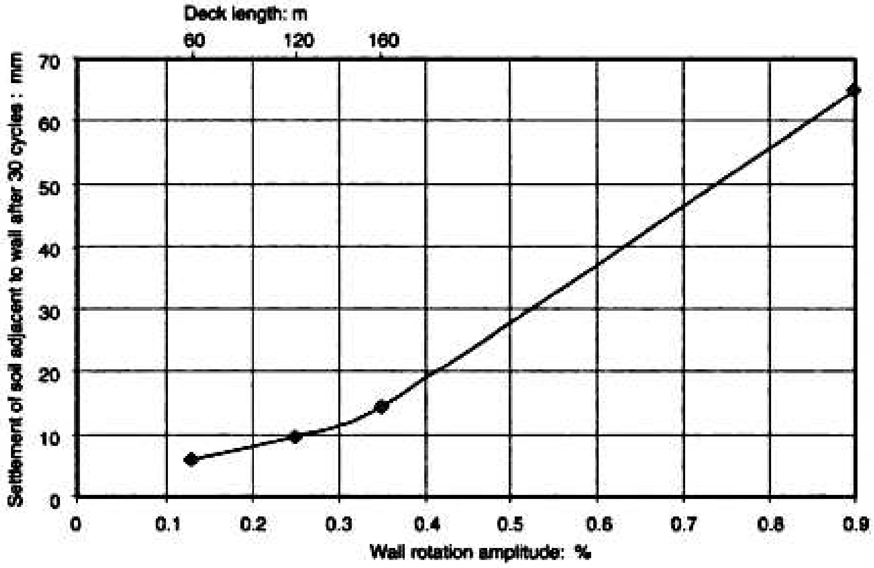

Figure 4.11 Influence on soil settlement close to the wall on wall rotation amplitude *d/2H* after 30 cycles

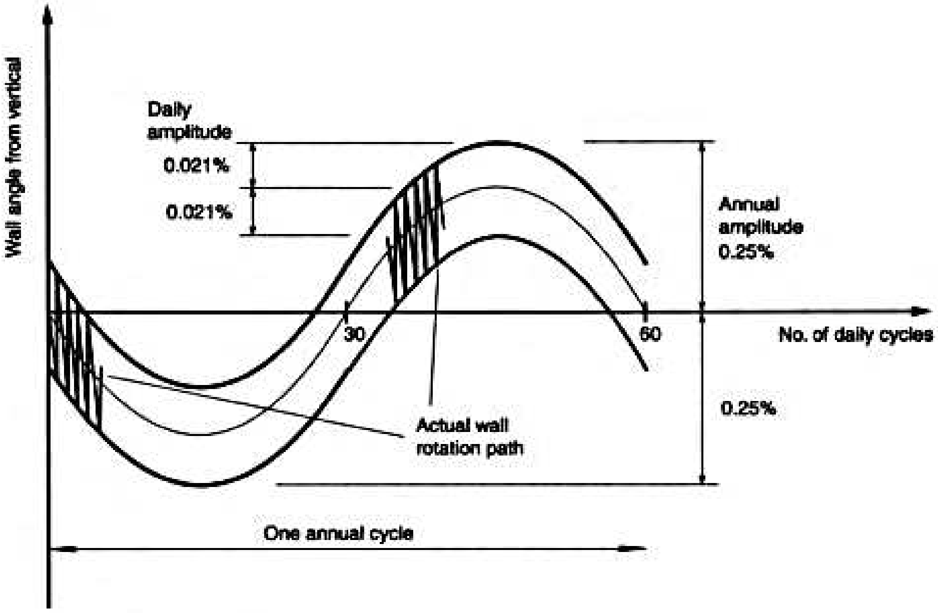

Figure 4.12 Form of the double cycles used in test DW25, for a 'seasonal' wall rotation amplitude $d/2H = \pm 0.25\%$ and a 'daily' cycle magnitude of 0.042%

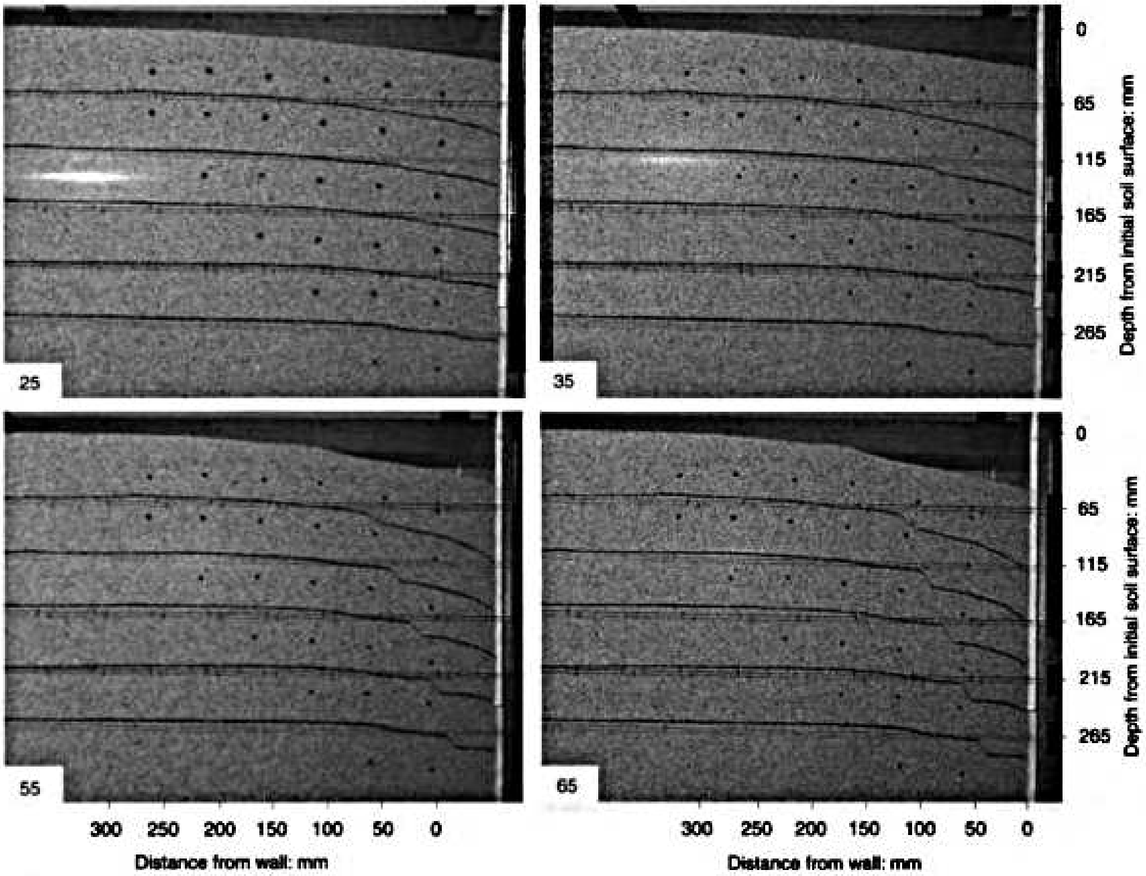

Figure 4.13 Deformation of Leighton Buzzard backfill material after 25, 35, 55 and 65 seasonal cycles in test DW25 (see Table 4.2). The wall is in the datum vertical position. The progressive development of the shear slip band is readily apparent

5 Numerical simulations

The new constitutive model for describing the response of granular soil to cyclic loading and the new semi-empirical retaining wall analysis developed in this project are described in Part 2 of this book. A computer program, QSand, linking the soil model to the retaining wall analysis was prepared to study the cyclic soil–structure interaction between the integral bridge abutment and the backfill soil. The program was implemented on a Pentium PC. The validation of the numerical model and the verification of the computer program are described in Appendix 1.1. In this chapter the findings from a series of parametric studies carried out using QSand are reported. (Comparisons of the findings with those from experimental tests and final recommendations are contained in Chapter 7.)

5.1 Input data for soil and structure

The simulations forming the basis of the parametric study are defined in Figures 5.1 and 5.2. Table 5.1 lists the values of the parameters for the bridges considered, including their temperatures and data on the backfill granular soil. The material parameters for the backfill are specified according to the element test results on Leighton Buzzard sand, and are listed in Table 5.2.

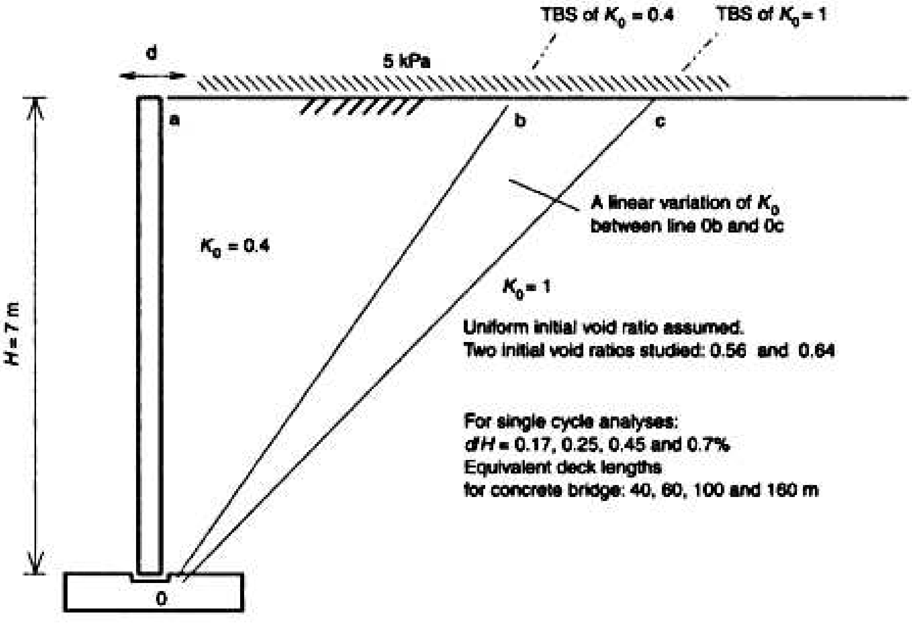

Figure 5.1 Initial soil conditions and wall dimension for the numerical simulations. *d* is the overall cyclic wall displacement. The transitional boundary surface (TBS) is defined in Chapter 11

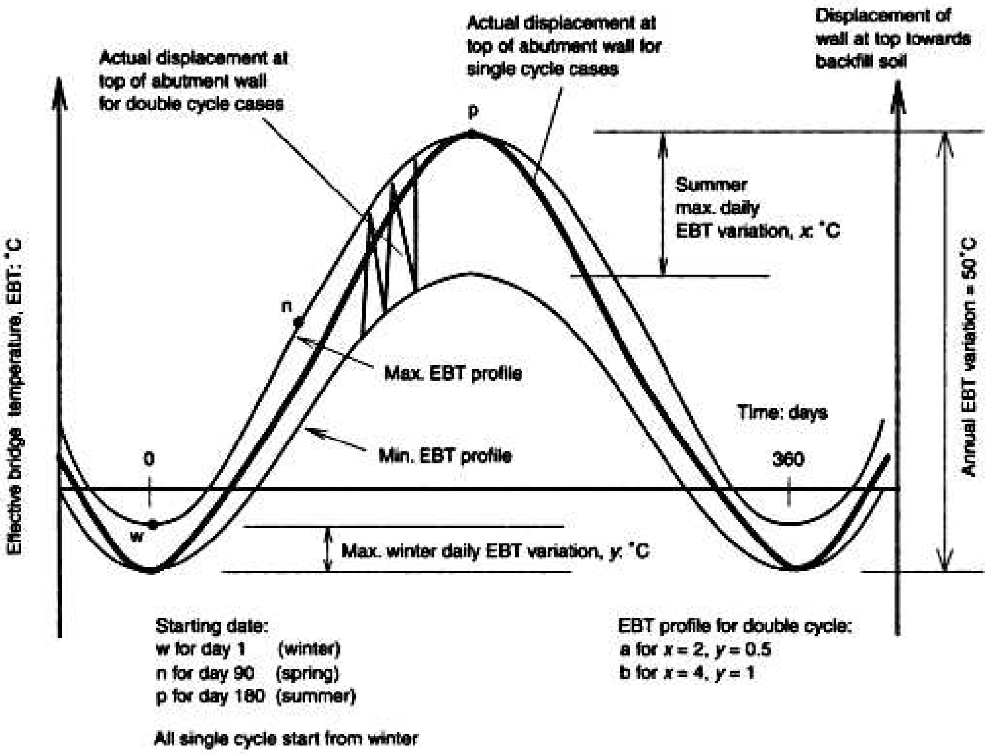

Figure 5.2 Effective bridge temperatures (EBTs) and corresponding wall rotation magnitudes investigated in the numerical simulations

Table 5.1 Boundary data defining the numerical simulations

Parameter[a]	Value
Bridge data	
Type	Concrete
Thermal expansion coefficient	12×10^{-6}/°C
Deck lengths	40, 60, 100 and 160 m
Abutment wall height, *H*	7 m
Seasonal EBT variation	50°C
Seasonal wall rotation magnitude, *d*/*H*	0.17%, 0.25%, 0.45% and 0.7%
Daily EBT profile	0.5°C (winter) to 2°C (summer) (profile A in Figure 5.2) 1.0°C (winter) to 4°C (summer) (profile B in Figure 5.2)
Starting dates of service life[b]	Day 1 (winter) (w in Figure 5.2) Day 90 (spring) (n in Figure 5.2) Day 180 (summer) (p in Figure 5.2)
Soil data[c]	
Type	Leighton Buzzard sand (see Table 5.2) T sand (see Table 5.3)
Initial void ratio	0.56 and 0.64 (for both types of sand)
Unit weight at initial density	18 kN/m^3 (at a void ratio of 0.56 for both types of sand)
Traffic load	5 kN/m^2
Initial wall reaction ratio	0.4
Initial soil stress distribution in the whole soil mass	See Figure 5.1

[a] EBT, effective bridge temperature; *d*, total horizontal movement of the abutment wall at the backfill surface

[b] Starting from minimum EBT for all single-cycle cases

[c] Material parameters are defined according to the new constitutive model as described in Part 2 of this book

In order to examine the influence of a different backfill material, the 'stiffer' T sand (created numerically) was used. Its material parameters are listed in Table 5.3. The stiffer stress–strain response for T sand under monotonic loading is shown in Figure 5.3 together with the response of Leighton Buzzard sand for comparison.

Simulations which involve repeated seasonal fluctuations of temperature only are denoted as *single-cycle* cases. Simulations involving coupled daily and seasonal temperature fluctuations are denoted as *double-cycle* cases; they contain 360 daily cycles within each seasonal cycle. The annual temperature change is the same for single- and double-cycle simulations. The details are given in Figure 5.2.

Table 5.2 Leighton Buzzard sand: soil model parameters*

Parameter	Value	Parameter	Value
E_0	950	n	0.5
η_0	0.53	ν_*	0.15
E_{∞}	1200	λ	0.027
η_{∞}	3.4	σ_{∞}	100 kPa
κ	0.0183	e_{∞}	0.8
α	0.2		

*Values for E_0 and E_{∞} are based on stresses in kPa. Parameters are defined according to the new constitutive model as described in Part 2 of this book

Table 5.3 T sand: soil model parameters (modified data from Table 5.2 in bold type)*

Parameter	Value	Parameter	Value
E_0	**1950**	n	0.5
η_0	0.53	ν_*	0.15
E_{∞}	**1800**	λ	0.027
η_{∞}	3.4	σ_{∞}	100 kPa
κ	**0.014**	e_{∞}	0.8
α	0.2		

*Values for E_0 and E_{∞} are based on stresses in kPa. Parameters are defined according to the new constitutive model as described in Part 2 of this book

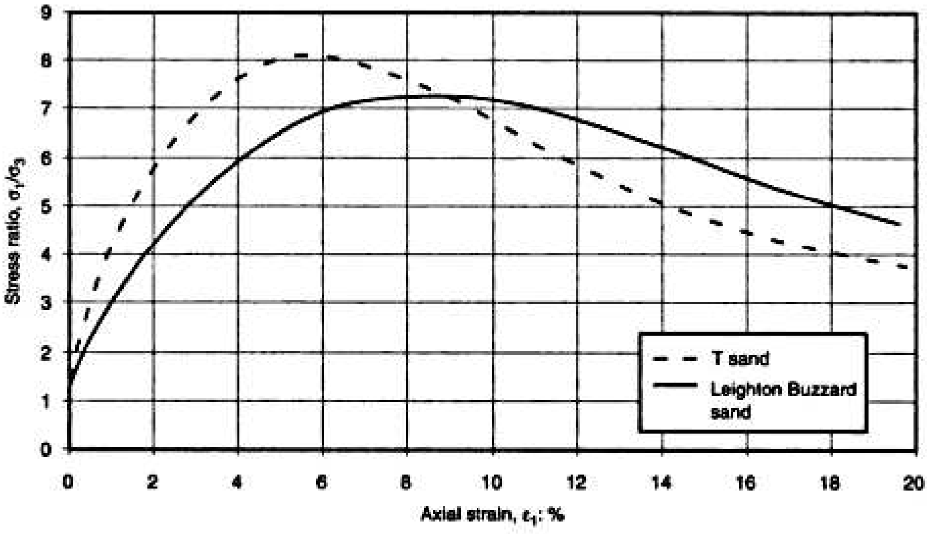

Figure 5.3 Comparison of the stress–strain responses for T sand and Leighton Buzzard sand under plane strain monotonic loading (initial void ratio 0.52, $\sigma_3 = 20$ kPa)

- *Simulations with Leighton Buzzard sand.* In total, 32 cases were studied: 8 single cycle (4 rotational amplitudes and 2 void ratios) and 24 double cycle.
- *Simulations with T sand.* In total, 18 cases were studied: 8 single cycle and 10 double cycle.

For easy reference, the case number is assigned in a manner that defines the boundary data of the simulation (see Figure 5.2). Definitions for the simulation case code parameters are given in Table 5.4 and the parametric case studies themselves are listed in Table 5.5.

In order to give meaningful comparisons for the integral bridge problem, the following terms are used throughout:

Table 5.4 Definitions of the simulation case code numbers in Table 5.5

Single-cycle cases		Double-cycle cases	
S	Single cycle	D	Double cycle (i.e. 360 daily cycles within each seasonal cycle)
17 (25, 40, 70)	0.17% wall rotation magnitude	40 (60, 100, 160)	Bridge deck length (40 m)
56 (64)	Initial void ratio 0.56	56 (64)	Initial void ratio 0.56
L	Leighton Buzzard sand (see Table 5.2)	L	Leighton Buzzard sand
T	T sand (see Table 5.3)	T	T sand
		a, b	Daily EBT magnitude (see Figure 5.2)
		w, n, p	Starting date (see Figure 5.2)

Starting from minimum EBT for all single-cycle cases, i.e. winter starts

Table 5.5 Details of boundary data for the numerical simulations[*]

Cases for Leighton Buzzard sand			
D40/56Lan	D60/56Lan	D100/56Lan	S17/56L
D40/64Lan	D60/64Lan	D100/64Lan	S17/64L
D40/56Lbn	D60/56Lbn	D100/56Lbn	S25/56L
D40/64Lbn	D60/64Lbn	D100/64Lbn	S25/64L
D40/56Lap	D60/56Lap	D160/56Lan	S45/56L
D40/64Lap	D60/64Lap	D160/64Lan	S45/64L
D40/56Law	D60/56Law	D160/56Lbn	S70/56L
D40/64Law	D60/64Law	D160/64Lbn	S70/64L
Cases for T sand			
D40/56Tan	D60/56Tan	S17/56T	S45/56T
D40/64Tan	D60/64Tan	S17/64T	S45/64T
D40/56Tbn	D60/56Tbn	S25/56T	S70/56T
D40/64Tbn	D60/64Tbn	S25/64T	S70/64T
	D100/56Tan		
	D100/64Tan		

[*] See Table 5.4 for code notation. 500 cycles for single-cycle cases S17/56L and S17/64L; 200 cycles for all other single-cycle cases. 50 seasonal cycles for double-cycle cases D60/56Lan and D60/64Lan; 30 seasonal cycles for all other double-cycle cases. Deck lengths relate to concrete bridges

- In single-cycle simulations, *number of cycles* has the same meaning as *number of years*.
- The term, *magnitude* of wall rotation (*d/H*) is used in addition to *amplitude* (*d/2H*) to define the overall cyclic rotation of the wall. *d* is the overall movement at the top of the wall and *H* is the wall height.
- *Settlement* generally refers to the settlement of the soil adjacent to the abutment wall.
- *Bridge lengths* are shown alongside the wall rotation magnitude only to provide a rough comparison; they refer to concrete bridges with 7 m high abutments. The bridge lengths are calculated by assuming an equal share of deck movement to both abutment walls.
- The terms, *maximum wall reaction ratio* and *minimum wall reaction ratio* relate to the maximum and minimum values of a seasonal cycle (i.e. a year), respectively.

5.2 Results for a 60 m bridge

Due to the huge amount of output data for each numerical simulation, it is not possible to include all the numerical results in this chapter. Thus the case S25/56L, for a 60 m long bridge, is reported here to indicate:

- the detailed behaviour of some soil elements,
- the variation in the maximum and minimum wall reaction ratios year by year, and
- the gradual changes in horizontal strain, shear strain and void ratio which occur throughout the whole soil mass.

5.2.1 Observations at the soil–abutment interface

Figure 5.4 shows the escalation in the maximum wall reaction ratio K year by year. Although a steady-state value of $K = 1.2$, is reached after 200 years, the continuous soil settlement adjacent to the wall indicates that soil properties change continuously (Figure 5.5). The reason why K can stablize while the soil settlement continues can be seen from Figures 5.6 and 5.7. The different directions of the ratcheting shear strains of the two soil elements A and B (at the same depth of 1 m but at different distances from the wall) shown in Figure 5.6 demonstrate 'granular flow' (positive ratcheting shear strain implies the accumulation of compressive horizontal strains and extensional vertical strains) (see Chapter 3). The granular flow away from the wall tends to reduce the soil pressure on the wall. In contrast, the densification of soil adjacent to the wall (see Figure 5.7) increases the stiffness of the soil and tends to increase the soil pressure on the wall. When these two opposing behaviours are of comparable magnitude a balance can be reached and the overall soil pressure, and hence K, can stablize.

5.2.2 Observations for backfill soil mass

The pattern of the 'granular flow' is illustrated by the topological plots in Figures 5.8 to 5.10. The overall observation is that the soil densifies with a negative ratcheting shear strain (extensional horizontal strain) in a zone bounded by the wall and a plane emanating from close to the toe and at approximately 30° to the wall face. The soil between planes at 40° and 45° exhibits positive ratcheting shear strain with little densification (in some elements on the 45° plane, a small amount of dilation has been observed). These observations identify two important features:

- the soil disturbed by the cyclic wall rotations is mainly confined between the wall and the 45° plane; and
- although densification is the general response of the backfill soil to cyclic wall movements, heaving of the soil surface can still occur in the long term due to the accumulated 'granular flow'.

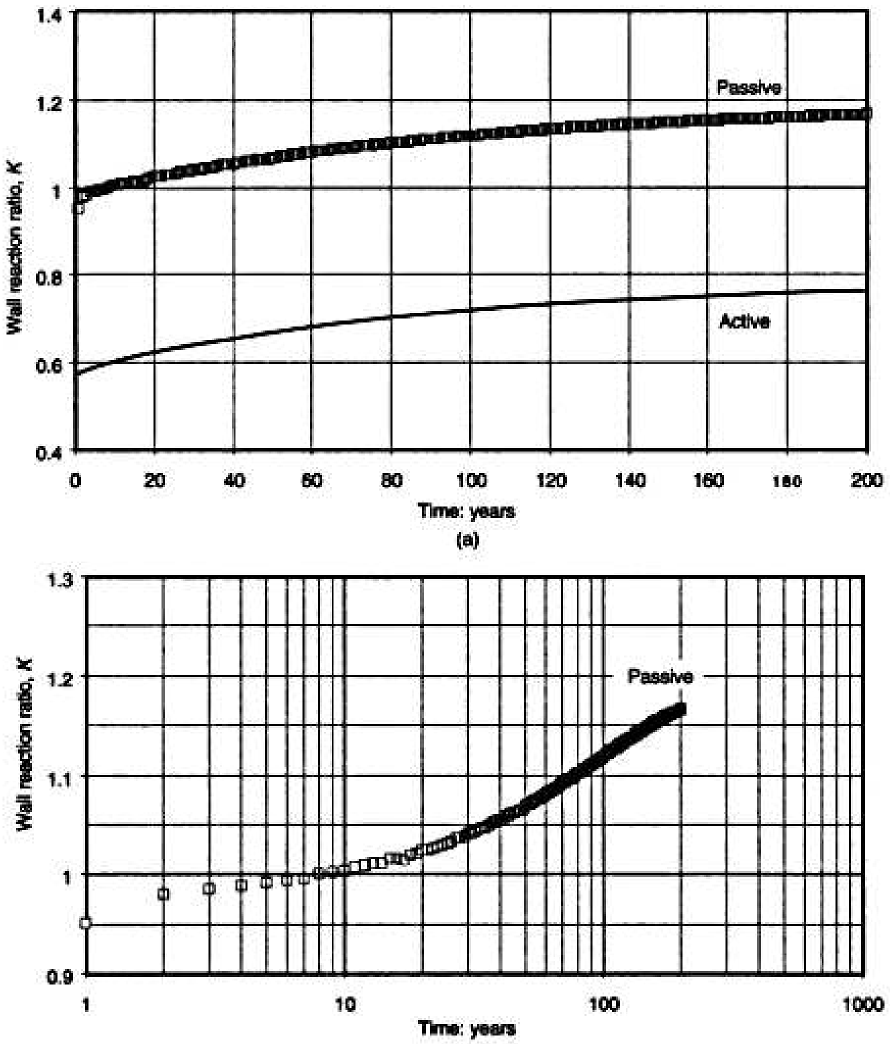

(a)

(b)

Figure 5.4 Wall reaction ratios over 200 years, for a 60 m long bridge (0.25% rotation magnitude), single seasonal cycles and an initial void ratio of 0.56: (a) maximum and minimum ratios plotted on a linear scale; (b) maximum ratios plotted on a logarithmic scale of time

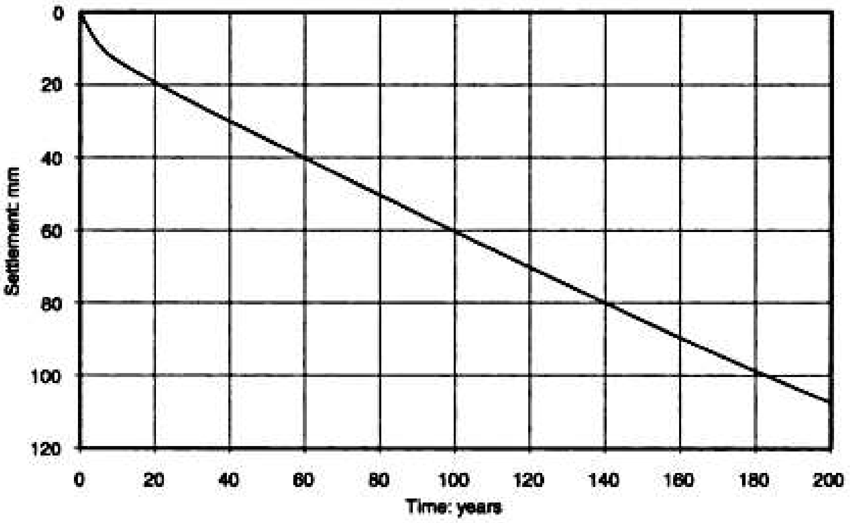

Figure 5.5 Settlement of soil adjacent to the wall over 200 years for a 60 m long bridge (0.25% rotation magnitude), single seasonal cycles and an initial void ratio of 0.56

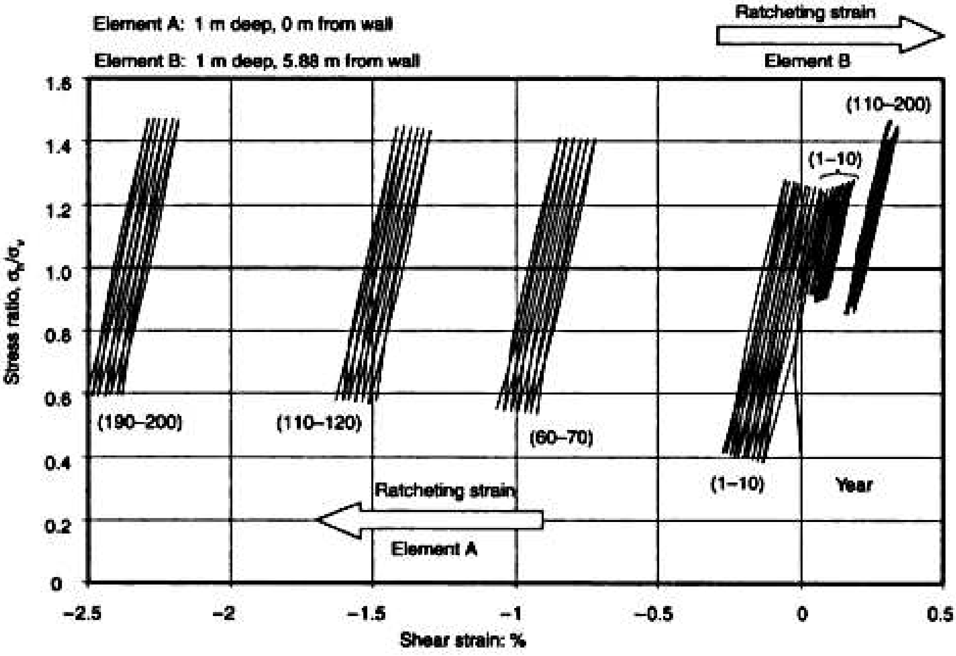

Figure 5.6 Ratcheting shear strains for two elements A and B over 200 years, for a 60 m long bridge (0.25% rotation magnitude), single seasonal cycles and an initial void ratio of 0.56

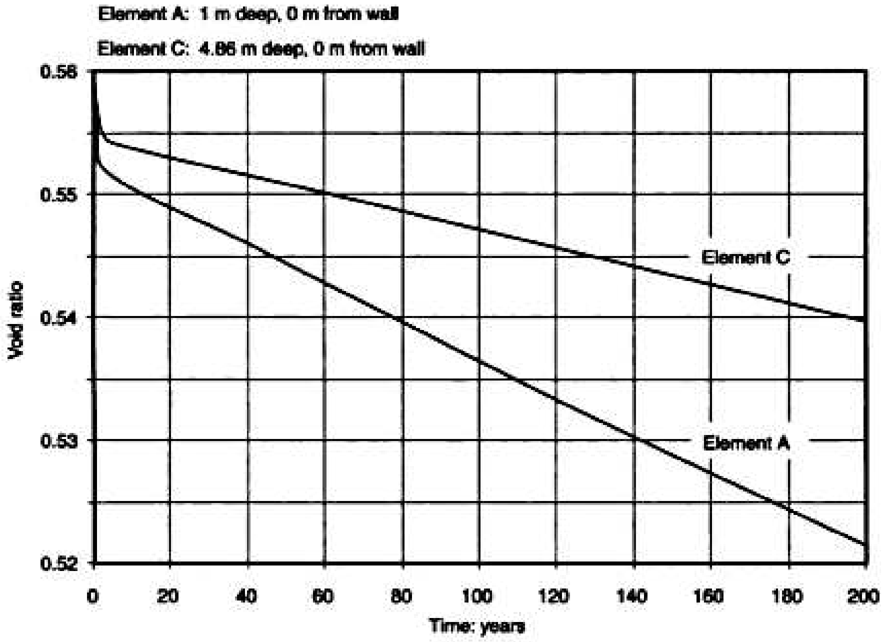

Figure 5.7 Change in the void ratios for two elements A and C over 200 years for a 60 m long bridge (0.25% rotation magnitude), single seasonal cycles and an initial void ratio of 0.56

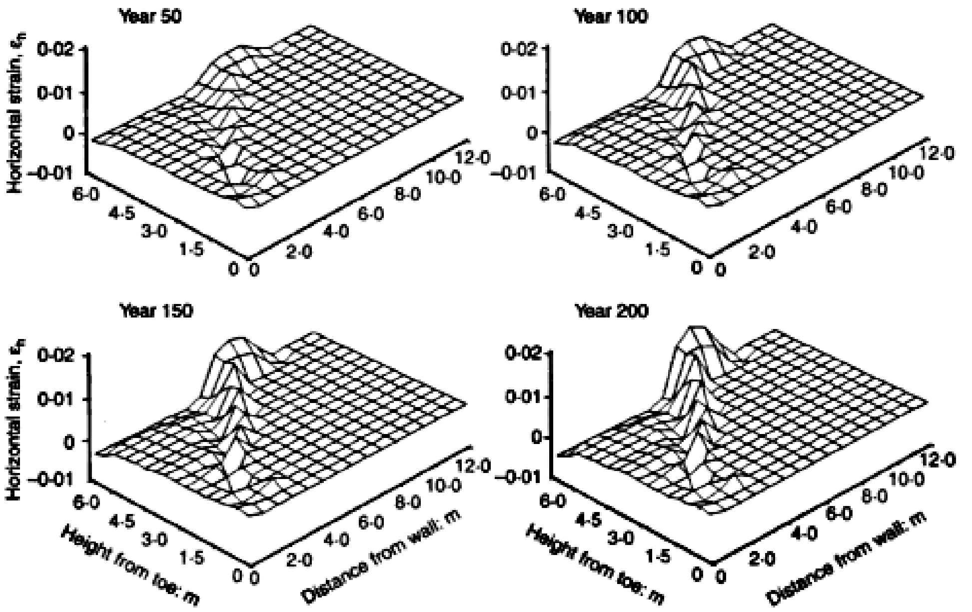

Figure 5.8 Topological plot of the accumulated *horizontal strain* (compression positive) in the backfill soil mass over 200 years, for a 60 m long bridge (0.25% rotation magnitude), with single seasonal cycles and an initial void ratio of 0.56

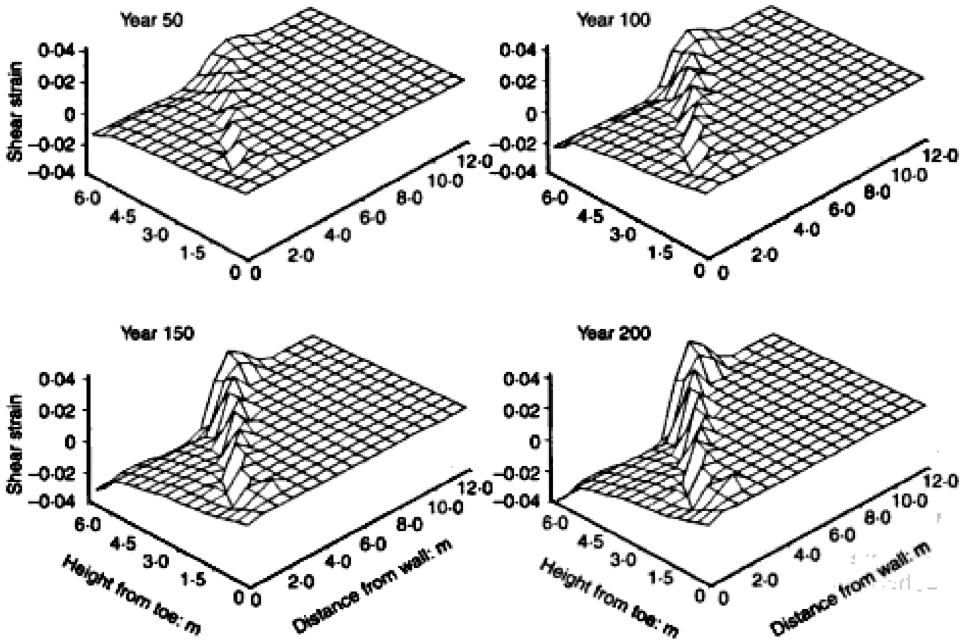

Figure 5.9 Topological plot of the accumulated *shear strain* in the backfill soil mass over 200 years, for a 60 m long bridge (0.25% rotation magnitude), with single seasonal cycles and an initial void ratio of 0.56

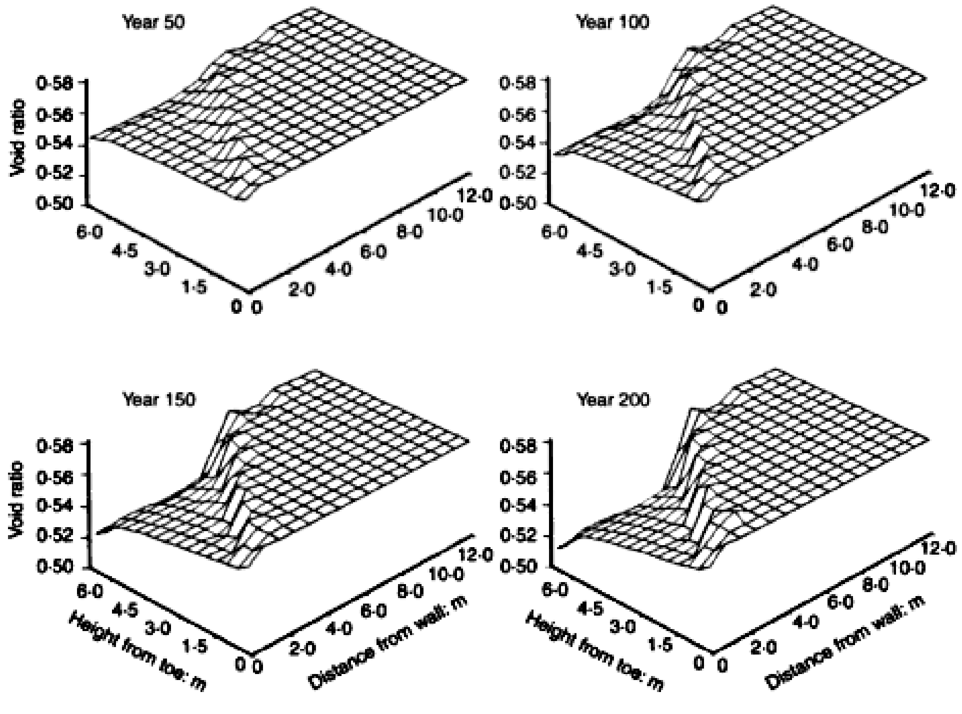

Figure 5.10 Topological plot of the *void ratio* changes in the backfill soil mass over 200 years, for a 60 m long bridge (0.25% rotation magnitude), with single seasonal cycles and an initial void ratio of 0.56

5.3 Wall stress escalation

5.3.1 Influence of cyclic wall rotations

The maximum and minimum wall reaction ratios K for four single-cycle analyses with different rotational magnitudes are shown in Figure 5.11. The figure indicates the following general behaviour:

- stress escalation is rapid during the first few years, resulting in the wall reaction ratio K changing from $K = K_0$ towards $K = 1$.
- the rate of stress escalation reduces considerably when $K > 1$; and
- fluctuations in the wall reaction ratios span the hydrostatic state, with a steady state for the maximum K being reached only after many years (>120 years in these examples, and therefore beyond the current design life for bridges in the UK).

In addition, the wall reaction ratio K is seen to be dependent on the magnitude of wall rotation. The values for maximum K after 100 years and at the steady state are shown in Figure 5.12 for a range of wall rotation magnitudes. It can be observed that there is an almost linear variation between K and the wall rotation magnitude.

An important observation is that for all the bridge deck lengths considered, the steady state is not reached within the current design life of 120 years. However, Figure 5.12 provides useful information in that at 100 years, one can expect to reach to within 92% of the steady-state values, for all bridge lengths up to 160 m.

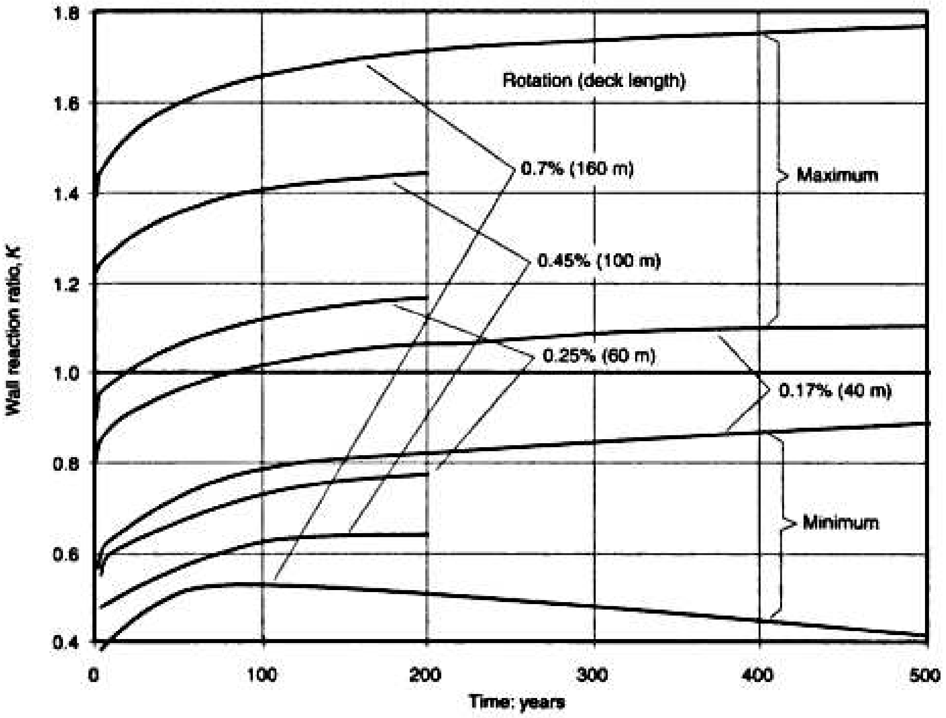

Figure 5.11 Variation in the maximum and minimum wall reaction ratios K with time for single-cycle simulations (initial void ratio 0.56)

5.3.2 Influence of initial soil density (initial degree of compaction)

The higher the initial void ratio (the lower the soil density) the closer the stresses become to the hydrostatic state (Figure 5.13). This effect, however, is slight and does not appear to be significant in the longer term. It may be concluded therefore that the initial void ratio will not usually be of any great significance in the evaluation of abutment–soil interface stresses in the long term.

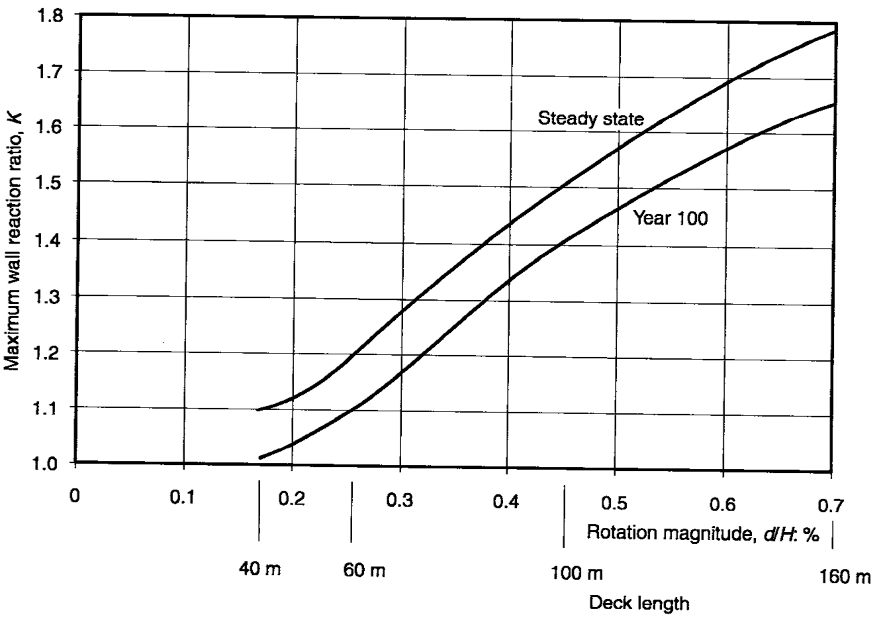

Figure 5.12 Variation in the maximum wall reaction ratio at year 100 and at steady state, with wall rotation magnitude for single-cycle simulations (initial void ratio 0.56)

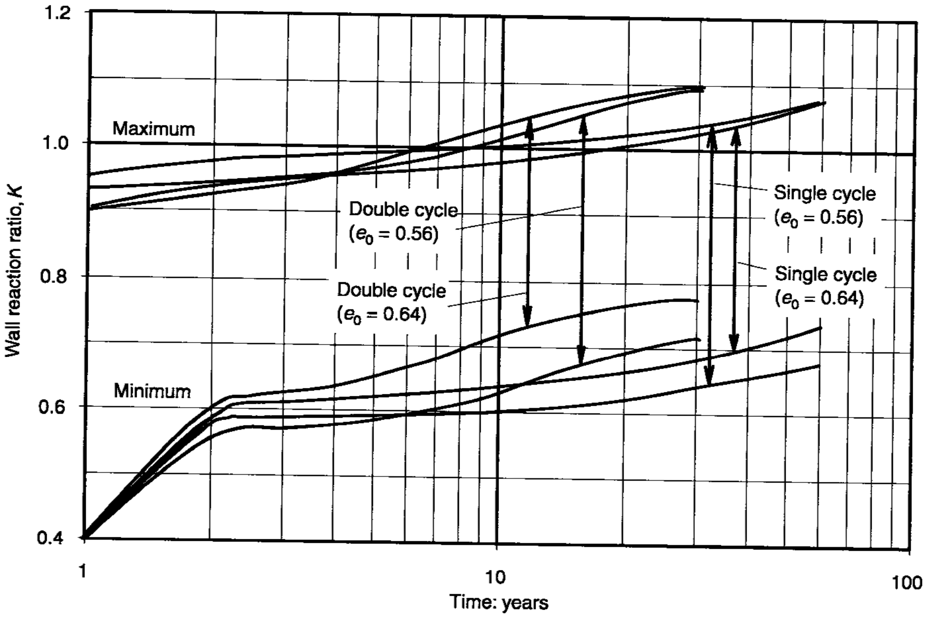

Figure 5.13 Variation in the maximum and minimum wall reaction ratios with time for two initial void ratios, 0.56 and 0.64 (wall rotation magnitude of 0.25%, 60 m bridge)

5.4 Soil settlement

See also Section 5.9 for details of heave at the soil surface.

5.4.1 Influence of bridge length

- The longer the bridge the greater is the settlement close to the wall after 200 years. The relationship between settlement and length of bridge is approximately linear.
- Settlement is approximately linear with time, i.e. with the number of cycles of wall movement. Unlike the changes in the interface stresses there is no evidence of a limiting settlement state.

Figures 5.14 and 5.15 provide supporting information.

5.4.2 Influence of initial soil density

Settlements are generally smaller for the denser soil (Figures 5.14 and 5.15).

5.5 Influence of daily temperature changes

The inclusion of daily temperature changes in addition to seasonal changes influences primarily the wall reaction ratios and soil deformations. More strain is imparted to the soil during double-cycle operation, and this creates greater opportunity for the development of ratcheting plastic strains and more granular flow. The consequences are:

- Stress escalation is more rapid and the steady state is reached faster (Figure 5.16).

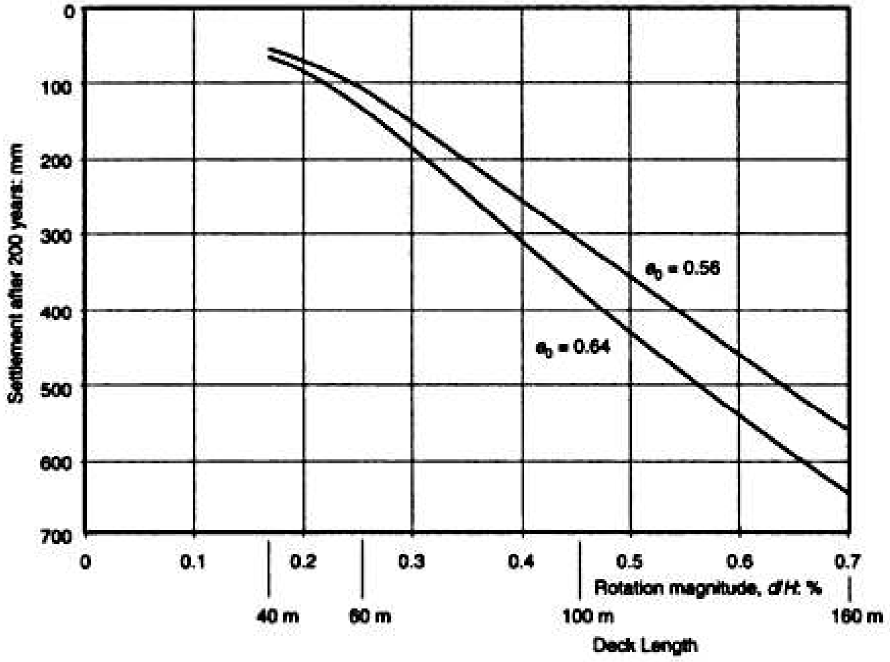

Figure 5.14 Comparison of the total settlement after 200 years for different magnitudes of wall rotation and for two initial void ratios (single-cycle simulations)

- The steady-state wall stresses and wall reaction ratio become closer to the hydrostatic state ($K = 1$) (Figures 5.16 and 5.17).
- Soil settlement close to the wall is increased significantly, approximately three-fold (Figures 5.18 and 5.19).
- Soil deformation is generally greater. There is more granular flow away from the wall and significantly greater soil disturbance close to the 45° plane, leading to heave of the soil surface. The soil disturbance after 30 years, for daily and seasonal cycles, is greater than that for 50 years of seasonal cycles alone, as shown in Figure 5.20.

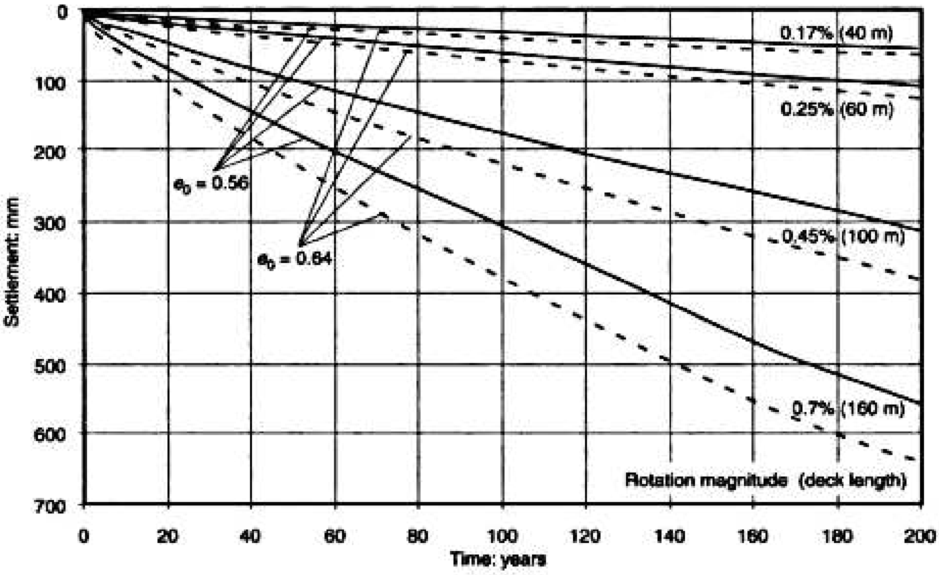

Figure 5.15 Comparison of settlement of soil adjacent to the abutment with time for four wall rotation magnitudes and two initial void ratios (single-cycle simulations)

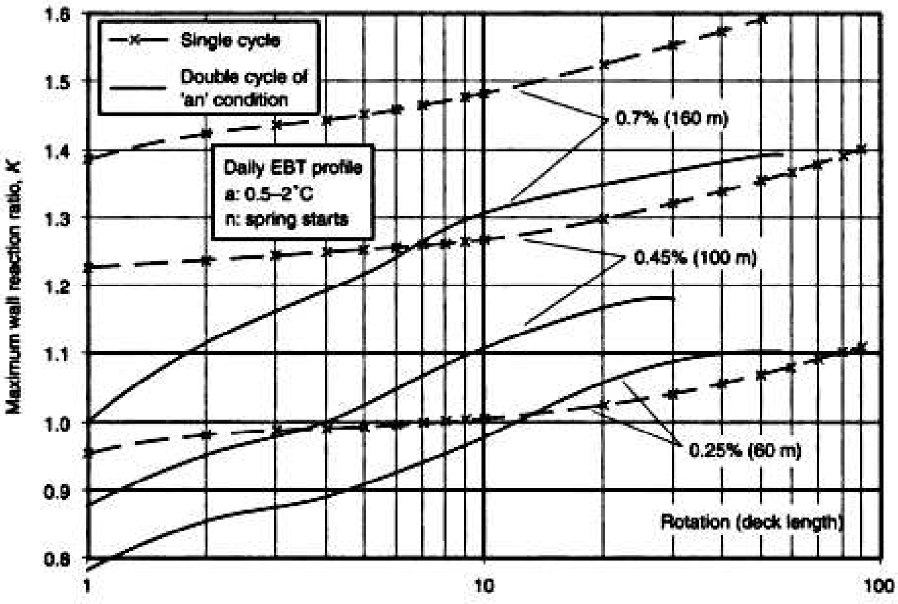

Figure 5.16 Variation in the maximum wall reaction ratio with time for single- and double-cycle simulations (initial void ratio 0.56; daily EBT profile *an*, see Figure 5.2)

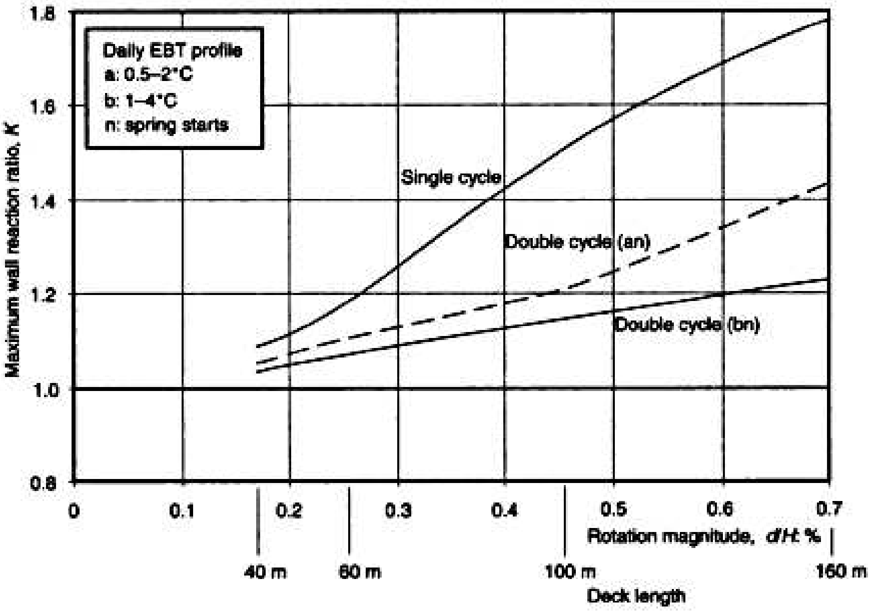

Figure 5.17 Variation in the maximum wall reaction ratio at steady state with magnitude of wall rotation, for single- and double-cycle simulations (initial void ratio 0.56)

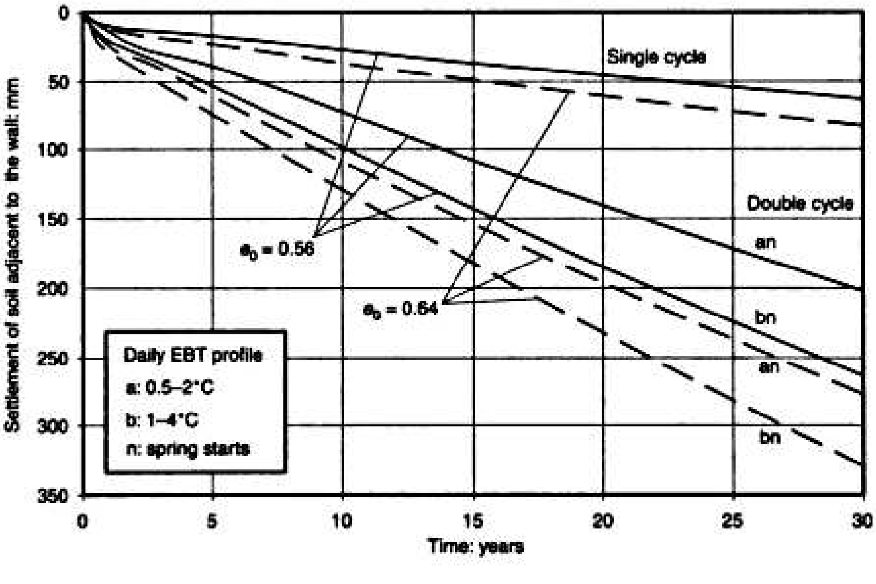

Figure 5.18 Variation with time of soil settlement adjacent to the abutment, caused by 0.45% seasonal wall rotation, for a bridge deck length of 100 m and two initial void ratios (single- and double-cycle simulations)

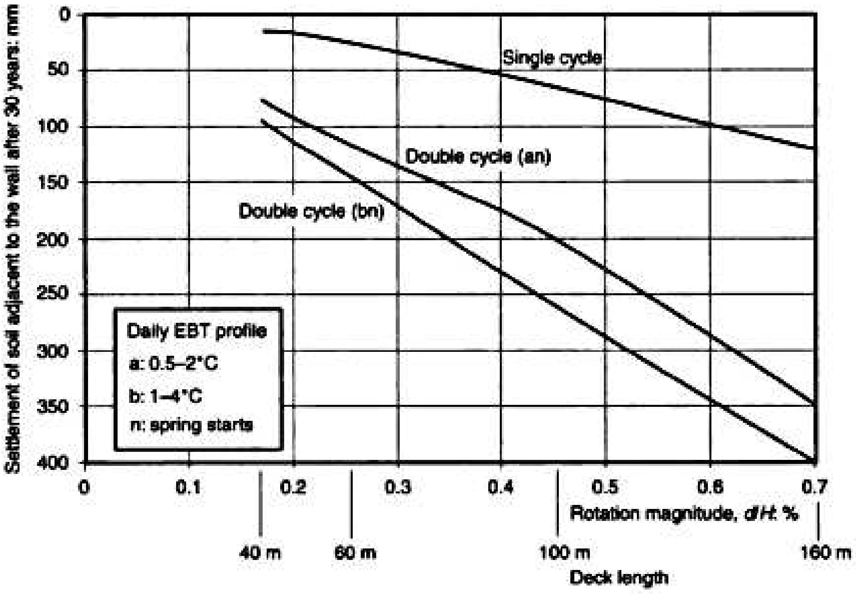

Figure 5.19 Variation in soil settlement after 30 years with magnitude of wall rotation, for single- and double-cycle simulations (initial void ratio 0.56)

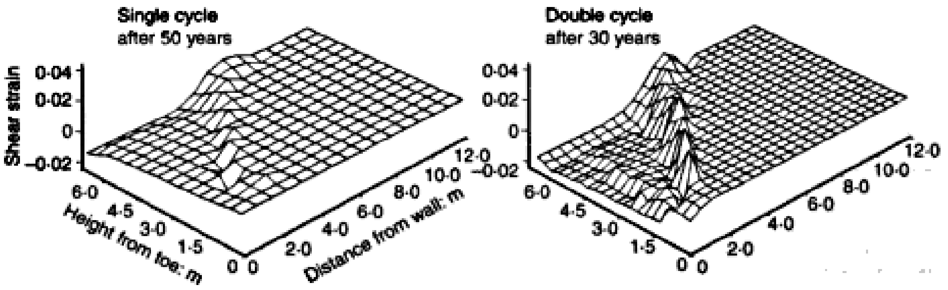

Figure 5.20 Topological plot of accumulated shear strain of the backfill soil mass for a bridge of 60 m span (wall rotation magnitude 0.25%) with an initial void ratio of 0.56 and daily EBT profile *an*

5.6 Influence of different daily EBT variations

Different daily temperature changes influence the wall reaction ratio *K* and soil deformations in a similar manner to the inclusion of daily temperature changes with seasonal changes. Any variation in the normal daily profile of temperature changes will create changes to the cyclic thermal displacements of the deck and hence changes in the cyclic behaviour overall. Table 5.6 gives information for two different profiles of daily temperature variation for a 100 m long bridge. Profile *bn* exhibits greater (on average over the year) daily variations in EBT (1–4°C) than profile *an* (0.5–2°C). This difference leads to:

- Greater granular flow and hence a lower maximum *K* value for profile *bn*, as compared to either profile *an* or the single seasonal cycle case (see Figure 5.17 and Table 5.6). The differences created by choosing either the *an* or *bn* profile are not significant for the 60 m bridge.
- Increased settlements for profile *bn* compared to *an* profile and the single seasonal cycle case (see Figures 5.18 and 5.19 and Table 5.6).

5.7 Influence of the bridge completion date

Generally, winter service-life starts lead to the highest early stresses, while summer service-life starts lead to the lowest early stresses. However, all long-term solutions are very similar. Figure 5.21 shows the form of the variations in the wall reaction ratio *K* towards the steady state solution, for the three seasonal starts of winter, spring and summer.

The season at which the structure enters service has an influence on the settlement but this ceases to be significant at long times (Figure 5.22). Winter starts generally give rise to slightly greater settlements.

5.8 Influence of a stiffer backfill material

T sand was created numerically to give a stiffer response than the Leighton Buzzard sand in order to examine the sensitivity of the soil–structure interaction solution to the performance of the backfill material. Two monotonic stress–strain responses, one for Leighton Buzzard sand and the other for T sand are compared in Figure 5.3. Both relate to plane strain behaviour for σ_3 = 20kPa and e_0 = 0.52. At an axial strain of 1%, the stress ratio σ_1/σ_3 is 3 for the Leighton Buzzard sand. The corresponding σ_1/σ_3 ratio for the T sand is 4.2. This increase in stress ratio represents a 40% stiffer response for the T sand at 1% axial strain.

Table 5.6 Effect of the magnitude of the daily temperature variations on the maximum wall reaction ratio *K* and soil settlement for a 100 m long bridge*

	Single cycle	Double cycle with EBT profile *an*	Double cycle with EBT profile *bn*
Seasonal EBT variation: °C	50	50	50
Maximum daily summer EBT variation: °C	NA	2	4
Maximum daily winter EBT variation: °C	NA	0.5	1
Maximum *K* at steady state	1.5	1.22	1.15 (–17% from *an*)
Total settlement (after 30 years) of soil adjacent to wall (mm)	70	200	260 (+30% from *an*)

*Initial void ratio 0.56. *a* and *b* denote two different daily EBT variation profiles of 0.5–2°C and 1–4°C (winter–summer) respectively; n defines spring starts

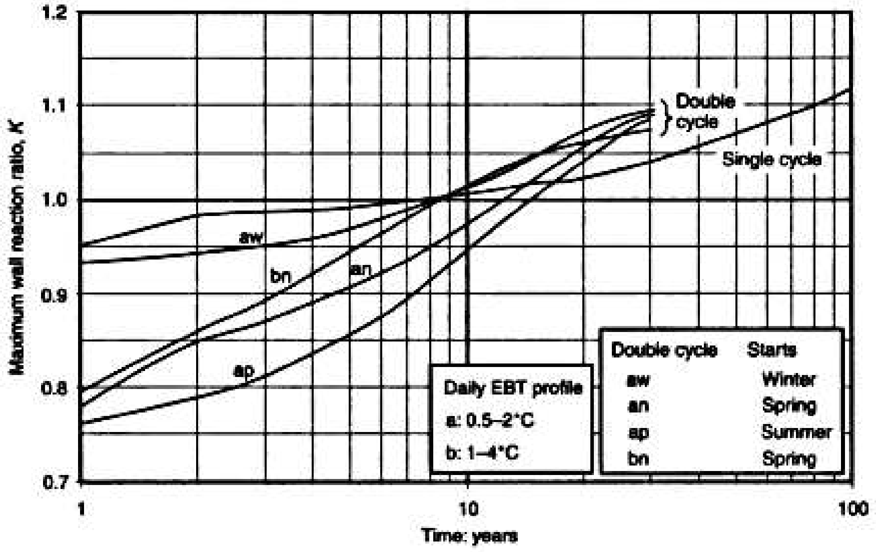

Figure 5.21 Variation in the maximum wall reaction ratio *K* with time, for three start dates and two daily EBT profiles (60 m bridge; initial void ratio 0.56; wall rotation 0.25%)

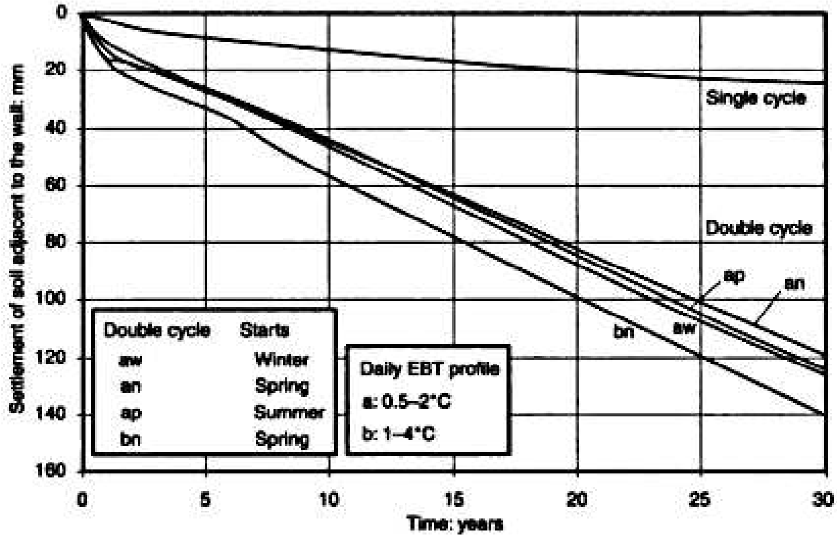

Figure 5.22 Comparison of soil settlement with time, for three start dates and two daily EBT profiles (60 m bridge; initial void ratio 0.56; wall rotation 0.25%)

The effect of this increased soil stiffness on bridge performance is reflected in:

- Increased wall reaction ratios *K* for all bridge lengths and temperature change effects (Figure 5.23 and Table 5.7).
- Reduced settlements for bridges longer than 60 m (Figure 5.24). The reduction is disproportionately greater for the longer bridges and results from the lower densification of the T sand, which sustains consistently higher soil stress ratios than the Leighton Buzzard sand.
- Increased heave of soil surface for all bridge lengths (see Figure 5.25).

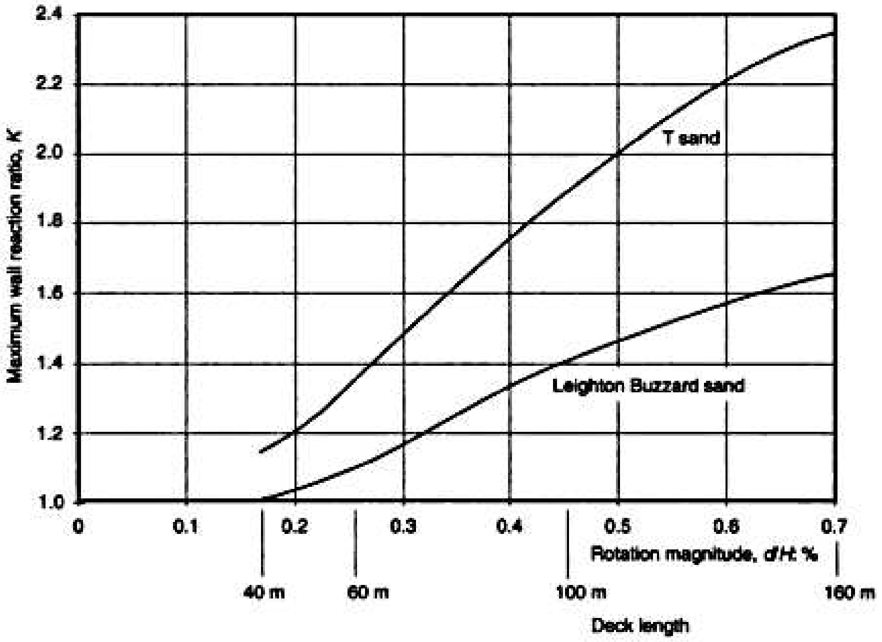

Figure 5.23 Variation of maximum wall reaction ratio, *K*, at steady state with wall rotation magnitudes (bridge lengths) for T sand and Leighton Buzzard sand; initial void ratio 0.56 and single cycles

Table 5.7 Comparison of soil stress ratio, R, and values of maximum wall reaction ratio, K, for T sand and Leighton Buzzard sand[a]

	Leighton Buzzard sand	T sand	T sand versus Leighton Buzzard sand: %
Soil stress ratio *R*[b]	3	4.2	140
Maximum *K* at year 100 under single-cycle loading	1.4	1.9	136
Maximum *K* at year 30 under double-cycle *an* loading	1.18	1.3	110

[a] Wall rotation magnitude 0.45%; 100 m long bridge

[b] At 1% axial strain in the soil element test

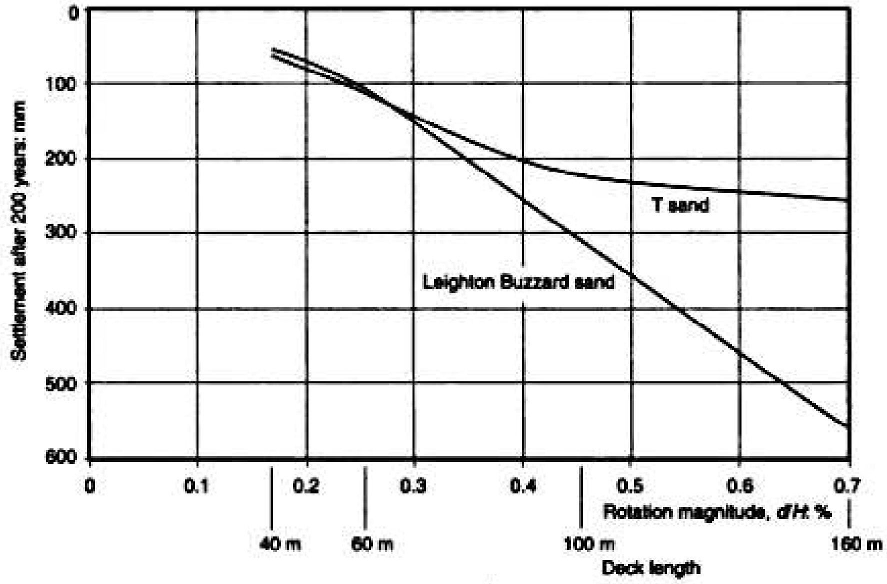

Figure 5.24 Variation of settlement after 200 years with wall rotation magnitudes (bridge lengths) for T sand and Leighton Buzzard sand; initial void ratio 0.56 and single cycles

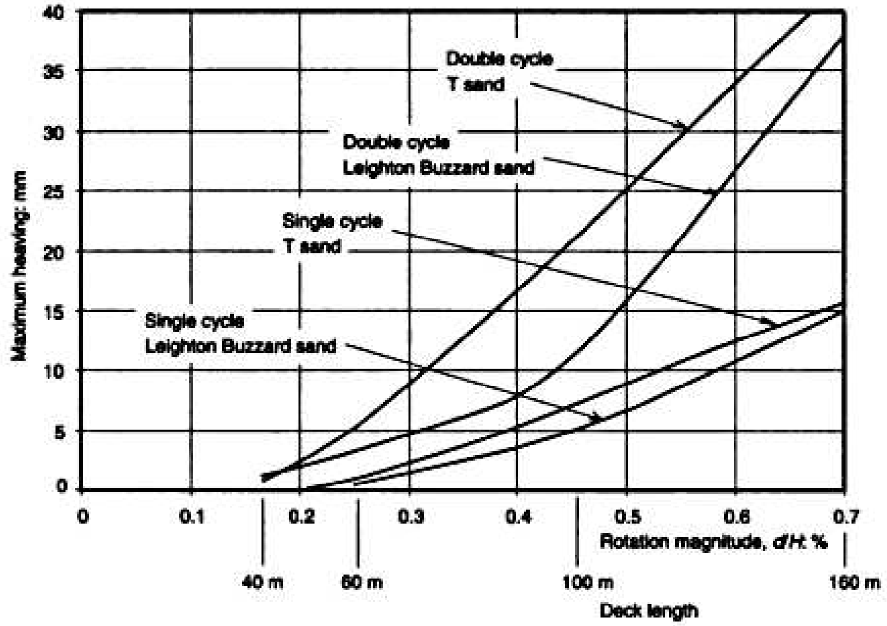

Figure 5.25 The effect of double temperature cycles and type of sand on the surface heave after 30 years (initial void ratio 0.56). The daily EBT variations are 0.5°C (winter) to 2°C (summer). Heave is recorded at a horizontal distance from the wall approximately equal to the wall height

5.9 Heave of soil surface

The maximum heaving of the soil surface occurred at a distance equal to approximately the wall height from the abutment. Unlike the settlement, the heave increases exponentially with the wall rotation magnitude for a given number of cycles. Soil stiffness plays an important role, as can be seen from Figure 5.25 where the stiffer T sand is shown to produce a greater heave than Leighton Buzzard sand for the same conditions.

The parameter which has the greatest influence on heave is the daily temperature fluctuation. This is undoubtedly due to the increased granular flow which results from the increased number of strain cycles and associated accumulated plastic strain. Figure 5.25 shows the enhanced heave created by the daily temperature cycles. Additional supporting information is displayed in Figure 5.20, where it can be seen clearly that the maximum accumulated positive shear strain is close to the 45° plane. This infers that upward granular flow occurs in this region.

5.10 Closing remarks

Conclusions from this chapter are presented in Chapter 7 along with other relevant information from the model retaining wall experiments described in Chapter 4. The transitional equilibrium method of retaining wall analysis used for the simulations in this chapter is described in Part 2 of this book. Validation checks for the numerical analyses are given in Appendix 1.1.

6 Settlement of abutment foundation

The following situations are discussed in this chapter:

- a rigid abutment–footing on a granular soil, subjected to cyclic rotations;
- a rigid bridge on a granular soil, creating translation of footing without rotation;
- a rigid bridge on a clay soil, creating translation of footing only;
- a non-rigid bridge on a clay soil, creating translation and rotation of footing;
- a cantilever sheet pile abutment wall.

6.1 Rigid abutment–footing on granular soil

The nature of and historical changes to the soil loading on the abutment and its footing during cyclic thermal changes in the length of the bridge deck are complex. An approach to the settlement calculation has been developed for a stiff abutment–footing subjected to rotational movements and founded on a granular soil, by comparing the initial and long-term stress states below the foundation, and in particular the stresses at the centre of the hardened soil core, which is assumed to become elastic at the shakedown state after many cycles (Figure 6.1(b)). The footing is thus assumed to rotate about some axis (yet to be determined) in the base plane. The assumption of a rigid abutment and a relatively soft beam (flexural stiffness) allows the longitudinal thermal expansion and contraction of the deck to be translated into maximum rotational movements of the footing. The abutment–footing structure is thus taken to undergo only rigid-body rotational movements, in the shakedown state. The logic has several stages and is applied here to a symmetrical bridge of span L (Figure 6.1(a)). One-half of the span is then considered.

6.1.1 Rotation of the footing

For a change in deck temperature ΔT the maximum horizontal displacement at the beam–abutment junction is,

$$d = L\alpha\,\Delta T/2, \tag{6.1}$$

where α is the coefficient of thermal expansion of the bridge deck.

The rotation of the footing θ is then the rotation of the rigid abutment, namely,

$$\theta = d/H. \tag{6.2}$$

6.1.2 Stresses below the footing

Previous work has indicated that cyclic rotations of a shallow foundation on granular soil lead to significant changes in the stress at the outer edges of the foundation where the largest plastic strains occur and to a central core which progressively densifies under monotonic loading. (This occurs because the axes of rocking move towards the uplift side of the footing during each half cycle of rotation.) A stable (vertical displacement) shakedown solution can exist if, or when, the densified core becomes elastic. In this elastoplastic shakedown condition rotations cause repeating elastic changes in the core material, and plastic shakedown stress reversals in the outer material. The shakedown stresses have values centred on the hydrostatic stress determined from the local vertical stress σ_H, and have peak cyclic values of σ_H/R and $R\sigma_H$ (Figure 6.2), where R is the shakedown stress ratio. (After many 'loading' cycles the soil responds with a repeating dilatency/stress ratio relationship for which the shakedown stress ratios can be determined (England *et al.*, 1997).) The width of the footing over which elastic behaviour occurs, and the magnitude of the stresses there are determined from separate calculations.

6.1.3 Width of the elastic core

Based on an elastic strain threshold ($\varepsilon_d^* = 0.05\%$) for the granular material and a depth of influence $D = \beta B$, where B is the width of the footing and $\beta \approx 2.5$, the repeating elastic surface displacement δ can be evaluated and related to the rotation θ of the footing over a width of, say, c (see Figure 6.1(b)). For a uniform elastic soil modulus E with depth, and an assumed linear variation of stress from zero at depth D to a maximum at the soil–footing interface, the relationship between the cyclic elastic surface displacement δ and the associated maximum elastic strain at the soil–footing interface is given by

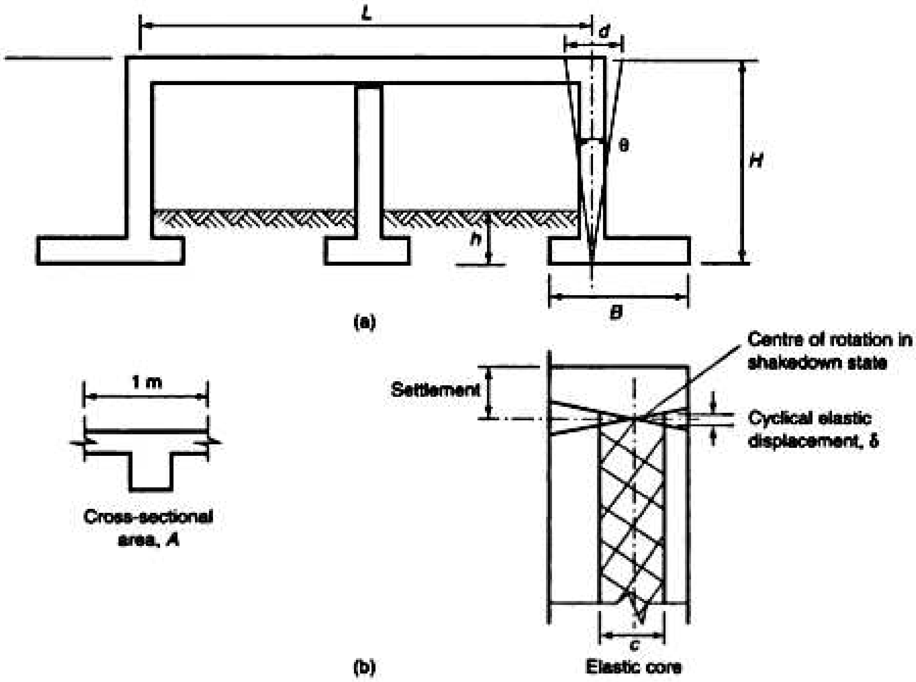

Figure 6.1 Integral bridge: (a) general dimensions; (b) settlement and location of the elastic soil core in the shakedown state

$$\delta = c\theta/2 = \beta B\varepsilon_{el}^{*}/2. \tag{6.3}$$

From Equation 6.3 it follows that the width of the elastic core is

$$c = \beta B\varepsilon_{el}^{*}/\theta. \tag{6.4}$$

6.1.4 Stress distribution below footing

With the width of the elastic core determined from Equation 6.3, the proportion of the foundation width over which the shakedown stresses act is known. What remains is to determine the location of the elastic core. The location is determined by considering the vertical equilibrium and the knowledge that the force supported by the core remains constant for extreme movements of the deck. For constant total vertical loading on the footing it then follows that the force contribution supported by the shakedown stresses, at both extreme movements of the deck, must remain unchanged also.

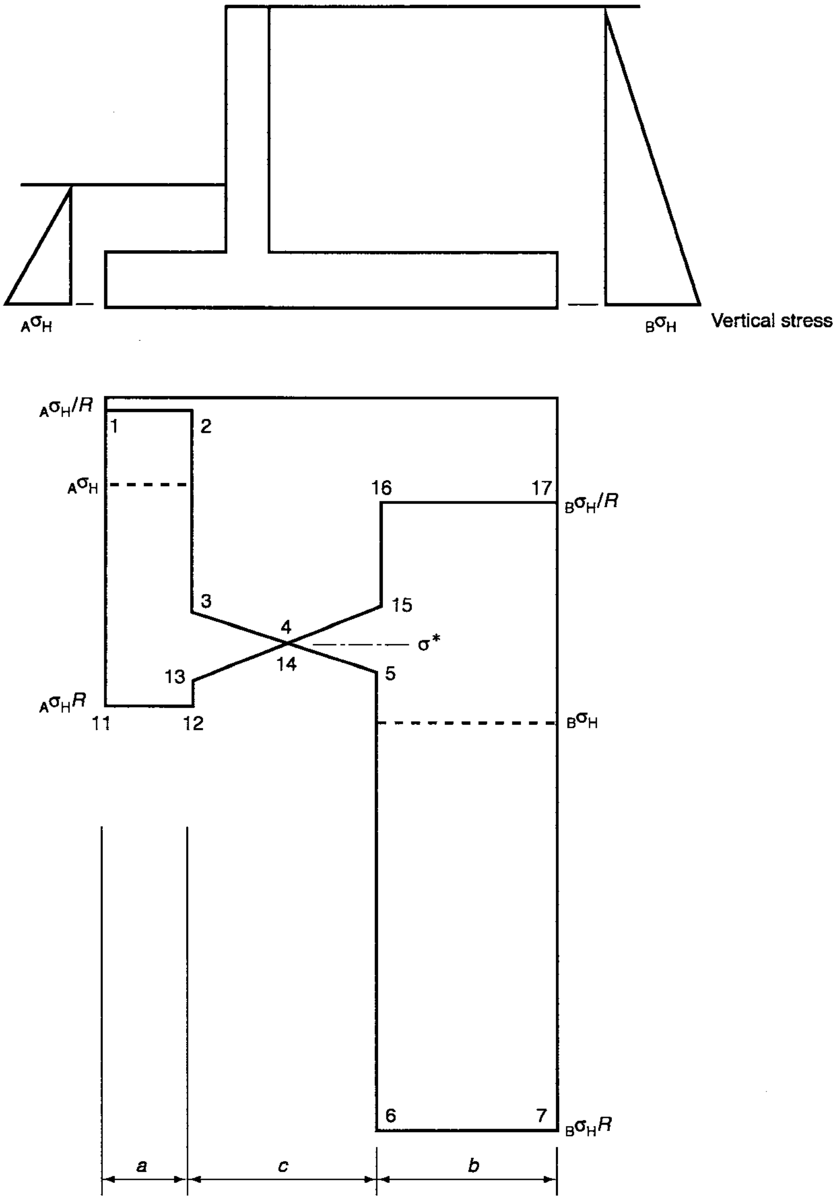

Figure 6.2 General form of shakedown stresses below the abutment footing

Thus if the local hydrostatic stresses for the soil on the embankment side of the abutment are denoted by ${}_B\sigma_H$ and on the non-embankment side by ${}_A\sigma_H$ acting over widths b and a of the footing (see Figure 6.2), respectively, the cyclic stress changes during a deck-displacement cycle are shown by the points 1-2-3-4-5-6-7 and 11-12-13-14-15-16-17. The changes of the shakedown stresses over a cycle must satisfy the following equation:

$$(R\,{}_A\sigma_H - {}_A\sigma_H/R)a = (R\,{}_B\sigma_H - {}_B\sigma_H/R)b, \qquad (6.5)$$

thus giving

$$a/b = {}_B\sigma_H/{}_A\sigma_H, \qquad (6.6)$$

which is equal to H/h in Figure 6.1(a).

Finally, the mean stress σ^* in the elastic core is evaluated from the vertical equilibrium, from Figure 6.2, as

$$a\,{}_A\sigma_H/R + b\,{}_B\sigma_H R + c\sigma^* = W_{\mathrm{tot}} \qquad (6.7a)$$

(see Figure 6.3 for W_{tot}) or

$$a\,{}_A\sigma_H R + b\,{}_B\sigma_H/R + c\sigma^* = W_{\mathrm{tot}}. \qquad (6.7b)$$

A check must be made to determine whether elastic soil behaviour can be sustained, i.e. is $\sigma^*/{}_B\sigma_H < 3$? If $\sigma^*/{}_B\sigma_H > 3$, it must be assumed that the foundation will be subjected to an indeterminate settlement, i.e. it is unstable. (Elastic behaviour can be guaranteed only when soil dilation does not occur.)

Another check which is necessary, is the consistency of Equations 6.7a and 6.7b with the form of solution obtained, i.e. are the values of a and b consistent with the local hydrostatic stresses ${}_A\sigma_H$ and ${}_B\sigma_H$ over the entire widths a and b? If not, the equations must be modified appropriately. The numerical example in Section 6.1.7 illustrates this feature.

6.1.5 Settlement of the footing

Settlement may be estimated from the increase in the stress in the elastic core from the time of completion of construction to the time at which the shakedown condition is reached. During this time the loading has been monotonic and settlement may be estimated from a monotonic loading curve for the soil over the change in the stress ratio defined by the initial and shakedown stress states.

6.1.6 Moment equilibrium

The structure must be designed to withstand the moment $(F\alpha'H - W_{\mathrm{tot}}e)$ in the beam (see Figure 6.5). Any out of balance moment increments due to the simultaneous changes of F and e during the cyclic thermal length changes in the bridge deck must also be supported in a similar way. It is assumed here that there is no horizontal shear force acting over the base of the footing in the shakedown state.

6.1.7 Numerical example: a stiff abutment–footing on granular soil

Figure 6.1 gives the general dimensions of a concrete integral bridge. The foundation stresses have two solutions;

(*a*) initial stresses at the completion of construction; and
(*b*) long-term stresses as dictated by repeated cyclic thermal displacements of the bridge deck.

Settlement of the footing is then estimated from the change in stress from state (*a*) to state (*b*) from a primarily monotonic stress–strain calculation.

The *initial stresses* relate to *active* soil pressures from the embankment–backfill to the abutments and before the establishment of longitudinal interface forces between the bridge deck and abutments. In this example a small *at-rest* stress distribution acts over the front of the abutment below road level.

The *long-term stresses* are evaluated as the limiting stresses after many thermal cycles of the bridge deck. During early thermal cycling some small lateral movement of the footings is likely to occur. Eventually this will cease and the footing will, cycle by cycle, rotate about some axis in the base plane of the footing. The location of this axis forms part of the analysis.

The total vertical loading W_{tot} over the base of the footing is taken to be a combination of the bridge loading W_B and that of the soil above the footing, shown simply as W_{S1} and W_{S2} in Figure 6.3.

Data used in the analysis

Bridge:
Overall span $L = 60$ m
Abutment height $H = 7$ m
Depth of abutment toe $h = 1.5$ m
Width of footing $B = 4$ m
Transverse area of cross section $A = 0.5$ m^2/m width
Density of concrete $\gamma_c = 24$ kN/m^3
Coefficient of thermal expansion of deck $\alpha = 12 \times 10^{-6}$/°C
Seasonal temperature change $\Delta T = 50$°C

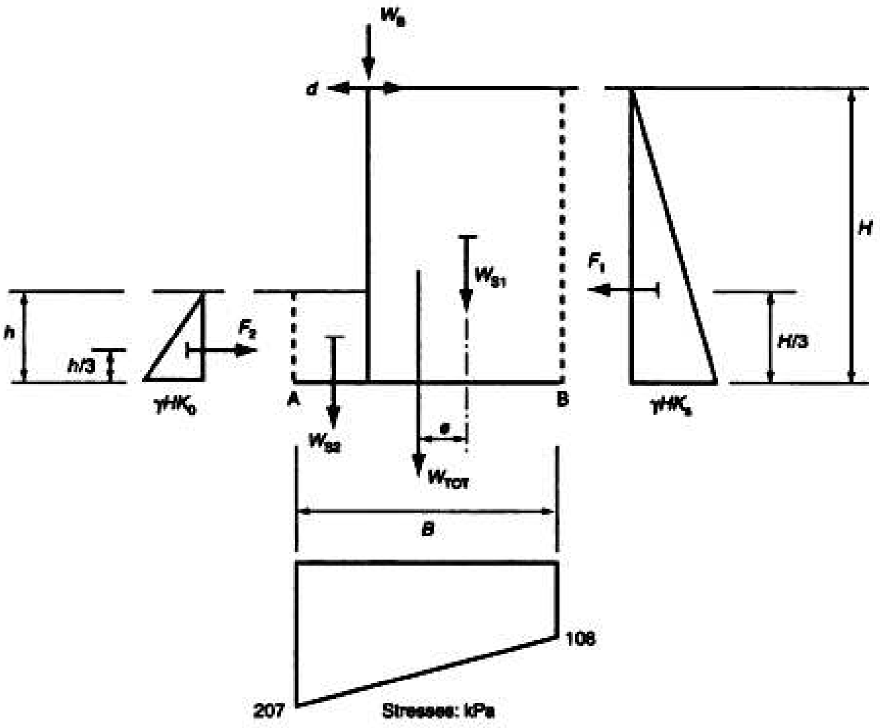

Figure 6.3 Loading details for the abutment footing and the initial stresses below the footing. The abutment is located 1 m in from the front of the footing

Soil:
Density of soil $\gamma_s = 20$ kN/m^3
Elastic shear modulus $G = 80$ MN/m^2
Threshold elastic strain $\varepsilon_{el}^* = 0.05\%$
Influential depth for strain $D = \beta B$ where $\beta \approx 2.5$ and B is width of footing

Loading (Figure 6.3 gives the details):
Bridge loading on abutment (per metre width) $W_B = \gamma_c AL/4 = 24 \times 0.5 \times 60/4 = 180$ kN max.
Loading on footing (per metre width) $W_{S1} = 7 \times 3 \times 20 = 420$ kN
$W_{S2} = 1.5 \times 1 \times 20 = 30$ kN
Total load on footing $W_{tot} = W_B + W_{S1} + W_{S2} = 180 + 420 + 30 = 630$ kN
Location of resultant from inner face of footing $x = [0.5 \times 30 + 2.5 \times 20 + 1 \times 180]/630 = 1.98$ m

Initial stresses (elastic calculation)

Using $K_a = 0.25$ and $K_p = 0.4$ in Figure 6.3 leads to

$$F_1 = 20 \times 7 \times 0.25 \times 7/2 = 122.5 \text{ kN}$$

$$F_2 = 20 \times 1.5 \times 0.4 \times 1.5/2 = 9.00 \text{ kN.}$$

The resultant moment acting on the centre line of the footing (anticlockwise) M is given by

$$M = 630 \times 0.02 + 122.5 \times 2.33 - 9.00 \times 0.5 = 132.9 \text{ kNm.}$$

The footing stresses at A and B are then

$$\sigma_{A,B} = W_{tot}/B \pm MB/2I,$$

where

$$I = 4^3/12 = 5.33 \text{ m}^4,$$

i.e.

$$\sigma_{A,B} = 630/4 \pm 132.9 \times 4/(2 \times 5.33) = 157.5 \pm 49.9 \text{ kPa.}$$

The initial footing stresses are shown in Figure 6.3.

Long-term stresses (elastic–plastic shakedown calculation)

The thermal expansion of deck (half span) is

$$d = L\alpha\,\Delta T/2 = 60 \times 12 \times 10^{-6} \times 50/2 = 0.018 \text{ m,}$$

and the rotation of abutment about footing base is

$$\theta = d/H = 0.018/7 = 2.571 \times 10^{-3} \text{ rad.}$$

The elastic core is defined in Figure 6.1 in relation to the abutment rotation θ and the cyclic surface elastic displacements δ at the periphery of the core. The value of δ is determined from an integration of the strains over depth D for a uniform elastic soil modulus $E \approx G/2$.

The depth of the strain influence is

$$D = \beta B = 2.5 \times 4 = 10 \text{ m,}$$

the incremental settlement is

$$de = \varepsilon \, dz,$$

and the surface settlement is

$$\delta = \int de = \int_0^D \varepsilon \, dz$$

where $\varepsilon = \varepsilon_{el}^*(1 - z/D)$, i.e.

$$\delta = \varepsilon_{el}^* D/2.$$

Hence,

$$\delta = 0.0025 \text{ m}.$$

Then,

$$\theta = 2\delta/c$$

and finally,

$$c = 2\delta/\theta = 2 \times 2.5 \times 10^{-3}/2.571 \times 10^{-3} = 1.945 \text{ m}.$$

Foundation stresses in the shakedown state

Figure 6.2 shows the expected form of the solution. The dimensions a and b need to be determined. From Equation 6,

$$a/b = \mathrm{H/h} = 7/1.5 = 4.67.$$

Then, since $(a + b + c) = 4$, it follows that $a = 1.692$ m and $b = 0.362$ m.

Observation shows that $a > 1$ m. This solution therefore needs to be considered in relation to the form of wingwall construction, the local hydrostatic stress, σ_H, the shakedown stresses, σ_H/R or $\sigma_H R$ and the corresponding areas below the foundation designated by a and b in Figure 6.4. Two possibilities are considered.

(*a*) *Case 1*: the wingwalls return at an angle $\theta < 45°$ to the bridge axis.
(*b*) *Case 2*: the wingwalls are perpendicular to the bridge axis.

Case 1 solution. The hydrostatic stress relating to the soil height h is assumed to apply to the forward part of the foundation defined by $a = 1.692$ m. The soil height H determines the local hydrostatic stress for the rearward portion of the foundation defined by $b = 0.362$ m. The width of the elastic core c is 1.945 m.

The mean stress in the elastic core σ^* is obtained from Equation 6.7a as

$$\sigma^* = [630 - 1.692 \times 7.5 - 0.362 \times 560]/1.945 = 213 \text{ kPa}.$$

A check calculation using Equation 6.7b yields the same value for σ^*.

The maximum variation in the stress across the elastic core is $\Delta\sigma$, where

$$\Delta\sigma = \varepsilon_{el}^* E \approx \varepsilon_{el}^* 2G = 5 \times 10^{-4} \times 2 \times 80 = 0.08 \text{ MPa},$$

i.e.

$$\Delta\sigma = 80 \text{ kPa}.$$

The final stresses at shakedown are as illustrated in Figure 6.4.

Case 2 solution. For this solution the local hydrostatic stresses are governed by the soil height h in front of the abutment and by the height H behind the abutment. The modified solution is now taken to have the form of Figure 6.6, for which

$$1 + a + b + c = 4.$$

The dimensions of the elastic core remain unchanged at $c = 1.945$ m.

New values of a and b need to be determined. Equation 6.5 is redefined as follows:

$$1(R_{A}\sigma_{H} - {}_{A}\sigma_{h}/R) + a(R_{B}\sigma_{H} - {}_{B}\sigma_{h}/R) = b(R_{B}\sigma_{H} - {}_{B}\sigma_{h}/R). \tag{6.8}$$

Equation 6.6 then becomes,

$$a = b - {}_{A}\sigma_{h}/{}_{B}\sigma_{H} = b - h/H. \tag{6.9}$$

Then, for this example, $a = 0.42$ m and $b = 0.63$ m.

A consequence of the changes to Equations 6.5 and 6.6 is that Equations 6.7a and 6.7b must also change. They become

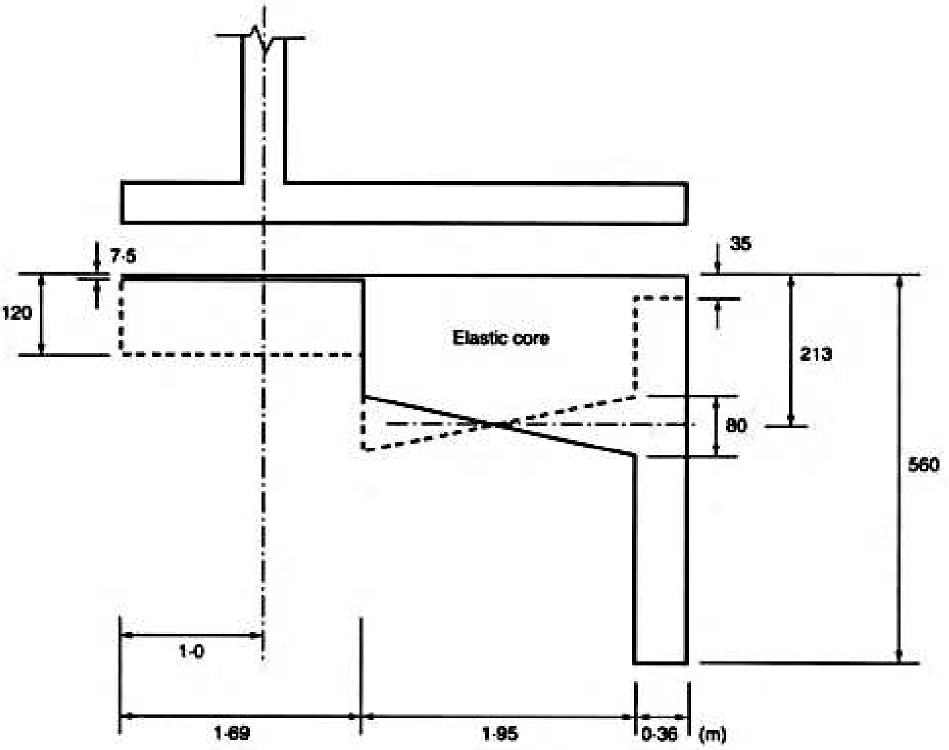

Figure 6.4 Shakedown stresses (in kPa) below footing: case 1 solution

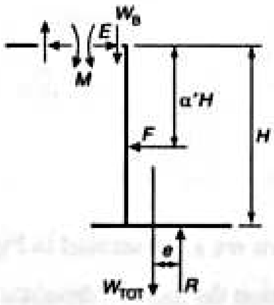

Figure 6.5 Abutment actions. F is the cyclically varying resultant horizontal soil force. $R = W_{tot}$ is the constant soil reaction acting at eccentricity e (cyclically variable) with the resultant downward force on the footing

$${}_{A}\sigma_{H}/R + a\,{}_{B}\sigma_{H}/R + b\,{}_{B}\sigma_{H}R + c\sigma^{*} = W_{tot} \tag{6.10a}$$

and

$${}_{A}\sigma_{H}R + a\,{}_{B}\sigma_{H}R + b\,{}_{B}\sigma_{H}/R + c\sigma^{*} = W_{tot}. \tag{6.10b}$$

From Equation 6.10a

$$30/4 + 0.42 \times 140/4 + 0.63 \times 140 \times 4 + 1.945\sigma^{*} = 630,$$

giving

$$\sigma^{*} = 131 \text{ kPa}.$$

The check from Equation 6.10b leads to

$$30 \times 4 + 0.42 \times 140 \times 4 + 0.63 \times 140/4 + 1.945\sigma^{*} = 630,$$

giving

$$\sigma^{*} = 130 \text{ kPa}.$$

The maximum variation of stress across the elastic core is $\Delta\sigma$, where

$$\Delta\sigma = \varepsilon_{d}^{*}E \approx \varepsilon_{d}^{*}2G = 5 \times 10^{-4} \times 2 \times 80 = 0.08 \text{ MPa},$$

i.e.

$$\Delta\sigma = 80 \text{ kPa}.$$

The final stresses at shakedown are as illustrated in Figure 6.6.

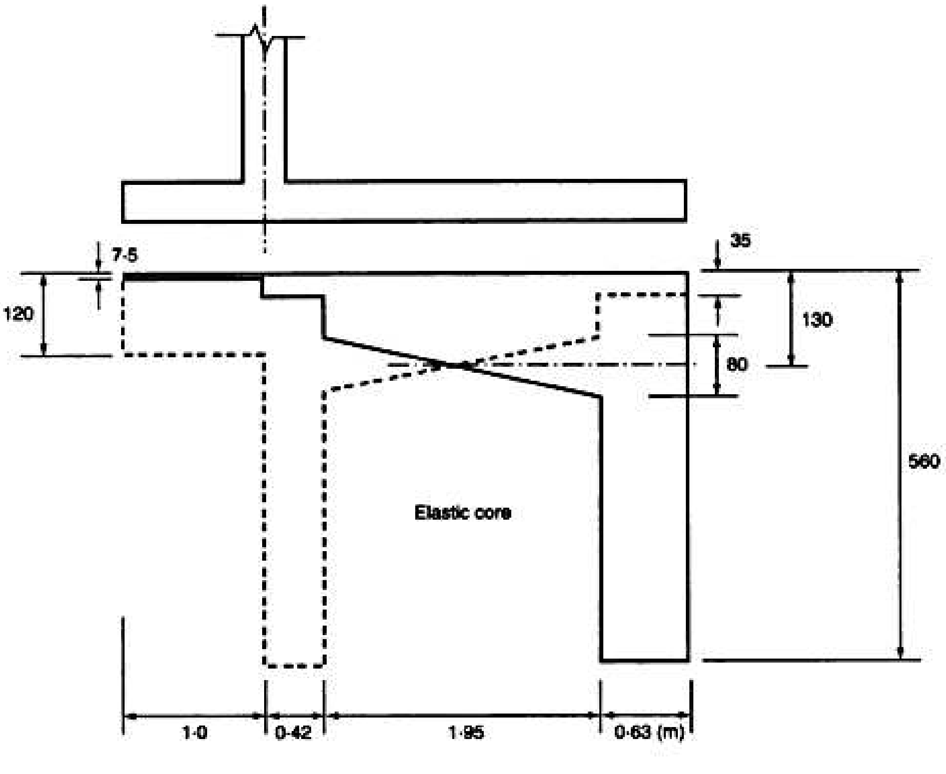

Figure 6.6 Shakedown stresses (in kPa) below the footing: case 2 solution

Settlement of the footing

The settlement within the elastic core takes place as the result of a monotonically increasing stress until the shakedown state is reached. The change in stress from the initial condition to the shakedown state allows an estimate of settlement to be made as described below.

Case 1 solution. The initial stress σ_{init} at the centre of the elastic core (i.e. 2.57 m from the front of the footing) is, from Figure 6.3,

$\sigma_{init} = 207 - 2.57 \times 99/4 = 143$ kPa.

The local vertical stress is

$\sigma_V = 140$ kPa,

and hence the stress ratio is

$R_{init} = 143/140 = 1.02$.

At shakedown the core stress is $\sigma^* = 213 \pm 40$ kPa, leading to a stress ratio that varies between

$R_1 = 253/140 = 1.81$

and

$R_2 = 173/140 = 1.24$.

The vertical surface strain resulting from the change in the stress ratio from R_{init} to R_1 is shown in Figure 6.7a as $\varepsilon_1 \approx 0.5\%$. This equates to a mean surface settlement of $\delta_1 = \varepsilon_1 D/2$, where $D = 10$ m in this example, i.e. $\delta_1 = 25$ mm.

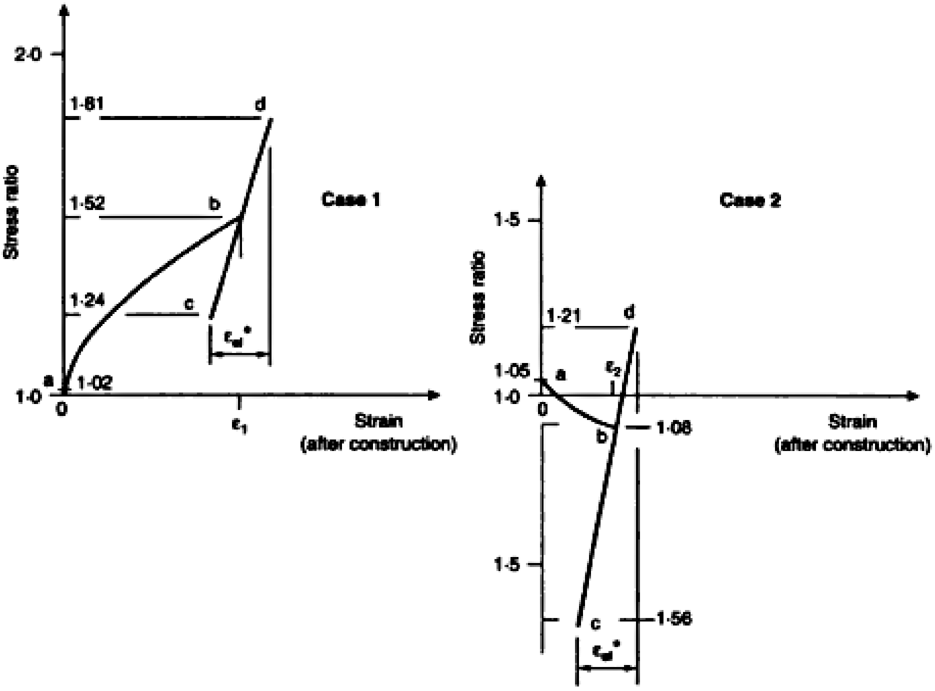

Figure 6.7 Changes of stress in the elastic core for case 1 and case 2 solutions. a–b, centre line of the elastic core under monotonic loading. c–d, shakedown at the boundary of the elastic core under cyclic loading

Case 2 solution. Here

$\sigma_{\text{init}} = 207 - 2.40.99/4 = 147$ kPa.

Then

$R_{\text{init}} = 147/140 = 1.05.$

At shakedown

$\sigma^* = 130 \pm 40$ kPa.

The stress ratios at shakedown are then

$R_1 = 170/140 = 1.21$

and

$R_2 = 90/140 = 0.64,$

i.e.

$1/R_2 = 1.56.$

The vertical surface strain caused by the change in the stress ratio from R_{init} to R_1 is shown in Figure 6.7b as $\varepsilon_2 \approx 0.3\%$. This equates to a mean surface settlement δ_2 of 15 mm.

6.2 A rigid bridge on granular soil

In this situation cyclic translational movements of the footing will dominate. These will subject the soil below the footing to repeating simple shear deformations. These deformations will be plastic near to the soil–footing interface and elastic at greater depth. In the plastic region a shakedown state will eventually develop, and consequently volume change will occur. The integrated effect could be expansion or contraction depending on the initial void ratio and the maximum shear strain amplitude. As the ratio τ/σ (shear stress/direct stress) will decay rapidly with depth below the footing, the shakedown behaviour will be limited to the soil close to the footing.

6.3 A rigid bridge on clay soil

Horizontal displacements will cause either elastic deformation or local dilation of the clay near to the footing–clay interface, which will result in a local failure of the clay. Continued cycling will result in a progressive fall in clay strength to its residual value with an angle of friction, $\phi \approx 10$–$12°$. Further cycling will be associated with local horizontal slip and no settlement (assuming that the clay was sufficiently overconsolidated and capable of supporting the initial design loading elastically).

6.4 A non-rigid bridge on clay soil

In this situation the footing is subjected to translational and rotational movements. The rotational displacements will generally be absorbed in elastic deformation, and the horizontal displacements will either be absorbed into elastic shear strain or else will cause clay failure and a move towards its residual strength, albeit at a slower rate than for the rigid bridge. Again, if the clay was sufficiently overconsolidated and capable of supporting the initial design loading elastically, no significant settlement will result.

6.5 A cantilever sheet pile abutment wall

The use of this type of retaining wall construction for the abutments of integral bridges involves two issues:

- lateral earth pressure escalation and soil densification for both the granular backfill and the soil in front of the wall; and
- settlement of the cantilever abutment.

6.5.1 Cut-off point in a cantilever wall

Figure 6.8 illustrates the deformation of the sheet pile during cyclic movement of the pile cap (the bridge deck). Under monotonic loading it is possible to define a position x–x, known as the cut-off point, above which there is no out of balance lateral force on the wall, and below which plastic soil deformations can be assumed not to occur. The position of this cut-off point can be evaluated for static loading. However, during cyclic transverse movements of the pile at its upper end, the location of a cut-off point has yet to be identified, if such a single point can exist at all.

6.5.2 Soil behaviour during cyclic movements of the wall

For a soil element close to the wall (element A in Figure 6.8) the combined effect of the wall–soil friction and the changing lateral earth pressures is to create a combination of cyclic rotation of the major principal stress direction and cyclic changes in the maximum principal stress ratio. Figure 6.9 shows the initial stress condition for the soil element after backfilling against the abutment. Contraction of the bridge deck will cause a reduction in the shear stresses on the element (and consequently on the wall also) with possible reversal of their directions. Subsequent deck expansion will reinstate the initial stress directions. Figure 6.9 shows also the form of the principal stress rotations caused by the cyclic wall movements. Such rotations have been studied by Arthur *et al.* (1980, 1991) and Dunstan *et al.* (1988) who identified a combination of critical rotation angles coupled with different magnitudes of stress ratio which give rise to increased fluidity of the soil, i.e. to a cyclically mobilized granular flow. Therefore, it can be expected that the combined influence of friction at the cantilever wall–soil interface and the transverse cyclic wall movements, will be to encourage significant granular flow and densification of the soil close to the wall.

Cyclic wall movements will thus change the distribution of friction in the upper part of the wall, causing more vertical loading to be transferred to the lower portion. Soil densification will occur behind the wall, and to some extent in front of the wall also. The probable consequence of the soil densification will be to cause the location of the cut-off point to rise. This in turn will improve overall stability but impose higher bending stresses in the upper part of the sheet pile abutment. The critical condition for the stability of the wall is thus during the early cycles of movement when the wall–soil interface friction undergoes redistribution and before the soil adjacent to the wall has densified. Design of the embedded length of the lower portion should therefore relate to the total vertical loading from the bridge without any relief from surface wall friction above the cut-off point. For long-span bridges it may also be necessary to increase the loading to accommodate for shear stress reversals (i.e. reversed wall–soil interface friction) during the contraction phase of the bridge deck movements.

The embedded length of pile below the cut-off point may be evaluated using the following equation to define the frictional resistance R_s:

$$R_s = \sigma_H' A \tan \delta,$$

where σ_H' is the average effective lateral earth pressure on the pile below the cut-off point, δ is the effective wall–soil interface friction angle, and A is the surface area of the pile over which friction is acting.

6.5.3 Settlement

During the installation of the sheet pile wall some initial wall friction will develop and become distributed in a self-equilibrating manner, with uplift acting over the lower part. Placement of the bridge deck will require the wall to support vertical loading. Generally this will be supported initially by interface friction, mainly over the upper part of the wall. Cyclic movements of the wall will then cause a redistribution of vertical interface stresses as the wall friction over the upper part of the wall is released. The bridge loading will then become supported by increased frictional stresses over the lower part of the wall. The redistribution of stress within the wall will cause some elastic settlement within the sheet pile itself while the increase in interface friction at depth will give rise to additional monotonic shear deformation of the soil and attendant settlement of the wall.

6.5.4 Further studies required

Experiments need to be done to identify the existence and location of an effective cut-off point, and its dependence on soil type, wall stiffness, amplitude of the cyclic deck displacements and abutment height. In addition, it is necessary to develop an understanding of wall movements, leading to the prediction of an effective cut-off point. Finally, experiments should be done to investigate the development and magnitude of settlement during the cyclic redistribution of interface wall friction.

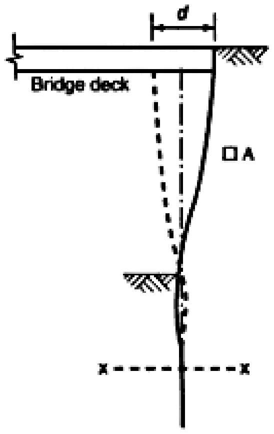

Figure 6.8 Sheet pile abutment retaining wall showing the cut-off point at depth x–x. The soil element A is close to the retaining wall and supports stress states, as shown in Figure 6.9

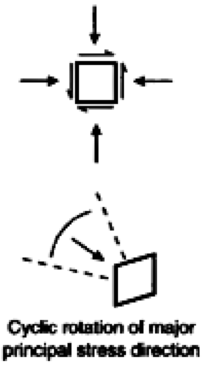

Figure 6.9 Stresses associated with soil element A in Figure 6.8 during cyclic movements *d* of the bridge deck

7 Conclusions and recommendations

The conclusions and recommendations of this chapter are specific to integral bridges with abutment walls hinged at their bases. They relate primarily to:

- The escalation of lateral earth pressure through
  - the wall reaction ratio parameter K, the ratio of total lateral soil force acting on the wall to the total lateral force of a triangular hydrostatic stress distribution acting over the height of the wall (i.e. $R = 1$ over the whole wall), and
  - the soil stress ratio K^*, the design soil stress ratio (σ_h/σ_v) acting over the top half of the wall; assumed constant in BA 42.
- The deformation of the backfill soil, namely settlement close to the abutment and heave of the free surface away from the abutment.

The conclusions and recommendations are drawn from the following information:

- A summary of the major findings.
- An assessment of the numerical simulations (for a full-scale 7 m high abutment wall) in conjunction with the model test results (for a 1 in 12 scale model retaining wall).
- Collective observations from the experimental and numerical sections, brought together to produce bounding limits for design purposes. These are then related to the current standard BA 42.
- An analysis of current limits, to our knowledge, and the requirements of further study.

7.1 Major findings

7.1.1 Wall reaction ratio, *K*

The major parameters that influence the magnitude of K are identified in Figure 7.1. A determination of K requires a detailed analysis. The primary input parameters for this analysis are the effective bridge temperature (EBT) and its variations during the year. The variations in EBT determine horizontal deck displacements and abutment rotations. Then, through the interaction with the backfill soil, the soil stresses and eventually K can be determined.

- *K* quickly changes during the early temperature cycles to span the hydrostatic wall reaction ratio, $K = 1$. (Illustrative values from a single-cycle test with an overall wall rotation *d*/*H* of 0.25% and for a 60 m bridge: maximum value of *K* increases from 1.4 in the first cycle to 2.5 in the 120th cycle.) Thereafter the escalation of soil–abutment stresses leads to an escalation of *K* at a progressively decreasing rate until a limiting or steady-state value K_{ss} (illustrative value, as above: $K_{ss} \approx 2.7$) is approached after many years. (See Figure 4.8 (experimental results) and Figure 5.11 (numerical simulations).)
- The extent of the stress escalation and the time required to reach the steady state are determined primarily by the bridge dimensions and the nature of the EBT fluctuations, both seasonally and daily. (See Figure 4.7 (experimental results) and Figure 5.12 (numerical simulations).)
- Daily EBT variations help to keep the value of *K* closer to the hydrostatic state than would otherwise be the case for seasonal fluctuation of EBT alone; for the same soil density. However, Daily EBT variations produce additional densification of the backfill and hence increase *K*. The combined response is to produce a *K* value very similar to the value of *K* for seasonal fluctuations only.
- The long-term value of *K* is not significantly influenced by either the initial density of the backfill material or the completion date of the construction. (See Figures 5.13 and 5.21 (numerical predictions).)
- K_{ss} is higher for backfill material with a higher internal angle of friction ϕ. (See Figure 5.23.)

7.1.2 Soil deformations: settlement and heave

- Settlements are maximum adjacent to the wall. (Illustrative values from a single-cycle test with an overall wall rotation *d*/*H* of 0.25% for a 60 m bridge are 150 mm for 7 m of backfill in 120 years.) The extent of the settlement is determined primarily by the magnitude of the EBT fluctuations and the bridge dimensions. Unlike the steady state for soil stresses, settlement is continuous throughout the life of the bridge. (See Figure 4.10 (model test results) and Figure 5.15 (numerical prediction).)
- Settlement is greater for larger EBT fluctuations and is increased further by the daily temperature fluctuations. (See Figure 4.10 (experimental results) and Figure 5.19 (numerical prediction).) Settlement adjacent to the wall increased by a factor of approximately three when the daily

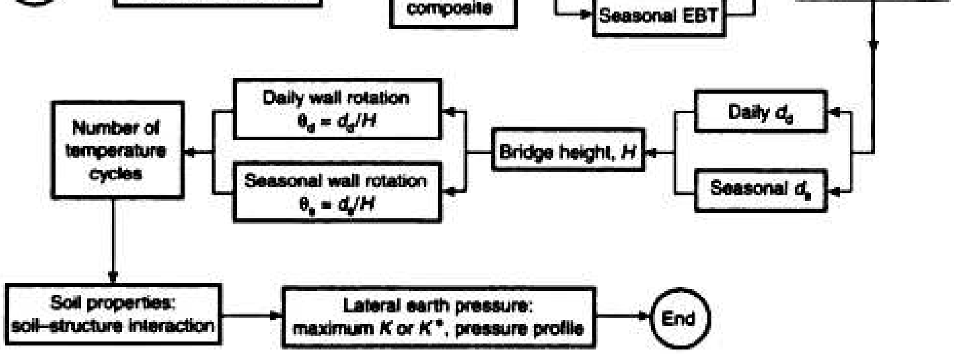

Figure 7.1 Flow chart showing the parameters that influence the determination of the wall reaction ratio *K*

temperature fluctuations were added. This was observed for both the model test results and the numerical simulations.

- Settlement is not particularly sensitive to the initial soil density. (Illustrative values, as above, are: an 18% increase when the initial void ratio was changed from $e_0 = 0.56$ (95% compaction) to $e_0 = 0.64$ (90% compaction).)
- Settlement is lower for a stiffer backfill material.
- The date at which construction is completed has little influence on settlement.
- Soil heave at a distance from the wall equal to approximately the abutment height is possible, e.g. 50 mm after 120 years, for a 100 m long bridge. Heave is less for a lower initial soil density.
- Greater heave results from stiffer backfill material, because K is generally higher and soil densification is slower.

7.1.3 Settlement of the wall foundation

- Settlement of the abutment foundation (strip footing) due to seasonal EBT variations for a bridge less than 60 m long is not significant according to the theoretical evaluation given in Chapter 6.
- Settlement of a cantilever sheet pile wall is believed to be larger than that of a strip footing, but this cannot be quantified without further experimental testing and investigations.

7.2 Bounding limits for design

Two bounding limits on the wall reaction ratio K are proposed. Because the soil stress ratios, R, recorded from the experimental model are always higher than those for a full-scale structure they can be treated as *upper bound values* for design purposes. The numerical simulations underpredict the soil stress ratios R, and can be treated as *lower bound values*. The validity of these two statements is justified below.

7.2.1 Lower bound on the wall reaction ratio K

The numerical analysis currently predicts slight underestimates of the wall reaction ratio K because:

- The soil model is known to overestimate the ratcheting strains associated with imposed stress fluctuations. These in turn overestimate the flow and result in lower values of K.
- The retaining wall analysis does not model the discontinuities associated with the formation of shear slip planes at large wall rotations. The absence of slip results in lower K values.

The under-prediction of K will occur equally when comparing the experimental results from the 1 in 12 scale model and for the prototype 7 m high structure. The results from the numerical analysis are thus taken to be lower bound values.

7.2.2 Upper bound on the wall reaction ratio K

Because granular soils exhibit stiffer (in terms of stress ratio to strain) behaviour at lower confining pressures, the experimental results for K from the 1 in 12 scale model retaining wall will be higher than corresponding values from the prototype 7 m high, structure for the same angular rotations of the wall. The experimental result may then be regarded as an upper bound value, albeit a very conservative one.

An improved upper bound (i.e a lower value) has been developed here by scaling the experimental results to reflect, in part, the lower K value to be expected in the prototype structure. The scaling was carried out on the basis of the hydrostatic stress σ_{hyd} at the midheight of the wall. This scaling is based on a reduction in K from $\sigma_{hyd} = 20$ kPa (the actual value for the model is $\sigma_{hyd} = 4.5$ kPa) to $\sigma_{hyd} = 60$ kPa for the prototype structure. A conservative estimate of K was thus guaranteed. The inset (for σ_1/σ_3 plotted against strain for the two cases $\sigma_3 = 20$ and 60 kPa) in Figure 7.2 shows how this was achieved from available data relating to monotonic loading. The three values of K for the experimental model (corresponding to bridge lengths of 60, 100 and 160 m) were located on the 20 kPa curve for σ_1/σ_3 plotted against strain. The corresponding values of σ_1/σ_3 for the prototype structure were then derived from the lower 60 kPa curve for the same strains as the original points. These new values of σ_1/σ_3 then define the new values of K (the lower curve in Figure 7.2). The new K values are considered to be upper bound values for design purposes.

(*Note*: A check of the scaling procedure was performed by using the numerical analysis to predict K values for two walls of 520 mm and 7 m height, and then comparing the 7 m solution with the results obtained from scaling the 520 mm solution in the same way as described previously. The resulting scaled solution for K was above that for the 7 m simulation, thus indicating that the scaling procedure does lead to an upper bound solution.)

The upper bound values of K are displayed in Figure 7.3 for a range of bridge lengths. The curves have been extrapolated linearly to the origin where $K = 1$.

7.3 Comparison with the current Highways Agency standard

In BA 42 the following rules are specified for the assessment of the design lateral earth pressure on the abutment wall.

The *lateral earth pressure distribution* is derived as a uniform stress ratio K^* from the surface to a depth of one-half the height of the wall, and then a uniform pressure of $\gamma K^* H/2$, over the bottom half of the wall, subject to the proviso that the stress ratio everywhere cannot be less than K_o.

The *value of* K^* is found from the larger of the two values from the following equations:

$$K^* = (d/0.05H)^{0.4} K_p \tag{7.1a}$$

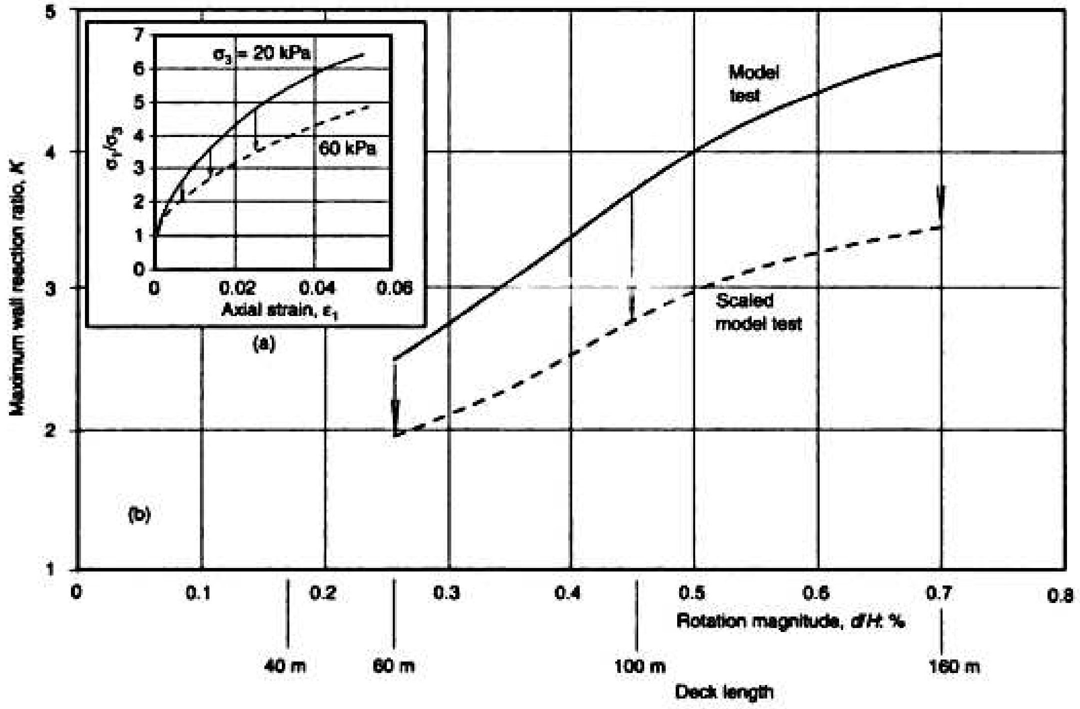

Figure 7.2 Scaling of wall reaction ratios K: (a) monotonic stress ratio response for Leighton Buzzard sand (initial void ratio 0.56); (b) scaling procedures for K, according to the stress ratios in (a) (model test after 120 single cycles)

$$K^* = K_p/3, \tag{7.1b}$$

where d is the total horizontal movement of the abutment wall at the backfill surface.

The relationship between the wall reaction ratio K as defined in this book, and K^* is

$$K = 0.75K^*. \tag{7.2}$$

In the following sections three different comparisons are made with the recommendations from BA 42.

Firstly, the maximum wall reaction ratio K, as determined from experiments (and as scaled to reflect the differences in the confining pressure between the 1 in 12 scale model and the 7 m high prototype structure), is compared with BA 42 recommendations through Equations 7.1.

Secondly, the recorded soil stress ratios (here called *measured* K^*) over the upper half of the model wall (and after similar scaling of K^* to that described above for K) are compared directly with the recommendations of Equations 7.1. The graphical comparisons shown in Figure 7.6 are for the *scaled* K^* values.

Finally, a modification is suggested to the BA 42 equation (Equations 7.1 here) in order to represent better the cyclic nature of the problem by using $K^* = K_0$ as a minimum value.

7.3.1 Upper bound K (experimental) and required K_p from BA 42

The upper bound values of K, as obtained from experimental data (scaled model test) and shown in Figure 7.2, are compared with BA 42 recommendations through the use of Equations 7.1 for selected values of K_p to satisfy the upper bound requirements. Code bounds for $K_p = 9$ and $K_p = 10$ are included in Figure 7.4. It should be noted that for bridge lengths of 60m or less, the proposed upper limit is lower than the code design value which is controlled by $K^* = K_p/3$.

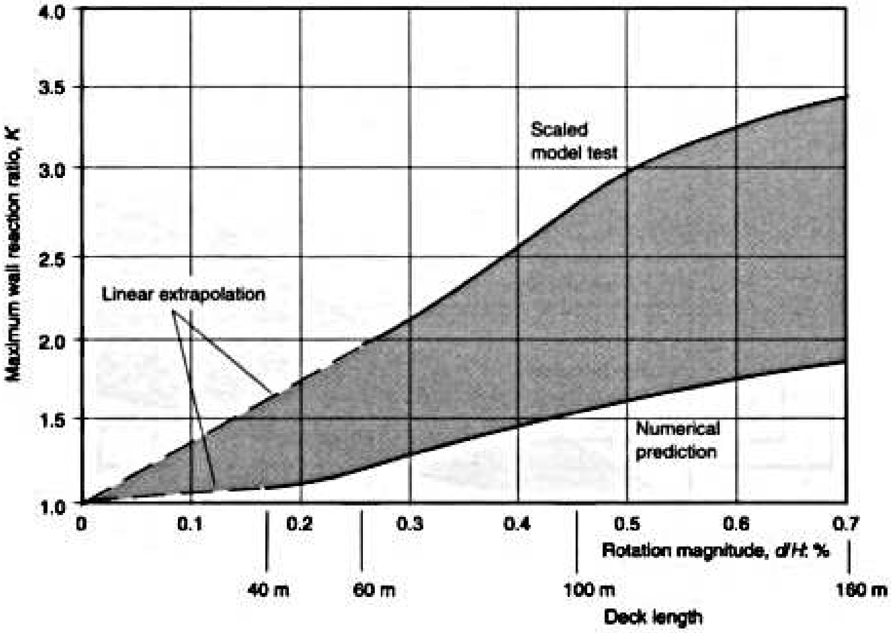

Figure 7.3 Upper bound values for wall reaction ratio K (initial void ratio 0.56 for prediction and 0.58 for the test; after 120 single cycles)

7.3.2 Upper bound K^* (experimental) and required K_p from BA 42

The model retaining wall results (see Chapter 5 and Appendix 1.2) indicate that the lateral earth pressure increases from the surface to a depth of approximately one-half the height of the wall with a constant stress ratio. This agrees well with the BA 42 assumption. However, over the lower half of the wall the recorded earth pressures during *passive* rotations reduce with depth and the stress ratio tends towards K_0 at the wall toe. Overall, therefore, the BA 42 assumption may still be considered as acceptable.

The escalation of the measured K^* values from the model wall tests are plotted in Figure 7.5. By using the same scaling method as specified in Section 7.2.2 to account for the influence of confining pressure, the scaled K^* values for 30 and 120 years are compared with the BA 42 code values in Figure 7.6, for $K_p = 9.2$ and $K_p=12.5$. Again, for bridge lengths of 60 m or less, the design value $K^*=K_p/3$ from BA 42 is very conservative.

7.4 Recommendations

Note: Recommendations provided in this section are based on limited experimental data obtained from model tests on a retaining wall hinged at its base. Therefore, they should not be extracted into practical design without due care.

- Although the lateral earth pressure distribution assumed in BA 42 is acceptable, the evaluation of K^* (Equations 7.1) with an origin at $K = 0$ is fundamentally incorrect. The additional criteria of K^* not less than $K_p/3$ is also too conservative. It is therefore recommended to replace Equations 7.1 by

$$K^* = K_0 + \left(\frac{d}{0.03H}\right)^{0.6} K_p. \qquad (7.3)$$

The additional restriction that $K^* \geq K_p/3$ always, can then be removed.

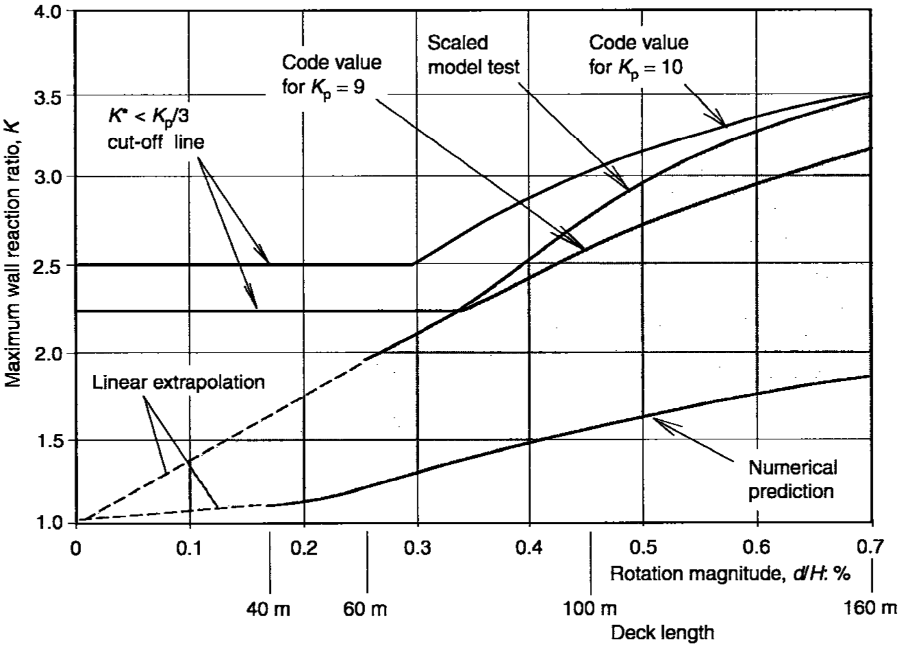

Figure 7.4 Comparison of upper bound values for the wall reaction ratio *K* obtained from experiments and the BA 42 code recommendations for design. Code values were calculated using Equations 7.1 and 7.2 (after 120 single cycles)

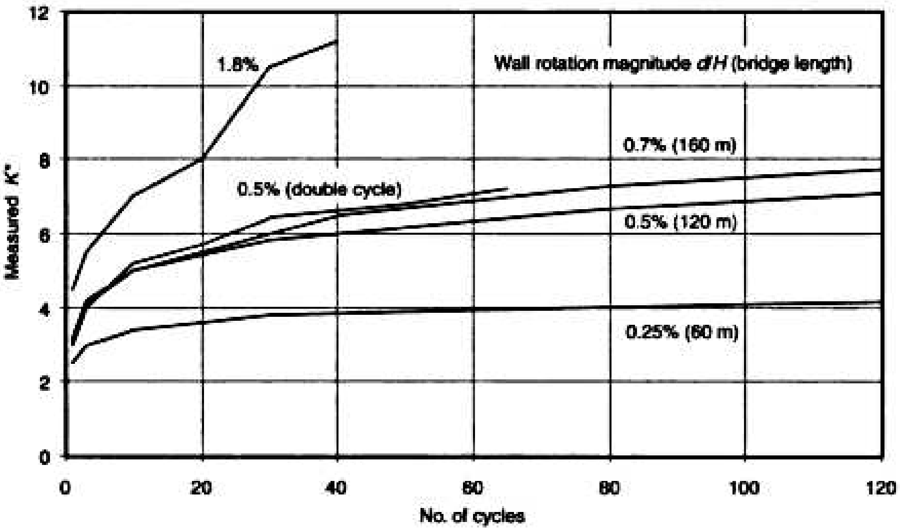

Figure 7.5 Measured K^* values from model retaining wall tests for various wall rotations d/H

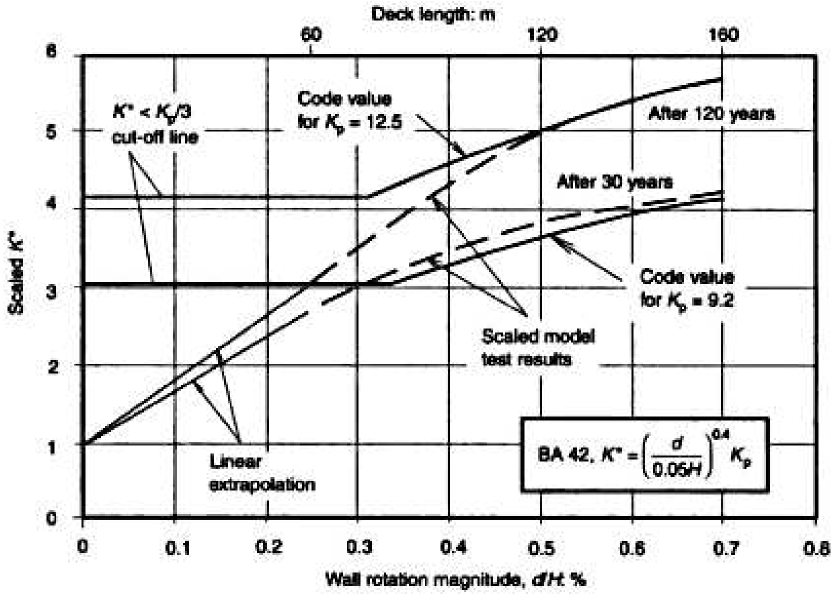

Figure 7.6 Comparison of scaled K^* from model retaining wall tests with BA 42 code values (calculated using Equations 7.1)

Justification for this recommendation is provided by Figure 7.7, which compares: the experimental values for scaled K^*; the BA 42 recommendations (from Equation 7.1); and the proposed modifications to BA 42 as defined by Equation 7.3.

- When using Equation 7.3, the following points should be noted:
  - Equation 7.3 is only applicable to abutment retaining walls that are hinged at their bases.
  - K_0 is the initial at-rest stress ratio after completion of backfill and is not associated with the cyclic rotations of the wall.
  - K_p, on the contrary, increases as the density of the backfill soil increases, and hence should be estimated as the value at the end of the bridge service life, i.e. after the backfill has densified.
  - The value $K_p = 12.5$ (see Figure 7.7) was derived in connection with experiments using Leighton Buzzard sand and incorporates the influence of interface friction over the face.
- Settlement of abutments, for bridges up to 60 m long and with strip footings, is not considered to be significant. However, no recommendation can be given concerning the settlement of cantilever sheet pile walls.
- If run-on slabs are used to span the settlement region adjacent to the abutment, a highly compacted backfill should be avoided in order to reduce the heave which could cause buckling of the pavement slab.
- Due to the existence of significant granular flow in the backfill material, wing walls of reinforced soil construction are not recommended.
- The current limit of a 60 m maximum bridge length for integral bridges is considered reasonable and should be maintained until a better understanding of the consequences resulting from the formation of *active* slip planes in longer span bridges can be developed.
- Because seasonal and daily temperature cycles each play an important role in defining the interaction problem both should be considered in calculations.
- No recommendation can be made for the evaluation of settlement to the backfill material because there is no evidence to support the existence of a limiting settlement during the normal lifespan of an integral bridge, and the interaction between the seasonal and daily cycles is not yet fully understood.

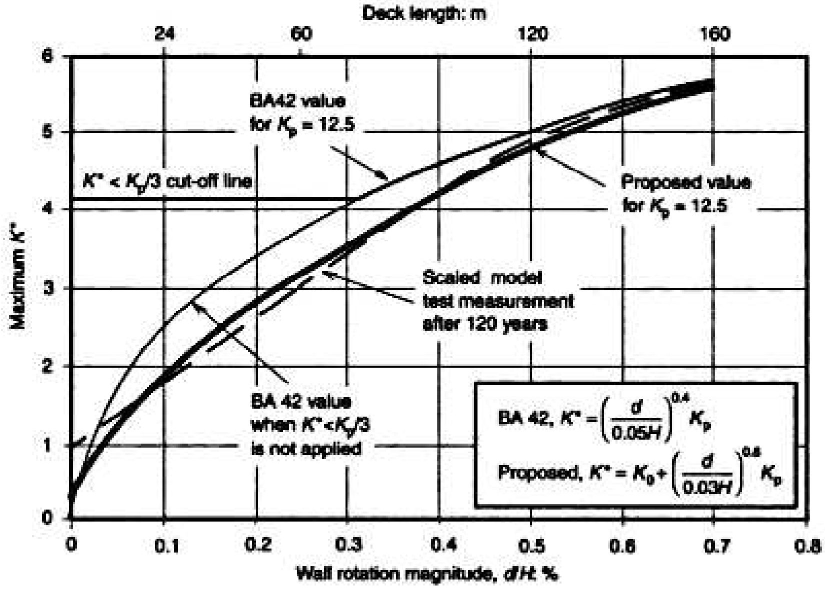

Figure 7.7 Comparison of the proposed upper limit for K^* (Equation 7.3) with the current BA 42 Code (Equation 7.1) and the model retaining wall scaled results

7.5 Further studies

- The numerical analysis needs to be improved in order to handle *active* slip planes and to include soil–wall friction.
- The retaining wall analysis should be extended to handle flexible cantilever walls.
- Experiments should be done to validate the theoretical approach used to assess abutment settlements.
- Investigations are needed into the use of elastic inclusions between the backfill and the abutment interface.
- Investigations are needed into the use of georeinforcement to restrict the formation of *active* slip planes.
- Investigations are needed to determine the cyclic escalation of K_p values for real granular backfill materials.

Appendix 1

1 Validation of the retaining wall analysis

The numerical simulations described in Chapter 5 were generated using the computer program, QSand, run on a Pentium PC. The program was prepared according to the logic of the transitional equilibrium method (TEM) created in this research project. The retaining wall analysis requires soil data, from the new constitutive soil model, to be used in conjunction with the TEM; both are described in Part 2 of this book.

This appendix serves to validate the computer program and retaining wall analysis for the numerical simulations of the project. The predictions of a series numerical simulations are compared with the experimental results from model tests: P2, SW13, SW25 and SW35 (see Chapter 4 for the test details). For clarity, only the maximum wall reaction ratio *K* and settlement of the soil adjacent to the wall are compared. These are the two most important engineering parameters needed for design calculations.

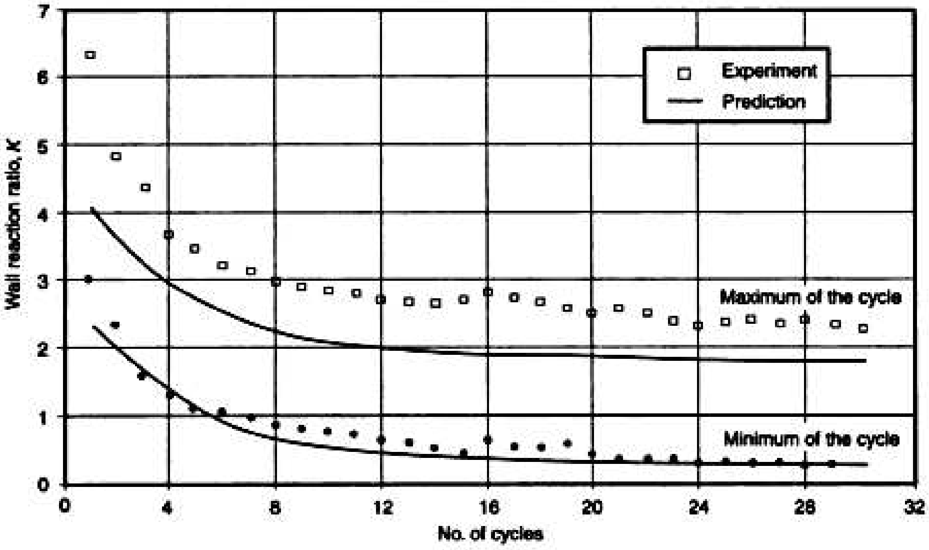

Figure A1.1 Comparison of numerical predictions and model test results for wall rotations between +0.9% and +0.81% (model test P2)

- Good agreement is seen between experiment and prediction for the cyclically dependent changes in the wall reaction ratio K as it approaches a steady repeating, or shakedown, state. The predicted rate of approach is however slightly too high (Figure A1.1).
- The form of the cyclically dependent changes in the wall reaction ratio to span the hydrostatic stress for $K = 1$, is well predicted for the conditions of tests SW13, SW25 and SW35 (Figures A1.2 to A1.4, parts (a)).
- Soil settlements were reasonably well predicted for the three experiments SW13, SW25 and SW35 (Figures A1.2 to A1.4, parts (b)).

Overall, the general predicted behaviour is acceptable. The shakedown form of the results observed in the experiments, with long-term values of K spanning the hydrostatic ($K = 1$) stress state was predicted in all cases. Settlements were less well predicted, particularly for the larger wall displacement amplitudes. The mismatches identified represent errors in the predictive model procedures. Some can be readily identified:

- the new constitutive soil model is known to overestimate the incremental ratcheting strains (for details see Part 2 of this book);
- the soil–structure interface friction is not modelled currently; and
- the retaining wall analysis does not contain logic for handling soil discontinuities caused by shear slip planes, as were observed to develop in the retaining wall tests for the larger amplitudes of wall rotation.

It may be concluded that, although modifications should be made to the retaining wall analysis in order to predict reliably the behaviour of bridges for which slip planes form (i.e. bridges not longer than 60 m), the present analysis without modification is satisfactory for the work of this project (i.e. for bridges longer than 60 m).

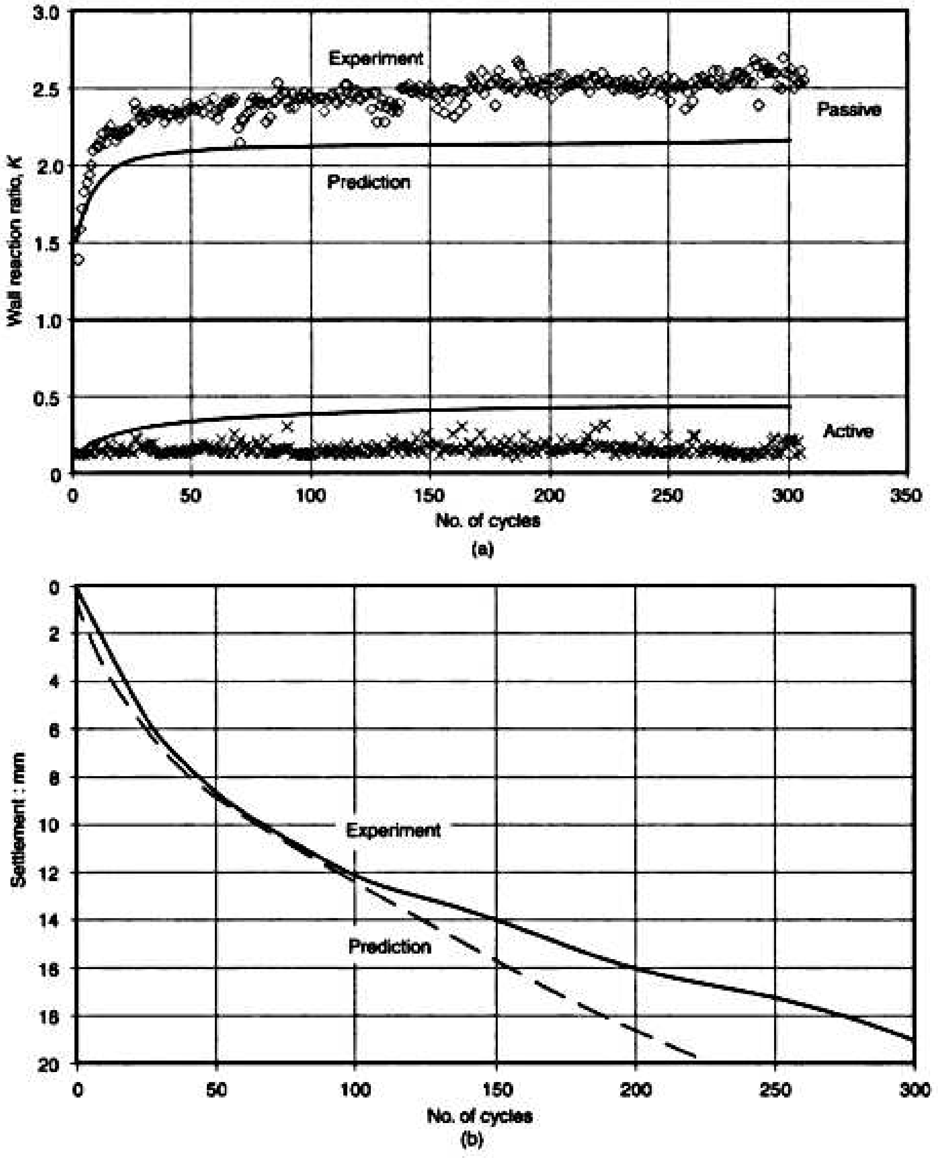

Figure A1.2 (a) Comparison of numerical predictions and model test results for a wall rotation amplitude of ±0.125% (60 m bridge) for single temperature cycles (model test SW13): wall reaction ratios. (b) Comparison of numerical predictions and model test results for a wall rotation amplitude of ±0.125% (60 m bridge) for single temperature cycles (model test SW13): settlement of soil adjacent to the wall

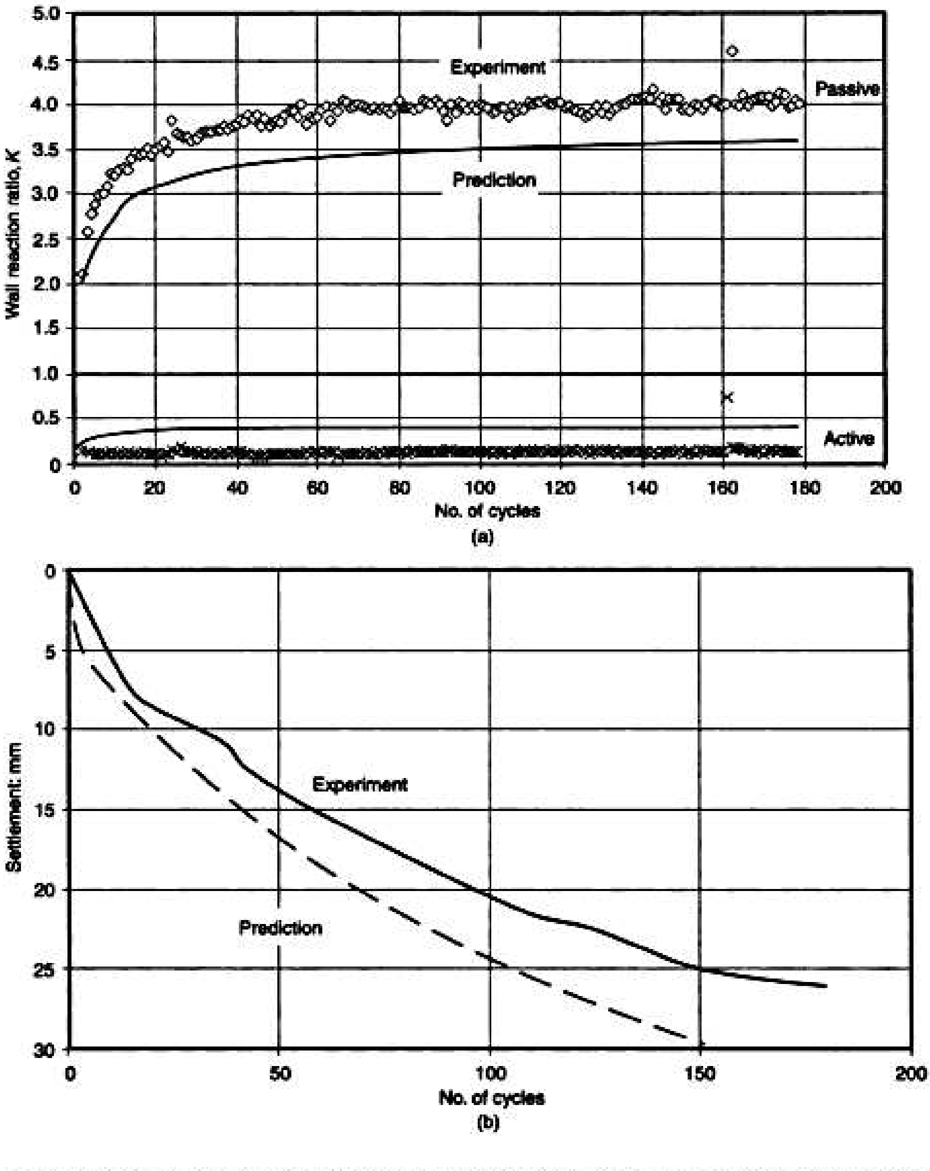

Figure A1.3 (a) Comparison of numerical predictions and model test results for a wall rotation amplitude of ±0.25% (120 m bridge) for single temperature cycles (model test SW25): wall reaction ratios. (b) Comparison of numerical predictions and model test results for a wall rotation amplitude of ±0.25% (120 m bridge) for single temperature cycles (model test SW25): settlement of soil adjacent to the wall

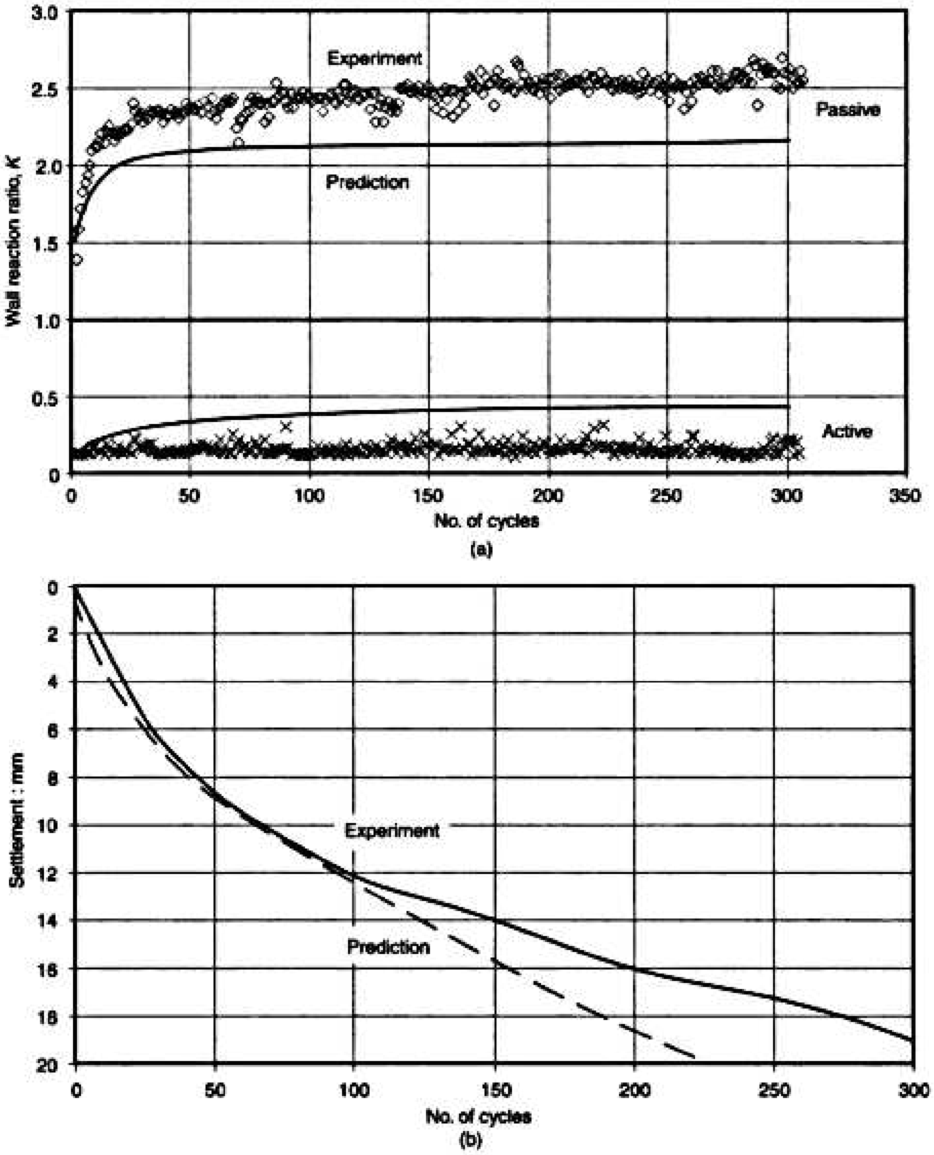

Figure A1.2 (a) Comparison of numerical predictions and model test results for a wall rotation amplitude of ±0.125% (60 m bridge) for single temperature cycles (model test SW13): wall reaction ratios. (b) Comparison of numerical predictions and model test results for a wall rotation amplitude of ±0.125% (60 m bridge) for single temperature cycles (model test SW13): settlement of soil adjacent to the wall

Appendix 1

2 Additional results from model retaining wall tests

The detailed model retaining wall results for test SW13 (60 m bridge) are presented in Chapter 4. Here the results (in graphical form) for other tests, namely SW25, SW35 and DW25, are presented. Table A1.1 provides an index for the figures which display the results for each test.

Table A1.1 Figure numbers for the model retaining wall test results (for test details see Chapter 4)

Test code No.	Wall rotation amplitude	Lateral soil stress and stress ratio vs depth	Wall reaction ratio, *K* vs wall rotation: %	Max. and min. *K* vs No. of cycles	Settlement vs No. of cycles
SW25	±0.25%	Figure A1.5	Figure A1.6	Figure A1.7	Figure A1.8
SW35	±0.35%	Figure A1.9	Figure A1.10	Figure A1.11	Figure A1.12
DW25	±0.25% (seasonal)	Figure A1.13	NA	Figure A1.14	Figure A1.15

Test SW25

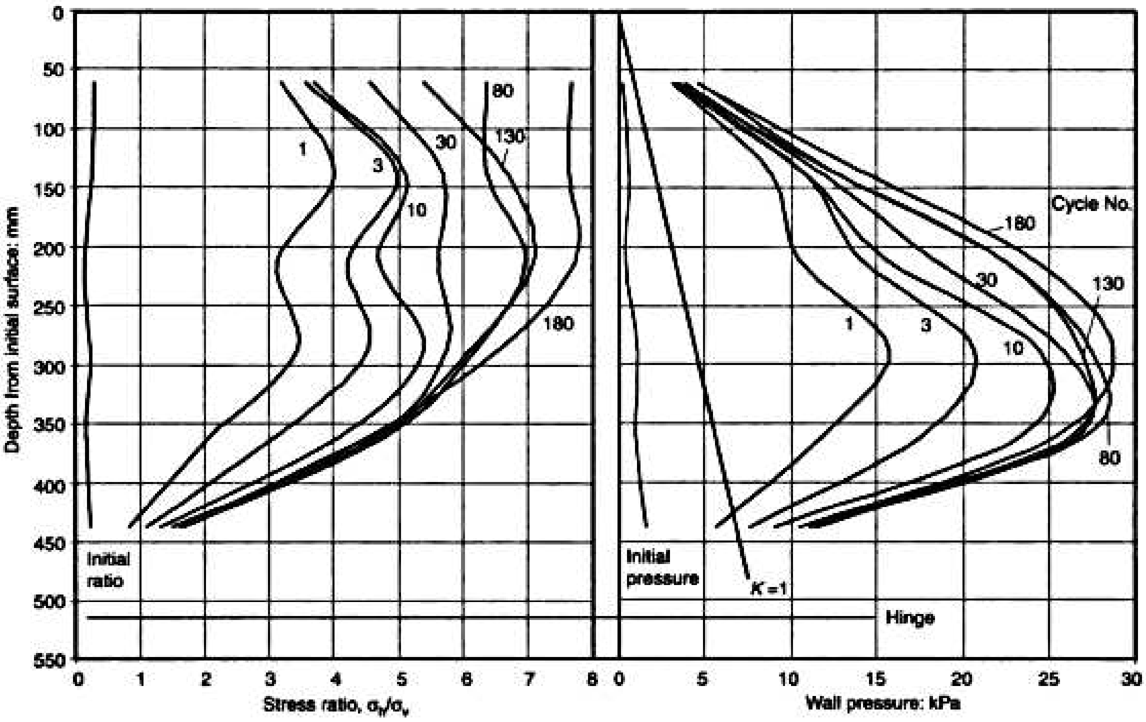

Figure A1.5 Recorded values of the lateral soil pressure and stress ratio (σ_h/σ_v) during cyclic wall rotations of amplitude ±0.25% (120 m bridge)

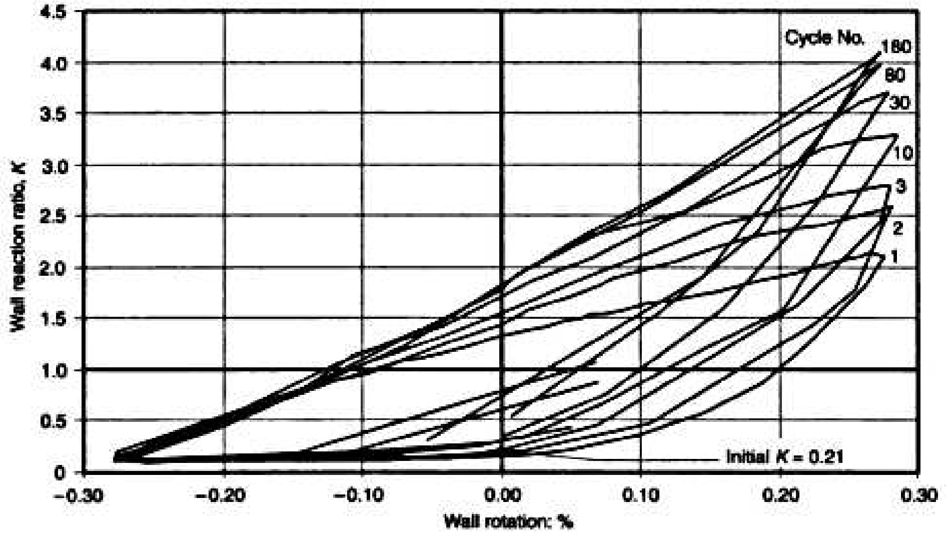

Figure A1.6 Variation in the wall reaction ratio *K* during cyclic wall rotations of amplitude ±0.25% (120 m bridge)

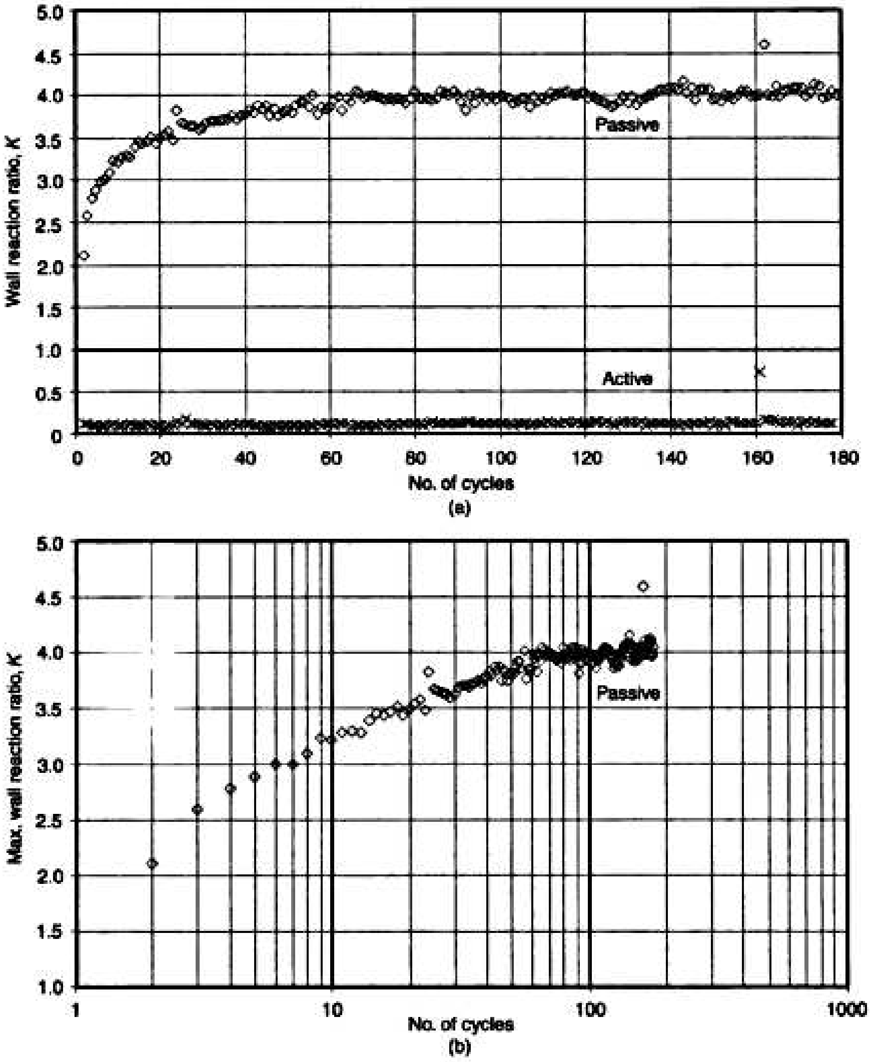

Figure A1.7 (a) Variation in the wall reaction ratio *K* with number of wall rotation cycles of amplitude ±0.25% (120 m bridge): maximum *active* and *passive* values (linear plot). (b) Variation in the wall reaction ratio *K* with number of wall rotation cycles of amplitude ±0.25% (120 m bridge): maximum *passive* values (logarithmic plot)

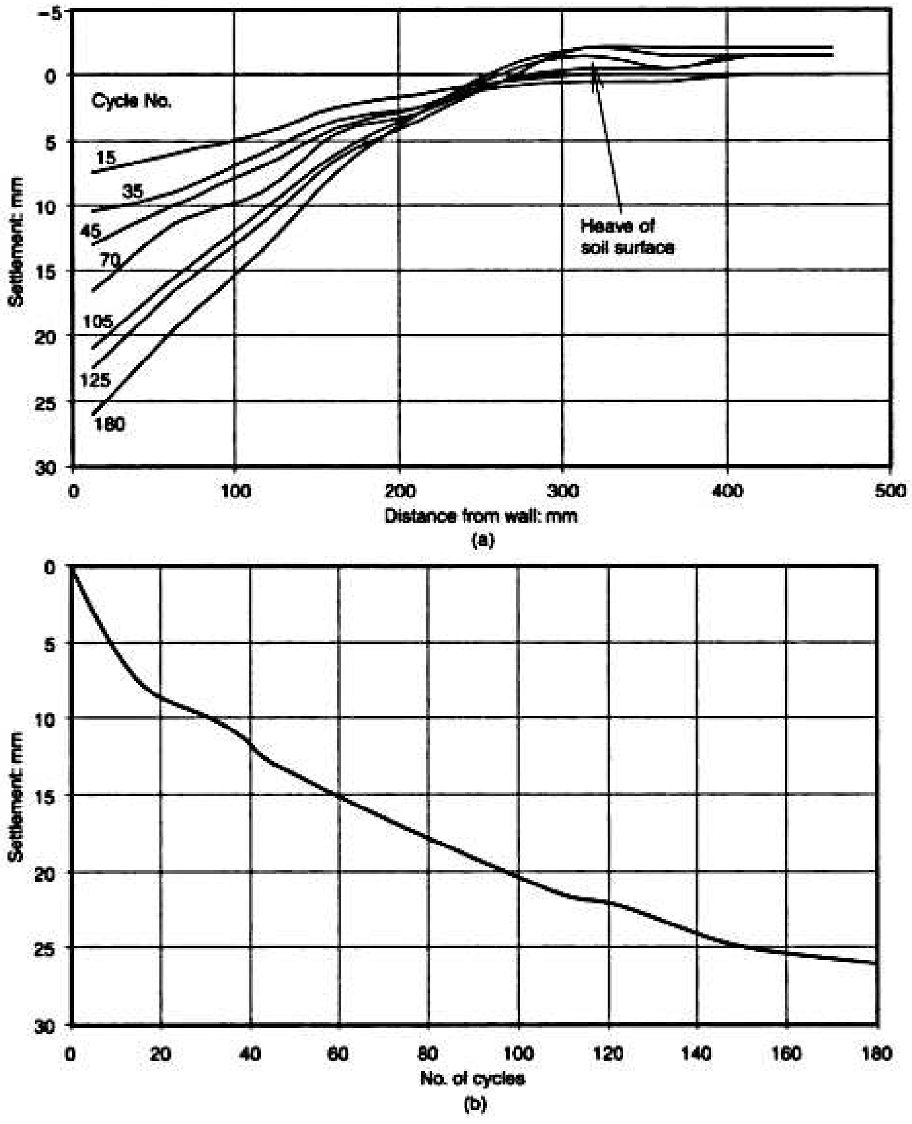

Figure A1.8 (a) Soil settlement as influenced by the number of wall rotation cycles of amplitude ±0.25% (120 m bridge): surface profile. (b) Soil settlement as influenced by the number of wall rotation cycles of amplitude ±0.25% (120 m bridge): settlement of soil close (10 mm) to the wall

Test SW35

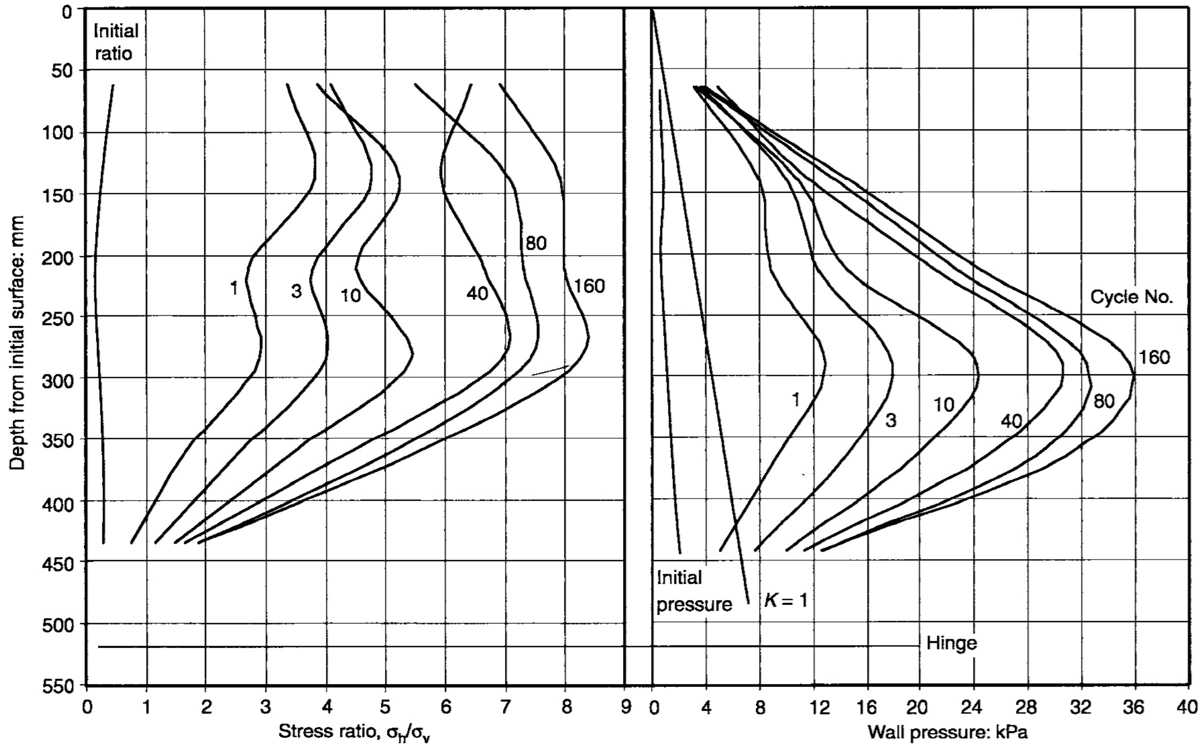

Figure A1.9 Recorded values of the lateral soil pressure and stress ratio (σ_h/σ_v) during cyclic wall rotations of amplitude ±0.35% (160 m bridge)

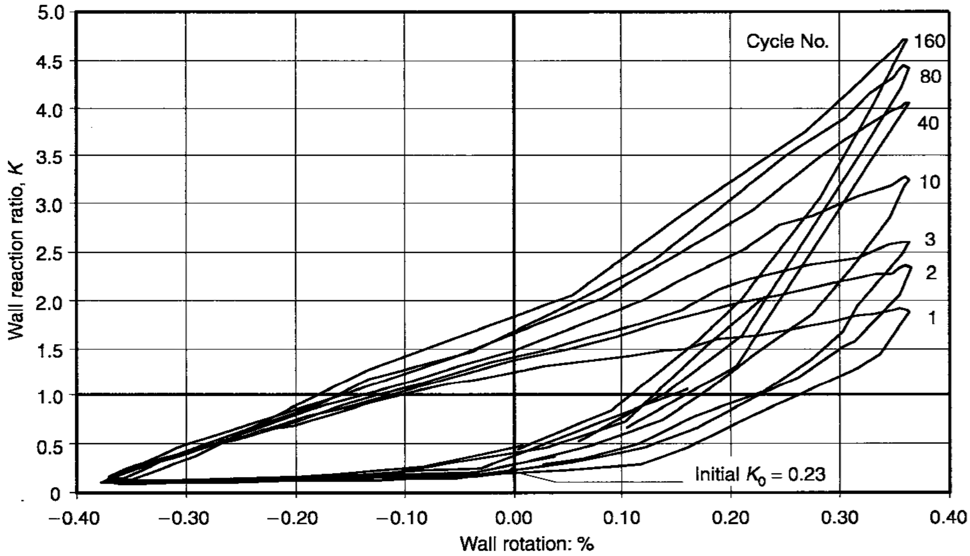

Figure A1.10 Variation in the wall reaction ratio *K* during cyclic wall rotations of amplitude ±0.35% (160 m bridge)

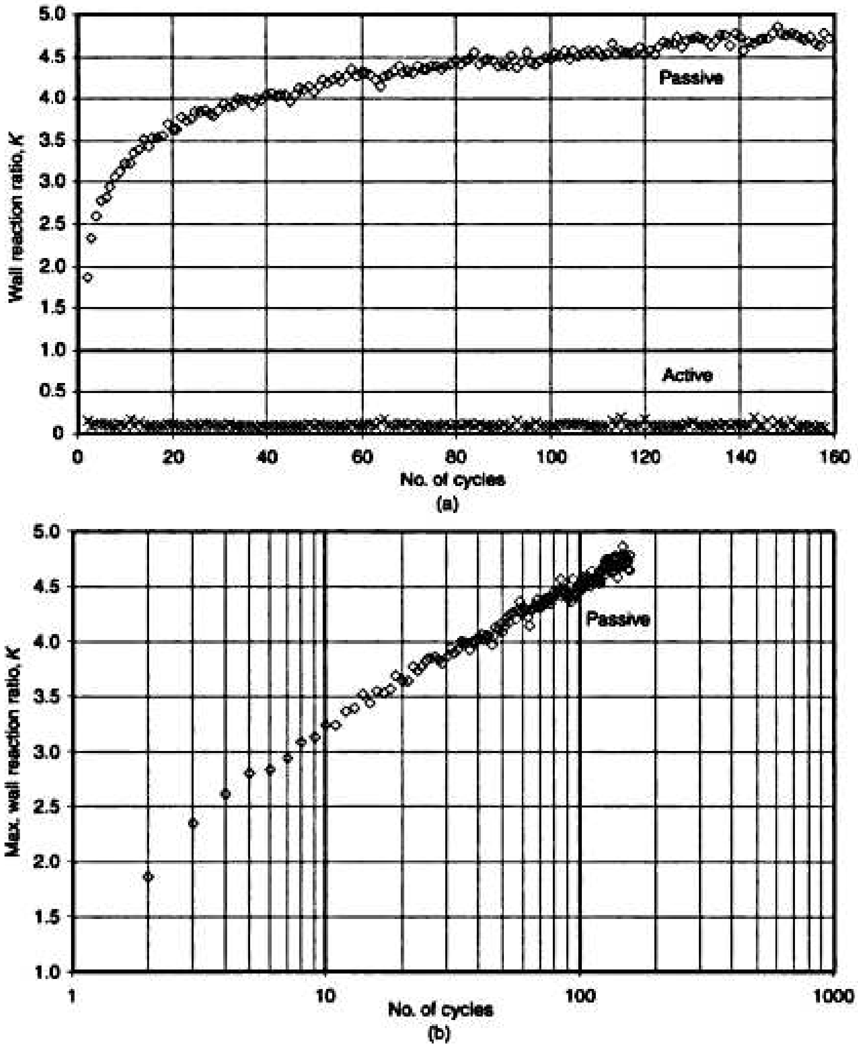

Figure A1.11 (a) Variation in the wall reaction ratio *K* with the number of wall rotation cycles of amplitude ±0.35% (160 m bridge): maximum *active* and *passive* values (linear plot). (b) Variation in the wall reaction ratio *K* with the number of wall rotation cycles of amplitude ±0.35% (160 m bridge): maximum *passive* values (logarithmic plot)

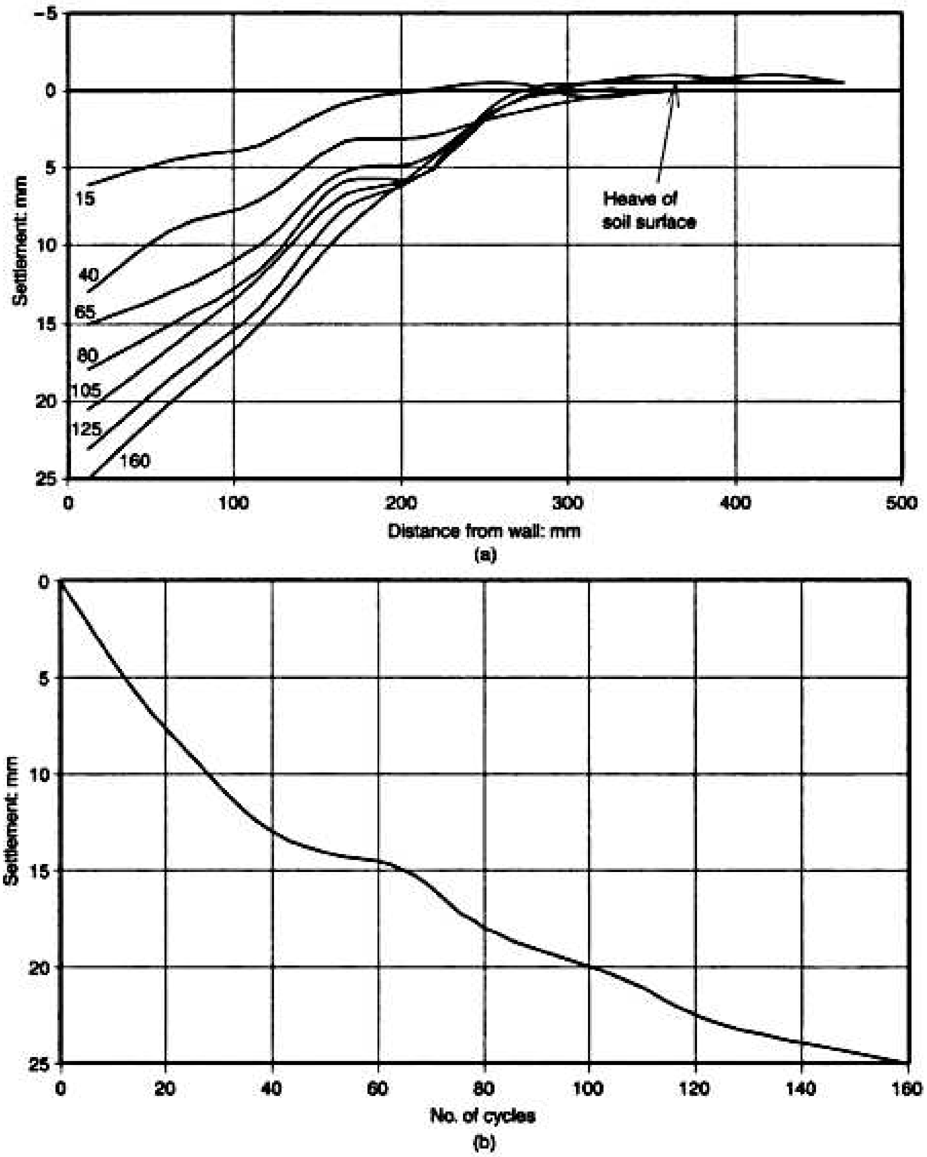

Figure A1.12 (a) Soil settlement as influenced by the number of wall rotation cycles of amplitude ±0.35% (160 m bridge): surface profile. (b) Soil settlement as influenced by the number of wall rotation cycles of amplitude ±0.35% (160 m bridge): settlement of soil close (10 mm) to the wall

Test DW25

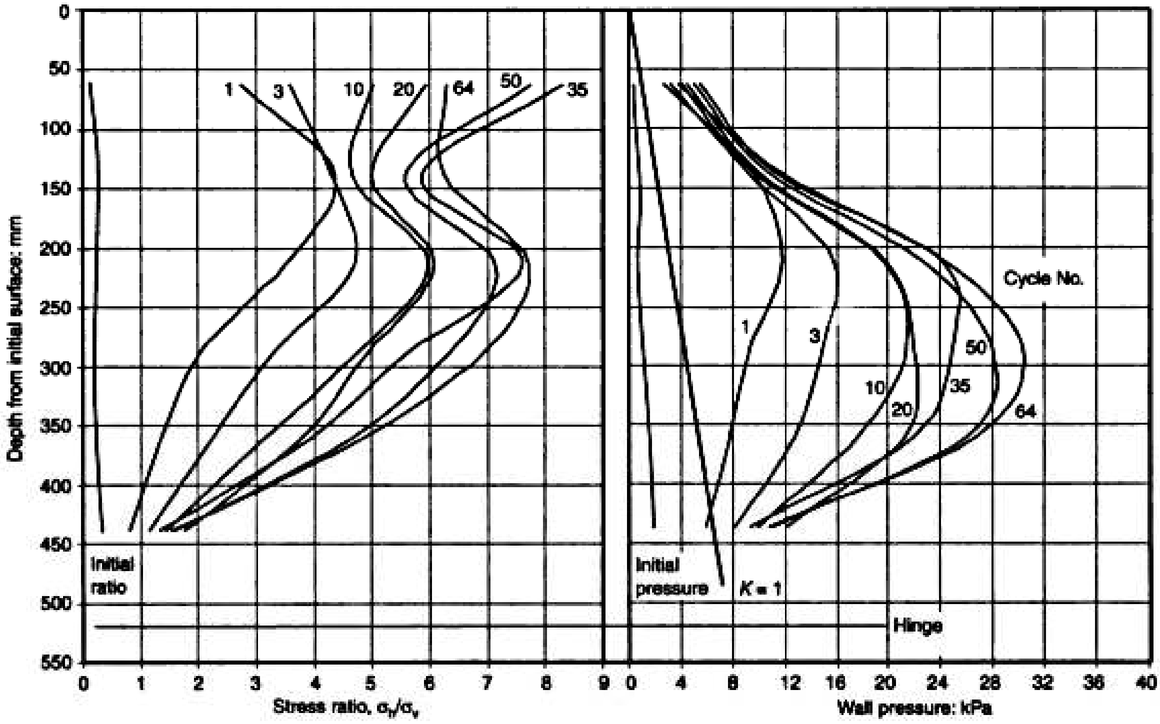

Figure A1.13 Recorded values of the lateral soil pressure and stress ratio (σ_h/σ_v) during double-cycle tests with seasonal amplitudes of ±0.25% (120 m bridge)

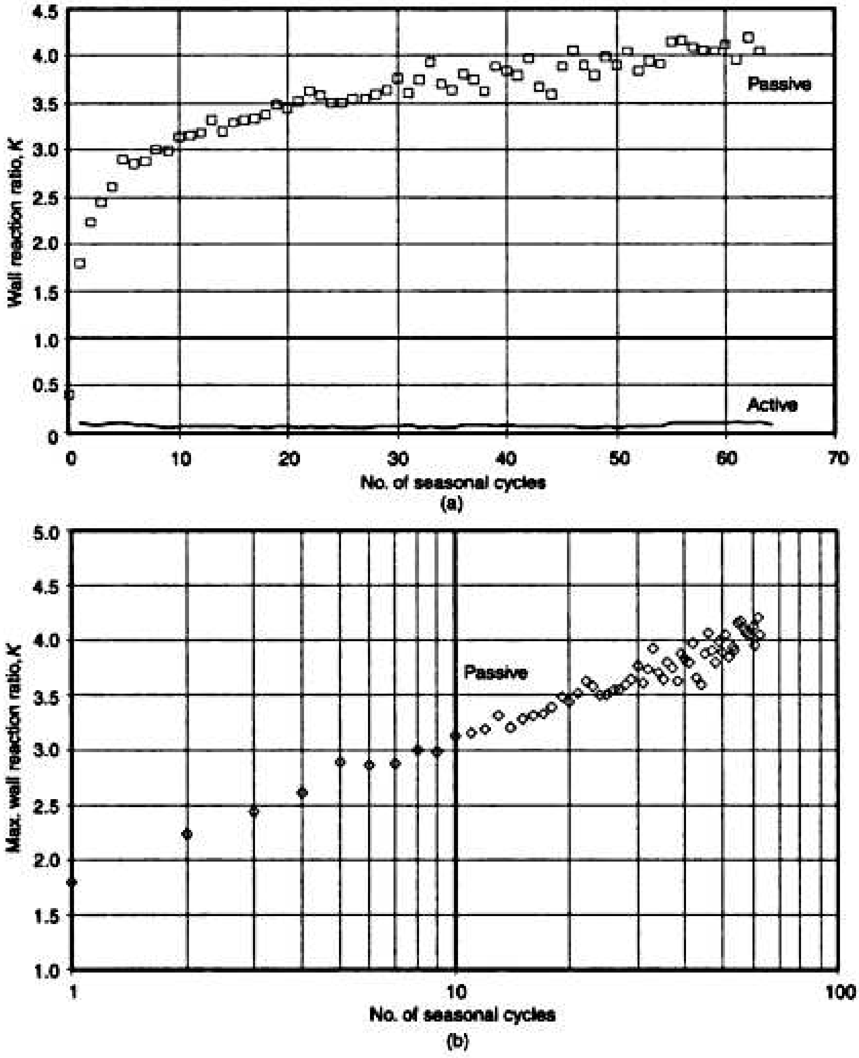

Figure A1.14 (a) Variation in the wall reaction ratio *K* with the number of seasonal wall rotation cycles during double-cycle tests with seasonal amplitudes of ±0.25% (120 m bridge): maximum *active* and *passive* values (linear plot). (b) Variation in the wall reaction ratio *K* with the number of seasonal wall rotation cycles during double-cycle

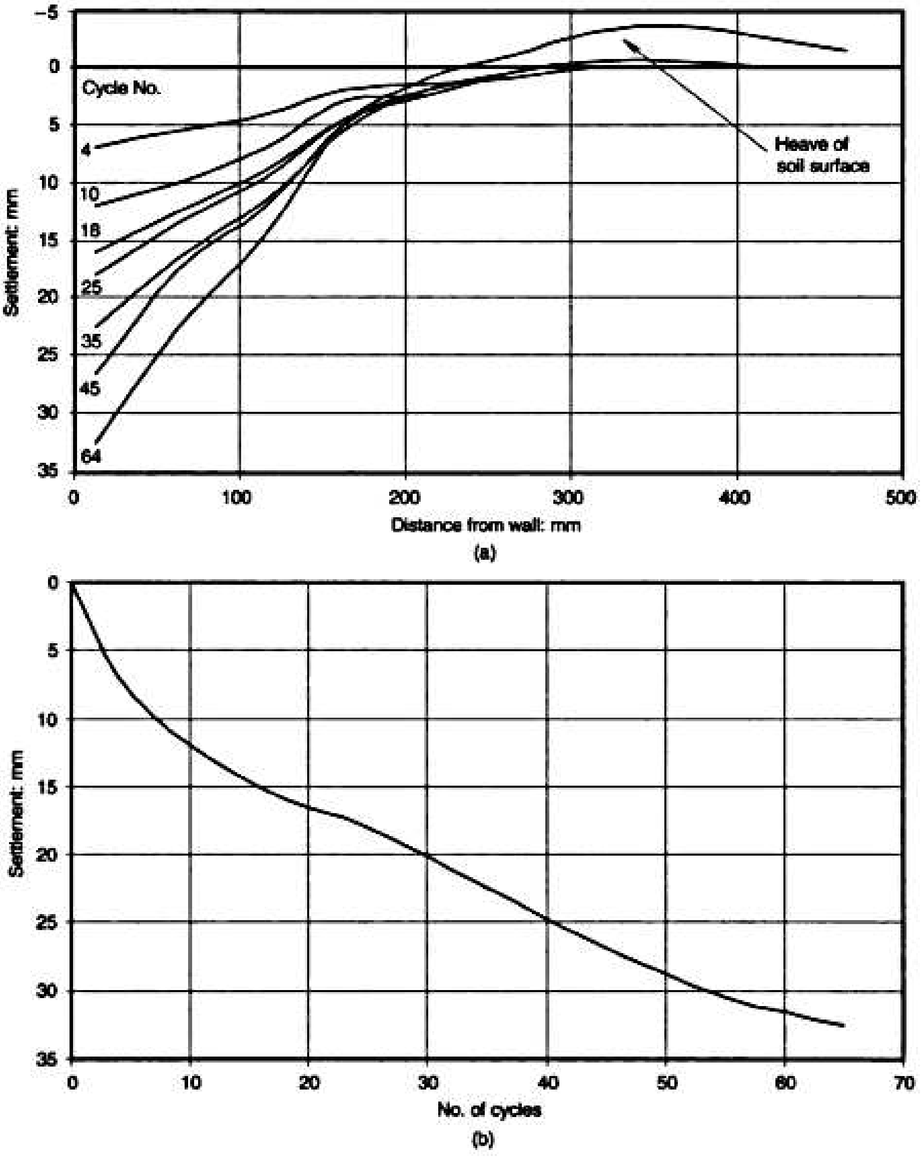

Figure A1.15 (a) Soil settlement as influenced by the number of seasonal wall rotation cycles during double-cycle tests with seasonal amplitudes of ±0.25% (120 m bridge): surface profile. (b) Soil settlement as influenced by the number of seasonal wall rotation cycles during double-cycle tests with seasonal amplitudes of ±0.25% (120 m bridge): settlement of soil close (10 mm) to the wall

Part 2
Granular soil

8 Cyclic behaviour of granular material

There are two fundamentally different types of cyclic loading which form the basis of many laboratory experiments:

- constant amplitude cyclic displacement imposition, and
- constant amplitude cyclic stress imposition.

The first category of experiments are performed to provide data under repeating strain conditions. Useful understanding of soil behaviour can be obtained from tests of these forms. However, because most soil–structure interaction problems relate to elastic structures, cyclic stress variations in the soil are generally accompanied simultaneously by cyclic strain changes. Such problems thus relate to a unique mixture of stress and strain imposition which can be defined only by the structure under consideration.

It has long been recognized, from observations of biological filter bed retaining structures subjected to cyclic temperature changes (England, 1994), that granular soils exhibit a number of unique characteristics for this type of displacement-imposed soil–structure interaction problem. Repeated strain cycling created by temperature changes in the elastic wall causes the soil to be subjected to fluctuating displacements at the soil–structure interface. The soil responds by stiffening, with an increase in compressive radial stress and an increase in extensional radial strain. This paradoxical situation cannot be modelled or predicted from monotonic stress–strain data for the soil. Similar behaviour has been observed in element experiments (see Section 8.4).

The experimental data reported here relate to published work, where relevant, and in part to the results of the test programme set up for the Highways Agency, UK. Plane strain tests were performed in a biaxial tester at University College London for imposed cyclic stress fluctuations and imposed cyclic displacement fluctuations. Details of the apparatus are given in Section 12.1.

8.1 General description and identification of influential parameters

There are two important changes that influence the behaviour of granular soils during cyclic loading. The first is volume change, usually densification and leading to greater soil homogeneity, strength and stability. The second relates to the internal packing and contacts of the particles and is described as 'fabric', namely the build-up of 'hard' or load-bearing contact paths in the major principal stress direction during an increase in stress. Fabric is intrinsically anisotropic. This build-up of internal structure inhibits densification yet allows the development of a stiffer, stronger and more elastic material, albeit with reduced stability. The creation of fabric is strongly related to the stress history and the manner in which the magnitude and direction of the major principal stress change during the loading operation.

Continuous rotation of or 90° jump changes in the major principal stress directions in cyclic loading situations can produce fabric that is stiffer and stronger than would be obtained during monotonic loading to the same stress ratio. Important parameters are therefore:

- *The amplitude of imposed fluctuating strains.* Small strains create densification (leading to greater stability) while large strains may create dilation (leading to greater instability). Stresses converge towards a shakedown state (closely associated with an isotropic stress state) after many cycles with an average (over one strain cycle) void ratio linked directly to the strain amplitude (England *et al.*, 1997). During the approach to the shakedown state the material behaves like a fluid insofar as it is able to under the imposed strain, and the maximum shear stress supported by the material gradually reduces.
- *The magnitude of imposed fluctuating stress ratio.* High stress ratios in the absence of fabric cannot be supported and will lead to run-away failures if any attempt is made to impose them. However, when a soil is cycled progressively under a slowly increasing stress ratio regime, two changes occur simultaneously. Firstly, some densification takes place, and this provides an enhanced stability and strength. Secondly, the build-up of fabric at the current density creates a higher strength and stiffer material than would have resulted from monotonic loading. The amplitude of the cyclic strains thus reduces progressively during repeated stressing of the material and may reach a limit defined by the elastic strain response of the particle fabric.
- The *initial void ratio* and subsequent changes during cyclic loading.
- The *form of the principal stress variations*: i.e. unidirectional; jump changes of direction; smoothly rotating.

Descriptions relating to the integral bridge are restricted to the behaviour of granular materials under plane strain loading and for a drained state.

8.2 Strain cycling: stress ratio drifting to shakedown

Cyclic straining at fixed amplitude generally leads to progressive volume change on a cycle-by-cycle basis together with incremental volume changes (densification and dilation) within each strain-imposed cycle. When the imposed fluctuating strains are centred on an initial state with no offset initial strain, the principal stresses immediately exhibit jump changes of direction during cycling and quickly become centred on the isotropic stress state. Continued strain cycling produces progressive stiffening of the soil and an increase in the peak stress ratio. A shakedown limit is reached when the stresses no longer increase and the soil then responds without volume change during any complete cycle. Some results displaying this behaviour are shown in Figure 8.1(a) for cyclic shear tests performed on Leighton Buzzard sand (Wood and Budhu, 1980). Of equal interest is the result of a test started with an initial offset strain (Budhu, 1979) and then performed in a similar manner to the previous tests. Figure 8.1(b) gives the details. For this test the stresses during each half of the strain cycle were initially different but approached a symmetrical form after several cycles, thus indicating that the shakedown state, with stresses centred on the isotropic stress state, is the preferred condition for the soil after many strain cycles.

Figures 8.2 and 8.3 show results for Leighton Buzzard sand tested in a drained plane strain condition, in a biaxial tester (see also Section 12.1). Fluctuating strains of magnitude 1% and 0.3% were imposed from different offset strain origins, as shown in the figures. A constant stress was imposed on the third face of the cubic sample. Observations again reveal that, during the cyclic straining process, the maximum stresses move so as to centre further changes closer to the isotropic state. The asymmetry of the cyclic stress–strain loops in these examples is due to the cyclic changes in confining pressure which occur as a consequence of the imposition of one constant principal stress.

8.3 Stress cycling: ratcheting displacements

The behaviour of granular soil under constant amplitude fluctuating stresses depends strongly on the nature of the imposed cyclic stress changes and on the stress and strain states in the orthogonal directions of the soil. The following two examples help to clarify this statement.

- *Plane strain.* Boundary conditions: (a) constant-amplitude fluctuating stress $\delta\sigma_1$ applied in the major principal stress direction, and (b) constant $\sigma_3 = 20$ kPa. $\varepsilon_2 = 0$ and σ_2 is not controlled. The resulting behaviour is ratcheting compressive strains $\delta\varepsilon_1$ with ratcheting *extensional* strains $\delta\varepsilon_3$ and overall densification $\delta\varepsilon_v$. The details are given in Table 8.1.
- *Triaxial.* Boundary conditions: (a) constant-amplitude fluctuating stress $\delta\sigma_1$ applied in the major principal stress direction, and (b) constant σ_3. Here, $\sigma_2 = \sigma_3 = 20$ kPa (Regier, 1997). The resulting behaviour is ratcheting compressive strains $\delta\varepsilon_1$ with ratcheting *compressive* strains $\delta\varepsilon_3 = \delta\varepsilon_2$, and overall densification (but significantly greater than that in plane strain conditions above). The details are given in Table 8.1.

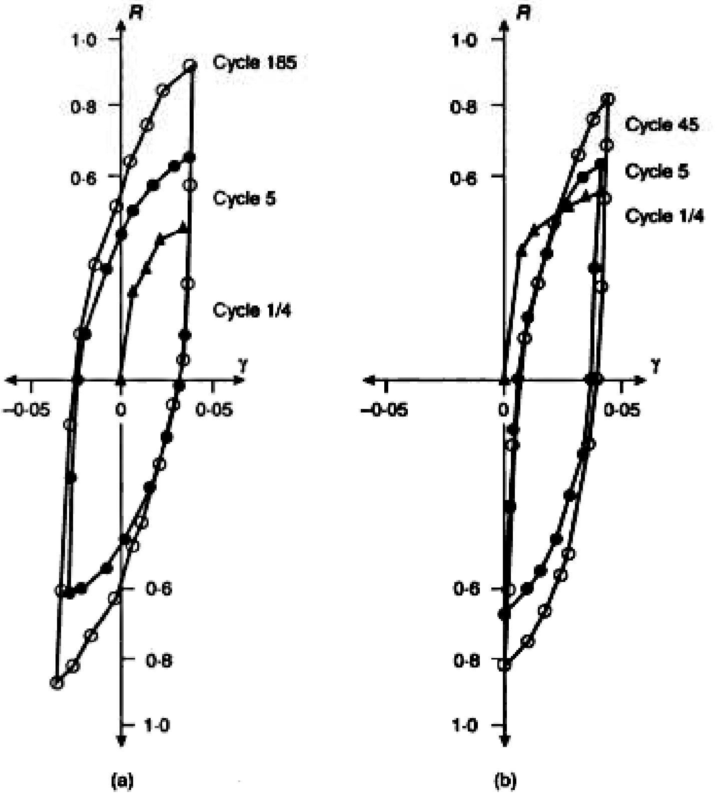

Figure 8.1 Repeated cyclic shear strain γ leading to shakedown of stresses about the isotropic stress state, for loose sand tested in simple shear: (a) without initial offset strain (after Wood and Budhu, 1980); (b) with initial offset strain (after Budhu, 1979). *R* is the ratio of shear stress τ to the direct stress σ

Generally the cyclic strain responses (in plane strain), without jump changes in the principal stress directions, are specific to the level of the peak stress ratio and to the amplitude of the fluctuating stresses. Ratcheting strains accelerate at stress ratios of $\sigma_1/\sigma_3 = R > 3$, and decelerate when $R < 3$. The responses are softer, i.e exhibit more non-elastic strain as the lower peak stress ratio approaches the isotropic state, namely $R \rightarrow 1$. These features are illustrated by the results from plane strain tests in which both the peak stress ratio and the amplitude of the fluctuating stress were varied (Figures 8.4–8.6).

If jump changes in the principal stress directions occur during the imposition of constant-amplitude fluctuating stresses, the material stiffens with a progressively reducing strain amplitude. At constant confining pressure high stress ratio fluctuating stresses can be supported (Figure 8.7). For a specified amplitude of the fluctuating stresses one of two solutions appears to be possible; either the material stiffens towards an elastic behaviour, or the material develops increasing amplitudes of strain and runs to failure.

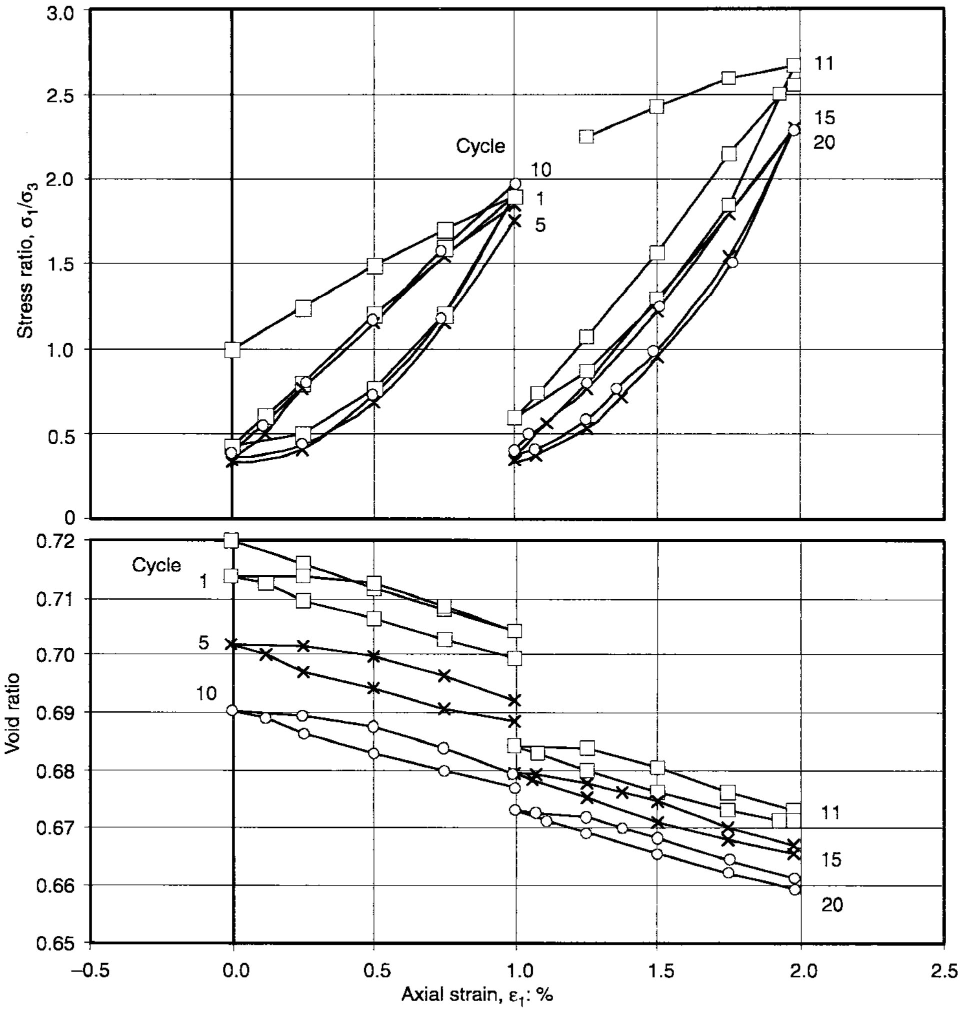

Figure 8.2 Stress ratio drifting, for initially *loose* Leighton Buzzard sand, during application of fluctuating strains of 1% amplitude, from offset strains of 1% and 2%. Changes in the void ratio are shown in the lower figure

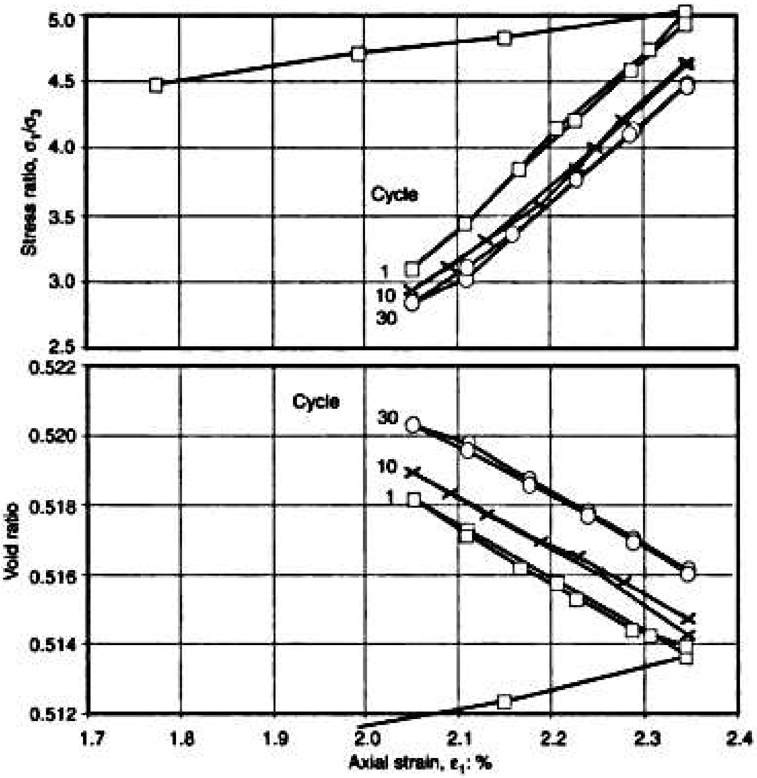

Figure 8.3 Stress ratio drifting, for initially *dense* Leighton Buzzard sand, during application of fluctuating strains of 0.3% amplitude, from offset strains of 2%. Changes in the void ratio are shown in the lower figure

Table 8.1 Cumulative ratcheting strains (%) during ten cycles of stress increment reversal ($1 < \sigma_1/\sigma_3 < 4$) for two types of test on loose sands ($\sigma_3 = 20$ kPa). Considerable variation of ratcheting behaviour is displayed

	Axial strain, ε_1	Intermediate principal strain, ε_2	Minor principal strain, ε_3	Volume strain, ε_v
Triaxial test (Regier, 1997)	0.8	0.25	0.25	1.3
Plane strain test (Bolouri-Bazaz, 1999)	0.5	0	−0.28	0.22

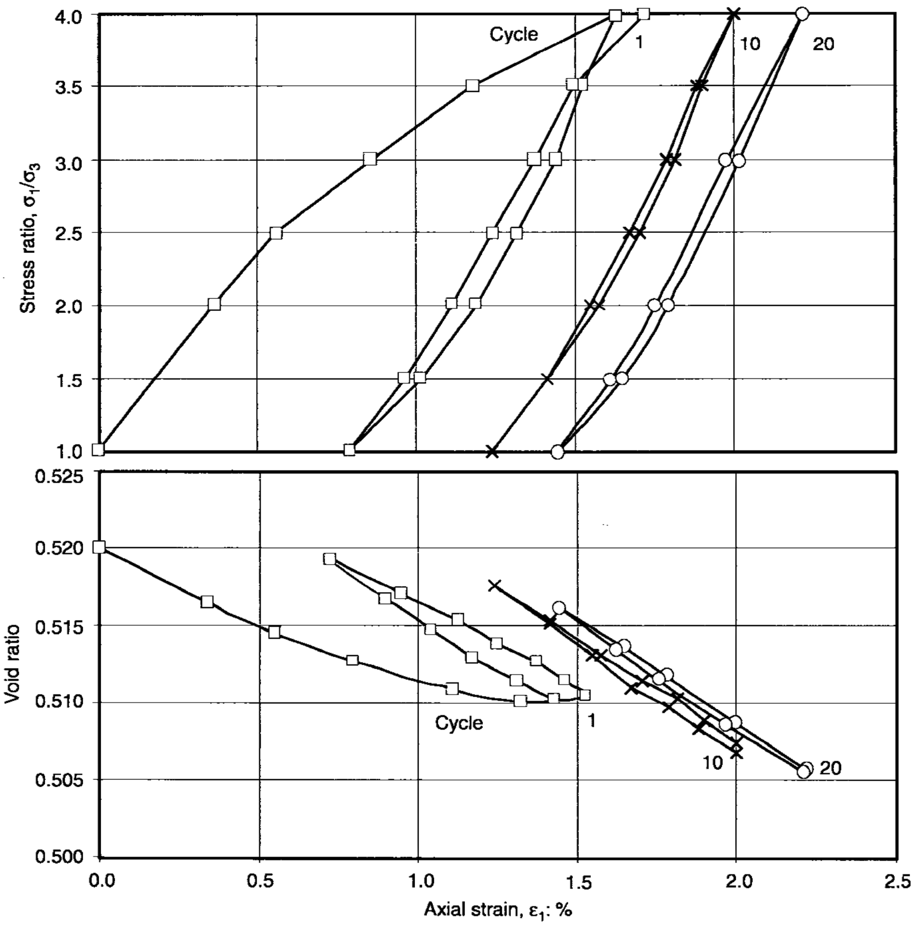

Figure 8.4 Development of ratcheting strains, for initially *dense* Leighton Buzzard sand, during application of fluctuating stresses between stress ratios $R = 1$ and $R = 4$. Changes in the void ratio are shown in the lower figure

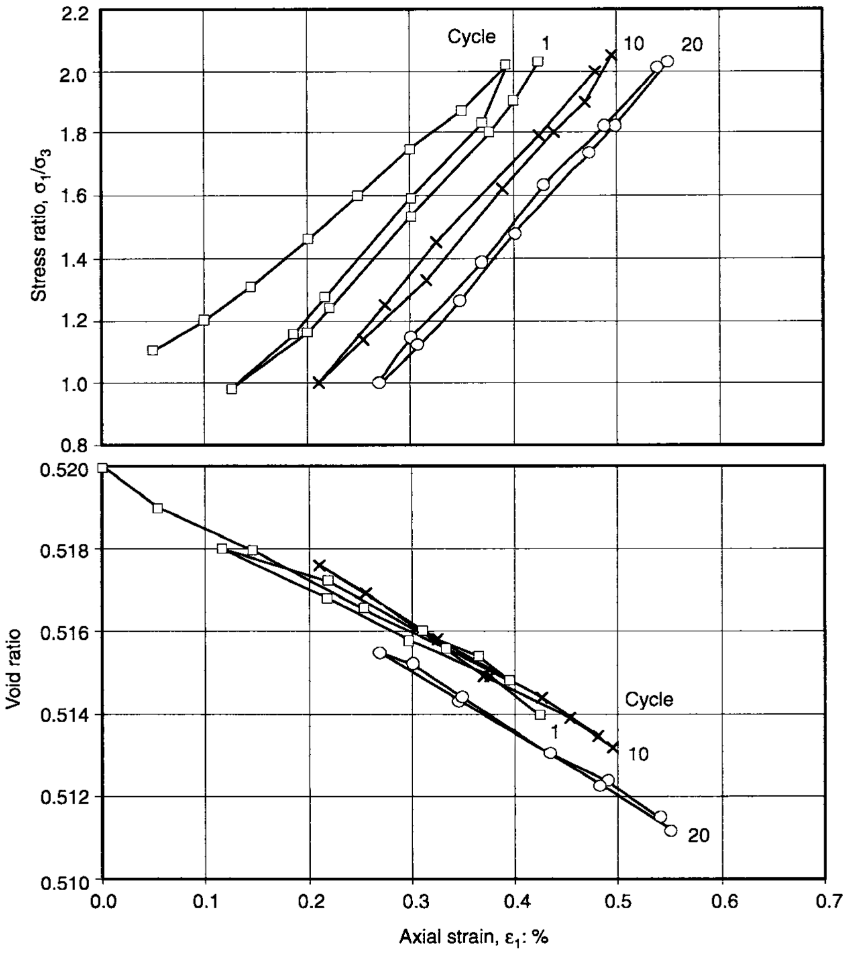

Figure 8.5 Development of ratcheting strains, for initially *dense* Leighton Buzzard sand, during application of fluctuating stresses between stress ratios, $R = 1$ and $R = 2$. Changes in the void ratio are shown in the lower figure

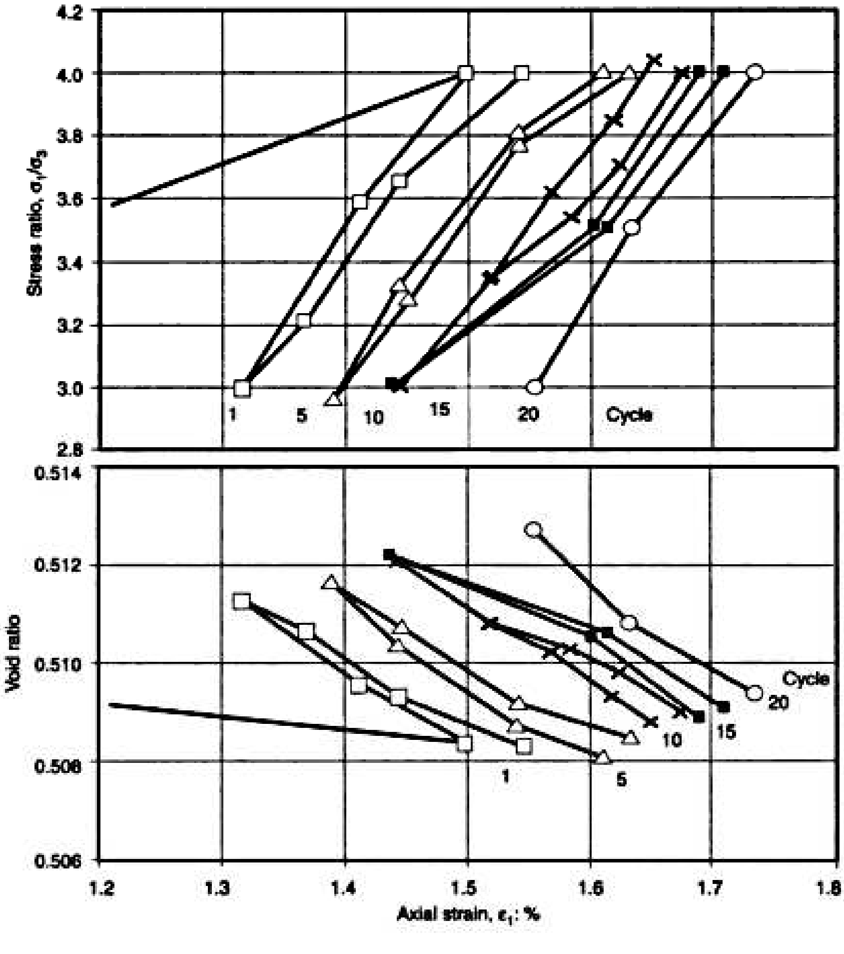

Figure 8.6 Development of ratcheting strains, for initially *dense* Leighton Buzzard sand, during application of fluctuating stresses between stress ratios $R = 3$ and $R = 4$. Changes in the void ratio are shown in the lower figure

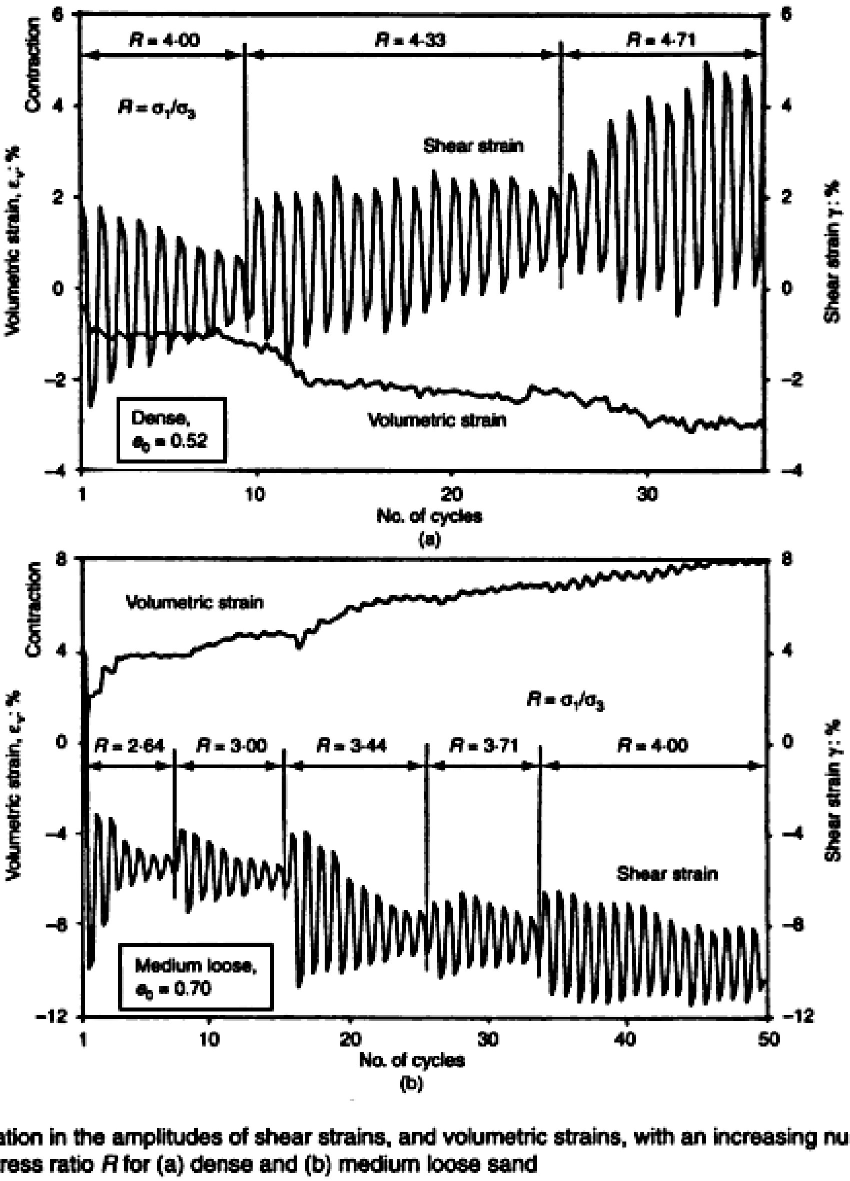

Figure 8.7 Variation in the amplitudes of shear strains, and volumetric strains, with an increasing number of cycles and maximum stress ratio *R* for (a) dense and (b) medium loose sand

8.4 Cyclically changing stresses and strains

Any displacement imposed on a soil element adjacent to the retaining wall must satisfy simultaneously equilibrium in the soil and the structure. When the structure is elastic and is subjected to fluctuating temperatures, the thermally induced strains in the structure cause the contact interface between the soil element and the structure to be subjected simultaneously to fluctuating stresses and fluctuating displacements. This behaviour can be described in relation to the idealized two-element model (England and Dunstan, 1994) shown in Figure 8.8. In this figure, element 1 is the soil element and element 2 represents the elastic structure which is to be subjected to fluctuating temperature changes, $T_0 \rightarrow (T_0 + \Delta T) \rightarrow T_0$, etc. The two elements have a contact interface a–a and their overall length is maintained constant at the original lengths defined by the datum temperature T_0. During successive temperature fluctuations the contact stress σ_x increases, ($\sigma_x/\sigma_z < 1$ initially), causing compressive strains in element 2 and extensional strains in the soil element. A repeating or shakedown state, centred on the isotropic stress state, will terminate further incremental strain and stress changes. A full description of the incremental ratcheting strain processes together with the development of an interaction diagram (the superposition of the stress–strain response for the soil and the load–displacement characteristic for the structure), which permits a quantification to be made of the aggregate soil strains and the shakedown stresses, is given in Appendix 2.1.

Supporting experimental evidence to the belief that the soil prefers to be close to the isotropic state is provided by the information shown in Figures 8.9–8.11 (England, 1994). The results are from plane strain tests performed on Leighton Buzzard sand with σ_z held constant. Cycling was confined by the two inclined lines, a–a and b–b, which simulated the elastic influence of a structure in contact with the soil element in the *x* direction. When the cycling commenced with $\sigma_x/\sigma_z < 1$, σ_x increased cycle by cycle. For $\sigma_x/\sigma_z > 1$ initially, σ_x decreased, and finally when cycling commenced about the isotropic state $\sigma_x/\sigma_z = 1$ there was no significant change in the strain or the stress.

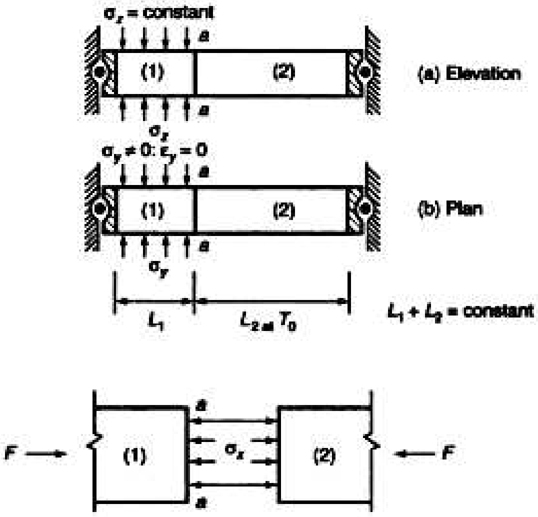

Figure 8.8 Two-component soil–structure interaction model. The granular material element 1 is subjected to constant vertical stress σ_z and to plane strain in the lateral direction *y*. Element 2 is elastic and is subjected to cyclic temperature changes ΔT, from an initial datum temperature T_0. (After England and Dunstan, 1994)

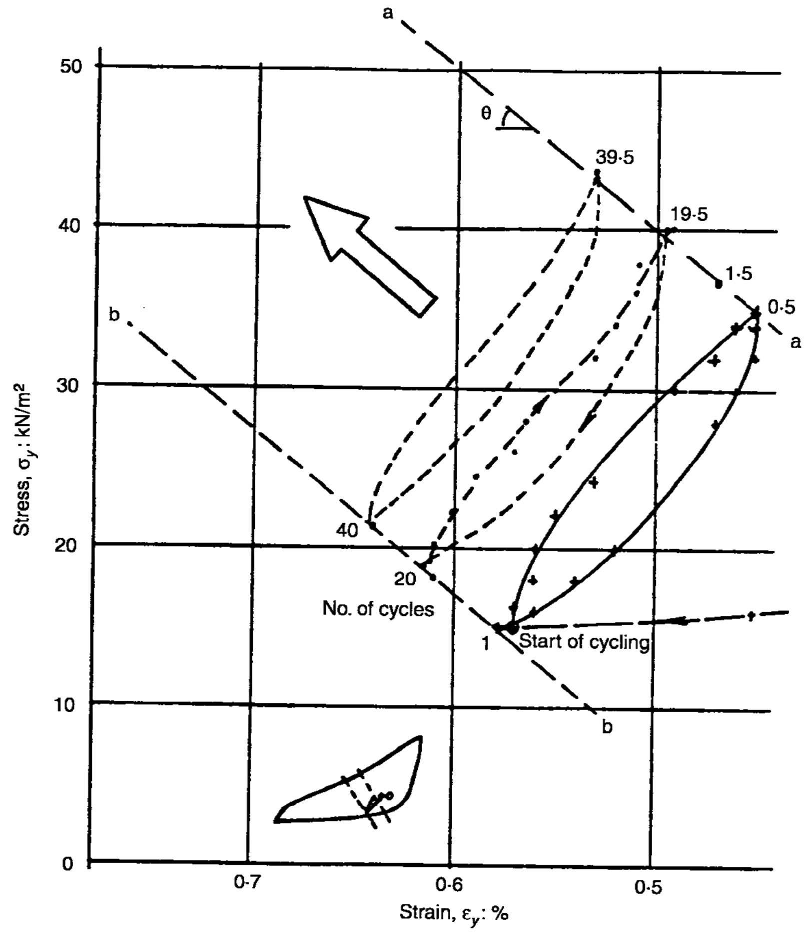

Figure 8.9 Repeated stress and strain cycling, for Leighton Buzzard sand, from an initial state *below* the isotropic stress value. Lines a–a and b–b simulate the effects of thermal cycling in an elastic structure during cyclic soil–structure interaction. (After England, 1994)

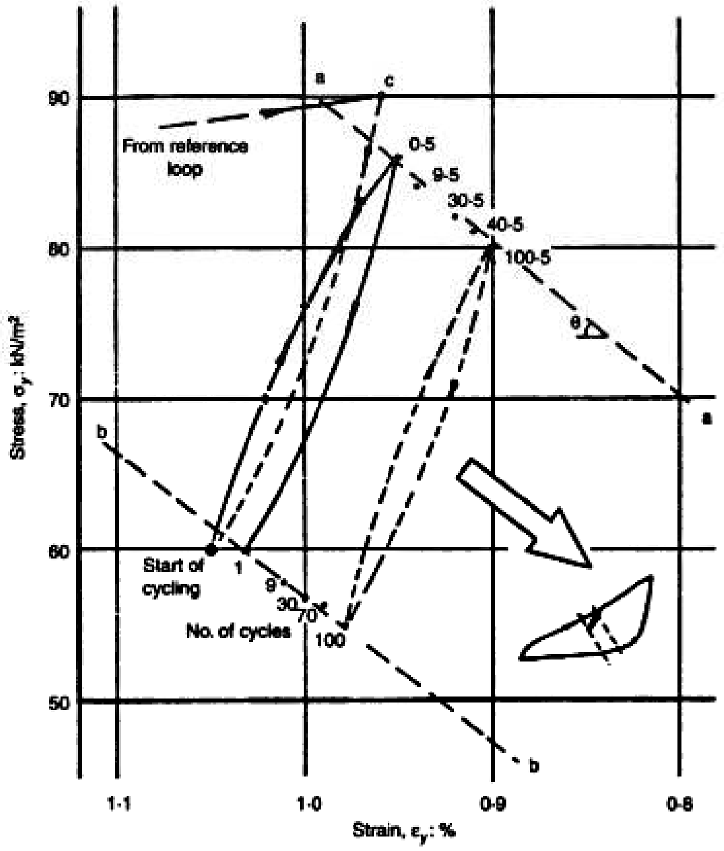

Figure 8.10 Repeated stress and strain cycling, for Leighton Buzzard sand, from an initial state *above* the isotropic stress value. Lines a–a and b–b simulate the effects of thermal cycling in an elastic structure during cyclic soil–structure interaction. (After England, 1994)

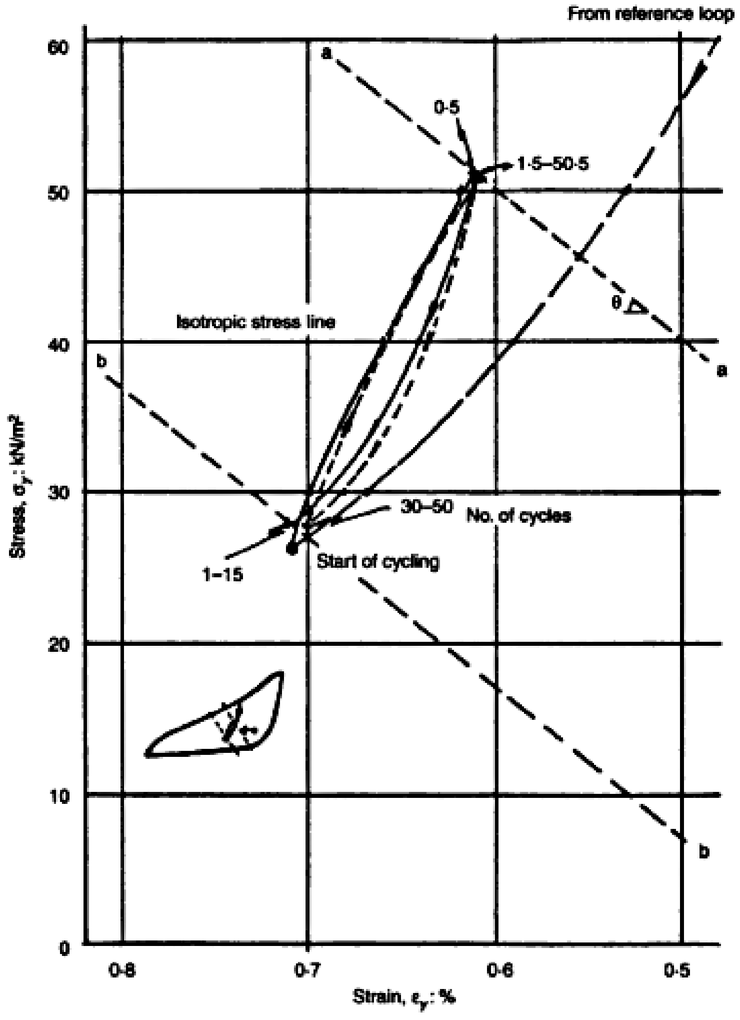

Figure 8.11 Repeated stress and strain cycling, for Leighton Buzzard sand, from an initial state *centred around* the isotropic stress value. Lines a–a and b–b simulate the effects of thermal cycling in an elastic structure during cyclic soil–structure interaction. (After England, 1994)

8.5 Cyclic rotation of the principal stress direction

Friction between the backfill soil and the surface of a sheet pile cantilever type abutment causes cyclic rotation of the principal stress directions. This type of cyclic loading also occurs directly below the foundation of a bank seat abutment when σ_1 is assumed to remain unchanged during cyclic movements of the abutment. The soil at these locations will undergo flow, leading to either stable or unstable deformational behaviour (Arthur *et al.*, 1991; Wong and Arthur, 1986) depending on the principal stress ratio and amplitude of the shear deformation. High stress ratios σ_1/σ_3 and/or large fluctuating horizontal displacements can lead to soil instability and large structural settlements. Figure 8.12 shows some interesting results for Leighton Buzzard sand where the cyclic amplitude (degrees) of rotation of the principal stress axes and the stress ratio (ϕ_m in Figure 8.12) were both varied. The results of two tests (Nos. 52 and 53) are of particular importance. They identify the existence of a watershed state in the sand between stable and unstable deformational behaviour. Test 52 with a cyclic amplitude of 80° exhibited stable behaviour for $\phi_m = 37°$. In test 53 the cyclic amplitude was reduced to 70°, while ϕ_m was increased to 38.5°. The strain behaviour was then unstable.

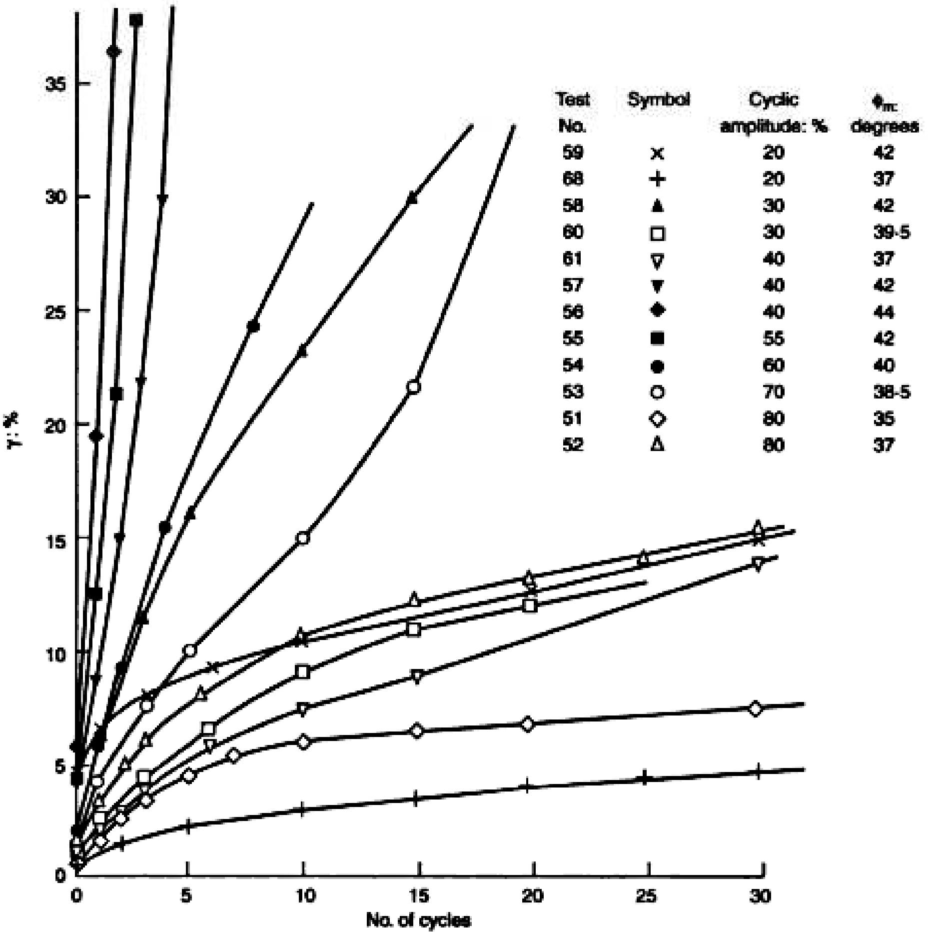

Figure 8.12 The development of shear strain in dense Leighton Buzzard sand during continuous and cyclic rotation of the principal stress directions at σ_3 = 30 kPa. (After Wong and Arthur, 1986)

9 Numerical soil model

9.1 Background

Because existing soil models cannot adequately model many aspects of cyclic loading behaviour a new model is introduced here. It has the appearance of a viscoelastic model, but this in fact is not so because the traditional time variable is replaced by elapsed strain in the formulation. This allows the granular soil to be viewed as a material that undergoes non-elastic changes of stress, only when strain is changing. When strain is not changing, stresses are stationary in time. In this chapter the character of the new model is briefly described. A detailed formulation is given in Appendix 2.2.

9.2 Underlying philosophy for the new model

Two basic viscoelastic elements are used, namely a Maxwell element to model the elastic and flow properties of the soil, and a Kelvin element to model aspects of fabric (anisotropy) development. The two elements are connected in series to form a Burgers element (see Figure 9.1(a)). The stress in the Maxwell spring is termed the soil stress. The stress in the Kelvin spring is termed the internal stress (interparticular friction). The internal stress always shows a phase lag with regard to the soil stress during a change in stress but tends always to the same value as the soil stress as a limiting value.

The elastic and flow components of behaviour (i.e. the Maxwell element) are modelled in three-dimensional stress–strain for a plane strain formulation (see Appendix 2.2). Volumetric strains are modelled through the elastic and flow Poisson ratio terms, incorporating appropriate dilatancy relationships coupled to the stress ratio in the plane of strain. The model is then set up on an incremental basis whereby, after the application of an increment of strain, the soil stress is permitted to relax with regard to the flow component of the model, and the Kelvin stress is then permitted a change to restore internal compatibility (see Figure 9.1(b)).

In this form the soil stress always relaxes towards the isotropic state of stress and the Kelvin stress always moves towards the soil stress in order to minimize their difference. The deviation of the soil stress from the isotropic state leads to a stress ratio in the plane of strain, while the deviation of the Kelvin stress from the isotropic state is treated as a measure of soil fabric.

The general behaviour of the soil stress and Kelvin stress are similar in that both exhibit decay responses with an increase of applied strain. The soil stress is always seeking to become closer to the mean confining stress, and the Kelvin stress seeks the soil stress as its target. The exact forms of the exponential equations are given in Appendix 2.2.

9.3 Identification of model parameters

Although it cannot readily be seen from the form of the general equations (in Appendix 2.2), it is possible to establish that the model parameter primarily responsible for defining the critical state stress ratio, is η_0, a basic material constant contained within the Maxwell dashpot parameter η. The parameter η is the effective value of η_0 corresponding to the particular void ratio and confining stress. Validation tests indicate the value of η_0 to be approximately 1.1 sin ϕ_{crit}, where ϕ_{crit} is obtained from a conventional plane strain test. The soil modulus plays no part in defining the critical state behaviour.

Obervations

- If the soil stress and Kelvin stress can be simultaneously coincident with the isotropic stress, then fabric is absent (i.e. there is no anisotropy). Also, under monotonic loading to failure, the Kelvin stress becomes equal to the soil stress at large strains (i.e. the soil exhibits steady flow characteristics without further changes in anisotropy at this time).
- The inherent phase lag of the Kelvin stress during cyclic stress changes indicates that the model will generally predict the presence of a degree of anisotropy when the soil stress is returned to the isotropic state. Such behaviour has been observed in experimental tests (Arthur *et al.*, 1977; Rodriguez, 1977)

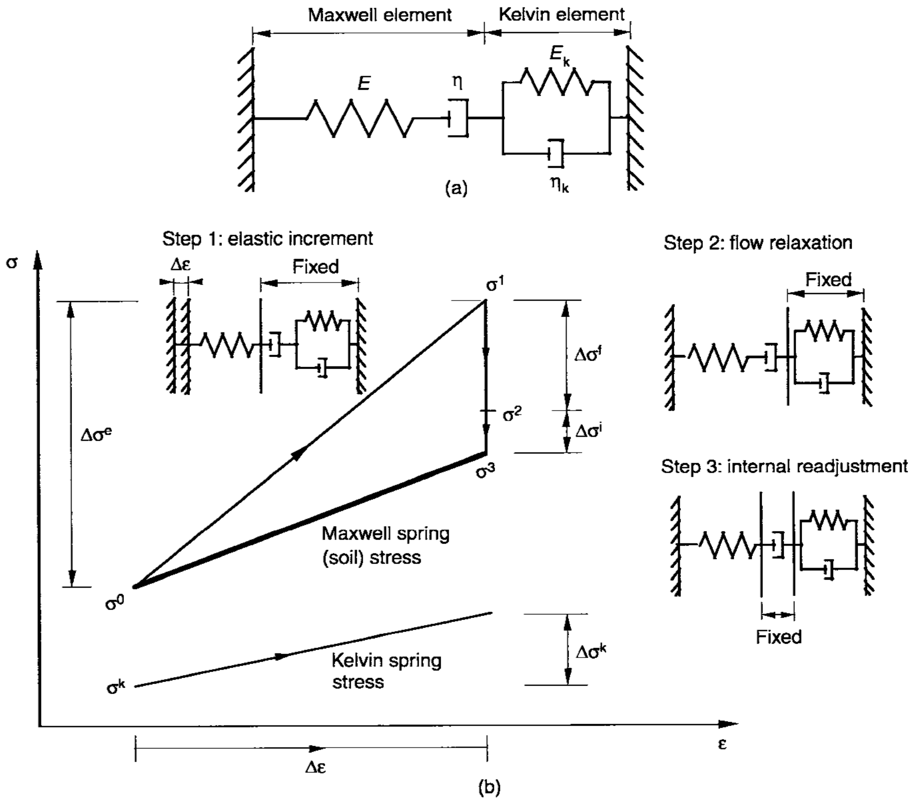

Figure 9.1 (a) The rheological representation of the new numerical model. (b) Stress changes in each component due to an imposed strain increment $\Delta\varepsilon$

The model predicts flow strains at all stress levels without the need to specify plastic yield surfaces. Also, the magnitude of flow is always moderated by the amount of fabric present through the Kelvin stress. It is this feature which allows predictions similar to the cyclic experimental observations shown in Figures 8.4–8.6 to be made.

9.3.1 Monotonic behaviour

During monotonic loading, change in density becomes responsible for predicting strain hardening followed by strain softening for initially dense sands. It thus follows that soil strength is not a fundamental property of the soil but is simply a consequence of the initial void ratio and the subsequent straining process. The model predicts a range of strengths depending upon the initial void ratio of the soil. Predictions are based solely on the current state of the soil parameters and the change in stress or strain thereafter; there is no requirement to store stress history during the computational process. This feature makes the model simple and economic to use.

As an aid to understanding the physical concepts associated with the strain hardening and softening features which the model is able to capture, it is important to note the influence that the soil modulus E and flow parameter η have in defining the stress–strain response. The parameter η is responsible primarily for the behaviour at large strains close to the critical state, whereas E has greater influence near to the time of initial stressing. Both influence the build-up of stress during continued straining. In mathematical terms η defines a steady-state solution. Because both E and η are variables dependent on the void ratio e (through a void function F_e, which is itself dependent on the critical state void ratio e_{cr}; see Appendix 2.2, Equation A2.7)) and the confining stress σ_c, many stress–strain responses are possible. It is thus clear that initial void ratio alone cannot define soil behaviour. Figures 9.2 and 9.3 show the stress–strain responses for two conditions:

(*a*) for E and η assumed to be constants for the material, and
(*b*) for σ_c assumed to be constant while E and η are variables as described above.

In (a) a steady-state stress ratio is defined by η and the form of the transient curve is influenced also by the value of E. In (b), because the void ratio e (and hence F_e) changes continuously with straining, the effect is to generate a stress ratio trajectory which is at all times seeking a continuously changing steady-state stress ratio limit. This feature results in the stress firstly increasing and moving towards a steady state which is above its current value, and secondly to a reversed situation where the stress seeks a steady state which is below its new current value, now at larger strain. The effect is to produce the 'humped' curve (strain hardening–softening) shown by the *full line* in Figure 9.3. The limiting steady-state stress ratio, corresponds to the limiting value of the void function F_e. This is the critical state

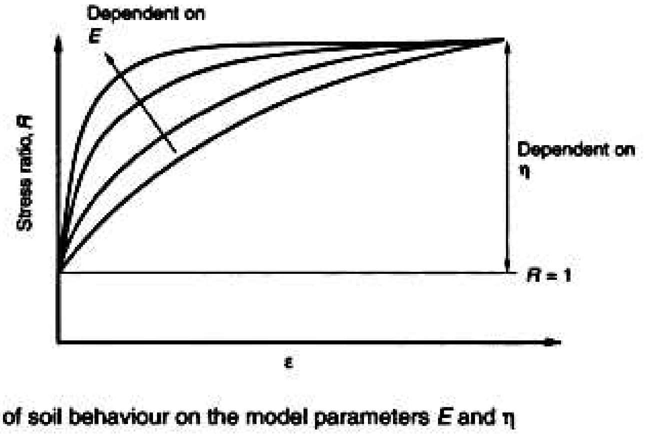

Figure 9.2 Dependence of soil behaviour on the model parameters E and η

for the soil. Figure 9.3 thus demonstrates the strain hardening–softening phenomenon due to changing void function (void ratio). The effect of changing confining pressure is demonstrated in Figure 9.4, which also illustrates the importance of the initial void ratio in defining the stress–strain response. Confining pressure explicitly changes the void function F_e through the dependence of the critical void ratio on confining pressure. For a higher confining pressure (line b, compared to line a, in Figure 9.4(a)), the critical void ratio drops (Figure 9.4(c) line b) and hence F_e has the form shown in Figure 9.4(b), line b. The confining pressure thus determines the degree of hardening and softening in the analysis. Model predictions compare well with experimental observations.

9.3.2 Cyclic behaviour

During cyclic loading it is important to recognize the significant effect that fabric build-up has on the development of non-elastic strains. For a soil taken to a given stress level, then partially unloaded and reloaded to the same stress level, the fabric which developed during the initial loading is retained to a large extent and influences the reloading such that the soil appears stiffer until the stress again approaches that of the first loading. A parameter has been established to control this behaviour by modifying the flow parameter η. It has been termed a *fabric factor* ψ, and has been validated numerically by comparing model predictions with experimental data for both ratcheting strain development under fluctuating stress states and stress ratio drifting during the application of fluctuating strains. Figure 9.5 illustrates the effect of this parameter on the ratcheting strains developed during repeated stress cycling. When $\psi > 1$ the fabric factor reduces the rate of strain ratcheting as shown in Figure 9.5(b). A fuller description of the derivation of ψ is given in Appendix 2.2.

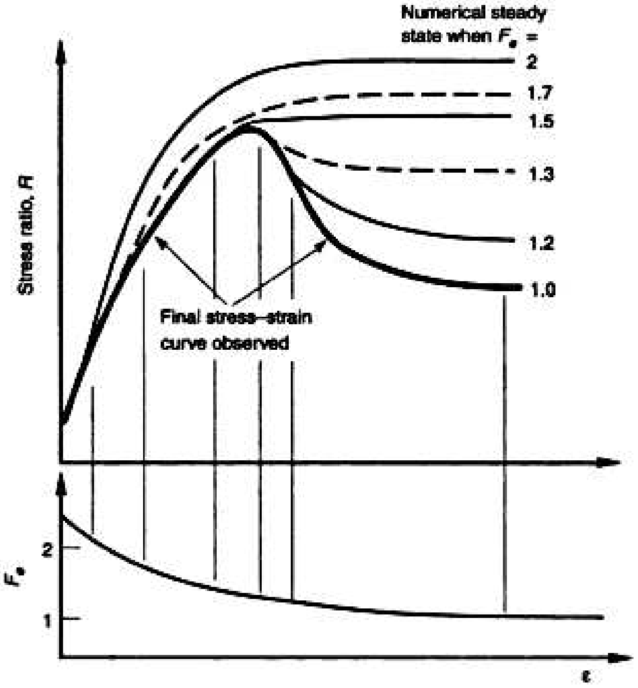

Figure 9.3 Dependence of soil behaviour on the model parameter F_e

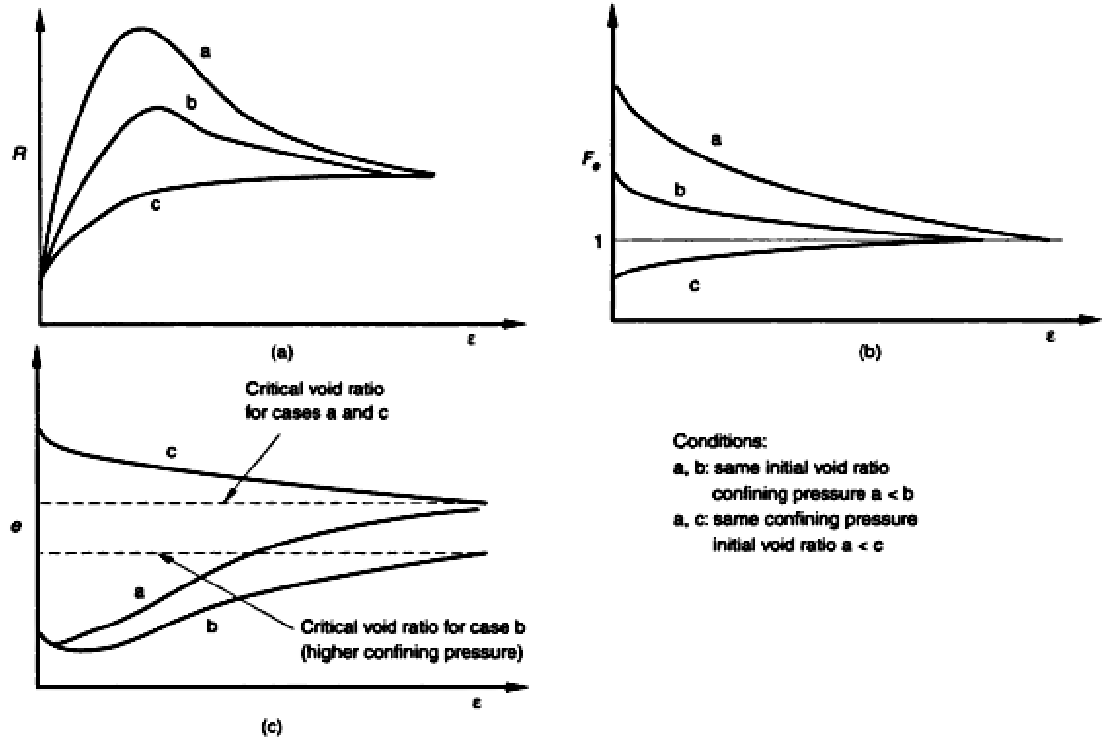

Conditions:
a, b: same initial void ratio
confining pressure a < b
a, c: same confining pressure
initial void ratio a < c

Figure 9.4 Strain hardening and softening as affected by the void ratio and the confining pressure

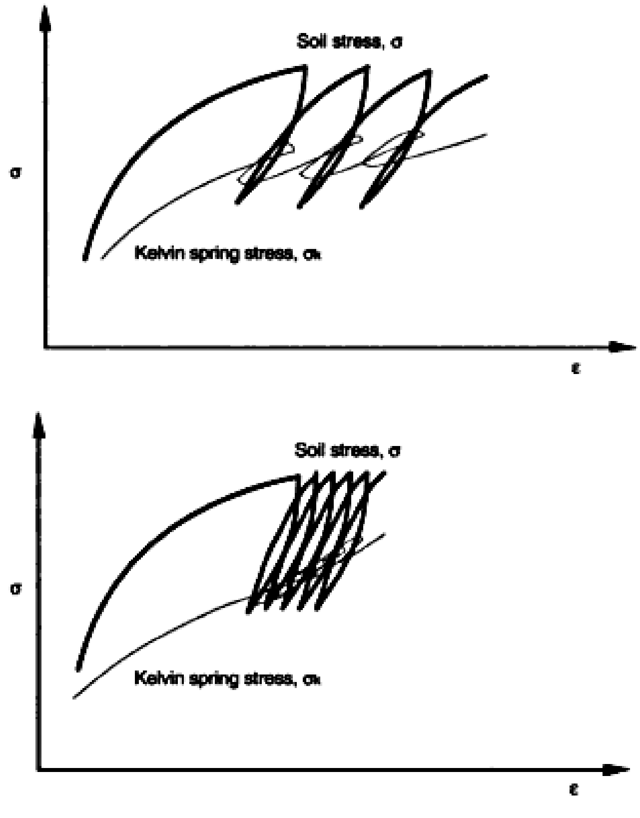

Figure 9.5 Influence of fabric factor ψ on the development of ratcheting strains: (a) ψ = 1 throughout; (b) ψ > 1 at unloading and reloading

9.4 Analysis using the soil model: soil element in plane strain

Because the analysis is of an incremental nature, with future behaviour being defined solely by the current state and future changes to the boundary conditions, any initial condition can be selected. Difficulty may be encountered, however, if it is necessary to define an initial anisotropy. Although this can be done, some previous experience of using the model would be helpful.

The analysis is set up in plane strain using a three-dimensional stress and strain formulation for the Burgers material representation. The boundary conditions are: constant vertical stress σ_x, imposed incremental strain $\Delta\varepsilon_y$ in the horizontal direction and zero strain in the third orthogonal direction, $\varepsilon_z = 0$. The stresses σ_y and σ_z are then variables in the analysis. This formulation was chosen to assist in the analysis of the retaining wall presented in Chapter 11. Also, because of the analogy between the analysis developed here, (using elapsed strain as a pseudo-time parameter), and a creep analysis in real time, it is possible to derive a closed form solution for σ_y and σ_z for each applied increment of strain $\Delta\varepsilon_y$. For simplicity the model is described in terms of the changes in stress in the horizontal direction only. The formal matrix coupling of σ_y and σ_z through the Poisson ratio terms is given in Appendix 2.2.

One step in the incremental computations requires the following sequence of operations to be followed:

(*a*) Apply a strain increment $\Delta\varepsilon_y$ and compute the instantaneous elastic stress change

$$\Delta\sigma^e = E\,\Delta\varepsilon_y$$

(see Figures 9.1(b) and A2.8 and Equation A2.23).

(*b*) Compute the components of stress relaxation at constant imposed strain:

  (i) $\Delta\sigma^f$ for the Maxwell component while the Kelvin dashpot is held 'frozen', and

  (ii) $\Delta\sigma^i$ from the effect of changes in the Kelvin component while the Maxwell dashpot is held 'frozen'.

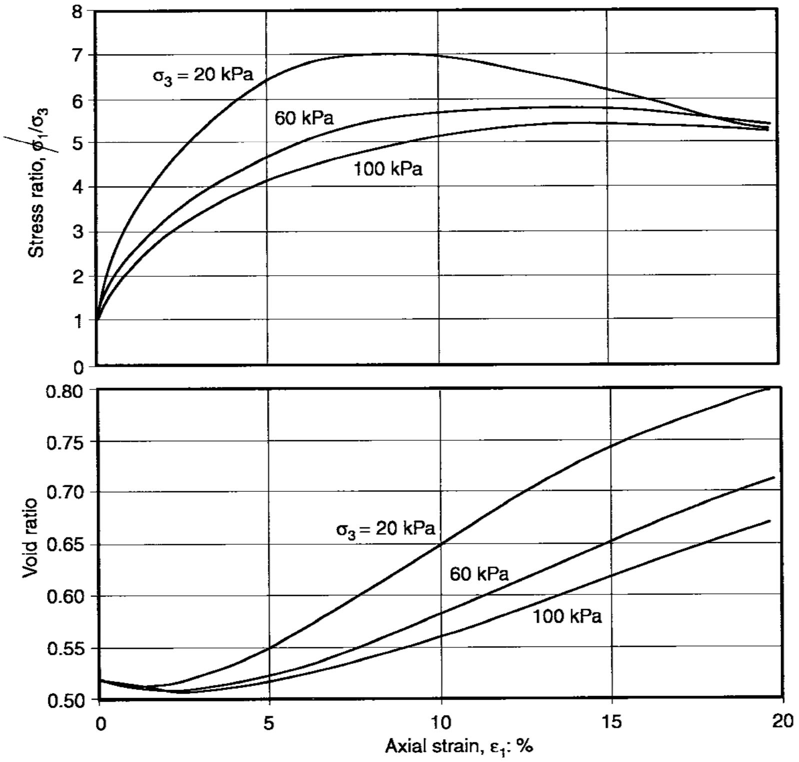

Figure 9.6 Influence of the confining pressure on the stress–strain response

(*c*) Compute the new soil stress σ_{new} as the sum of σ_{old} and the incremental changes, thus,

$$\sigma_{new} = \sigma_{old} + \Delta\sigma^{e} + \Delta\sigma^{f} + \Delta\sigma^{i}.$$

(*d*) The elastic, plastic and volume components of strain are then updated to provide the new current state of the material. The incremental calculation can then repeat after the application of another strain increment $\Delta\varepsilon_y$. The detailed operations which need to be performed to deduce these associated elastic and plastic strain increments, to the stress changes, are listed in Appendix 2.2.

In order that the steps just described may apply equally to cases of monotonic and cyclic loading, the additional parameter ψ is used in the analysis as a multiplier to control the flow behaviour, particularly during cyclic stress changes when anisotropy plays an important role. The dependence of ψ on strain increment direction (i.e. loading or unloading), stress ratio, soil fabric and void ratio is given in Appendix 2.2.

9.5 Predictive capacity of the model

Figures 9.6 and 9.7 are used here simply to illustrate the variation in the plane strain performance that the model is able to capture with respect to the initial void ratio, confining pressure and their changes during straining.

The strain responses for an initially dense sand ($e_0 = 0.52$) subjected to three different constant values of the minor principal stress are shown in Figure 9.6. The characteristic flattening of the stress–strain response at higher values of σ_3 is readily apparent. The influence of the initial void ratio, $e_0 = 0.52$–0.80, on stress–strain behaviour is shown in Figure 9.7 for a common value of σ_3. The changes in the stress and void ratio with increasing strain are typical of experimental observations. Some comparisons are presented in Chapter 10.

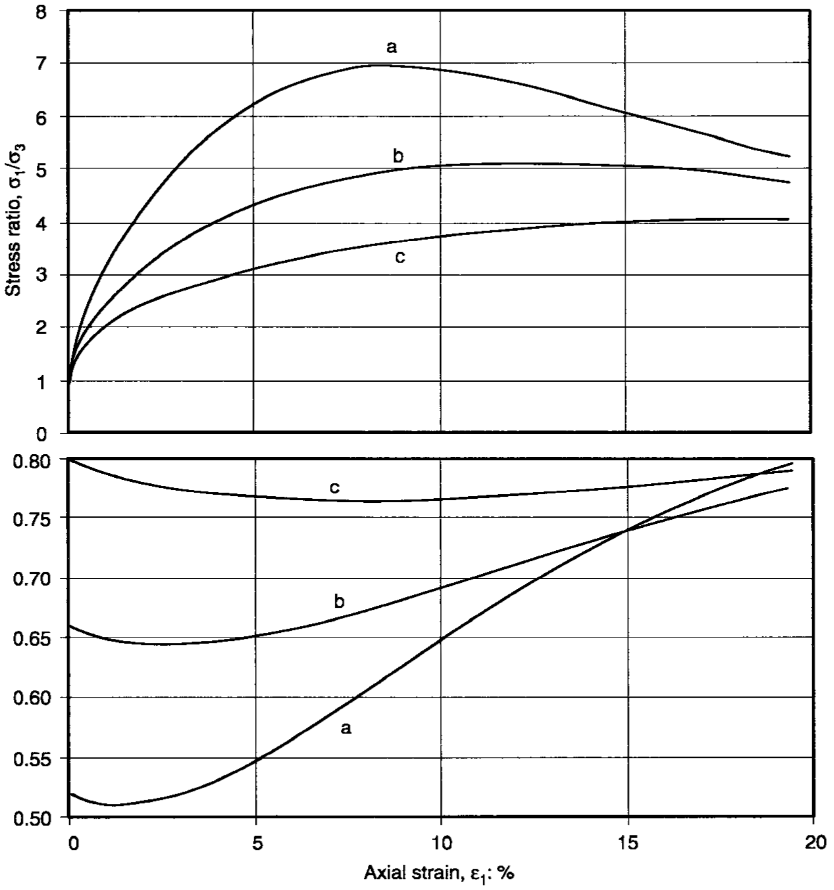

Figure 9.7 Influence of the initial void ratio on the stress–strain response (σ_3 = 20 kPa in all cases)

10 Validation of the soil model in plane strain

The results of the experiments described in this chapter were used to determine the various soil model parameters described earlier, and thus to validate the model for use in the retaining wall analysis presented in Chapter 11. Three sets of test results (eight tests in total) were used in the calibration process:

- monotonic loading,
- cyclic strain loading, and
- cyclic stress loading.

The tests were carried out on Leighton Buzzard sand in a biaxial tester at University College London. The results are all for a drained condition and for plane strain loading with $\sigma_3 = 20$ kPa, constant. All tests started from an isotropic stress state. Virgin loading was then applied to the required stress level, before starting the cyclic tests under either stress or strain control. The initial void ratio and other test conditions are listed in Table 10.1.

Table 10.1 Details of the calibration tests for the soil model

Test type	Test No.	No. of cycles	Initial void ratio	Cyclic strain magnitude, $\Delta\varepsilon_1$	Cyclic stress ratio
Monotonic	M1		0.52		
	M2		0.72		
Cyclic strain	N1	30	0.52	0.3% unload from $R = 5$	
	N2	10	0.72	1% unload from $R = 2$	
	N3	10	0.72	1% unload from $R = 2.7$	
Cyclic stress	S1	20	0.52		1–4
	S2	20	0.52		1–2
	S3	20	0.52		3–4

10.1 Soil model parameters

The following parameters were evaluated from the experiments: E_0, η_0, E_{k0}, η_{k0}, α and κ. The following parameters were obtained from literature: n, ν_e, λ, σ_{c0} and e_{c0}. E_0 was evaluated from a small stress–strain change close to the hydrostatic state. When ν_e is known, E_0 can be calculated from the three-dimensional equations in Appendix 2.2. The parameter η_0 is dependent on the critical state stress ratio. Because this could not be determined explicitly from the tests, a stress ratio of 3 was assumed and this was then refined from a curve fitting of the monotonic test results. E_{k0}, η_{k0} and α were evaluated by curve fitting the range of cyclic loading test results. Once determined these values were kept constant in all future uses of the model.

The parameter used to define the hydrostatic compaction swelling line, κ, was evaluated by a hydrostatic compaction test performed on a loose Leighton Buzzard sand ($e_0 = 0.72$). The range of confining pressure changes was 20–80 kPa. Other critical state parameters were obtained from Been *et al.* (1991), Cole (1967) and Stroud (1971). The derived set of soil model parameters is given in Table 10.2

In the following comparisons it is important to recognize that the model parameters are the same for each and that no one set of data has been fitted individually. Because it is important that the soil model should have the inherent capability to predict monotonic and various forms of cyclic stress–strain behaviour, all calibration test information was taken into account when defining the model parameters as listed in Table 10.2. These have then remained unchanged in all future uses of the model.

10.2 Monotonic loading

Figure 10.1 illustrates the model prediction for monotonic loading from two different initial void ratios.

10.3 Constant-amplitude cyclic strain fluctuations

Figures 10.2 and 10.3 show the results for fluctuating strains of 0.3% and 1%, both offset from the isotropic stress state. There are two sources of mismatch for the test results:

(*a*) The offset strain at the first unloading—this is due to error in the virgin loading strain (monotonic loading). For large strain, this error is not obvious, as shown in Figure 10.1. A 0.2% axial strain deviation at a stress ratio of 5 (see Figure 10.2) is not considered significant for a total of 2.3% strain to reach this stress level. It is also acknowledged that variations in strain between tests do occur.

(*b*) Densification of loose sand (see Figure 10.3) is overestimated in comparison with the test results. The corresponding stress–strain loops are also slightly wider than those measured in tests. It appears that the model overestimates the plastic response for loose sand during cyclic strain loading and generates higher overall densification.

Table 10.2 Values of soil model parameters (for Leighton Buzzard sand) from calibration tests*

Parameter	Value	Parameter	Value
E_0	950	n	0.5
η_0	0.53	ν_e	0.15
E_{k0}	1200	λ	0.027
η_{k0}	3.4	σ_{c0}	100 kPa
κ	0.0183	e_{c0}	0.8
α	0.2		

*Values for E_0 and E_{k0} are based on stresses in kPa

In general, the model captured the stress drifting behaviour of the sand well. In particular (see Figure 10.3), when the cyclic loading involved 90° jump changes in the major principal stress direction, the significant increase in plastic response as the stress ratio crossed the hydrostatic state was also captured by the model. This feature is important for the retaining wall analysis presented in Chapter 11.

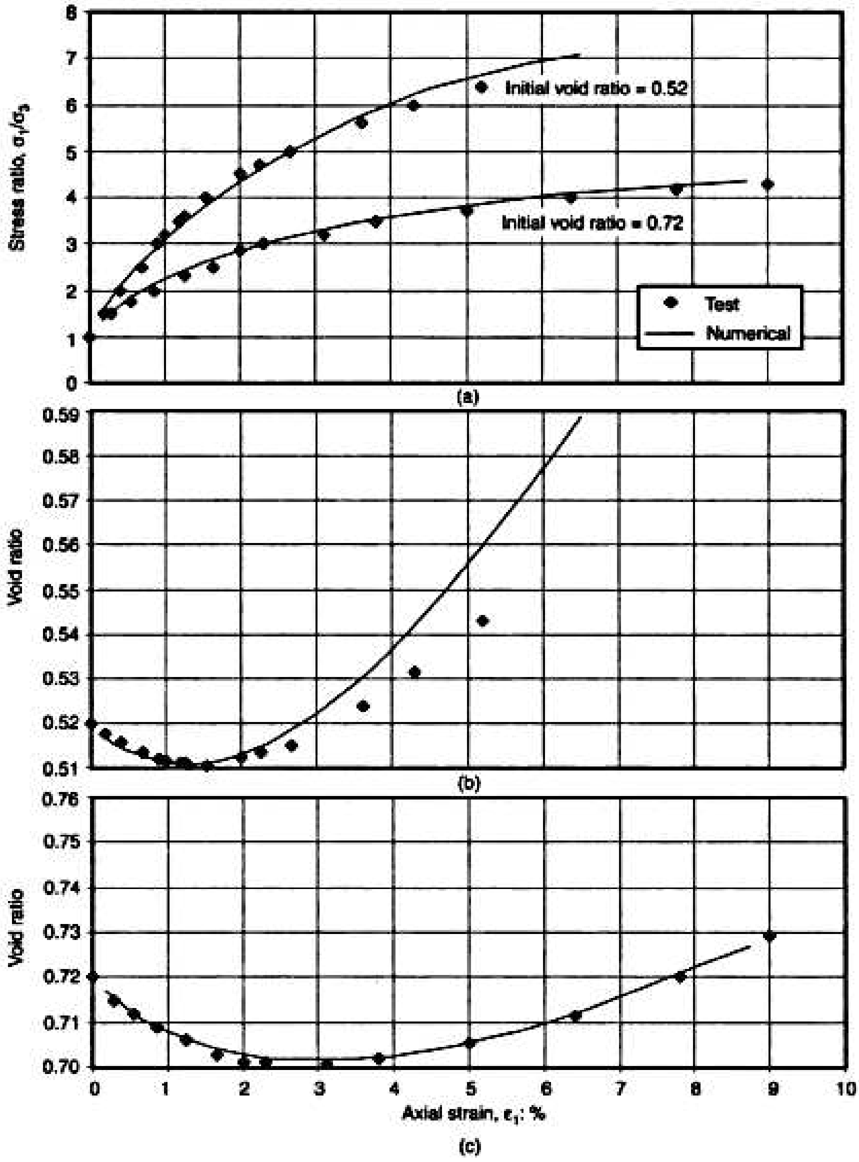

Figure 10.1 Comparison of model predictions with test data for plane strain monotonic loading (σ_3 = 20 kPa): (a) stress–strain response; (b) void ratio changes for initially *dense* sand (initial void ratio 0.52); (c) void ratio changes for initially *loose* sand (initial void ratio 0.72)

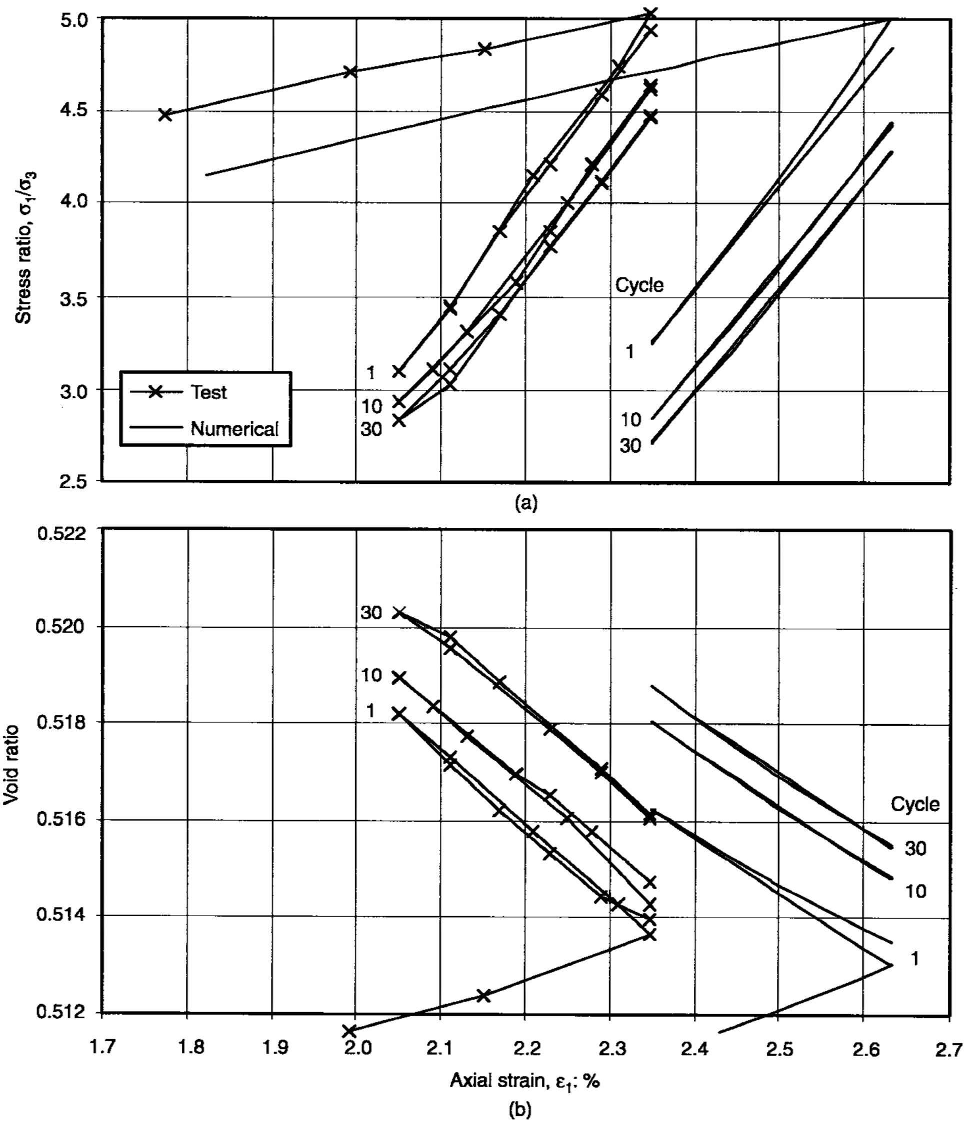

Figure 10.2 Comparison of model predictions with plane strain cyclic strain test results for fluctuating strains of 0.3% applied to a *dense* sand (initial void ratio 0.52; σ_3 = 20 kPa): (a) stress–strain responses; (b) void ratio changes

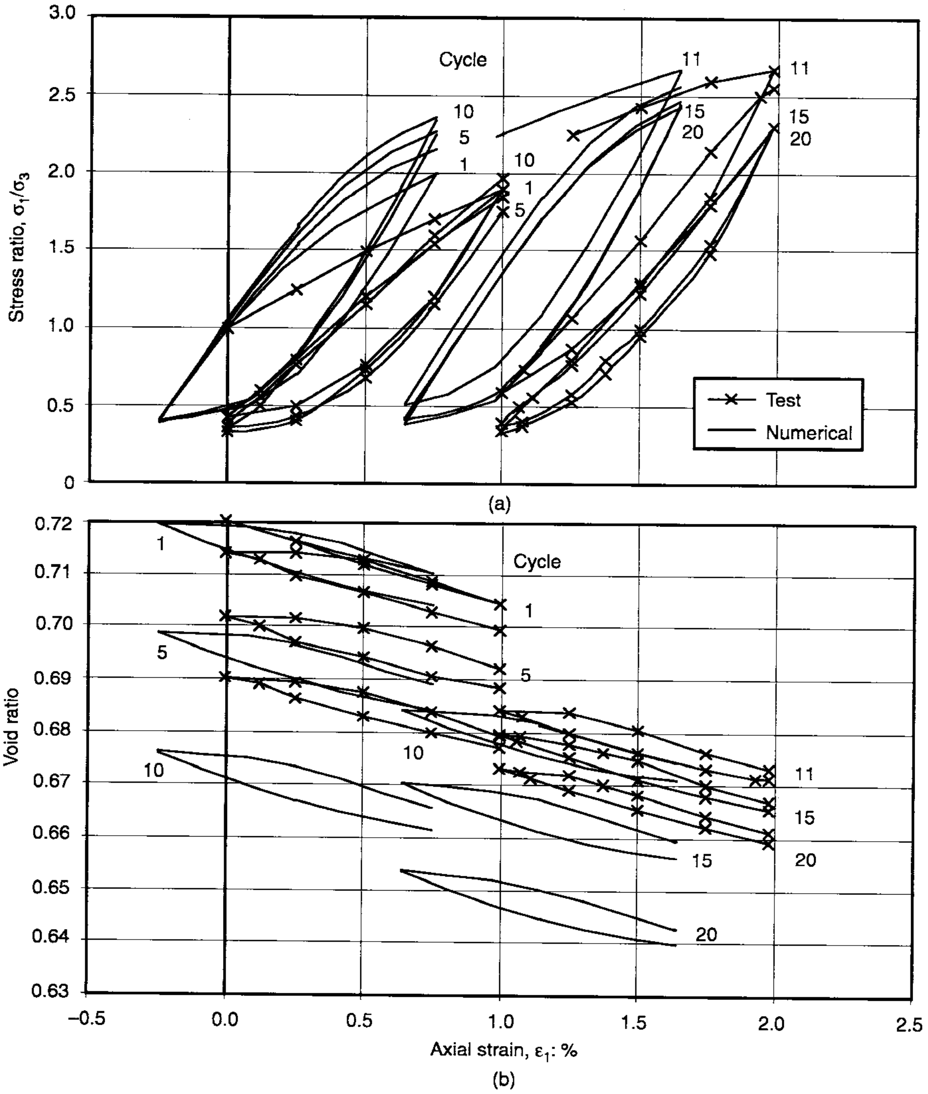

Figure 10.3 Comparison of model predictions with plane strain cyclic strain test results for fluctuating strains of 1% applied to a *loose* sand (initial void ratio 0.72; σ_3 = 20 kPa). Initial offset strains correspond to unloading from R = 2 and R = 2.7. (a) Stress–strain responses; (b) void ratio changes

10.4 Constant-amplitude cyclic stress fluctuations

Figures 10.4–10.6 show results for fluctuating stresses between stress ratios of $R = 1$ to 4, $R = 1$ to 2, and $R = 3$ to 4, respectively. Apart from the small initial strain error, mentioned in Section 10.3, another mismatch identified here is between the slight dilation predicted compared to the slight densification recorded after 20 cycles. Because the confining pressure varies more in these tests than previously, and because the model assumes a fully recoverable volumetric strain for hydrostatic compaction, the mismatch may be due to ratcheting volumetric strain, especially at the beginning of the cycling. This type of ratcheting behaviour is not currently understood. Additional understanding is therefore needed in this area in order to refine further the numerical model. In general the predicted ratcheting strains match quite well with all three sets of test data. This capability to model ratcheting strains with reasonable confidence at various stress levels is important in the retaining wall analysis which follows.

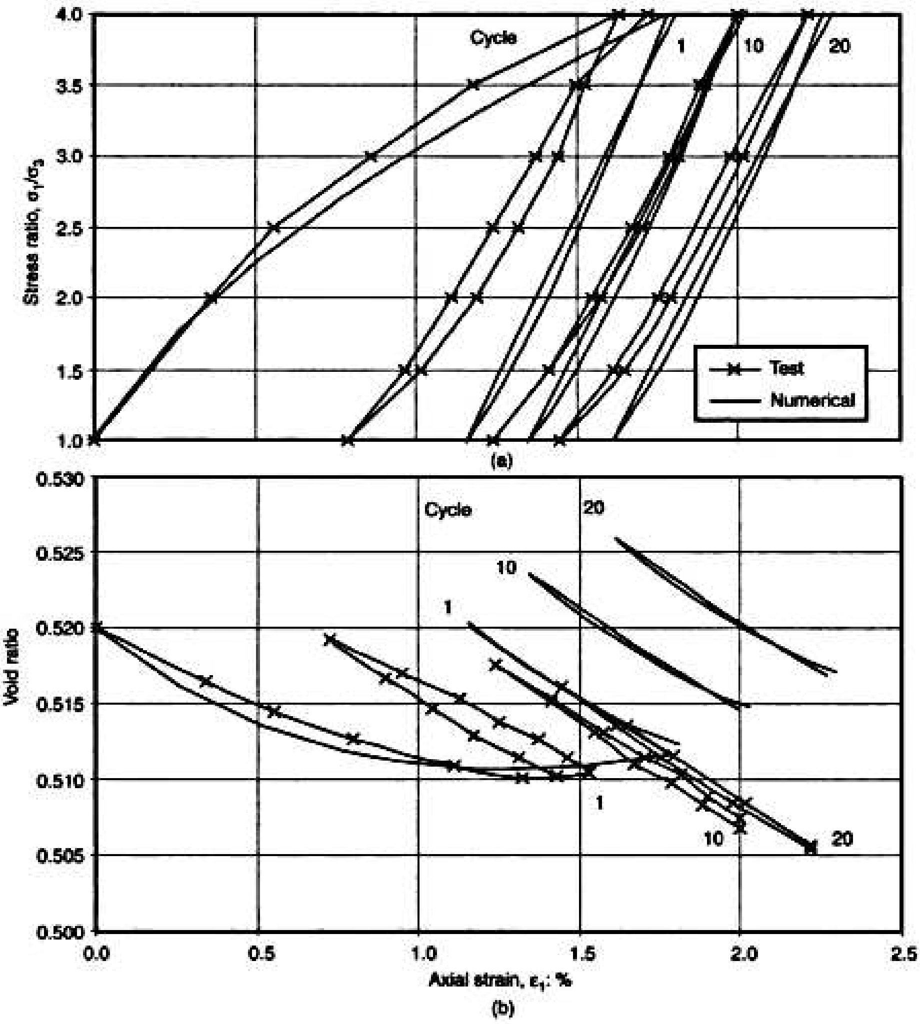

Figure 10.4 Comparison of model predictions with plane strain cyclic stress test data for stress fluctuations between stress ratios $R = 1$ and 4 for *dense* sand (initial void ratio 0.52; $\sigma_3 = 20$ kPa): (a) stress–strain responses; (b) void ratio changes

10.5 Remarks

The numerical simulations and predictions are considered to be satisfactory for the wide range of monotonic and cyclic test results investigated. Considerable importance has been attached to the fact that no single material constant was adjusted to suit an individual test result. All model parameters, once identified, featured in all predicted results. Both ratcheting strains under fluctuating stresses and drifting stress ratios under imposed fluctuating strains were predicted to a reasonable accuracy. Figure 10.7 summarizes the comparisons for the tests mentioned above and reflects the overall predictive capability of the model. The numerical model is therefore considered suitable for use in the analysis of the retaining wall, as presented in Chapter 11.

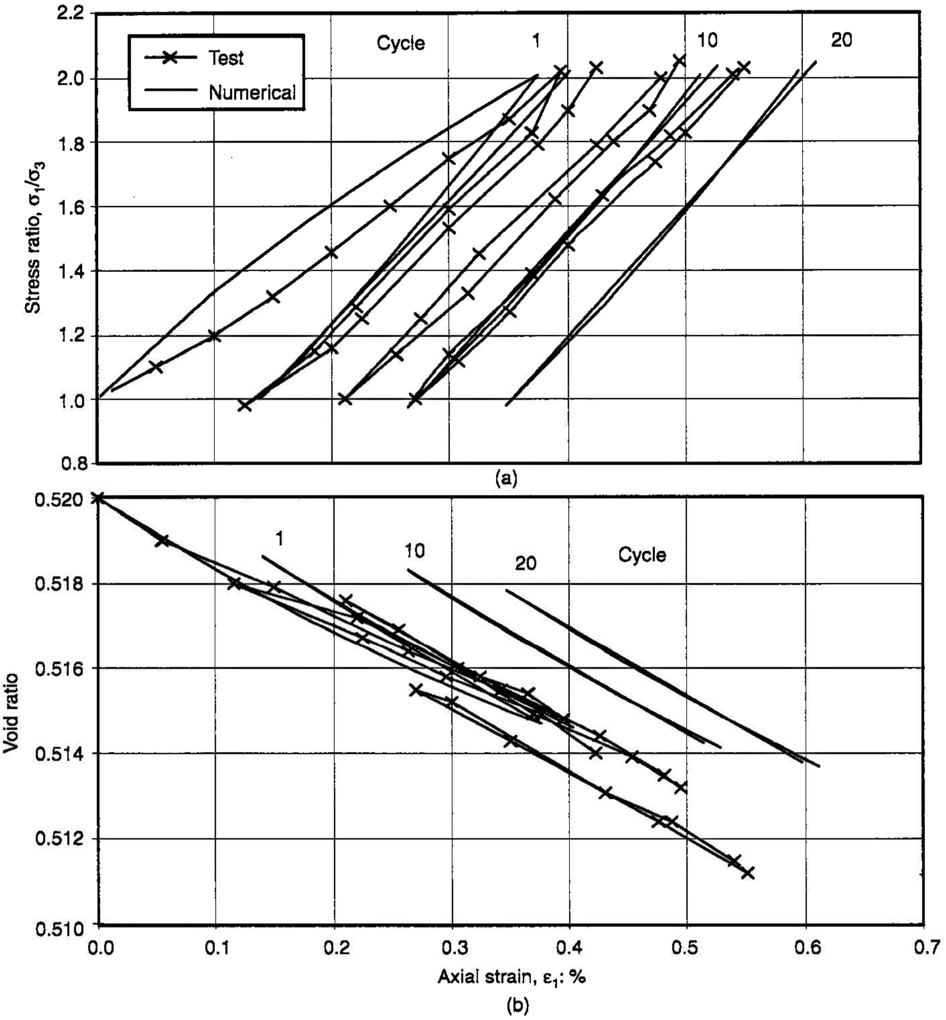

Figure 10.5 Comparison of model predictions with plane strain cyclic stress test data for stress fluctuations between stress ratios $R = 1$ and 2 for *dense* sand (initial void ratio 0.52; $\sigma_3 = 20$ kPa): (a) stress–strain responses; (b) void ratio changes

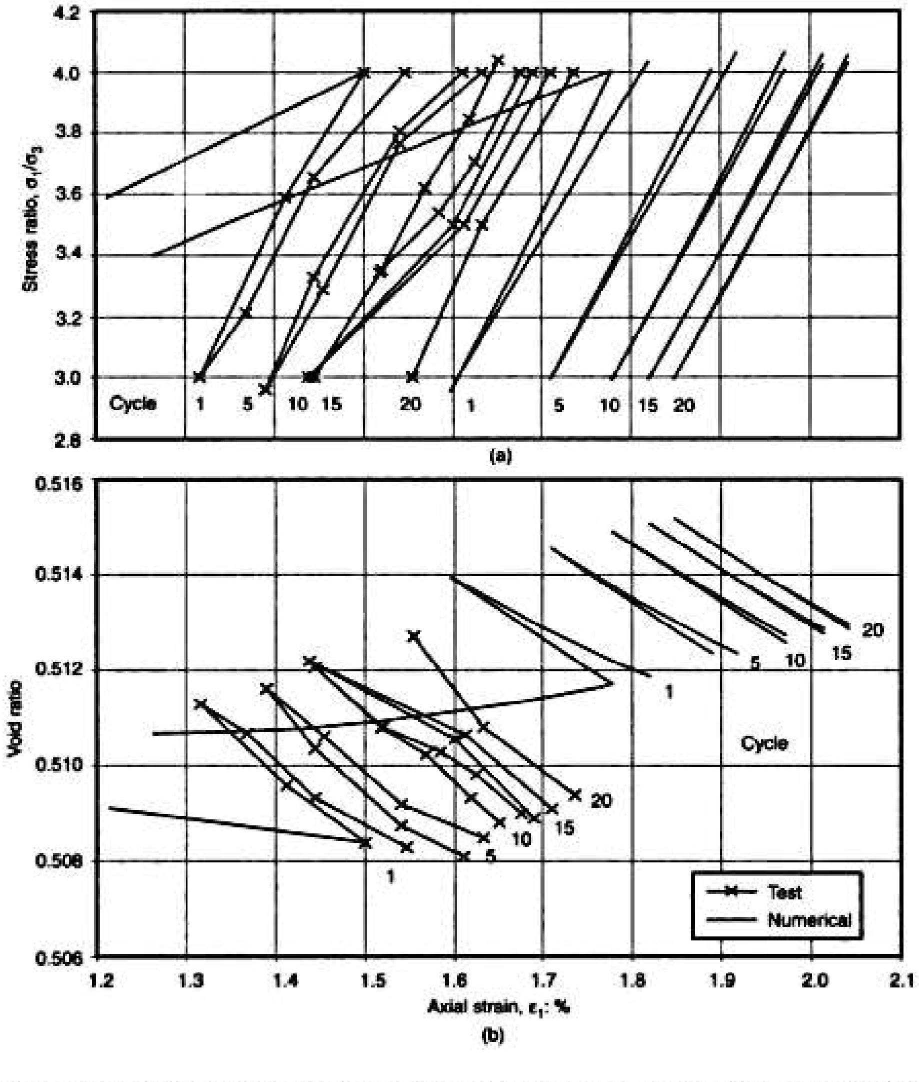

Figure 10.6 Comparison of model predictions with plane strain cyclic stress test data for stress fluctuations between stress ratios $R = 3$ and 4 for *dense* sand (initial void ratio 0.52; $\sigma_3 = 20$ kPa): (a) stress–strain responses; (b) void ratio changes

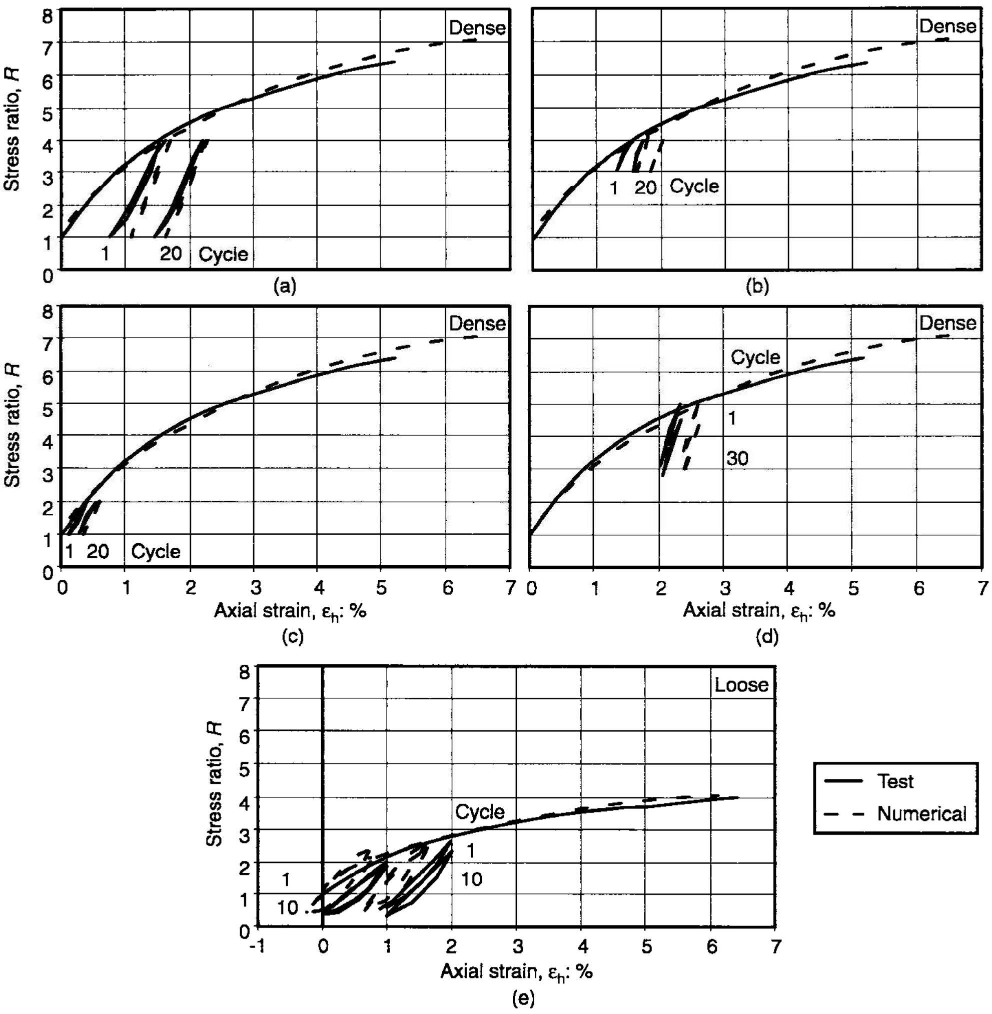

Figure 10.7 Summary of the soil model predictions: comparisons between observed soil behaviour and model predictions for Leighton Buzzard sand under plane strain loading $R = \sigma_1/\sigma_3$. (a) Fluctuating stresses between $R = 1$ and 4 (cycles 1 and 20); (b) fluctuating stresses between $R = 3$ and 4 (cycles 1 and 20); (c) fluctuating stresses between $R = 1$ and 2 (cycles 1 and 20); (d) fluctuating strain magnitude of 0.3% (unload from $R = 5$); (e) fluctuating strain magnitude of 1% (unload from $R = 2$ and $R = 2.7$). $\sigma_3 = 20$ kPa for all tests. Dense: $e_0 = 0.52$ for tests (a)–(d). Loose: $e_0 = 0.72$ for test (e) only

11 Retaining wall analysis program

11.1 Background

There are two common methods for the evaluation of lateral earth pressures acting against a vertical retaining wall, namely that attributed to Coulomb (1776) and that of Rankine (1857). Coulomb's method is based on the limiting equilibrium of a stiff soil wedge sliding (failing) against a soil mass, while Rankine's method is based on slip-line fields during soil failure. Both are classical limiting equilibrium methods based on the assumption of soil as a rigid plastic material. Although these two methods are still widely used in practice, they do not distinguish between modes of wall movement and provide no information on pre- and post-failure (force and deformation) performance. Model tests have been carried out by many researchers (Fang and Ishibashi, 1986; Terzaghi, 1943; James and Bransby, 1970; Rowe and Peaker, 1965; Schofield, 1961; Sherif and Mackey, 1982) in order to clarify the influence of wall–soil friction, mode of wall movement and other soil properties for the *active* and *passive* failures of the soil mass. While, in general, the theoretical evaluation by either Coulomb's or Rankine's method is in good agreement with the experimental results at the *active* failure condition, the *passive* pressure is often overestimated by the theories. Also, the *passive* rupture surface is not planar in shape as the theories imply. Investigations for various non-planar rupture surfaces for *passive* failure have been carried out (Caquot and Kerisel, 1948; Rosenfarb and Chen, 1972), and these yielded a better agreement with the records from field and model tests. Sokolovski (1960) presented a finite-difference solution; and Janbu (1957) and Shields and Tolunay (1973) proposed an approach to the earth-pressure problem similar to the method of slices used in slope-stability analyses.

The analytical methods mentioned above do not satisfy the requirement of overall equilibrium and compatibility for the whole soil mass and take no account of the deformational character of the soil. Non-linear finite element methods have been employed (Clough and Duncan, 1971; Nakai, 1985; Potts and Fourie, 1986) to gain more insight into the stress–strain distribution of the soil mass for both the *active* and *passive* movement of the wall and under various types of wall movement.

Finite element methods for the analysis of cyclic loading require a considerable amount of effort in computing time and resources, depending on the complexity of the non-linear material model employed. Equivalent non-linear elasticity based methods are the most common due to their simplicity. However, they are not able to capture the volume change and strain ratcheting behaviour, as mentioned before. Therefore, a balance is required between the complexity of the numerical analysis and the accuracy of the solution predicted. In order to achieve this balance and make it possible to simulate the retaining wall performance within the resource of the project allowed, a semi-empirical framework was developed for the retaining wall analysis, called here the transitional equilibrium method (TEM).

In his chapter the TEM is presented and its use for the retaining wall analysis described. A computer program, QSand, was written to carry out the simulations. A flow chart of the computer program is also presented here.

11.2 Transitional equilibrium method

The mass of soil behind a retaining wall which responds to an imposed displacement from the wall can be defined approximately by that mass (termed the *effective soil mass*) which is bounded by the position of the wall and a boundary plane passing close to the toe of the wall. The location of this boundary plane is assumed to be directly dependent on the stress state in the soil immediately behind the wall. When the wall rotates, the soil stress changes and so does the position of the boundary plane. This can be visualized in an extreme case.

When the soil stress ratio is at *active* failure, the slip surface of the soil is at an angle of $(45 - \phi_{max}/2)$ with the wall, where ϕ_{max} is the maximum frictional angle of the soil. The wall then rotates towards the soil until *passive* failure occurs. At *passive* failure, the slip surface is at an angle of $(45 + \phi_{max}/2)$ to the wall. If the stress state in the soil mass bounded by the slip surfaces is assumed to be uniform, then during wall rotation the boundary for the uniform stress moves progressively from the *active* slip plane to the *passive* slip plane. Because this boundary plane rotates during the imposition of cyclic displacements from the wall, it is termed the transitional boundary surface (TBS).

Currently, the TBS is defined in the analysis from the spatially mobilized plane (SMP) concept, which was introduced by Matsuoka (1974) for modelling frictional materials such as granular soil. The SMP is the plane on which particles are most readily mobilized (on average) under three-dimensional stress conditions. On the SMP, the shear stress to normal stress ratio is maximized and is considered to correspond to the potential sliding plane. Based on this concept, the angle θ between the TBS and the retaining wall can be expressed by the average wall stress ratio K as

$$\theta = \tan^{-1} K, \tag{11.1}$$

where K is the (total lateral earth force acting on the wall)/(total lateral earth force acting on the wall in the hydrostatic state with a triangular pressure block distribution assumed).

Additional approximations allow the soil to be represented by a set of horizontal slices in the form of a series of connected soil model elements as described in Chapter 9, connected to the retaining wall at one end and to the TBS at the other end. This simplification is similar to the simplified method of slices proposed by Bishop for slope stability work. The equilibrium of each horizontal soil layer inside the effective soil mass is always maintained. When the TBS moves (as stress changes occur during a reduction in wall displacements (Figure 11.1)), some elements fall behind the current boundary and are no longer subjected to the change in stress. The effective length of each soil layer is then defined in terms of the effective wall reaction ratio K as

$$L = h\sqrt{K}, \tag{11.2}$$

where h is the height of the layer above the toe of the retaining wall.

Interaction between the soil layers is accounted for in the current approach only indirectly. Because the stress ratio of each soil layer is not in general equal to the average wall stress ratio, the boundary calculated by the soil layer stress ratio R will differ from that calculated from the average wall stress ratio K. This difference is caused by the interaction between the soil layers and may cause a significant departure from a smooth boundary due to local stress concentrations. In order to stabilize the simulation computations, the boundary for each soil layer is defined in terms of the average position calculated from the use of K and R (substituted for K) taken separately in Equation 11.2. This averaged approach generates a TBS in the form of a smooth non-linear curve.

It has been observed from previous retaining wall experiments (Hambly and Burland, 1979; Terzaghi, 1934) that, under the same imposed displacement by the wall, the ratio of soil strain to wall displacement is smaller when related to *passive* loading than to the *active* condition (Figure 11.2). This observation is well explained by the 'effective soil mass' concept. Finite-element analyses carried out by Potts and Fourie (1986) and Nakai (1985) also indicated that there is little change in the stress state of the soil outside the effective soil mass in both *active* and *passive* monotonic wall rotations about the wall base.

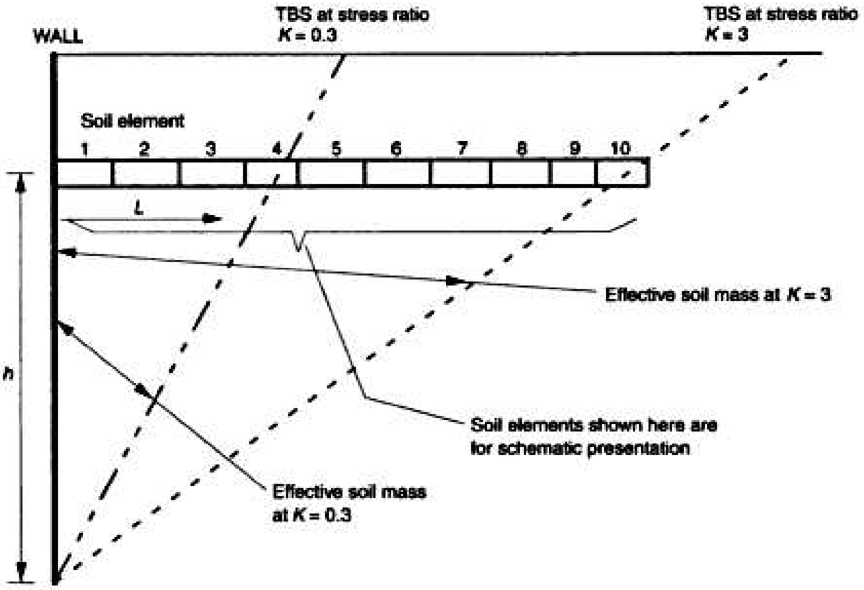

Figure 11.1 Schematic illustration of the transitional equilibrium method for retaining wall analysis. At $K = 0.3$ only elements 1–4 are undergoing strain; however, at $K = 3$, elements 1–10 take part in the straining process. Compatibility is maintained over all time, while equilibrium is only maintained within the current effective soil mass bounded by the wall and the TBS. L is defined in Equation 11.2

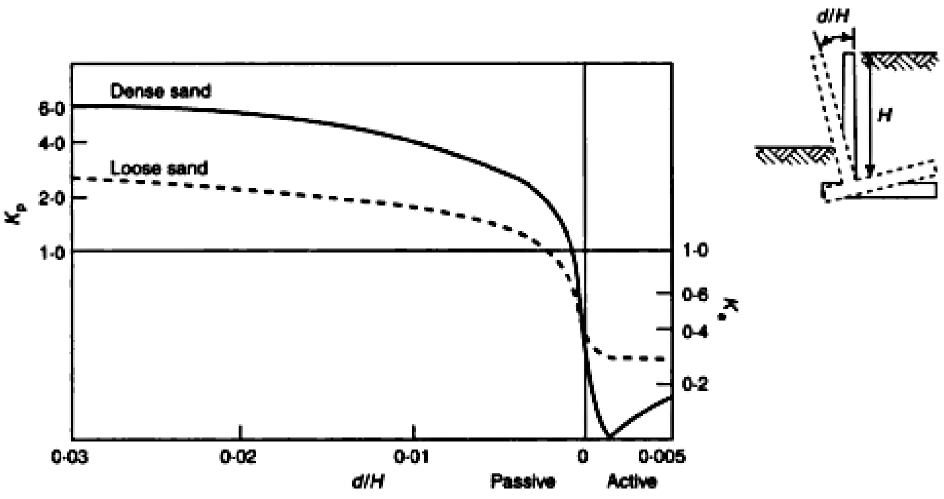

Figure 11.2 Wall reaction ratio versus wall displacement. (After Hambly and Burland, 1979)

Although friction between the wall and the granular soil is ignored in the simulations presented here, this feature is not considered to be influential because, as noted by Scott (1980), friction between the wall and the soil need not be considered due to the existence of traffic vibration, which makes it doubtful that the friction can be sustained.

In summary, the assumptions employed here are as follows:

- the TBS is defined using the SMP concept,
- wall friction is ignored,
- the soil is in plane strain,
- the granular backfill surface is horizontal initially, and
- the wall–soil interface is vertical initially.

11.3 Post-peak cyclic loading

Although it is unlikely that the granular backfill will ever be subjected to *passive* failure which requires a very large wall rotation, the possibility of *active* failure cannot be ruled out. Experiments (Hambly and Burland, 1979) have demonstrated that the amount of wall rotation needed to cause extensional failure is relatively much smaller than that required for compressive failure. During cycling, the soil properties (fabric and void ratio) of each element change at different rates depending on their relative location. Some elements will be 'weaker' than others. When a shear band is formed, a soil element may experience strain softening, while another may simply experience unloading (Figure 11.3). This causes a significant disparity in the changes in the void ratio, because strain softening always associates with dilation while unloading associates with densification. This phenomenon is handled in the computer program by the following assumptions:

- when the values of R_a for all elements in a layer of the effective mass differ by less than 5% from each other, a shear band forms on the TBS,
- when the values of R_a of all the elements in a layer differ by more than 5%, a shear band forms in the element with the highest R_a value, and
- the shear band width is 300 mm,

where R_a is the stress ratio σ_h/σ_v at *active* failure for a soil element.

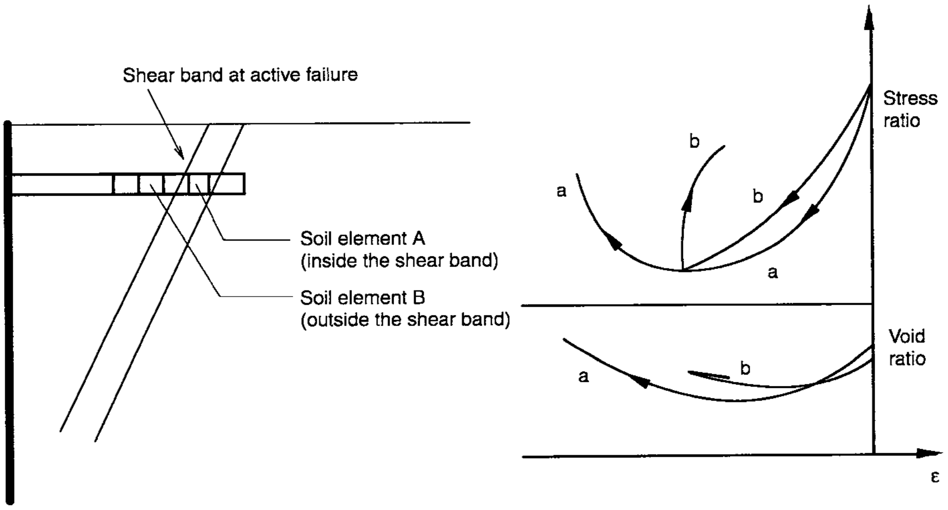

Figure 11.3 Schematic illustration of the variation in soil elements due to the formation of a shear band during *active* failure

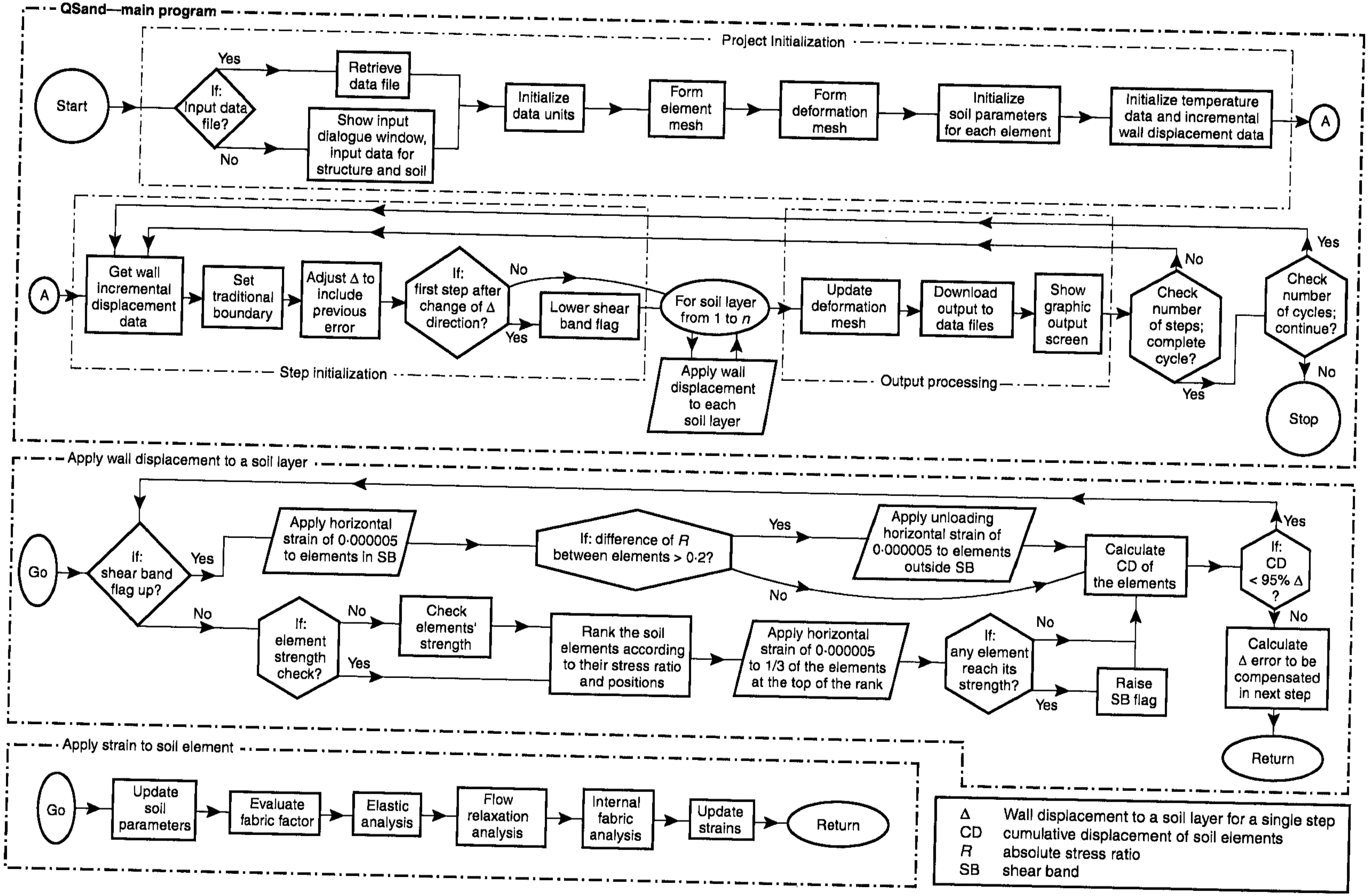

Figure 11.4 Flow chart for the retaining wall analysis computer program

11.4 Flow chart for the program

The program is divided into five major components, namely:

(*a*) project initialization,
(*b*) initialization for the wall displacement incremental step,
(*c*) application of the wall displacement to soil layers,
(*d*) application of strain to the soil elements, and
(*e*) output processing.

The interrelationship of these components is demonstrated in Figure 11.4. In summary, the wall rotation is applied step-by-step incrementally. The position of the TBS is updated at the beginning of each wall-displacement step. Different amounts of horizontal strain are applied to each of the soil elements to maintain their equilibrium, while the total deformation of soil elements in a horizontal slice is compatible with the wall displacement at that level, Δ.

12 Test equipment

12.1 Biaxial test equipment

The biaxial test apparatus of University College London has been described in detail by Arthur *et al.* (1980). Brief details are presented here to illustrate the original form of the apparatus (Figure 12.1) as used for tests with stress-controlled boundaries to the soil element. Recent modifications, which involved the removal of two opposing platens with air pressure bags and their replacement by stiff oil-filled metal platens (Figure 12.2), allow the apparatus to be used also under displacement boundary control. Figures 12.3 and 12.4 show the general layout of the complete apparatus at the time of conducting a test.

12.2 Model retaining wall apparatus

A model retaining wall apparatus was constructed to study the effects of temperature-induced loading on the abutments of integral bridge structures. The temperature variations were simulated by imposing rotational displacements to the retaining wall, and these were such as to model both seasonal and daily cycles. The general details of the apparatus are shown in Figure 12.5.

The retaining wall is 300 mm wide and 585 mm high, allowing soil depths of up to 570 mm to be tested. The stiff wall which is supported by a hanger frame is constrained to move between two glass side panels each 19 mm in thickness. Friction between the wall and glass panels is minimized by the use of adjustable PTFE seals along the full height of the wall. The wall rotational displacements are imposed by a geared drive with a fixed-hinge prop. The drive and the prop are 470 mm and 50 mm above the base, respectively. This provides an effective wall height of 520 mm for the test. Stress measurements were made on the face of the wall using ceramic pressure transducers (Figure 12.6). At the back of the wall, forces were recorded from load cells contained within the drive and the prop. Soil movements were recorded by monitoring markers placed close to the glass surface on the inside of the apparatus and by observing the distortion created to coloured sand marker lines installed during the initial filling of the apparatus. Surface displacements were also recorded.

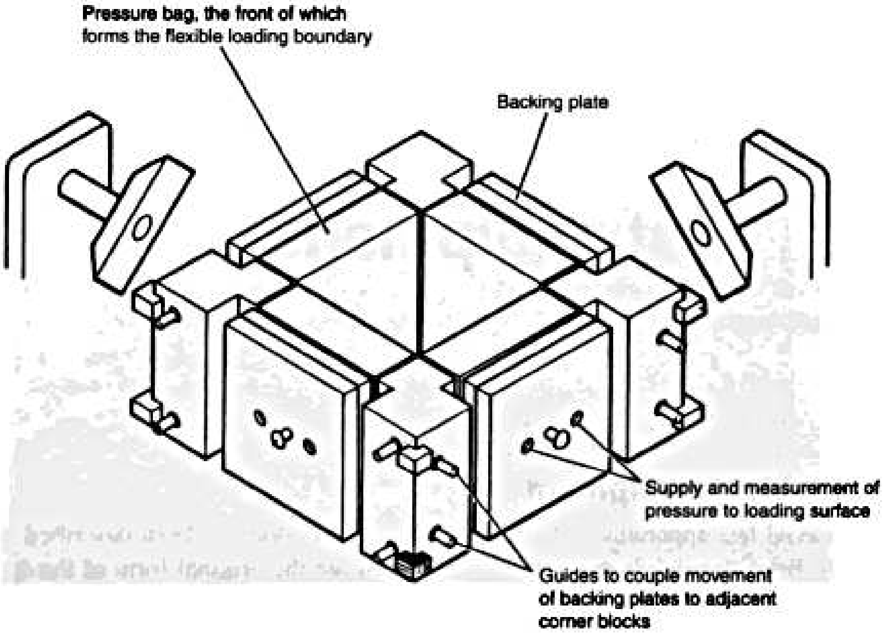

Figure 12.1 The biaxial tester with stress imposed boundary conditions

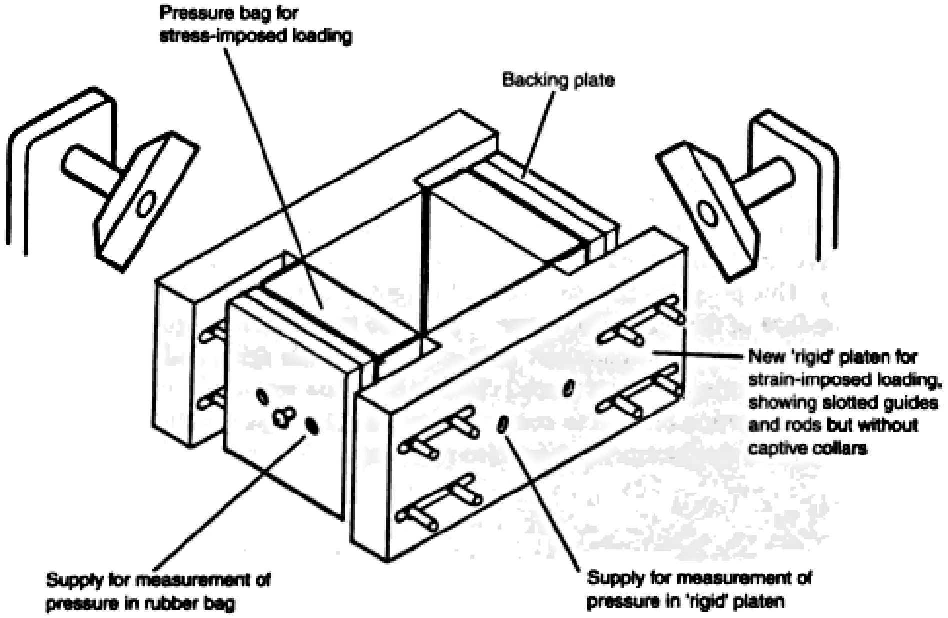

Figure 12.2 The biaxial tester with two pressure bags for stress imposition and two oil-filled metal platens for displacement imposition

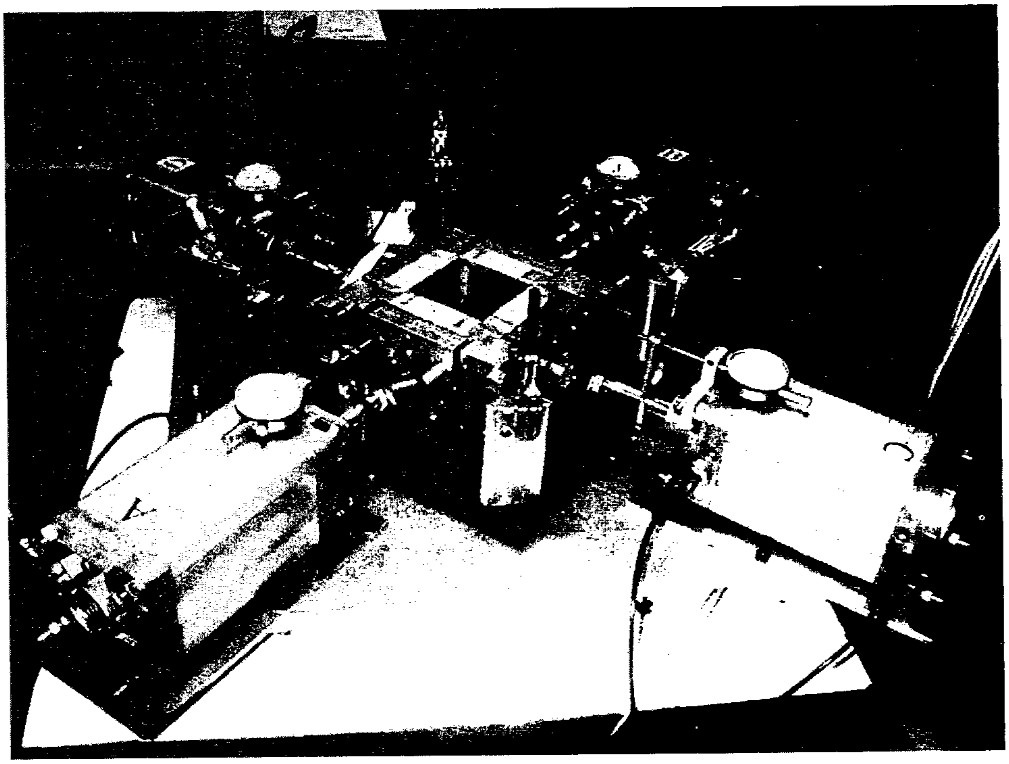

Figure 12.3 Biaxial tester set up for stress-controlled testing

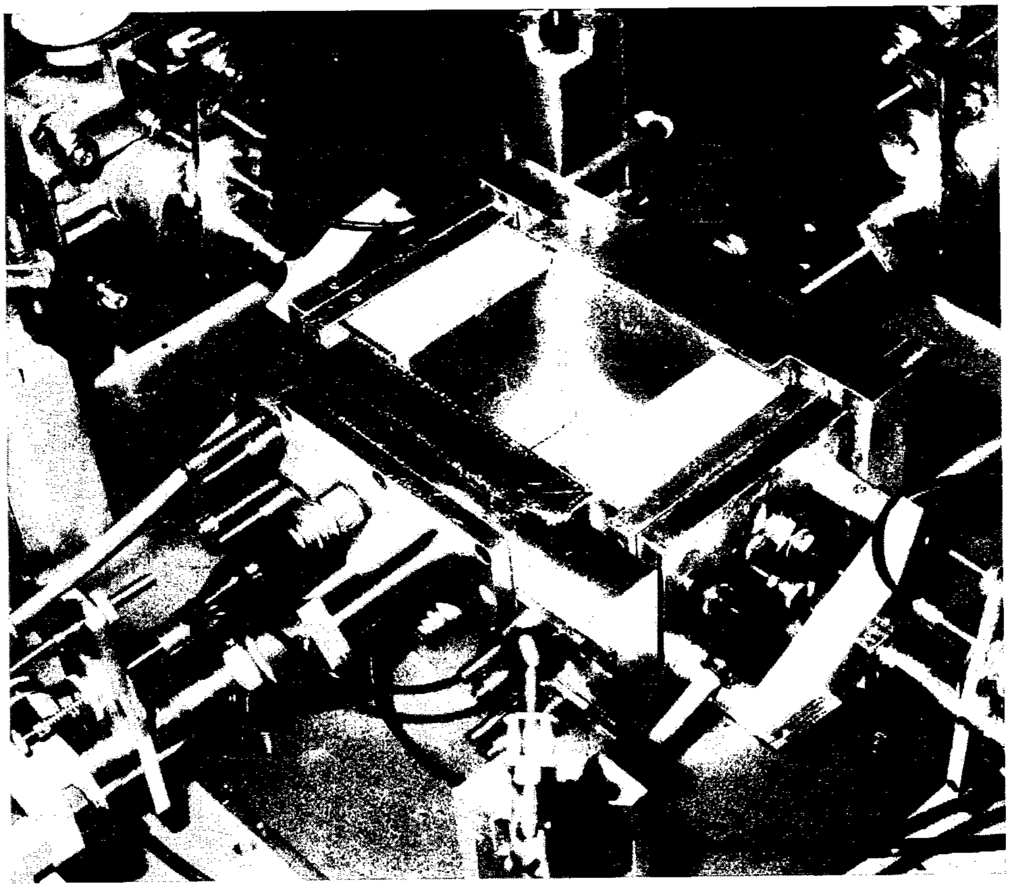

Figure 12.4 Biaxial tester set-up for strain-controlled testing

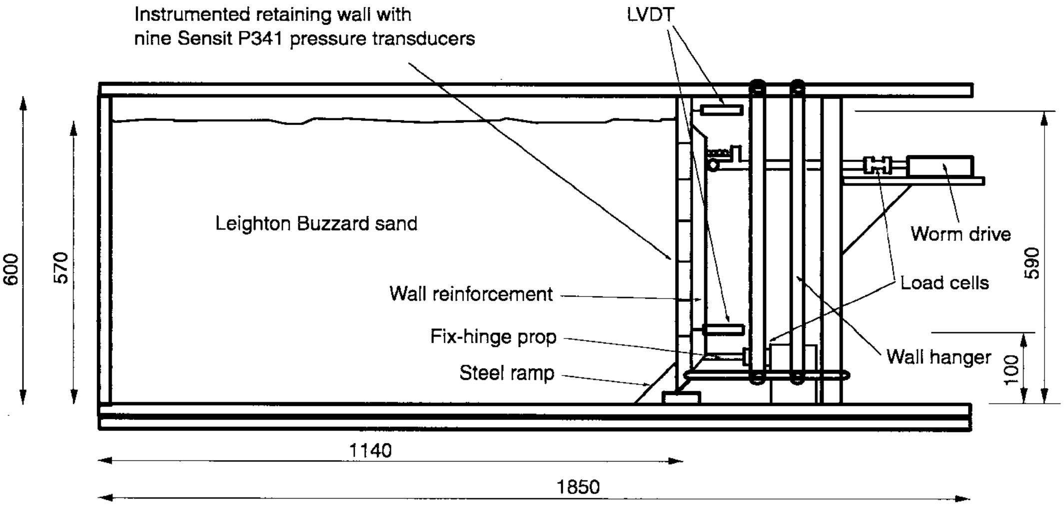

Figure 12.5 General details of the retaining wall apparatus (dimensions in mm)

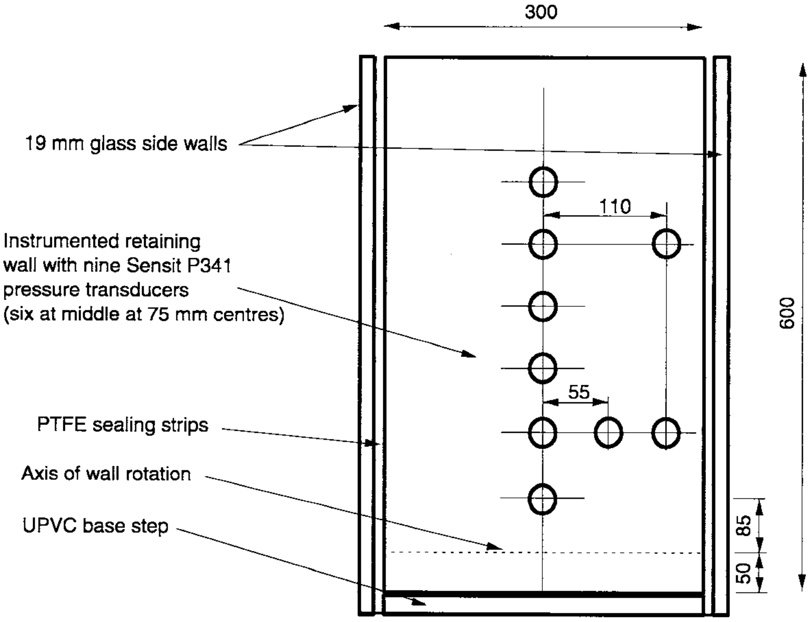

Figure 12.6 Layout of the ceramic pressure transducers installed in the face of the retaining wall (dimensions in mm)

Appendix 2

1 Explanation of strain ratcheting

Before the detailed cyclic behaviour of drained granular material (GM) is described, its basic stress–strain response is presented (Figure A2.1). The self-weight vertical stress of a contained GM, $\sigma_V = \gamma z$, creates horizontal stresses, $\sigma_H = K\sigma_V$, where K is initially taken to be a constant, z is the depth below the soil surface and γ is the unit weight of the GM. Initially, $K = K_0$, the coefficient of soil pressure at rest (point C in Figure A2.1). Compressive or extensional strains, applied in the horizontal direction, create stress changes defined by general points b and a on the virgin loading curves C–B and C–A. Reversal of the strains leads to responses on the curves b–A and a–B being traced. Additional cyclic strains follow paths which are no longer associated with the virgin loading paths. The cyclic responses to the application and removal of either stress or strain increments is both non-linear and generally non-repeating.

The GM is influenced by the geometrical dimensions and properties of both the structure and GM. At the element level the cyclic strain behaviour can be described in plane strain conditions by the two-component model shown in Figure A2.2.

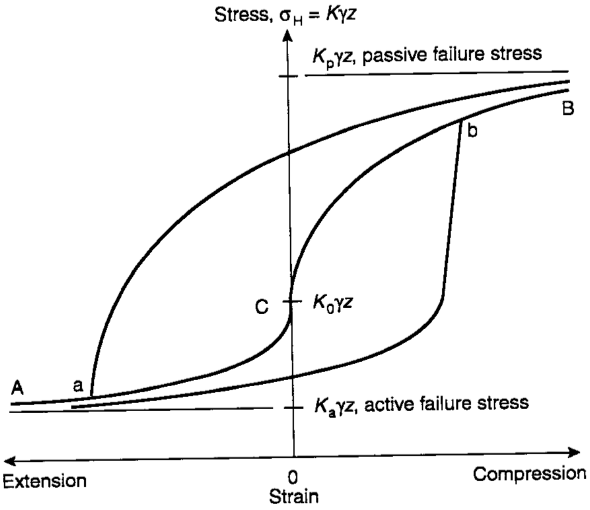

Figure A2.1 Stress–strain relationship of drained granular material under virgin load, unload and reload

Two-component model

The model shown in Figure A2.2 (England and Dunstan, 1994) is used to describe the displacement and stress development at the soil–structure interface due to temperature variations in the *structure component* (2), referred to now as StC. The *soil component* (1), referred to as SoC, is assumed to show no variation with temperature. To help quantify the magnitude of the fluctuating stress and strain amplitudes, the displacement of the soil–structure interface is described both in relation to the soil strains ε_x, and in terms of the system or structural displacement Δ^*; using the non-linear stress–strain relationship for the GM and the elastic load/displacement characteristics for the structure. The interface stress between the two components is σ_{x0} initially, at temperature T_0 in the StC. The vertical stress at depth h is $\sigma_v = \sigma_z = \gamma h$ = constant, and the horizontal stress $\sigma_H = \sigma_{x0}$, leads to $\sigma_{x0}/\sigma_z = K_0 < 1$ usually. When the StC is subjected to a constant temperature variation of $\pm\Delta T$, cyclic displacements are imposed on the SoC, such that interface stresses σ_x increase cycle by cycle simultaneously with a shortening of the elastic StC. This behaviour results initially because $\sigma_{x0} < \sigma_z$, and it persists thereafter for as long as σ_x remains smaller than the vertical stress σ_z during subsequent cycles. The shakedown state is reached when σ_x alternates (symmetrically in stress ratio terms) above and below the value of σ_z during a complete cycle.

The deformational behaviour illustrated in Figure A2.2 can be used to construct an interaction diagram (Figure A2.3) which defines the strain ratcheting behaviour and stress escalation leading to a shakedown state. The axes are suitably scaled to reflect the relationships between interface, or structural displacement Δ^* and GM strain ε_x; and between the interface stress σ_x and the axial force F. In general terms these relationships have the form

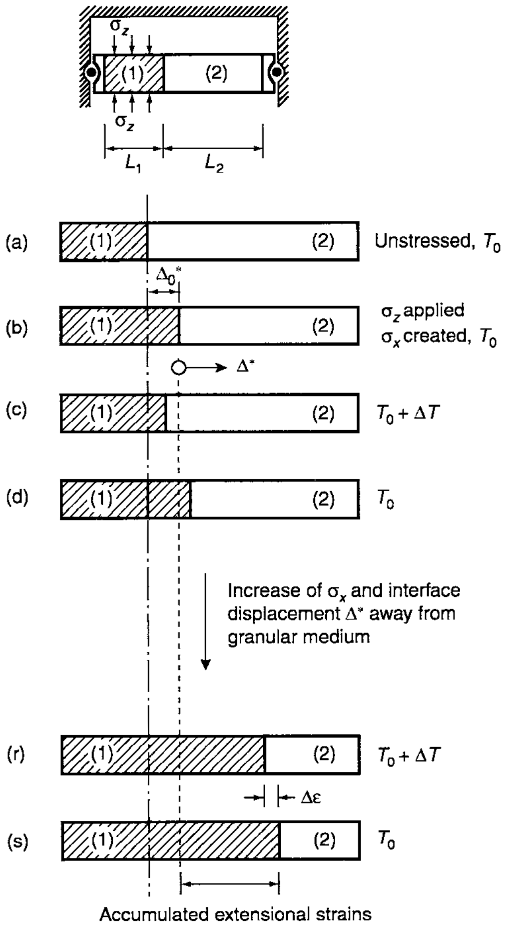

Figure A2.2 Deformational characteristics of the two-component model due to cyclic temperature variations. Element 1 is the soil component (SoC) and element 2 represents the elastic structure (StC) (see also Figure 8.8)

$$\Delta^* = \varepsilon_x \phi \tag{A2.1}$$

$$F = \sigma_x \psi. \tag{A2.2}$$

For the two-component problem discussed here, $\phi = L_2$ and $\psi = A$ is the cross-sectional area of the elements. The position of the GM–structure interface is described at all times to lie between the lines x–x or y–y in Figure A2.3; the slopes of which are defined by the structural stiffness k, and their horizontal separation Δ_α^* is the free thermal displacement resulting from the temperature change ΔT.

Also,

$$k = AE/L_2 \tag{A2.3}$$

$$\Delta_\alpha^* = L_2 \alpha \, \Delta T, \tag{A2.4}$$

where α is the coefficient of linear thermal expansion of the structure.

The stress escalation and ratcheting strains and displacements, caused by repeated temperature cycles, cease at the shakedown state. The upper shakedown stress $\sigma_{x_r} = \sigma_h + \Delta\sigma_1$, the lower shakedown stress $\sigma_{x_s} = \sigma_h - \Delta\sigma_2$, the magnitude of the fluctuating strain $\Delta\varepsilon_x$, and the total structure displacement are now evaluated. The parameter σ_h is the hydrostatic (i.e. isotropic) state of stress for $K = 1$. The amplitude of the fluctuating stress (from Figure A2.3) is evaluated as

$$\Delta\sigma = \Delta_\alpha^* / (\psi/k + \phi/k_s) \tag{A2.5}$$

$$\Delta\sigma = \Delta\sigma_1 + \Delta\sigma_2 \tag{A2.6}$$

$$\Delta\sigma_1 \neq \Delta\sigma_2.$$

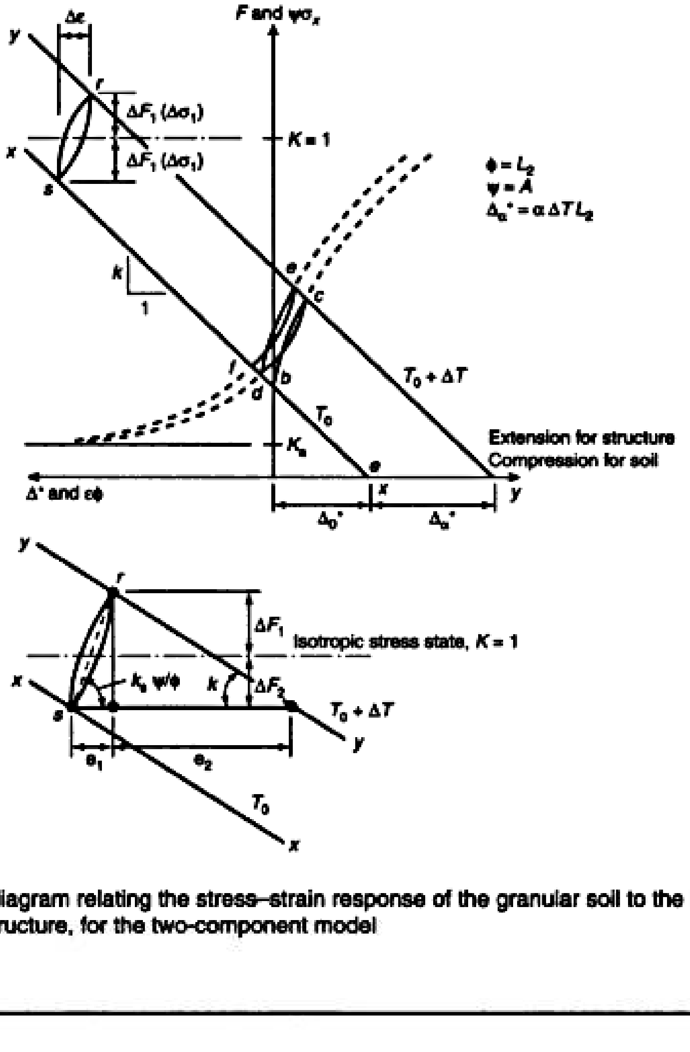

Figure A2.3 Interaction diagram relating the stress–strain response of the granular soil to the load–displacement behaviour of the elastic structure, for the two-component model

Appendix 2

2 Numerical soil model: detailed logic

Philosophy

Before describing the step-by-step procedures that are necessary to determine the soil element parameters during the application of each strain increment, it is appropriate first to describe the overall concept of using a pseudo-viscoelastic representation for the soil. The elastic and non-elastic behaviour of the soil is represented by a Burgers model (see Figure A2.10(a)) in each of the three orthogonal stress directions. In this representation the material behaviour is not, however, regarded as being viscous because the traditional time parameter in conventional viscoelastic formulations is replaced by *elapsed strain* for the soil modelling. This means that non-elastic strains develop only during the straining process. Stresses are thus time invariant when strain is not occurring. While, up to this point, the logic is similar to the endochronic representation for soil (Bazant and Krizek, 1976; Valanis, 1971), the new model introduced here uses a different approach to predict the plastic response.

The elements of the model are fully coupled in three dimensions through elastic and flow Poisson ratio terms for the Maxwell spring E and dashpot viscosity η. The Kelvin units are left uncoupled. Elastic behaviour is represented by the spring element, E. This defines the soil stress σ, and the flow component of strain is controlled by the dashpot parameter η. A flow Poisson ratio ν_f couples the overall flow behaviour and is responsible for satisfying plastic volume change. These material properties are all variables during the analysis. The Kelvin unit is included in the model fabric change, i.e. anisotropy.

Mathematically, the total change in stress is taken to consist of two components: *elastic stress* $\Delta\sigma^e$ and *plastic stress*. The plastic stress is further divided into *flow* $\Delta\sigma^f$ and *internal fabric* $\Delta\sigma^i$ components. The model is then set up on an incremental basis whereby, after the application of an increment of strain, the soil stress is permitted to relax at fixed strain with regard to the flow component only of the model (Maxwell dashpot). Then the Kelvin stress is permitted a change simultaneously with a change in Maxwell spring stress to maintain internal compatibility; the Maxwell dashpot is 'frozen' during this operation. Figure A2.10 shows the Burger unit and the corresponding steps for evaluating the three stress components. The importance of the changes in void ratio and confining pressure are taken into account in the numerical calculation by updating the void ratio and confining pressure between each incremental step of the analysis such that the changes introduced between any two incremental steps are always consistent with other soil parameters, in particular with the current principal stress ratio. The stress–dilatancy relationship proposed by Rowe, as modified by Wan and Guo (1998, 1999), is employed to provide this information.

The material properties that must be updated at the beginning of each strain increment are first described. Then, the plane strain formulation for evaluation of stress–strain is presented. For a more detailed description, the reader is referred to Tsang (1998).

Material functions

The two most influential parameters are the void ratio e and the mean confining stress σ_c. The elastic and flow parameters are strongly linked to e and σ_c through a void function F_e defined as

$$F_e = (A - e)^2/(1 + e), \tag{A2.7}$$

where

$$A = e_{cr} + \sqrt{(1 + e_{cr})} \tag{A2.8}$$

and e_{cr} is the critical state value of e.

The soil elastic modulus is the Maxwell spring modulus:

$$E = E_0 F_e (\sigma_c)^n. \tag{A2.9}$$

In this equation E_0 and n are obtained from experimental results during a normalization of E with respect to the void ratio and confining stress. The value of n is typically between 0.4 and 0.5.

Similarly, the flow parameter is defined as

$$\eta = \eta_0 F_e (\sigma_c)^m. \tag{A2.10}$$

For the model to satisfactorily predict a critical state stress ratio which is unique and independent of confining pressure, $m = 1$ is the required condition.

For the Kelvin element similar representations have been assumed to apply:

$$E_k = E_{k0} F_e (\sigma_c)^n \tag{A2.11}$$

$$\eta_k = \eta_{k0} F_e \sigma_c. \tag{A2.12}$$

The following additional information is needed to operate the model:

- A relationship linking the critical state void ratio e_{cr} and the mean confining stress. Thus,

  $$e_{cr} = e_{c0} - \lambda \ln \sigma_c/\sigma_{c0}. \tag{A2.13}$$

  Here e_{c0} and σ_{c0} refer to a reference condition for which the associated value of λ is obtained from experiments.
- A dilatancy relationship to link rate of change of volumetric strain with stress ratio and the flow Poisson ratio for the model. Rowe's dilatancy rule, as modified by Wan and Guo (1997), is taken to apply here. Hence,

  $$\sigma_1/\sigma_3 = (1 - \Delta\varepsilon_{v,p}/\Delta\varepsilon_{1,p})[1 + (e/e_{cr})^\alpha \sin\phi_{cr}]/[1 - (e/e_{cr})^\alpha \sin\phi_{cr}]. \tag{A2.14}$$

  $\Delta\varepsilon_{v,p}$ and $\Delta\varepsilon_{1,p}$ are respectively the plastic volumetric strain and plastic component of direct strain as applied to the model. The value of α is obtained from experiments; typically, α between 0.2 and 0.3.

The relationship between the flow Poisson ratio ν_f and the volumetric strain ε_v is determined as follows for an elemental cube, in terms of the corresponding plastic components of strain. For $\Delta\varepsilon_1 = \Delta\varepsilon_{1,p} + \Delta\varepsilon_{1,e}$ applied, the resulting plastic changes are $\Delta\varepsilon_{2,p} = \Delta\varepsilon_{3,p} = -\nu_f\,\Delta\varepsilon_{1,p}$. Thus,

$$\Delta\varepsilon_{v,p} = \Delta\varepsilon_{1,p} + \Delta\varepsilon_{2,p} + \Delta\varepsilon_{3,p} = \Delta\varepsilon_{1,p}(1 - 2\nu_f).$$

Giving

$$\nu_f = 0.5(1 - \Delta\varepsilon_{v,p}/\Delta\varepsilon_{1,p}). \tag{A2.15}$$

The elastic component of the applied strain increment $\Delta\varepsilon_{1,e}$ forms the subject of a separate calculation. This is described in Step 9 of the calculation procedures given at the end of this appendix.

The link between the stress ratio and the Poisson ratio is thus established through Equations A2.14 and A2.15.

Flow modifications to allow for anisotropy (fabric)

Residual soil anisotropy on return to the hydrostatic state has been recorded in experiments (Arthur *et al.*, 1977; Rodriguez, 1977). On reloading after one load–unload cycle soil behaves more stiffly, until the stress is close to the previously attained peak stress. Only when the soil stress is within the vicinity of this limit does the soil exhibit softer behaviour. In the modelling of this feature recognition has been given to the soil fabric, which has been created during earlier stressing by using the Kelvin element.

For the above analysis to apply to both monotonic and cyclic loading the additional parameter ψ has been introduced into Equation A2.10 to account for the changing plastic response due to anisotropy (fabric). This parameter is dependent on the sense of the strain increment used in the analysis (i.e. loading or unloading) and current values of the soil stress ratio $R = \sigma_1/\sigma_3$, the soil fabric through the Kelvin stress ratio $K = \sigma_1^K/\sigma_3^K$, and the void ratio. Equation A2.10 becomes

$$\eta = \eta_0 F_e \sigma_c \psi. \qquad \text{(A2.16)}$$

In building up a suitable logic, reference has been made to the monotonic stress–strain behaviour and, in particular, to the relationship between the soil stress ratio R and the amount of soil fabric in existence, defined in the model by the Kelvin stress ratio K. For a given initial void ratio and confining pressure the relationship between R and K is unique and allows the soil stress ratio to be interpreted as the strength of the current fabric defined by K. Figure A2.4 illustrates the relationship between R and K for two void ratios.

Thus, during monotonic loading (or *compressive straining*), knowledge of K defines an associated (maximum) fabric strength, denoted here by S_f. Results for different initial void ratios and confining pressures (Figure A2.5) have produced a family of R–K curves which have been normalized with respect to (e/e_{cr}) as shown in Figure A2.6. The linear portion of the normalized plot has the equation

$$(S_f - 1)(e/e_{cr})^{N_1} = a_1(K - 1) + b_1. \qquad \text{(A2.17)}$$

For Leighton Buzzard sand, $N_1 = 1.4$, $a_1 = 0.72$ and $b_1 = 0.82$.

For unloading (or *extensional straining*) the following equivalent equation to Equation A2.17 has been derived:

$$(1 - S_f)(e/e_{cr})^{N_2} = a_2K + b_2. \qquad \text{(A2.18)}$$

Experiments using Leighton Buzzard sand reveal $N_2 = 0.6$, $a_2 = -0.38$ and $b_2 = 0.88$.

Equations A2.17 and A2.18 have then been used to define the parameter ψ of Equation A2.16 through the following expressions:

- *Compressive straining*:

  $\psi = [(S_f - R)S_f + 1]^r$ for $(S_f - R) > 1$ and $\psi = 1$ for $(S_f - R) < 1$.

- *Extensional straining*:

  $\psi = [(R - S_f)/S_f + 1]^r$ for $(R - S_f) > 1$ and $\psi = 1$ for $(R - S_f) < 1$.

In these expressions $(S_f - R)$ is the difference between fabric strength and current soil stress ratios, and the power $r = 2$, here, was obtained from assessing experimental data for ratcheting strains.

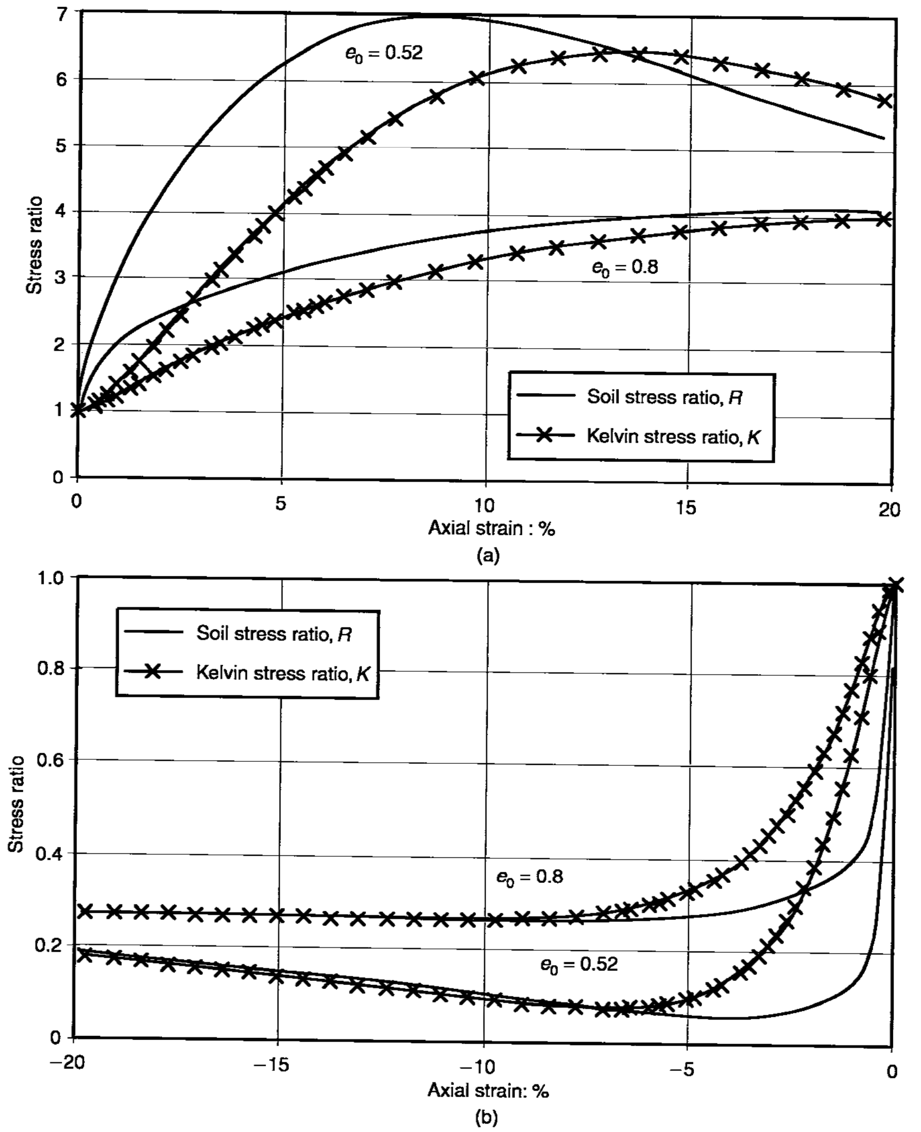

Figure A2.4 Typical numerical simulations displaying the soil stress ratios R and corresponding Kelvin stress ratios K for monotonic loading: (a) *passive*; (b) *active*

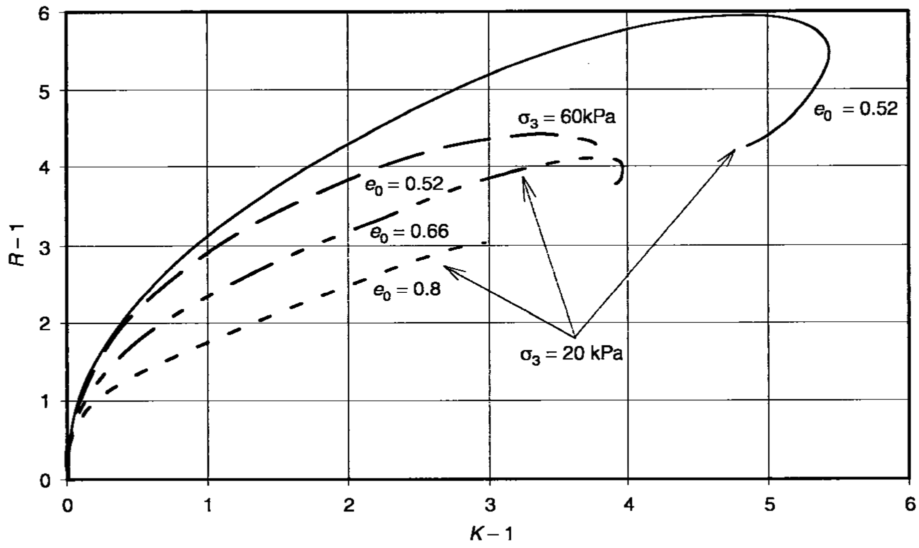

Figure A2.5 Relationship between the Kelvin stress ratio K and the soil stress ratio R for four *passive* monotonic load cases with various void ratios

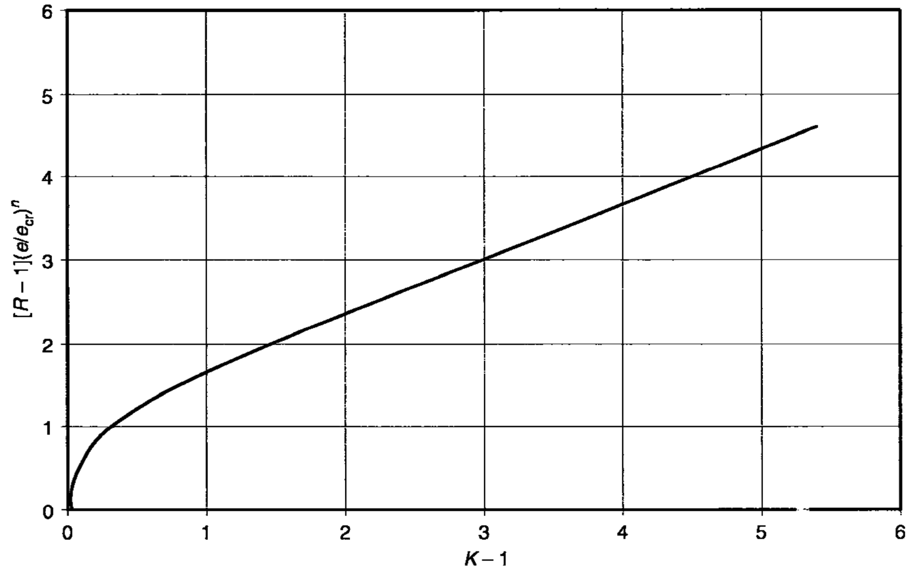

Figure A2.6 Normalized relationship between the Kelvin stress ratio K and the soil stress ratio R for the four monotonic load cases in Figure A2.5

Plane strain modelling

The soil model was formulated on the basis of applying repeated incremental strain steps and computing the new state of stress at every stage. The material properties updated at the beginning of each strain increment as above are kept constant during each strain step. The computations thus take the form of determining the state of stress after first assuming the strain change to take place elastically and then allowing stress relaxation to occur, consistent with the amount of imposed strain. Initially, the theory is formulated on a viscoelastic basis to obtain the basic stress–strain formulation. This is then converted to incremental form simultaneously with changing the time parameter in the viscoelastic formulation to a strain increment for the soil model.

The cube shown in Figure A2.7 describes the boundary conditions for the model. A viscoelastic analysis based on a Maxwell representation is first developed to describe the basic philosophy of the incremental analysis. Later, the Kelvin elements (to represent soil fabric) are introduced. When the Maxwell analysis is formulated in terms of deviator stresses, $s_y = (\sigma_y - \sigma_c)$ and $s_z = (\sigma_z - \sigma_c)$, it leads to the matrix differential form of Equation A2.20. Here σ_c is the mean confining pressure:

$$\sigma_c = (\sigma_x + \sigma_y + \sigma_z)/3 \tag{A2.19}$$

$$\begin{bmatrix} s_y \\ s_z \end{bmatrix} = e^{-\frac{E[V]t}{\eta}} \left\{ \begin{bmatrix} s_y(0) \\ s_z(0) \end{bmatrix} + \frac{\sigma_0}{3} \frac{(1-2\nu_f)}{(1-\nu_f)} \begin{bmatrix} 1 \\ 1 \end{bmatrix} \right\} - \frac{\sigma_0}{3} \frac{(1-2\nu_f)}{(1-\nu_f)} \begin{bmatrix} 1 \\ 1 \end{bmatrix}. \tag{A2.20}$$

In Equation A2.20 ν_f is the flow Poisson ratio; the terms $\sigma_0(1-2\nu_f)/3(1-\nu_f)$ are the steady-state values of s_Y and s_Z at infinite time, and the matrix $[V]$ has the form

$$[V] = \frac{1}{(1-\nu^2)} \begin{bmatrix} (1-\nu\nu_f) & (\nu-\nu_f) \\ (\nu-\nu_f) & (1-\nu\nu_f) \end{bmatrix}. \tag{A2.21}$$

In this expression, ν is the elastic Poisson ratio; and in Equation A2.20 $s_y(0)$ and $s_z(0)$ are the initial values of s_y and s_z, respectively.

In using Equation A2.20 to model soil behaviour the general form is retained, while time t is replaced by the imposed strain change $\Delta\varepsilon$ ($\Delta\varepsilon = \Delta\varepsilon_y$ here) during the incremental analysis. The steady-state terms $s_y(\infty)$ and $s_z(\infty)$ are zero when the soil is flowing at constant volume (e.g. in the critical state) and close to zero at other times. The significance of these terms has therefore been investigated for the incremental numerical analysis, and it has been possible to omit them from the soil model representation without any serious loss of precision. The resulting analysis is also simplified. The soil model equation when time t is replaced by strain ε is then

$$\begin{bmatrix} \sigma_y - \sigma_c \\ \sigma_z - \sigma_c \end{bmatrix} = e^{-\frac{E[V]\varepsilon}{\eta}} \begin{bmatrix} \sigma_y(0) - \sigma_c \\ \sigma_z(0) - \sigma_c \end{bmatrix}. \tag{A2.22}$$

Where, for the plane strain analysis, the soil is analysed for the initial isotropic stress condition: $\sigma_y(0) = \sigma_z(0) = \sigma_x = \sigma_0$. Thereafter σ_y and σ_z change due to the imposition of ε_y, applied successively as a series of increments $\Delta\varepsilon_y$ (Figure A2.8).

For $\varepsilon_z = 0$ the imposition of $\Delta\varepsilon_y$ gives the following incremental stresses for the elastic stage:

$$\begin{bmatrix} \Delta\sigma_y^e \\ \Delta\sigma_z^e \end{bmatrix} = \frac{E\,\Delta\varepsilon_y}{(1-\nu^2)} \begin{bmatrix} 1 \\ \nu \end{bmatrix}. \tag{A2.23}$$

The incremental flow-relaxation component of stress may be obtained from Equation A2.22 after rewriting it in the form

$$\begin{bmatrix} \sigma_y - \sigma_c \\ \sigma_z - \sigma_c \end{bmatrix} = e^{-\frac{E[V]|\Delta\varepsilon|}{\eta}} \begin{bmatrix} {}^1\sigma_y - \sigma_c \\ {}^1\sigma_z - \sigma_c \end{bmatrix}, \tag{A2.24}$$

where for the first step of the incremental analysis

$$\begin{bmatrix} {}^1\sigma_y \\ {}^1\sigma_z \end{bmatrix} = \begin{bmatrix} {}^0\sigma_y \\ {}^0\sigma_z \end{bmatrix} + \begin{bmatrix} \Delta\sigma_y^e \\ \Delta\sigma_z^e \end{bmatrix} \tag{A2.25}$$

and ${}^0\sigma_y = {}^0\sigma_z = \sigma_0$. It then follows that

$$\begin{bmatrix} \sigma_y - \sigma_c \\ \sigma_z - \sigma_c \end{bmatrix} - \begin{bmatrix} {}^1\sigma_y - \sigma_c \\ {}^1\sigma_z - \sigma_c \end{bmatrix} = \left(e^{-\frac{E[V]|\Delta\varepsilon|}{\eta}} - [I] \right) \begin{bmatrix} {}^1\sigma_y - \sigma_c \\ {}^1\sigma_z - \sigma_c \end{bmatrix}$$

i.e.

$$\begin{bmatrix} \Delta\sigma_y^f \\ \Delta\sigma_z^f \end{bmatrix} = \begin{bmatrix} \sigma_y - {}^1\sigma_y \\ \sigma_z - {}^1\sigma_z \end{bmatrix} = \left(e^{-\frac{E[V]|\Delta\varepsilon|}{\eta}} - [I] \right) \begin{bmatrix} {}^1\sigma_y - \sigma_c \\ {}^1\sigma_z - \sigma_c \end{bmatrix}. \tag{A2.26}$$

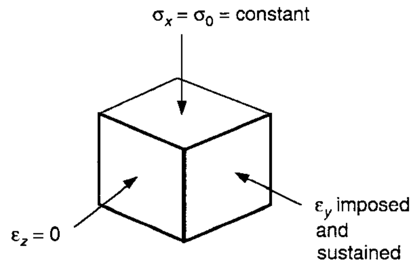

Figure A2.7 A soil element subjected to plane strain loading

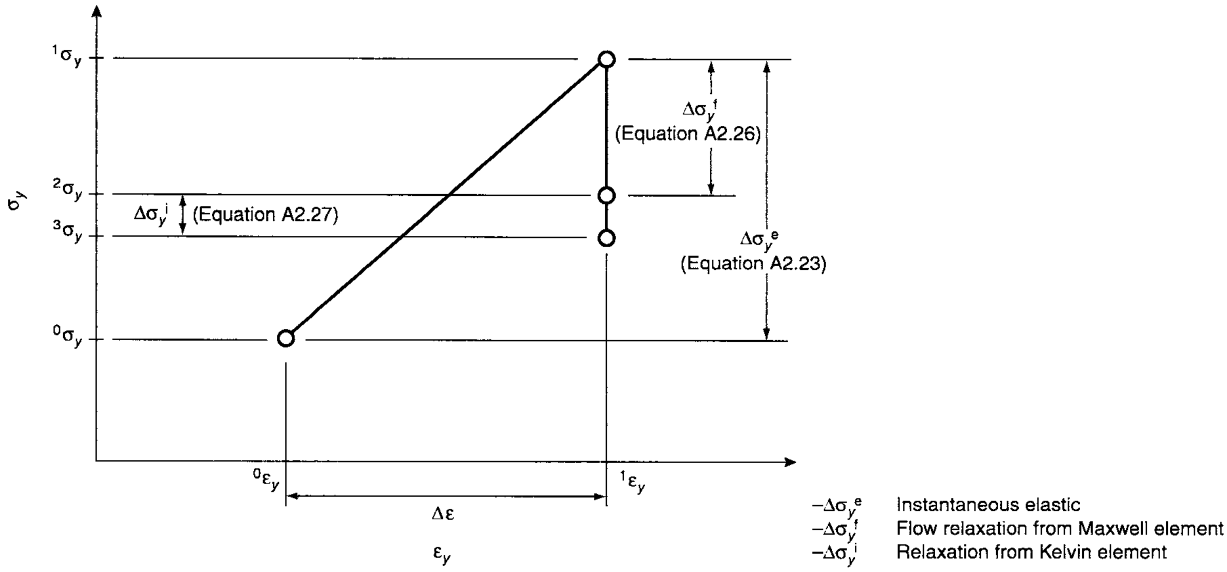

Figure A2.8 Stress increments for numerical analysis during application of the strain increment $\Delta\varepsilon$

For the uncoupled Kelvin elements, additional changes in stress occur as stress equilibrium is restored between the Kelvin and Maxwell components of the four-element Burgers representation shown in Figure A2.10. In stage (c) of the analysis the redistribution of stress between the Kelvin and Maxwell springs is defined by changes in stress $\Delta\sigma^K$ in the Kelvin spring and $\Delta\sigma^i$ in the Maxwell spring. These components have the values

$$\Delta\sigma^i = \frac{E}{E+E_k}\left(\sigma^K - {}^2\sigma\right)\left(1 - e^{-\frac{(E+E_k)|\Delta\varepsilon|}{\eta_k}}\right) \tag{A2.27}$$

and

$$\Delta\sigma^K = -\frac{E_k}{E}\Delta\sigma^i, \tag{A2.28}$$

where ${}^2\sigma$ is defined in Figure A2.8. Therefore,

$$\begin{bmatrix}\Delta\sigma_y^i\\ \Delta\sigma_z^i\end{bmatrix} = \frac{E}{E+E_k}\left(1 - e^{-\frac{(E+E_k)|\Delta\varepsilon|}{\eta_k}}\right)\begin{bmatrix}\sigma_y^K - {}^2\sigma_y\\ \sigma_z^K - {}^2\sigma_z\end{bmatrix}, \tag{A2.29}$$

where

$$\begin{bmatrix}{}^2\sigma_y\\ {}^2\sigma_z\end{bmatrix} = \begin{bmatrix}{}^0\sigma_y\\ {}^0\sigma_z\end{bmatrix} + \begin{bmatrix}\Delta\sigma_y^e\\ \Delta\sigma_z^e\end{bmatrix} + \begin{bmatrix}\Delta\sigma_y^f\\ \Delta\sigma_z^f\end{bmatrix}, \tag{A2.30}$$

and hence

$$\begin{bmatrix}{}^3\sigma_y\\ {}^3\sigma_z\end{bmatrix} = \begin{bmatrix}{}^0\sigma_y\\ {}^0\sigma_z\end{bmatrix} + \begin{bmatrix}\Delta\sigma_y^e\\ \Delta\sigma_z^e\end{bmatrix} + \begin{bmatrix}\Delta\sigma_y^f\\ \Delta\sigma_z^f\end{bmatrix} + \begin{bmatrix}\Delta\sigma_y^i\\ \Delta\sigma_z^i\end{bmatrix}. \tag{A2.31}$$

Finally,

$$\begin{bmatrix}\Delta\sigma_y^K\\ \Delta\sigma_z^K\end{bmatrix} = -\frac{E_k}{E}\begin{bmatrix}\Delta\sigma_y^i\\ \Delta\sigma_z^i\end{bmatrix}. \tag{A2.32}$$

Equations A2.23–A2.31 allow the incremental analysis to be described pictorially. Referring primarily to the stress σ_y (for convenience) the following procedures allow the stress–strain response to be defined from a general starting point $\sigma_y = {}^0\sigma_y$, say, at $\varepsilon_y = {}^0\varepsilon_y$ in Figure A2.8:

- Apply $\Delta\varepsilon$ and compute hypothetical elastic stress changes $\Delta\sigma_y^e$ and $\Delta\sigma_z^e$ from Equation A2.23, noting that E is a function of the void ratio and confining pressure.
- Compute new values of σ_y and σ_z; that is, ${}^1\sigma_y = {}^0\sigma_y + \Delta\sigma_y^e$ and ${}^1\sigma_z = {}^0\sigma_z + \Delta\sigma_z^e$.
- Compute the stress relaxation components $\Delta\sigma_y^f$ and $\Delta\sigma_z^f$ from Equation A2.26. This step requires the evaluation of E/η for the current confining pressure.
- The resulting values $\sigma_y = {}^2\sigma_y$ and $\sigma_z = {}^2\sigma_z$ are then modified by further relaxation components derived from the Kelvin elements, as shown in Equation A2.27. The final stresses are then ${}^3\sigma_y$ and ${}^3\sigma_z$, as given by Equation A2.31. These stresses then constitute the stresses at the start of the next incremental step.

Repeated application of incremental strain steps leads to the stress–strain response shown in Figure A2.9, where at large strains a critical state is predicted. This is characterized by new increments in stress $\Delta\sigma^e$ being identically balanced by new flow-relaxation increments $\Delta\sigma^f$, i.e. $\Delta\sigma^e + \Delta\sigma^f = 0$.

Figure A2.10 describes the sequence of stress changes for the four-element Burgers representation during the imposition of a strain increment $\Delta\varepsilon$. These changes are required in Step 8 of the analysis procedures given at the end of this appendix. First, $\Delta\varepsilon$ is applied instantaneously to the spring of the Maxwell element to generate an elastic stress $\Delta\sigma^e$. This is followed by stress relaxation within the

Maxwell element while the Kelvin element is held at zero strain; $\Delta\sigma^f$ results. At this stage the Maxwell dashpot is 'frozen' and stress change is allowed simultaneously within the Kelvin element and the Maxwell spring; $\Delta\sigma^i$ results.

Steps in the incremental analysis

An updated description of the incremental analysis follows. A single step in the analysis allows changes to be computed for the state of stress and strain. Thus assuming, $\sigma_y > \sigma_x$, the steps in the calculation are as follows

1. Determine the principal stress ratio: $\sigma_1/\sigma_3 = \sigma_y/\sigma_x$.
2. Compute the mean confining stress: $\sigma_c = (\sigma_1 + \sigma_2 + \sigma_3)/3$.
3. Determine the critical state void ratio e_{cr} from Equation A2.13.
4. Derive the void function F_e from Equations A2.7 and A2.8.
5. Evaluate E and η for the model from Equations A2.9 and A2.10.
6. Evaluate E_k and η_k for the Kelvin element from Equations A2.11 and A2.12.
7. Using the dilatancy expression (Equation A2.14), determine $\Delta\varepsilon_{v,p}$ for an applied strain increment $\Delta\varepsilon_y = (\Delta\varepsilon_{1,p} + \Delta\varepsilon_{1,e})$. $\Delta\varepsilon_{1,p}$ is described in Figure A2.10(d) (see also Steps 9 and 10). The flow Poisson ratio is then updated to become $\nu_f = 0.5(1 - \Delta\varepsilon_{v,p}/\Delta\varepsilon_{1,p})$.
8. Compute the changes in stress (in the y and z directions) at each stage, $\Delta\sigma^e$ from Equation A2.23, $\Delta\sigma^f$ from Equation A2.26, $\Delta\sigma^i$ from Equation A2.29 and $\Delta\sigma^K$ from Equation A2.32. The total soil stress change of this increment is $\Delta\sigma = \Delta\sigma^e + \Delta\sigma^f + \Delta\sigma^i$, and the new soil stress at the end of the increment is $\sigma_{new} = \sigma_{old} + \Delta\sigma$. Also, determine $\Delta\sigma_{new}{}^K = \Delta\sigma_{old}{}^K + \Delta\sigma^K$.
9. From $\Delta\sigma_z$ and $\Delta\sigma_y$ obtain $\Delta\varepsilon_{y,e} = [\Delta\sigma_y - \nu(\Delta\sigma_z + 0)]/E = \Delta\varepsilon_{1,e}$.
10. Deduce $\Delta\varepsilon_{y,p} = \Delta\varepsilon_1(\text{input}) - \Delta\varepsilon_{y,e}$. Set $\Delta\varepsilon_{y,p} = \Delta\varepsilon_{1,p}$ and obtain $\Delta\varepsilon_{v,p}$ from Equation A2.14.
11. Determine the change in volumetric strain due to hydrostatic compaction $\Delta\varepsilon_{v,c}$:
    (*a*) determine the new $\sigma_c = (\sigma_x + \sigma_y + \sigma_z)/3$;
    (*b*) determine the change in the void ratio $\Delta e_c = \kappa \ln(\sigma_{c.old}/\sigma_{c.new})$, from experimental data; and
    (*c*) form $\Delta\varepsilon_{v,c} = \Delta e_c/(1 + e)$.
12. Form the total volumetric strain change $\Delta\varepsilon_{v,tot} = \Delta\varepsilon_{v,p} + \Delta\varepsilon_{v,c}$. Then deduce $\Delta\varepsilon_x = \Delta\varepsilon_{v,tot} - \Delta\varepsilon_1$.
13. Update the void ratio $e_{new} = e_{old} + \Delta\varepsilon_{v,tot}(1 + e_{old})$.

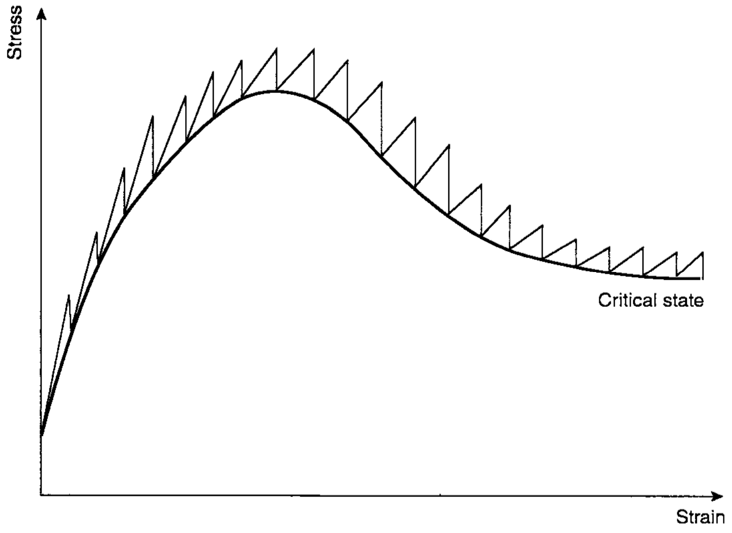

Figure A2.9 Stress–strain response from incremental analysis during monotonic loading

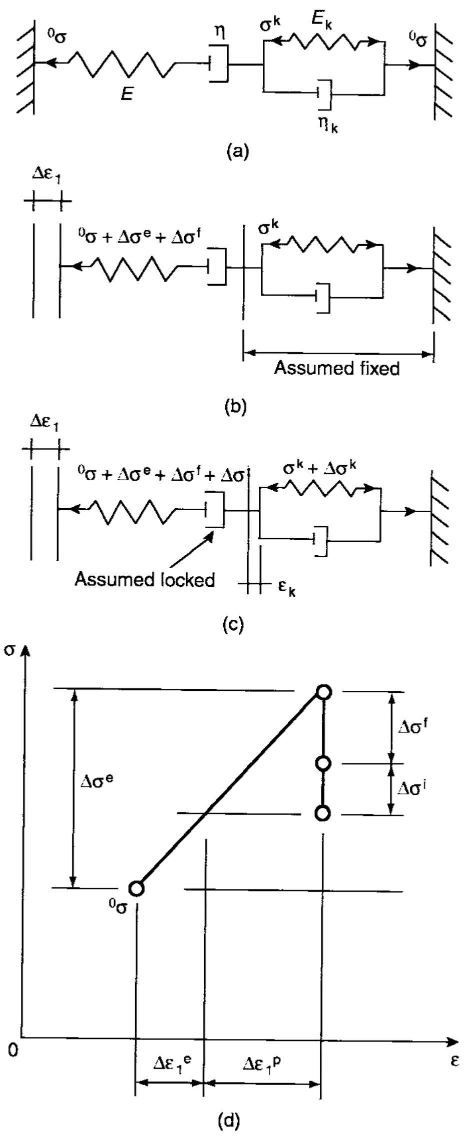

Figure A2.10 The logic for incremental analysis. (a) General stress condition; $\sigma > \sigma^K$ assumed. (b) $\Delta\varepsilon_1$ applied, causing an instantaneous elastic change in the stress $\Delta\sigma^e$ followed by a relaxation $\Delta\sigma^f$ due to flow in the Maxwell dashpot. The Kelvin element is frozen. (c) With the Maxwell dashpot frozen and the Kelvin element unfrozen, stress changes $\Delta\sigma^i$ and $\Delta\sigma^K$ restore the internal equilibrium. (d) Development of the stress–strain response after all incremental stress changes have been taken into account

References

Arthur, J. R. F., Dunstan, T. and Chua, K. S. (1977). Induced anisotropy in sand. *Géotechnique* **27**, 13–30.

Arthur, J. R. F., Dunstan, T., Chua, K. S. and del Rodriguez, C. (1980). Principal stress rotation: a missing parameter. *Proceedings of the ASCE* **106**(GT4), 419–433.

Arthur, J. R. F., Dunstan, T., Dalili, A. and Wong, R. K. S. (1991). The initiation of flow in granular materials. *Powder Technology* **65**, 89–101.

BA 42 (Highways Agency) (1996). *The Design of Integral Bridges. Design Manual for Roads and Bridges.* The Stationary Office, London, Vol. 1.2.12.

Bazant, Z. P. and Krizek, R. J. (1976). Endochronic constitutive law for liquefaction of sand. *Journal of the Engineering Division of the ASCE* **102**(EM2), 225–238.

Been, K., Jefferies, M. G. and Hachery, J. (1991). The critical state parameters. *Géotechnique* **41**(3), 365–381.

Bolouri-Bazaz, J. (1999). Sand subject to biaxial cyclic loading. PhD Thesis, University of London.

Broms, B. M. and Ingleson, I. (1972). Lateral earth pressure on a bridge abutment. *Proceedings of the 5th European Conference on Soil Mechanics and Foundation Engineering, Madrid* **1**, 117–123.

Budhu, M. (1979). Simple shear deformation of sands. PhD Thesis, Cambridge University.

Card, G. B. and Carder, D. R. (1993). *A Literature Review of the Geotechnical Apects of the Design of Integral Bridge Abutments.* Transport Research Laboratory, Crowthorne, Report PR 52.

Caquot, A. and Kerisel, J. (1948). *Tables for the Calculation of Passive Pressure, Active Pressure and Bearing Capacity of Foundation.* Gauthier-Villars, Paris.

CIRIA (1976). Design and construction of circular biological filter walls. CIRIA, London, Report 58.

Clough and Duncan (1971). Finite element analyses of retaining wall behaviour. *Journal of the Soil Mechanics and Foundation Engineering Division of the ASCE* **97**(SM12), 1657–1673.

Cole, E. R. (1967). The behaviour of soils in the simple shear apparatus. PhD Thesis, University of Cambridge.

Coulomb, C. A. (1776). Essai sur une application des regles de maximic et minimis a quelques problemes de statique relatifs a l'architecture. *Memoires de l'Academie Royale des Sciences, Paris* **5**(7), 343–382.

Dunstan T., Arthur J. R. F., Dalili A., Ogunbeken, O. O. and Wong, R. K. S. (1988). Limiting mechanisms of slow dilatant plastic shear deformation of granular media. *Nature* **336**, 52–54.

Emerson, M. (1973). *The Calculation of the Distribution of Temperature in Bridges.* Transport and Road Research Laboratory, Department of Environment, London, Report 561.

Emerson, M. (1976). *Bridge Temperatures Estimated from the Shade Temperature.* Transport and Road Research Laboratory, Department of Environment, London, Report LR 696.

Emerson, M. (1976). *Extreme Values of Bridge Temperatures for Design Purposes.* Transport and Road Research Laboratory, Department of Environment, London, Report LR 744.

Emerson, M. (1977). *Temperature Differences in Bridges: Basis of Design Requirements.* Transport and Road Research Laboratory, Department of Environment, London, Report 765.

England, G. L. (1994). The performance and behaviour of biological filter walls as affected by cyclic temperature changes. Serviceability of earth retaining structures. *ASCE Geotechnical Special Publication* **42**, 57–76.

England, G. L. and Dunstan, T. (1994). Shakedown solutions for soil containing structures as influenced by cyclic temperatures. *Proceedings of the 3rd Kerensky Conference; Global Trends in Structural Engineering.* Singapore, pp. 159–170.

England G. L., Dunstan T., Tsang C. M., Milhajlovic N., Bazaz J. B. (1995). Ratcheting flow of granular materials. In: M. Evans and R. Fragaszy (eds), *Static and Dynamic Properties of Gravelly Soils. Geotechnical Special Publication No. 56.* ASCE, 1995, pp. 64–76.

England, G. L., Dunstan, T, Wan, R. and Tsang, C. M. (1997). Drained granular material under cyclic loading with temperature-induced soil–structure interaction. *Applied Mechanics Review of the ASME* **50**(10), 553–579.

Fang, Y. S. and Ishibashi, K. (1986). Static earth pressure with various wall movements. *Journal of the Geotechnical Engineering Division of the ASCE* **112**(3), 317–333.

Hambly, E. C. and Burland, J. B. (1979). *Bridge Foundations and Substructures.* HMSO, London.

James, R. G. and Bransby, P. L. (1970). Experimental and Theoretical investigations of a passive earth problem. *Géotechnique* **20**, 17–38.

Janbu, N. (1957). Earth pressure and bearing capacity calculations by generalized procedure of slices. *Proceedings of the of the 4th International Conference, International Society of Soil Mechanics and Foundation Engineering* **2**, 207–213.

Matsuoka, H. (1974). A microscopic study on the shear mechanism of granular materials. *Soils and Foundations* **14**(1), 29–43.

Nakai, T. (1985). Finite element computations for active and passive earth pressure of retaining wall. *Soils and Foundations* **25**(3), 98–112.

Potts, D. H. and Fourie, A. B. (1986). A numerical study of the effects of wall deformation on earth pressures. *International Journal of Numerical and Analytical Methods in Geomechanics* **10**, 386–405.

Rankine, W. J. M. (1857). On the stability of loose earth. *Philosophical Transactions of the Royal Society, London* **147**(1), 9–27.

Regier, K. (1997). The stress-dilatancy behaviour of sands: pressure and density dependencies in both monotonic and cyclic loading regimes. MSc Thesis, University of Calgary.

Rodriguez, J. (1977). Induced anisotropy in a loose sand. PhD Thesis, University of London,

Rosenfarb, J. L. and Chen, W. F. (1972). *Limit Analysis Solutions of Earth Pressure Problems.* Fritz Engineering Laboratory, Lehigh University, Report 355.14.

Rowe, P. W. and Peaker, K. (1965). Passive earth pressure measurements, *Géotechnique* **15**(1), 57–78.

Schofield, A. N. (1961). The development of lateral force of sand against the vertical face of a rotating model foundation. *Proceedings of the 5th International Conference, International Society of Soil Mechanics and Foundation Engineering* **2**, 479–485.

Scott, C. R. (1980). *An Introduction to Soil Mechanics and Foundations*, 3rd edn. Applied Science, London.

Sherif, M. A. and Mackey, R. D. (1982). Earth pressures against rigid retaining walls. *Journal of the Geotechnical Engineering Division of the ASCE* **108**(GT5), 679–695.

Shields, D. H. and Tolunay, A. Z. (1973). Passive pressure coefficients by methods of slices. *Journal of Soil Mechanics and Foundations* **99**(SM12), 1043–1053.

Sokolovski, V. V. (1960). *Theoretical Soil Mechanics.* Wiley, New York.

Springman, S. M. and Norrish, A. R. M. (1993). Soil–structure interaction: centrifuge modelling of integral bridge abutments. *Henderson Colloquium: Towards Joint-Free Bridge.* Pembroke College, Cambridge.

Stroud, M. A. (1971). The behaviour of sand at low stress levels in simple shear apparatus. PhD Thesis, University of Cambridge.

Terzaghi, K. (1934). Large retaining wall tests, I-pressure of dry sand. *Engineering News Record* **112**, 136–140.

Terzaghi, K. (1943). *Theoretical Soil Mechanics.* Wiley, New York.

Tsang, C. M. (1998). Life-time analysis of continuous beam bridges with integral abutments using rheological models. PhD Thesis, University of London.

Valanis, K. C. (1971). A theory of viscoplasticity without a yield surface. *Archives of Mechanics (Varsovie)* **23**, 517–551.

Wan, R. G. and Guo, P. J. (1998). A simple constitutive model for granular soils: modified stress–dilatancy approach. *Computer and Geotechnics* **22**(2), 109–133.

Wan, R. G. and Guo, P. J. (1999). A pressure and density dependent dilatancy model for granular materials. *Soils and Foundations* **39**(6), 1–11.

Wong, R. K. S. and Arthur, J. R. F. (1986). Sand sheared by stresses with cyclic variations in direction. *Géotechnique* **36**(2), 215–226.

Wood, D. M. and Budhu, M. (1980). The behaviour of Leighton Buzzard Sand in cyclic simple shear tests. *International Symposium on Soils under Cyclic and Transient Loading.* Swansea.

Index

Integral bridges

A fundamental approach to the time-temperature loading problem

England, Tsang and Bush

Integral bridges have become increasingly popular in the UK over recent years. Problems and costs associated with failed expansion joints in conventional bridges not only make integral bridges a cost-effective option but also means they have longer lifespans that their counterparts. The Highways Agency standards now require that, wherever possible, all new bridges of less than 60 m length should be of integral form.

The growing importance of integral bridges has highlighted the need for more information and guidance to assist in improving bridge design. This book presents the results of research commissioned by the Highways Agency into the thermally induced soil/structure interaction created by environmental temperature changes and the associated cyclical displacements imposed on the granular backfill of bridge abutments. It:

- develops a better theoretical understanding of temperature-induced cyclic displacements; in particular the strain ratcheting in backfill soil in contact with a 'stiff' structure
- identifies the governing soil parameters and examines their influence
- develops numerical modelling procedures to predict soil behaviour
- identifies and quantifies the controlling features of bridge structures relevant to the interaction problem

This book provides essential information for bridge designers to aid their understanding of the cyclical changes in backfill pressures and settlement due to diurnal and annual changes in bridge deck temperature - a crucial factor when designing integral bridges.

HIGHWAYS AGENCY

Imperial College
OF SCIENCE, TECHNOLOGY AND MEDICINE

Thomas Telford

ISBN 0-7277-2845-8
9 780727 728456